Universität der Bundeswehr München

EXPERIMENTAL VALIDATION OF A CONTROL FRAMEWORK FOR ACTIVE STRUCTURAL STABILIZATION OF THERMOMECHANICAL DISTORTIONS

Florian Möller

Vollständiger Abdruck der von der
Fakultät für Luft- und Raumfahrttechnik
der Universität der Bundeswehr München
zur Erlangung des akademischen Grades eines

Doktor-Ingenieurs (Dr.-Ing.)

angenommenen Dissertation.

Vorsitzender:	Univ.-Prof. Dr.-Ing. Alexander Koch
1. Gutachter:	Univ.-Prof. Dr.-Ing. Roger Förstner
2. Gutachter:	Univ.-Prof. Dr.-Ing. Philipp Höfer

Die Dissertation wurde am 29.05.2024 bei der Universität der Bundeswehr München eingereicht und durch die Fakultät für Luft- und Raumfahrttechnik am 24.09.2024 angenommen. Die mündliche Prüfung fand am 25.10.2024 statt.

Kurzfassung

Damit weltraumgestützte Sensoren auf unterschiedlichsten Wellenlängen Messungen mit höchster Genauigkeit und Stabilität ausführen können, dürfen die Plattformen, auf denen diese Sensoren üblicherweise montiert sind, keinerlei Verformungen oder Spannungen ausgesetzt werden. Neben den bisherigen, zumeist rein passiven Methoden der Strukturstabilisierung durch Verwendung entsprechend entwickelter Materialien oder Konstruktionen, sind in den letzten Jahren im Forschungsgebiet der „Intelligenten Strukturen“ Methoden der aktiven Kontrolle entwickelt und untersucht worden. Bei diesen aktiven Verfahren messen Sensoren Veränderungen bestimmter Parameter, beispielsweise Verzerrungen oder Temperaturgradienten, gegenüber einem Referenzzustand. Mit Hilfe eines mathematischen Modells der Struktur können diese Veränderungen analysiert und bewertet werden, um eine bestimmte, kontrollierte Reaktion durch spezielle Aktuatoren auf dieser Struktur zu erreichen. Ein solcher patentierte Ansatz besteht im aktiven Kontrollieren von durch Veränderungen der thermischen Randbedingungen hervorgerufenen Verformungen einer Struktur im Mikrometerbereich durch gezielte Einbringung von Wärme auf Basis von Temperaturmessungen an ausgewählten Stellen dieser Struktur.

In dieser Arbeit soll dieser spezielle Ansatz experimentell validiert werden. Dazu wird das bestehende mathematisch-theoretische FEM-Modell mit Filter und Regler für eine reale Anwendung modifiziert sowie ein Versuchsaufbau zur Demonstration des Ansatzes unter Laborbedingungen in einer Thermal-Vakuumkammer entwickelt. In einem ersten Schritt wird dabei gezeigt, dass die dem Ansatz zu Grunde liegenden theoretischen Annahmen der Verwendung von Übertragungsfunktionen zwischen der Änderung des Wärmeeintrags an einer Stelle der Struktur und der daraus resultierenden Temperaturänderung an jeder anderen Stelle der Struktur zutreffend sind. Darüber hinaus wird nachgewiesen, dass die Rekonstruktion des Temperaturfelds der Struktur auf Basis von thermischen Moden möglich ist. In einem zweiten Schritt wird belegt, dass durch adäquates Einstellen der Systemparameter des geschlossenen Filter- und Regler-Kreises für verschiedene Störungsarten eine Reduzierung der Verschiebungen von ausgewählten Punkten auf der Struktur auf bis zu einem Sechstel der unkontrollierten Verschiebungen möglich ist. Damit wird bewiesen, dass mit diesem Ansatz Stabilitätskriterien für weltraumgestützte, hochpräzise Messverfahren erreicht werden können, die mit rein passiven Methoden bisher nicht möglich gewesen sind.

Abstract

In order for space-based sensors operating at various wavelengths to perform measurements with the highest accuracy and stability, the platforms on which these sensors are typically mounted must not be subjected to any deformations or stresses. In addition to the existing, mostly passive methods of structural stabilization through the use of appropriately designed materials or constructions, research in the field of smart structures has in recent years developed and investigated methods of active control. In these active approaches, sensors measure changes, such as occurring stresses or temperature gradients, compared to a reference state. With the help of a mathematical model of the structure, these changes can be analyzed and evaluated in order to achieve a specific controlled response through special actuators on this structure. One such patented approach involves actively controlling deformations in the micrometer range caused by changes in thermal boundary conditions by selectively introducing heat based on temperature measurements at selected points of this structure.

In this work, this specific approach is experimentally validated. To achieve this, the existing mathematical-theoretical FEM model with filter and controller is modified for a real application, and an experimental setup for demonstrating the approach under laboratory conditions in a thermal vacuum chamber is developed. In a first step, it is shown that the theoretical assumptions underlying the approach, involving the use of transfer functions between the change in heat input at one location of the structure and the resulting temperature change at any other location of the structure, are accurate. Furthermore, it is demonstrated that the reconstruction of the temperature field of the structure based on thermal modes is possible. In a second step, it is proven that by appropriately adjusting the system parameters of the closed filter and controller loop, this approach enables a reduction in the displacement of selected points on the structure to as little as one-sixth of the uncontrolled reference displacements for various types of disturbances. Thus, it has been demonstrated that this method can achieve stability criteria for space-based, highly precise measurement techniques which have not been possible with purely passive methods thus far.

Acknowledgements

The completion of this dissertation would not have been possible without the diverse support from many individuals across various fields. To all of them, I extend my deepest gratitude. I would like to specifically acknowledge and highlight the contributions of several individuals in the following section.

First and foremost, I would like to thank Prof. Dr.-Ing. Roger Förstner, my doctoral advisor, for his supervision of this dissertation and for integrating me deeply into his Institute of Space Technology and Space Applications. Despite not being an official member of his institute, I always felt as much a part of it as my colleagues. Without the provided infrastructure, technical equipment and personnel support, such a practical-focused project would have been impossible.

I am grateful to Prof. Dr.-Ing. Philipp Höfer, my second reviewer, for his numerous suggestions, extensive discussions and guidance, especially in the final stages of this work.

In addition to all my scientific colleagues and the chief engineer at the institute, the practical implementation of my experiments would never have been possible without the craftsmanship, dedication and tireless support of the technician. Thank you, Hermann, for the hundreds of hours in the laboratory over the past years.

A university without students is inconceivable, and over the past seven years, I have mentored many through exercises and practicals. In return, the numerous bachelor's and master's theses greatly helped me to break down large and complex work packages into smaller, more manageable units. Moreover, working on weekends and late evenings is much more enjoyable with company. In this regard, thank you, Jannis, Lucas, Jan, Lukas, Sebastian, Thilo and Elias!

As my primary role during seven years of scientific work was teaching Mathematics and Computer Science for Aeronautical Engineering, I am particularly grateful to my bosses – Prof. Dr.-Ing. Reinhard Finsterwalder and Prof. Dr. rer. nat. Dominik Bayer – from the Institute of Mathematics and Computer Science for granting me considerable freedom and unwavering support beyond my academic duties.

I also thank my military superiors – Leo, Chris, Ken and Avro – who consistently refrained from burdening me with military obligations beyond the necessary minimum (and sometimes even less).

Finally, I express my deepest gratitude to my family, friends and especially my partner in crime, Kevin, for their emotional and moral support, infinite patience and trust, particularly during phases of self-doubt and discouragement when weeks of testing resulted in failures.

Thank you all!

Contents

List of Figures

List of Tables

List of Abbreviations

CME	coefficient of moisture expansion
CRE	coefficient of radiation expansion
CS	cold side
CTE	coefficient of thermal expansion
CtE	coefficient of temporal expansion
DAS	Data Acquisition System
DASYLab	Data Acquisition System Laboratory
DC	direct current
DIC	Digital Image Correlation
DOC	degrees of constrain
DOF	degrees of freedom
ESA	European Space Agency
FBG	Fiber Bragg Gratings
FEM	Finite Element Method
GRACE-FO	Gravity Recovery and Climate Experiment Follow-On
HE	Heating Element
HS	hot side
IR	Infrared
IRASSI	InfraRed Astronomy Satellite Swarm Interferometer
LISA	Laser Interferometer Space Antenna
LPM	Lumped Parameter Method
LQR	Linear-Quadratic Regulator
MIMO	Multi Input Multi Output
PCM	Perturbation Compensation Method
PCMs	Phase-Change Materials

PCU	Process Cooling Unit
PE	Peltier element
PEASSS	Piezoelectric Assisted Smart Satellite Structure
PLATO	Planetary Transits and Oscillation of Stars
PTFE	Polytetrafluoroethylene
RTD	Resistance Temperature Detector
SeRANIS	Seamless Radio Access Networks for Internet of Space
SISO	Single Input Single Output
TC	Thermocouple
TEC	Thermoelectric Cooler
TEG	Thermoelectric Generator
TVC	Thermal Vacuum Chamber

List of Symbols

B	Compression modulus
c_p	Specific heat capacity
C_V	Specific heat
E	Young's modulus
H_{Tq}	Transfer function between temperature T and heat flux q
H_{uT}	Transfer function between displacement u and temperature T
H_{uq}	Transfer function between displacement u and heat flux q
J	Cost function
M	Number of selected mechanical modes
N	Number of selected thermal modes
n	Number of nodes
n_n	Number of modes
q	Heat flux
$\dot{q}$	Heat flux density
q_{leak}	Leakage rate
s	Complex frequency variable
T	Temperature
T_e	Environmental temperature
U	Control input in quadratic cost function
V	Volume
Y	Output in quadratic cost function

α	Coefficient of thermal expansion
α_Z	Temperature coefficient of resistor
β	Coefficient of moisture expansion
ΔM	Absorbed moisture
Δp	Pressure difference
ε	Emissivity
ε_S	Strain
η	Coefficient of temporal expansion
Θ	Approximation parameter

λ	Thermal conductivity
μ_S	Static coefficient of friction
ν	Transverse contraction coefficient
ρ	Density
ρ_R	Specific resistance
ρ_W	Relative weight factor in LQR cost function
σ_{SBC}	Stefan-Boltzmann constant
σ_H	Standard deviation heater elements
σ_S	Standard deviation temperature sensors
Ψ	Coefficient of radiation expansion
ω	Complex frequency parameter
$[C]$	Thermal capacity matrix
$[C_K]$	Observation matrix of the Kalman filter
$[C_u]$	Damping matrix
$[F]$	View factor matrix between surface elements
$[F_T]$	Mechanical load matrix
$[\mathcal{F}_T]$	Transformed mechanical load matrix
$[H]$	Matrix of transfer functions
$[H_c]$	Matrix of transfer functions, only control contribution
$[H_{pert}]$	Matrix of transfer functions, only perturbation contribution
$[I]$	Identity matrix
$[K]$	Conductivity matrix
$[K_K]$	Kalman innovation gain
$[K_{LQR}]$	LQR gain matrix
$[K_u]$	Stiffness matrix
$[M_u]$	Massmatrix
$[P]$	Solution of the discrete-time algebraic Riccati equation
$[P_K]$	Covariance matrix of the errors
$[Q]$	Weighting matrix output variables for LQR
$[Q_K]$	Covariance matrix of the process noise
$[R]$	Weighting matrix control variables for LQR
$[R_K]$	Covariance matrix of the measurement noise
$[R_q]$	Heat flux matrix
$[R_r]$	Radiating surface matrix
$[T_{eq}]$	Temperature matrix for steady state (equilibrium)
$[\Gamma]$	Matrix of the standard deviations of the heater elements
$[\gamma]$	Eigenvalue matrix of $[M_u^r]^{-1}[K_u^r]$
$[\epsilon]$	Emissivity matrix
$[\zeta]$	Damping contribution in modal transformation
$[\vartheta]$	Eigenvectormatrix of $[M_u^r]^{-1}[K_u^r]$

$[\lambda]$	Eigenvalue matrix of $[H_T]$
$[\Pi]$	Mapping matrix
$[\phi]$	Eigenvectormatrix of $[H_T]$
$[\Psi]$	Transformation matrix for thermal field reconstruction
$\{F_e\}$	View factor vector between surface elements environment
$\{q_{eq}\}$	Heat flux vector steady state
$\{q_{pert}\}$	Perturbation heat flux vector
$\{q_{rad}\}$	Heat flux vector of the radiating surfaces
$\{R_q\}$	Heat flux vector
$\{T_e\}$	Environmental temperature vector
$\{T_{eq}\}$	Temperature vector steady state (equilibrium) solution
$\{T_s\}$	Surface temperature vector
$\{\delta q\}$	Change of heat flux
$\{\delta q_c\}$	Control heat flux
$\{\delta q_{pert}\}$	Perturbation heat flux
$\{\delta T\}$	Actual change in temperature
$\{\delta \hat{T}\}$	Estimated change in temperature of Kalman Filter
$\{\delta T_c\}$	Change in temperature due to control elements
$\{\delta T_{pert}\}$	Change in temperature due to perturbation heat flux
$\{\delta T_{sensor}\}$	Measured temperature changes
$\{\delta u\}$	Change of displacements
$\{\epsilon_{\Delta T}\}$	Error in temperature measurement due to noise
$\{\epsilon_T\}$	Error in temperature measurement due to bias
$\{\eta\}$	Modal coordinates vector mechanical model
$\{\tau\}$	Modal coordinates vector thermal model

Chapter 1

Introduction

1.1 Motivation and Research Status

As platforms, sensors and instruments become more powerful, greater precision and accuracy are necessary. Often the quality of a measurement is limited not only by the instrument itself, but also by the environment in which the instrument is operating. For example, in the Planetary Transits and Oscillation of Stars (PLATO) mission [1], a relative alignment stability of the catadioptric telescopes of 0.2 arcseconds must be ensured over a period of 14 hours [2]. To achieve this, the platform on which the instrument is mounted must be decoupled as far as possible from disturbances caused by the space environment or the satellite itself. In the Gravity Recovery and Climate Experiment Follow-On (GRACE-FO) mission to determine the Earth's gravitational field, the distance between the two satellites flying in formation must be determined with an accuracy of a few micrometers using a microwave instrument operating in the Ka-band, which places high demands on the structural stability of the satellites [3].

Within the InfraRed Astronomy Satellite Swarm Interferometer (IRASSI) mission study, a formation consisting of five satellite platforms was investigated, which in combination will act as a telescope in the infrared range. By spatially distributing the telescope across multiple platforms, higher resolutions can be achieved compared to telescopes with a fixed aperture on a single platform [4]. For IRASSI to be able to resolve wavelengths of up to 50 µm, the satellite separation must be determined with an accuracy of less than 5 µm [5]. To ensure the structural stability of a satellite geometry on this scale, traditional passive methods, such as thermal decoupling of certain structures or using materials with a low coefficient of thermal expansion (CTE) and high stiffness, are no longer sufficient.

For active structural stabilization, the occurring perturbations must first be characterized. On the one hand, the structure can be influenced by low-frequency perturbations with periodic durations of several hours or days. These perturbations usually have a thermal origin due to changes in the radiation exchange or due to energy dissipation

from internal devices and cause displacements and stresses in the structure. On the other hand, high-frequency perturbations can occur, ranging from a few Hz to several thousand Hz. These vibrations usually have their origin in mechanical processes within the satellite. In [6] an approach to compensate for low-frequency thermally induced displacements as a simulation has been developed. Based on the combination of a thermal and a mechanical Finite Element Method (FEM) model of the satellite structure, transfer functions are used to establish a relation between changes in the applied heat at a surface element and temperature changes at each node in the model, as well as between the temperature changes and the resulting displacements. The combination of these models into a thermomechanical model, the characterization of the expected thermal perturbations in the frequency domain as well as the thermal field reconstruction based on a few discrete temperature measurements allow the calculation of control heat input by a Linear-Quadratic Regulator (LQR). In addition, a Kalman filter estimates the overall temperature field based on noisy measurements and influenced by erroneous commands of the control elements, thus enhancing the modeled values through weighting them with the predictions. According to the simulations, an improvement of the displacement stability by a factor of 100 compared to the uncontrolled case can be achieved [6]. This approach has already been patented [7].

With this thesis evidence is provided for the operability of that framework for active structural stabilization through simulation, modeling and experimental validation.

1.2 Research Objectives

The main objective of this work is the experimental validation of the approach developed and simulated in [6] for active stabilization of thermally induced displacements in satellite structures. To achieve this, the existing mathematical model, originally designed solely for simulations, is adapted to be applicable to a real structure in a laboratory experiment [8]. This experimental setup is developed for tests in a Thermal Vacuum Chamber (TVC), representing a satellite structure such as an optical bench. The assumptions and simplifications underlying the approach are validated using an initial, simple model and experimental setup [9]. Building upon these findings, a more complex and improved model, along with an experimental setup, is developed to demonstrate various types of perturbations [10, 11, 12]. For the experimental setup, it is necessary to not only find a suitable structure but also to mount it in the TVC in a way that resembles a satellite structure. Additionally, an appropriate sensor and actuator strategy for the control aspect and a strategy for demonstrating improvements in deformation and displacements must be developed.

This work aims to lay the foundation for adapting this approach to validate its operability on the ATHENE-1 satellite as part of the Seamless Radio Access Networks for Internet of Space (SeRANIS) project [13] in orbit.

1.3 Thesis Overview

The structure of this dissertation follows the classic triad of a laboratory-based work: simulation and developing a model, realizing the model in an experimental setup, and analyzing and discussing the results. However, since theory and practice are mutually dependent, aspects are occasionally mentioned that will be described in detail later. To provide the reader with a coherent thread, cross-references will be used throughout the work. Since simulation and modeling are closely interlinked, the design of an experimental setup for that model is an iterative process. This work is therefore not structured linearly in terms of time, but rather thematically. Many detailed descriptions, for example of the mathematical model or more complex parts of the experimental setup, will therefore be found in the appendix of this thesis.

Chapter 2 starts with the theoretical foundations and fundamentals of a framework for active structural stabilization. This includes the definition of dimensionally stable structures and a brief overview of the thermomechanical FEM model, which was largely derived in [6]. In the subsequent Chapter 3, the model of the structure to be controlled as well as the experimental setup is described along with all its necessary components. The procedure for determining the system parameters for the closed-loop filter and controller framework is outlined as well. The chapter concludes with an estimation of the magnitude and influence of the error sources due to the assumptions made, the modeling, and the experimental setup itself. Chapter 4 describes and discusses the results of the simulations and experimental validation for different configurations and types of perturbations in detail. The conclusions derived for a technical application for a flight experiment, for example on the ATHENE-1 satellite, as well as suggestions for adaptations and modifications of the approach are explained in Chapter 5. Finally, a summary and outlook for future work can be found in Chapter 6.

Chapter 2

Fundamentals of a Framework for Active Structural Stabilization

This foundational chapter delineates what dimensionally stable structures entail, identifies the origins of perturbations to this stability, and elucidates methods by which these perturbations can be minimized. Subsequently, a brief overview of the thermo-mechanical model developed in [6] and the closed-loop filter and control framework for minimizing thermally induced displacements is presented.

2.1 Dimensional Stable Structures

Dimensional stability is a general property of a material or structure that allows it to remain in its shape, size or any dimension. In contrast, dimensional instability is the generic term for all distortions, deformations, displacements or strains that a material or structure undergoes when it is subject to a change in boundary conditions or external influences. The simplified Duhamel-Newman relation can be used for a measure of dimensional instability and describes the one-dimensional strain in a structure as the sum of several different influences according to [14]

$$\varepsilon_S = \frac{\Delta\sigma}{E} + \alpha\Delta T + \beta\Delta M + \eta\Delta t + \Psi\Delta q + ... \tag{2.1}$$

These different external influences could be applied stress σ, temperature T, absorbed moisture M, time t or radiation and heat fluxes q with the corresponding material properties Young's modulus E, CTE α, coefficient of moisture expansion (CME) β, coefficient of temporal expansion (CtE) η and coefficient of radiation expansion (CRE) Ψ. Dimensional stability encompasses all material properties of a structure that lead to a change relative to a reference state. In addition to the influences mentioned here, factors such as material composition, pressure, electrical and magnetic fields, gravity, or changes in thermo-optical properties may also be relevant [15]. By minimizing

the coefficients mentioned above, a dimensionally stable structure is obtained. Even though the mathematical relationships in two- or three-dimensional stress conditions are more complex, this one-dimensional representation is sufficient for understanding the underlying idea. In this approach, dimensional stability with respect to changing thermal boundary conditions is examined for an application under vacuum. Mechanical stresses due to external or internal forces that are not caused by thermal loads are excluded. The influence of absorbed moisture on displacements can be neglected as well. For this approach, neither degradation of material properties nor irreversible processes are to be considered, leading to an exclusion of temporal effects.

For the classification of structural perturbations, instead of their origin or physical properties, the frequency of the acting perturbation itself can be utilized. Low-frequency, slow-acting perturbations with periods ranging from hours to days or even weeks or years are usually of thermal origin due to a certain form of heat transfer. Changes in thermal conditions lead to temperature variations. Temperature variations, in turn, result in stresses or deformations, depending on the type of support and the structure's characteristics. As the frequency increases, the damping of thermal perturbations becomes more and more significant, making them completely negligible in the high-frequency range.

The most relevant high-frequency perturbations, ranging from a few Hz to several thousand Hz, are vibrations, and hence, purely mechanical perturbations. These cause oscillations in the structure, leading to misalignment between individual points. Mechanical perturbations can have a variety of causes and are often attributed to moving parts of the satellite, such as those used for attitude control, payload deployment, antenna or solar panel movement, or engine ignition. However, other types of external and internal perturbations that lead to rigid-body motion of the spacecraft, such as solar radiation pressure, gravity gradients, or fuel sloshing, can also induce stresses and deformations that affect a structure requiring stabilization.

During space missions, the structure experiences maximum vibrations and significant temperature fluctuations during launch, which can lead to undesirable thermomechanical effects. After the satellite or spacecraft reaches orbit or its mission destination and is in a vacuum, a new thermal equilibrium is established, which can be significantly different from the state before launch and often persists throughout the mission duration [16]. Characterizing this new thermal equilibrium presents a significant challenge and requires a combination of in-orbit measurements and modeling techniques. This steady-state condition plays a crucial role in the approach presented in this work, as only changes relative to this state can be controlled [6]. In addition to adequate pre-mission modeling, the structure needs to be calibrated for this expected steady state through thermal vacuum testing. In a second step, in-orbit calibration must be performed. This can be done by determining the temperature field and measuring the displacements and deformations that have already occurred. To compensate for mea-

surement errors and inaccuracies caused by modeling, it is recommended to combine multiple different measurement methods, especially for high-precision applications.

To control stresses or displacements in a structure, a distinction can be made between passive and active methods.

Passive methods in the field of structural stabilization refer to techniques where the stability and stiffness of a structure are achieved through the selection of appropriate materials and design principles without the use of external energy sources or active control systems. These methods are based on the concept of pre-planning and incorporating characteristics into the structure's design to minimize distortions and unstable movements. Symmetrical or balanced structures can reduce the tendency for deformation and distortion. Additional reinforcements or struts can be employed to increase the stiffness and stability of the structure. The integration of damping systems, such as vibration isolators or shock-absorbing materials, can also contribute to improved stability. Key properties of highly stable structures include a low CTE and high stiffness. Thermal conductivity and heat capacity also impact the structure, as they describe how quickly thermal changes propagate within the structure from their source and how much the temperature change is influenced by a change in heat fluxes. Ceramics or composite materials are typically used in aerospace applications for such purposes [17, 18, 19]. The application of passive control methods offers several advantages, including lower complexity, reduced costs, and no need for continuous power supply. They provide robust and reliable stabilization of structures [14]. Furthermore, the design of the structure itself plays a crucial role. Additively manufactured materials, for example, can be engineered to have zero or negative CTE, when combining two metals to a bimaterial unit. Such design structures are called meta-materials [20, 21, 22], where the desired macroscopic properties do not coincide with the material properties of the individual components. Another widely used method is thermal control, which aims to minimize overall temperature fluctuations. This can be achieved in two ways. Firstly, by designing the surfaces that participate in radiation exchange and varying their view factors. Secondly, the radiation exchange between different components can be influenced by choosing thermo-optical properties such as surface texture or color, as this directly impacts emissivity and absorptivity. Depending on the orbit, application, or mission, specific surfaces of the satellite are used as radiators to dissipate heat energy or as heat sources to absorb solar radiation. Heat pipes are used to utilize the effect of heat conduction via an evaporation and condensation circuit and, thus, to transport the heat within the satellite to a radiator [23]. In recent research approaches, Phase-Change Materials (PCMs) are being investigated, which involve the use of a wax-like substance with a specific melting point embedded in a lattice structure [24, 25].

Active control methods, on the other hand, involve the use of sensors to measure changes in certain parameters of the structure. With the help of a mathematical model of the structure, these changes can be analyzed and evaluated, and desired modifica-

tions to those parameters can be applied to the structure through actuators. In sensor technology and actuation, various approaches and strategies exist for optimizing active control. Depending on the control strategy, different sensors can be used. If thermally induced deformations need to be controlled, the use of temperature measurement sensors is appropriate. These include Thermocouple (TC) [26], Resistance Temperature Detector (RTD) [27] and Fiber Bragg Gratings (FBG) [28, 29, 30] or Infrared (IR) sensors [26]. Displacements can be directly measured through piezoelectric sensors [31] or strain gauges [32]. Actuators are used in active control to implement the necessary adjustments to the structure. Depending on the application spectrum and control method, various actuator strategies can be pursued. Heat can be introduced into the structure through heating elements mounted on its surface or embedded as cartridges in the structure [33, 34], by Peltier elements (PEs) [35], or through radiators or other radiation sources [34]. Deformation can be induced by using piezoelectric actuator [36] through applying a certain voltage. Structures in which changes measured by sensors are altered from a modeled or predicted behavior by means of actuators are referred to as smart structures in the literature [37, 38, 39]. The approach presented here can be effectively integrated into this field of research.

2.2 Thermomechanical Control Framework

In [6], an approach to minimize thermally induced displacements due to low-frequency perturbations in the thermal conditions of a satellite structure was developed and simulated. For a complete and detailed mathematical derivation, refer to [6]. A simplified summary of the mathematical background, aimed at facilitating a better understanding of this work, is provided in Appendix A. This Section will present the basic ideas of this approach along with its key findings, characteristics, assumptions, simplifications, and the necessary prerequisites for experimental validation.

The development of the mathematical model and simulation was initiated based on the IRASSI mission study, in which a satellite constellation consisting of 5 satellites, positioned at the L2 point of the Sun-Earth system, was intended to conduct interferometric deep space observations. For interferometric measurements, the inter-satellite distance knowledge within the constellation must be accurate up to 5 µm, and the absolute pointing error should be below 0.4 arcsec. Figure 2.1 depicts the satellite in an early design phase. The scientific instrument is located on an optical bench, which is shielded from the rest of the satellite by thermal and sun shields, ensuring a stable thermal environment in the L2 orbit. At the other end of the optical bench, the metrology system is attached, aiming to determine the inter-satellite distance through laser measurements.

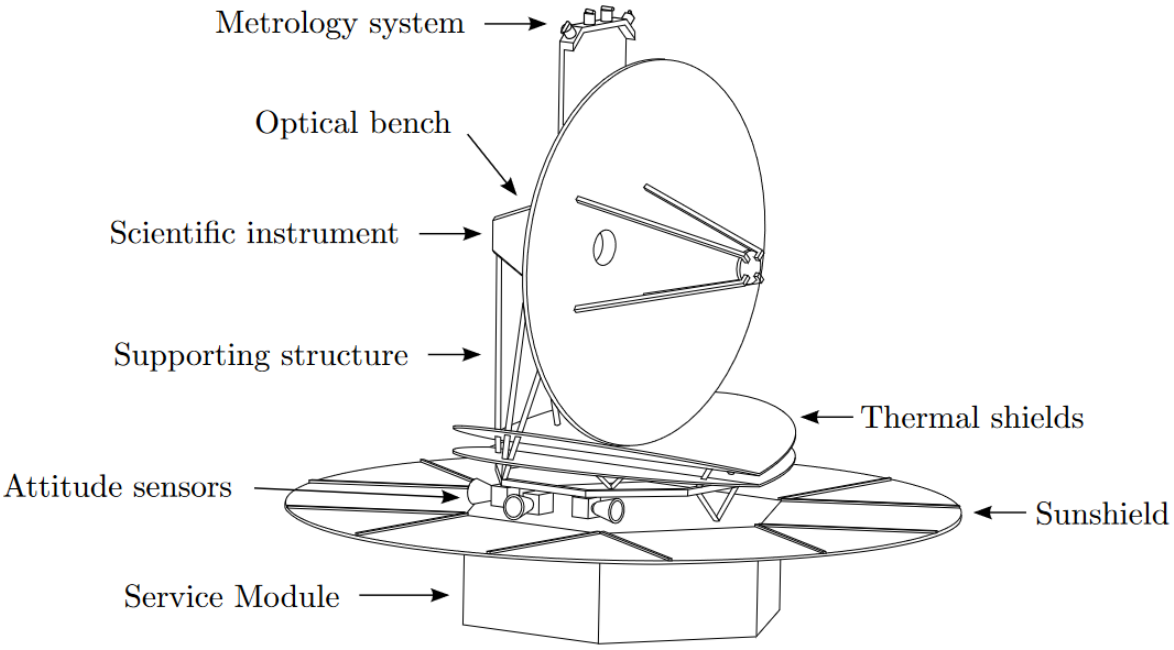

Figure 2.1 Schematic representation of the IRASSI satellite [5]

Figure 2.2 schematically illustrates the optical bench, the scientific instrument, and the laser terminals. The lever arms represented by the red lines symbolize the distances between the terminals and the instrument.

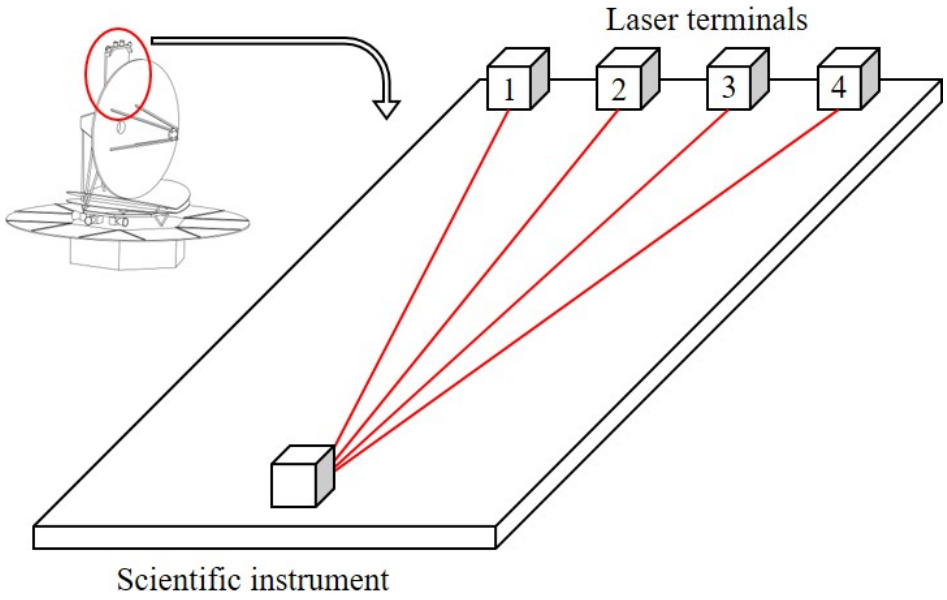

Figure 2.2 Stabilized lever arms within the optical bench of the IRASSI satellite

Throughout the feasibility study, it was determined that deformations of the optical bench due to slightly changing thermal boundary conditions through heat conduction into the structure and energy dissipation from the instruments can become significant,

despite the use of a glass-ceramic as the structural material, thermal shielding and appropriate thermal decoupling of the mounting and support from the satellite structure. These deformations could be large enough to violate the stability criteria described initially, rendering interferometric measurements impractical. To address this, additional active stabilization measures are proposed to minimize changes in distance between the terminals and the instrument as good as possible. For this purpose, the structure is represented by a thermomechanical FEM model. The mathematical derivation of this model is presented in Appendix A. As with any model, certain simplifications and assumptions are necessary.

In the first step, the thermal behavior of the structure must be analyzed. This includes determining the temperature field in the steady-state as well as the transient behavior when the boundary conditions change. Since the structure is in space, only heat conduction and radiation are relevant as forms of heat transfer. The calculation of the change in the temperature field in the FEM model typically occurs in the frequency domain. Since the radiation from a surface is proportional to the fourth power of its temperature, it must be linearized around the steady-state equilibrium, neglecting all higher powers of the temperature change if they are sufficiently small, in order to simplify the calculations. This leads to the first constraint for the experimental validation of the approach: To detect displacements adequately, temperature changes must be large enough. However, if these changes exceed a certain amplitude, the linearization of the radiation terms introduces a non-neglectable truncation error. For the design of the model, this limit must be determined through simulations.

After linearization, a linear relationship between changes in heat flux due to radiation or heat conduction and the change in the temperature of the structure can be established. Through modal transformation, a transfer function can be obtained that provides a functional relationship between these changes. This transformation is crucial for four key aspects:

1. With a known frequency of the perturbation, the temperature change can be determined at any location in the FEM model.
2. Different perturbations can be evaluated independently at different locations in the structure with different frequencies using the superposition principle.
3. A single perturbation can be described as one composed of many sub-perturbations with different frequencies.
4. For low frequencies of perturbation, the temperature field of the structure can be represented solely by a few thermal modes with the highest modal weights. This principle allows the reconstruction of the entire temperature field by measuring the temperature at a few locations in the structure. In [6], a frequency of 10^{-4} Hz was identified as the usability upper limit of this approach.

For validation, this limit frequency sets the second constraint besides the possible temperature changes. The proof of the usability of the transfer function as a basis for modal transformation is thus essential.

Analogous to the thermal model, a relation between temperature and displacement field is established in the mechanical model. To ensure the free thermal expansion of the structure, it must be mounted in a specific way. A widely used method is the use of an isostatic mounting, which has a significant impact on simulation, modeling, and practical implementation, and is detailed in Section 3.3. This constitutes another key aspect relevant to the validation of the approach.

Starting from a steady state, a transfer function between the change in temperature and the change in the displacement of the nodes of the FEM model is created through modal transformation and solving the mechanical problem in the frequency domain, analogous to the thermal model. This mechanical transfer function can be combined with the thermal one to form a thermomechanical transfer function, which describes a direct relationship between the change in heat flux and the change in displacements. This allows, if the perturbation is known, the precise calculation of the necessary heat flux needed to ideally compensate for the displacements arising from this perturbation. This method, known as Perturbation Compensation Method (PCM), serves as proof of this thermomechanical transfer function and as a reference for the control algorithm.

If only the origin of the perturbation is characterizable but not its amplitude, phase, and frequency, the LQR developed in [6] can determine the necessary control heating powers to minimize the resulting displacements. For the Multi Input Multi Output (MIMO) system underlying this approach, a control element is needed for each controlled degrees of freedom (DOF). If the displacement of a point in the structure is to be minimized in the three spatial directions, then 3 control elements capable of applying a certain heat flux are necessary. In addition to setting the system parameters of the LQR, this constitutes another boundary condition for the validation of the approach.

With the help of the aforementioned thermal modes, a strategy can be developed to reconstruct the entire temperature field by measuring the temperature at a few locations in the structure. Determining the number of sensors required for this purpose and their positioning on the test setup is another key aspect of this thesis. Since measurements are inherently inaccurate and noisy, a Kalman filter is used to improve the results. Designing this filter for simulation and application in experimental validation constitutes another boundary condition for this work.

The block diagram in Figure 2.3 schematically summarizes the described mathematical approach. A perturbing heat flux δq_{pert} acts on a structure, represented by a thermo-mechanical model. This perturbation generates a displacement field from which certain displacements δu are to be minimized. Sensors measure temperature changes $\delta T_{sensors}$ at selected locations in the structure due to the perturbation and feed this information back to the model. The measured temperatures are used to calculate the temperature field δT of the entire structure based on the thermal modes. The Kalman filter creates an initial system temperature estimation of the entire thermal field and updates this estimation based on newly arriving sensor measurements. Using the LQR state feedback, a control heat flux δq_c is computed from the temperature field $\delta \hat{T}$ estimated by the filter, which is then introduced into the system by the actuators. In the thermo-mechanical model, this control heat flux allows for an adjustment between the desired and actual effects for the next iteration step.

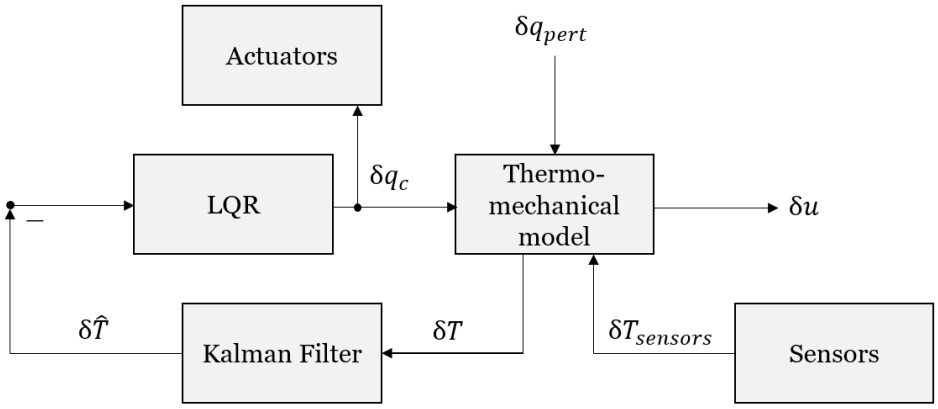

Figure 2.3 Block diagram state feedback with Kalman filter

In [6], the framework was solely simulated. Therefore, it has been necessary to simulate sensor measurements and control inputs as well. For the validation of the framework, the performance of such a simulation must be compared with the model of a physically existing experimental setup. This implies that every simulation that is to be validated by a real experiment is additionally described by a modified mathematical model. The mathematical description of these modifications can also be found in Appendix A. Parts of the derivations are described explicitly in the further course of this work if they are important for providing context at certain points.

Chapter 3

Modeling, Simulation and Design of the Experimental Setup

The experimental design of a structure to be stabilized and the modeling and simulation of the behavior of this structure are closely intertwined and mutually influential. In principle, it is possible to apply or extend the framework developed and simulated in [6] to many types of structural geometries, materials, or boundary conditions. However, some assumptions or simplifications, which will be discussed in more detail in this chapter, have already been established, limiting the design of the experimental setup. In the present case, a model of a non-existing experimental setup already existed, so the experimental setup was adapted to that model. However, various technical constraints had to be considered in the implementation of this experimental setup, necessitating adjustments to the model. Simulation and practical implementation are highly iterative. Prior to the final experimental setup, which is used to validate the framework developed and simulated in [6], a variety of structures made from different materials, various sensors and actuators, types of fixation and support, perturbations, boundary conditions, environmental conditions, and validation instruments were used throughout this work. While these may not be explicitly mentioned here, they have provided important insights that have contributed to the ultimate determination of the experimental setup and simulation. If these insights play an important and specific role at certain steps to underline the chain of argumentation, they are mentioned more detailed. Therefore, this chapter aims to summarize the steps in model development and simulation, as well as the design of the experimental setup, without strictly adhering to a correct chronological sequence.

Section 3.1 provides an overview of the experimental setup, outlining the components essential for its operation, which will be further detailed in subsequent sections of this work. The actual experimental structure is examined more closely in Section 3.2. Since the fixation of this structure within the TVC plays a crucial role, this aspect is thoroughly discussed and presented in Section 3.3. A high-resolution

camera system is employed for the validation of the framework, and its details are expounded in Section 3.4. The determination of the experimental design and all the necessary system parameters is elucidated in Section 3.5. The chapter concludes with Section 3.6 with an overview of the sources of error expected through simulation and the experimental setup and their impact on the accuracy of the measurements, enabling the interpretation of the results of the validation experiments.

3.1 Overview of the Experimental Setup

In Figure 3.1, the entire experimental setup, including all necessary components, is schematically depicted. Figure 3.2 illustrates the test object within the TVC.

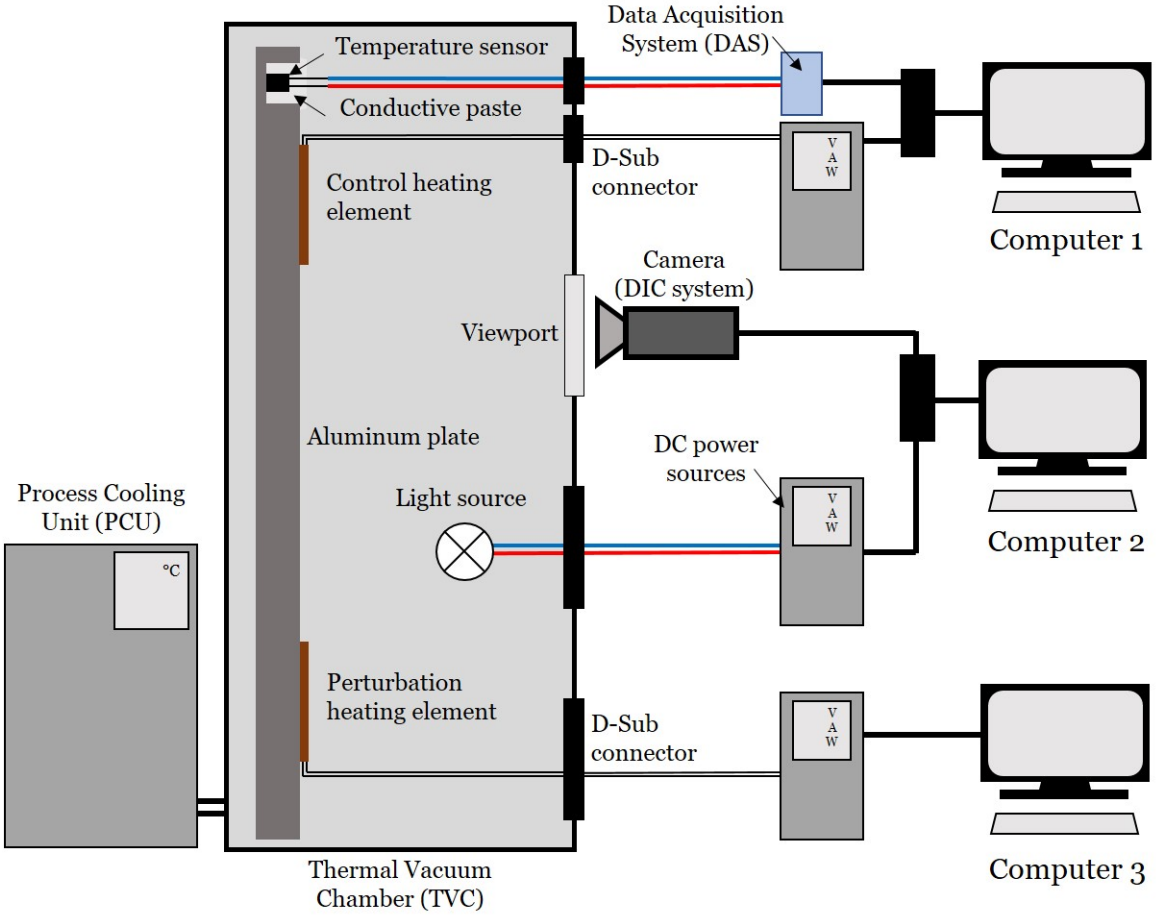

Figure 3.1 Schematic overview of the entire experimental setup

Through the use of the TVC, it is possible to create a high vacuum in the range of 10^{-7} mbar. The Process Cooling Unit (PCU) operates based on the principle of a heat exchanger. Copper pipes welded into the table and the chamber walls transport the temperature control medium needed to ensure a constant radiation background for this approach. In essence, temperatures in the range of $-90\,°C$ to $200\,°C$ with a stability of $0.05\,K\,min^{-1}$ [40] can be maintained by the system. For the model and validation,

only a constant background temperature is required, and thus the PCU is operated at a constant value of 5 °C. This choice was based on practical reasons. The thermal expansion coefficient for metals is constant in the range of 0 °C to 30 °C, and most other materials to be used in the experimental setup are suitable in that temperature range as well. Temperatures below 0 °C can easily be achieved with the PCU, but water condenses and freezes on many cold pipes outside the TVC. When the system is shut down, the ice melts, and the resulting meltwater needs to be collected and drained to prevent any short circuit in the laboratory equipment. However, if the temperature of the system remains constant above 0 °C, this issue becomes irrelevant. If the ambient temperature is too high, it increases the wear and degradation of the wiring. If the temperature is too close to room temperature, the PCU operates stably only for a short period since the required cooling or heating power is so low that the system often runs idle.

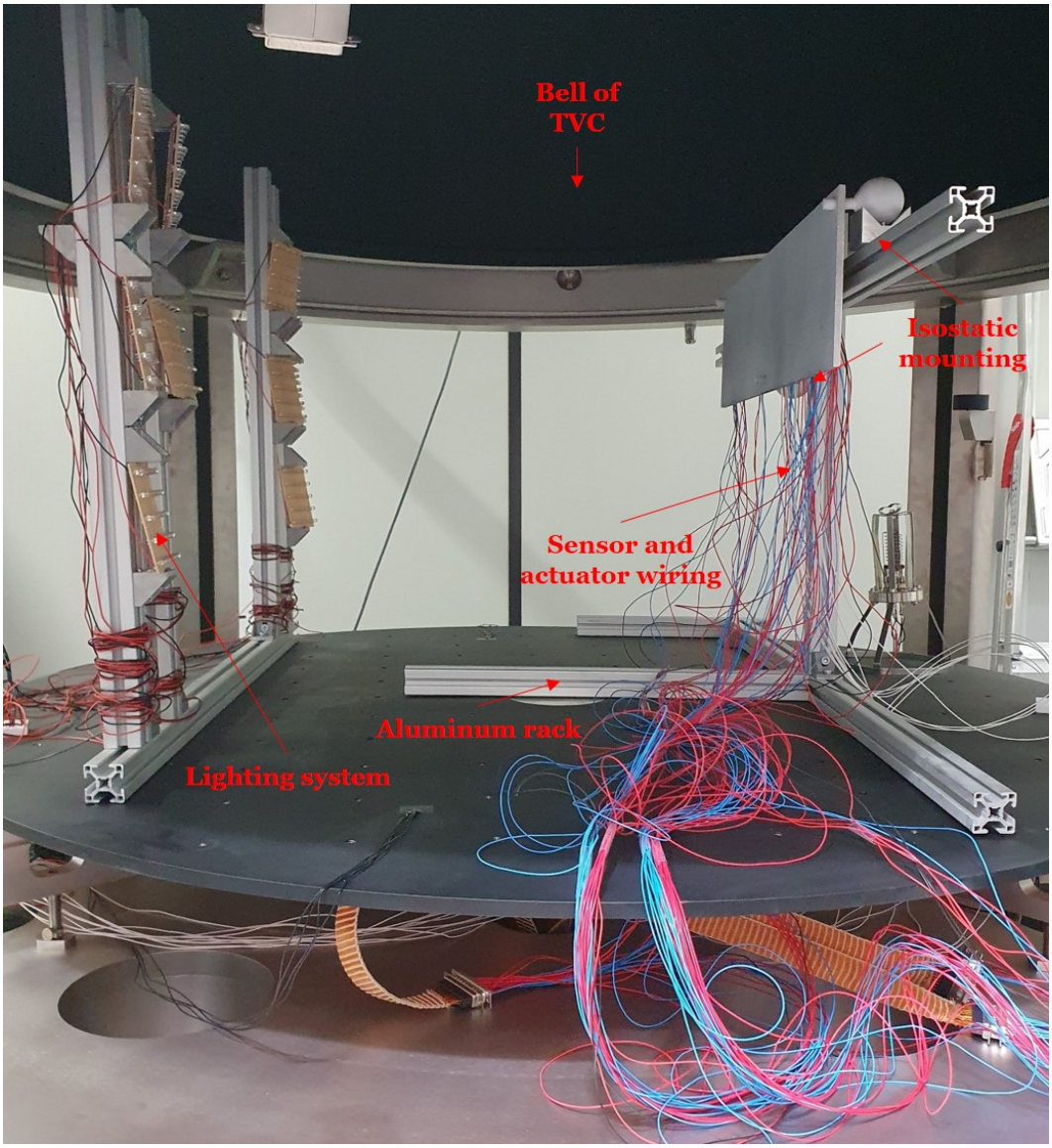

Figure 3.2 Experimental setup within TVC

On the other hand, if a constant cooling or heating power needs to be supplied, the system operates more stably over a longer period. In addition to the temperature fluctuations, it must be considered that the temperature set and commanded at the PCU does not correspond to the temperature actually prevailing on the inner wall of the TVC. The temperature control medium is transported from the PCU to the TVC through pipes. Depending on the commanded temperature and the laboratory's ambient temperature, losses in the range of 0.1 °C to 0.3 °C can occur. More detailed information on the TVC and PCU can be found in Appendix B.

The test object, detailed in Section 3.2, is suspended at a certain height on an aluminum rack through an isostatic mounting, allowing the front side of the object to be captured externally through a camera system via the viewport in the TVC, serving as an external validation instrument. Pt-100 temperature sensors are affixed to the test object with a high-vacuum-compatible, silver-based heat-conductive adhesive so that heat transfer between the test object and the sensor is maximized without forming a heat sink due to altered emissivity, which could introduce additional measurement inaccuracies. Heating Elements (HEs) embedded in a Kapton foil act as actuators for control, but also as perturbation elements, allowing various types of perturbations to be reproducibly applied. These HEs with known resistance can be selectively controlled by a direct current (DC) voltage source. Sensors and actuators can be connected to data acquisition or control devices outside the chamber via a total of 5 25-pin D-sub connectors integrated into the TVC. To prevent interactions between signal-carrying leads and electrical leads, they are connected to different connectors, resultung in a total of 4 connectors available for temperature measurement. Since each temperature sensor requires 4 leads, a maximum of 25 temperature sensors can be operated with a total of 100 pics from 4 connectors. The sensors are connected to a Data Acquisition System (DAS) that convert voltage signals into temperatures and provide discrete individual values at desired time intervals through special software, where measurement noise is filtered through appropriate signal processing and discrete values are obtained through averaging many measurements. This software interfaces with MATLAB, in which the filter-controller model is calculated and simulated, enabling the necessary heating powers for control in the form of voltage and current commands to be transmitted to the DC voltage sources. To ensure that the generation of perturbation, data acquisition and control, as well as external validation, are operated independently and separately from each other on the system side, 3 different computer systems are necessary. Due to the use of sensors and actuators, which inherently have a certain level of accuracy, and their attachment to the test object, as well as the processing of the data, numerous potential errors arise, which can be reduced or compensated for by calibration and the use of a Kalman filter. A description of these, as well as further details on sensors and actuators and on data acquisition and control, can also be found in Appendix B.

For the camera system to detect changes in the deformation of the test object, it must be equipped with an artificial pattern and illuminated by a lighting system. This black-and-white speckle pattern is visible on the front of the test object in Figures 3.2 and 3.13 in the further course of this work. LED light fields serve as the light source. The camera detects changes in the gray values of that speckle pattern when deformations occur by using a Digital Image Correlation (DIC) software called Istra4D [41]. The validation system is described in more detail in Section 3.4.

3.2 Test Object and Properties

The definition of the setup for the simulation and the experiment must fulfill the following aspects:

1. The geometry should not be too complex so that the model of this structure can also be sufficiently simple, allowing for minimal computational and simulation effort, considering the anticipated numerous iteration steps and changes. At the same time, the accuracy of the FEM model should not be unduly influenced by simplicity.

2. The resulting deformations and displacements of the points to be controlled on the structure must be large enough, despite small temperature differences, so that they can be validated by an external system.

3. The structure and all components must be vacuum-suitable, excluding certain composite materials due to outgassing constraints. The shape and size of the potential test object are limited by the dimensions of the TVC where the tests are to take place. To capture images of the structure through the viewport, the shape and size are further restricted. Simultaneously, the distances between the points to be controlled must be large enough, so that displacements can be detected.

4. In space, the mass of the structure plays a subordinate role due to weightlessness. However, the weight of the structure for the laboratory experiment must not be too large to block free expansion in a suitably dimensioned support due to friction.

For the approach of active structural stabilization, already very good passively stabilized structures made of materials with low CTE and high stiffness, such as ceramics like Zerodur [14, 15, 42], should be used. Nevertheless, in the presented demonstration an aluminum alloy was chosen as material for the experimental setup. Measurable deformations occur even with small temperature changes due to the high CTE. Results can thus be verified more effectively. Moreover, aluminum is easier and more robust to work with, for example when drilling holes for the mounting bracket.

Since the purpose of this work is to demonstrate the feasibility of the mathematical model of structural stabilization, the use of aluminum alloy is sufficient for the experi-

mental setup and can be adapted for other materials since the model is not dependent on material selection. A combination of different materials in one setup is possible as long as those materials are modelled properly within the FEM model. The material parameters for the aluminum alloy EN-AW-7075 used in the experiments are shown in Table 3.1. These are the thermal conductivity λ, the specific heat capacity c_p, the density ρ, the Young's modulus E, the transverse contraction coefficient ν, the coefficient of thermal expansion α and the emissivity ε.

Table 3.1 Material data EN-AW-7075 [43]

λ	c_p	ρ	E	ν	α	ε
$130\,\mathrm{W\,m^{-1}\,K^{-1}}$	$862\,\mathrm{J\,kg^{-1}\,K^{-1}}$	$2800\,\mathrm{kg\,m^{-3}}$	71 GPa	0.33	$23.4\,\mathrm{K^{-1}}$	0.098

A cuboid aluminum alloy plate with dimensions $600\,\mathrm{mm} \times 150\,\mathrm{mm} \times 6\,\mathrm{mm}$ is used as the test object. This plate is shown in Figure 3.3 in the basic configuration without any attached sensors or actuators.

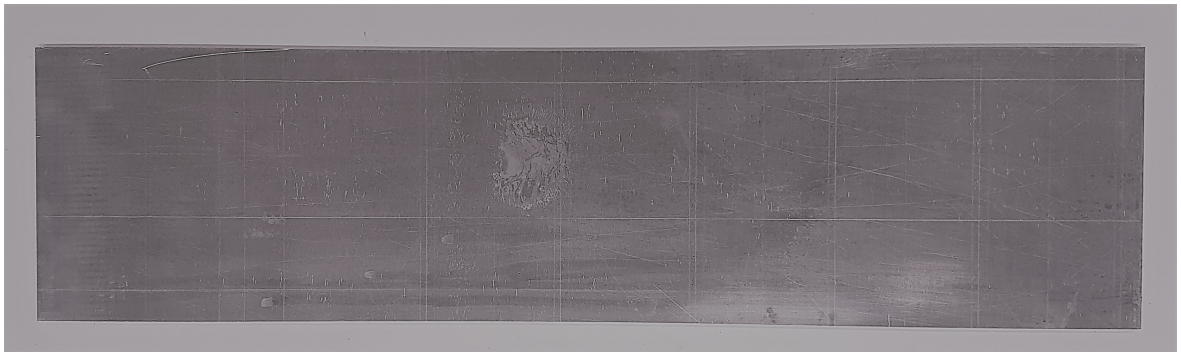

Figure 3.3 Aluminum plate in the basic configuration

With a width of 600 mm, two points on the object can be selected for stabilization through the approach and are far enough apart so that the displacements, without active control, are significant enough to allow improvement. To enable the camera system to capture the test object through the viewport, the height must be lower. Due to the rectangular shape of the plate and the resulting short distance between the points to be controlled in this spatial direction, this may lead to vertical displacements being too small to be accurately detected by the DIC system. It must be assumed that the results will have more significance for the improvement of displacements along the horizontally oriented long side of the plate than for the vertical displacements. Due to the small thickness of the plate and the fact, that only displacements in two dimensions are considered, the use of a single layer of $30\,\mathrm{mm} \times 30\,\mathrm{mm} \times 6\,\mathrm{mm}$ sized hexahedrons as finite elements is sufficient, resulting in 100 elements and 252 nodes bounding each of the elements at the eight corners. Figure 3.4 shows the model of the plate, the nodes are represented by blue dots. With these relatively large finite elements and the

small number of nodes, the model can still be described with sufficient resolution and accuracy due to the simple geometry.

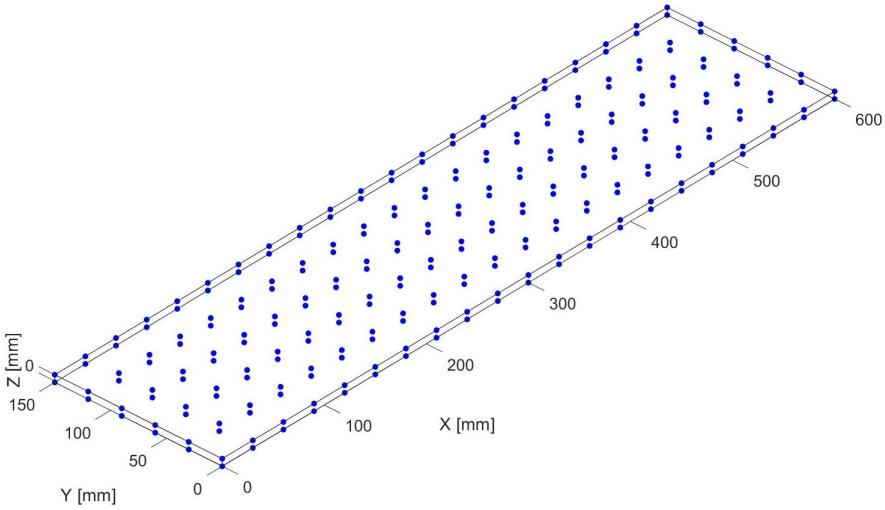

Figure 3.4 FEM model of the aluminum plate

The geometry of the test object is intentionally kept very unsophisticated. On the one hand, the FEM model is very simple, quick to modify and adapt, and not very computationally intensive due to its size. On the other hand, there is no need to determine any view factors between the surface elements of the structure, since each surface is in radiative exchange with its environment only. This further simplifies the calculation. Observing the front surface without casting shadows and complicating the illumination of the object is also ensured by the simple geometry.

Nevertheless, the use of a coarse mesh results in an error. By minimizing the size of individual finite elements and optimizing their meshing method, this error can be made sufficiently small. However, this is at the expense of the computational effort, which drastically increases with the number of nodes and elements. Therefore, a balance needs to be struck between a sufficiently fine mesh with an adequate number of nodes and the associated computational cost.

As described in Section 2.2 one control HE is required for each DOF to be controlled. Hence, the size of the control element must correspond precisely to one element of the FEM model. The model of the structure is created in the FEM analysis software Ansys. The object to be modeled can be designed and meshed there using a CAD tool. The coordinates of the nodes of the mesh as well as the assignment to elements and the determination of view factors for the radiation exchange can be exported so that the thermomechanical model and the filter and controller framework can be designed in MATLAB on this basis. For this purpose, the exclusive use of hexahedra as elements is necessary, which, in the geometry at hand, poses no restrictions but may need to be considered or adapted for more complex structures. The use of other element types, such as shell elements, was not further investigated here, as it has already been specified

in [6]. Even though, for the final simulations and the experimental implementation, only the FEM model implemented in Matlab was utilized, an initial comparison with the results of the Ansys simulations is advisable for validation. For the model in this approach, the relatively coarse mesh, previously shown in Figure 3.4 through the nodes of the mesh, was ultimately chosen. Simulations in both, Ansys and MATLAB, have shown that the discrepancies in the calculation of the steady-state temperature field for this coarse mesh deviate by about 1 % to 2 % from a much finer mesh with 4 times or 16 times the number of elements, as shown in Figures 3.5 and 3.6 considering a steady-state temperature of around 9 °C to 13 °C as reference.

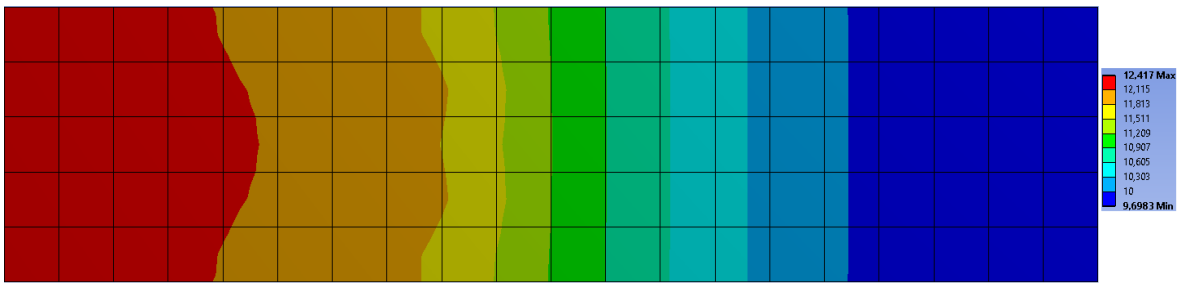

(a) Mesh size 30 mm × 30 mm

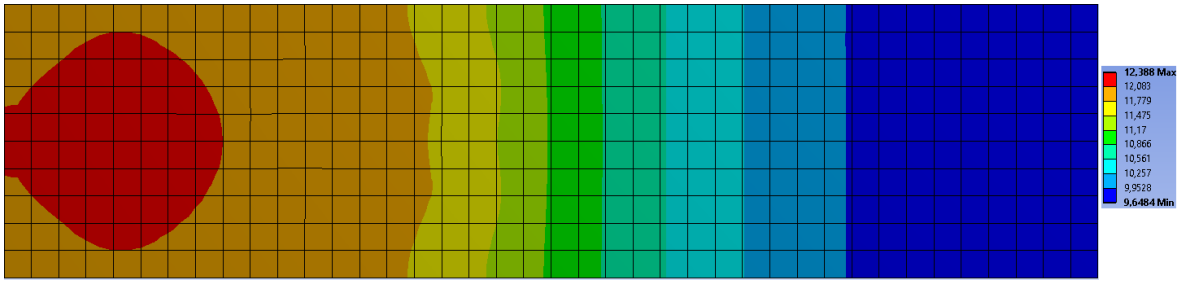

(b) Mesh size 15 mm × 15 mm

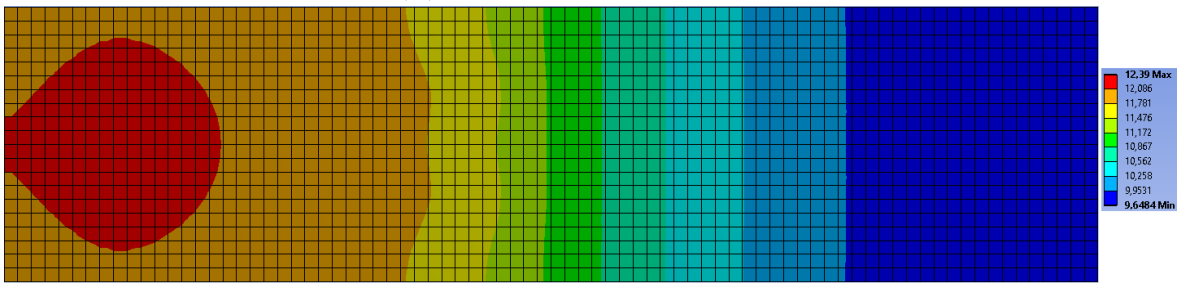

(c) Mesh size 7.5 mm × 7.5 mm

Figure 3.5 Comparison of temperature fields (°C) for different grid sizes, Ansys

For identical boundary conditions, the steady-state temperature field solution was simulated in Ansys for three different mesh sizes and MATLAB for two different mesh sizes. Figure 3.5a illustrates the coarse mesh utilized for this study, with a minimum node temperature of 9.69 °C and a maximum node temperature of 12.42 °C. With a fourfold refinement of the mesh, these temperatures change to 9.65 °C and 12.39 °C, respectively, as shown in Figure 3.5b. Further refinement by a factor of 4 brings no significant improvements (Figure 3.5c). Although the maximum and minimum node

temperatures vary slightly, observing the temperature field reveals that the resolution is notably poorer, especially on the left edge behind the perturbation HE, resulting in deviations. However, on average across all nodal temperatures, this difference remains far less than 0.1 K in total.

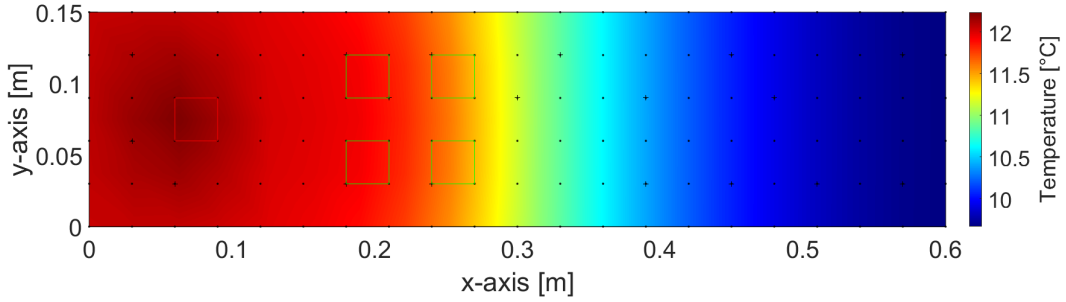

(a) Mesh size 30 mm × 30 mm

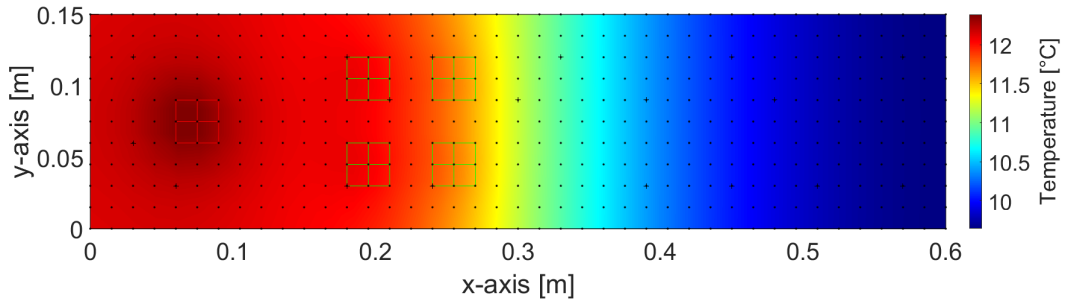

(b) Mesh size 15 mm × 15 mm

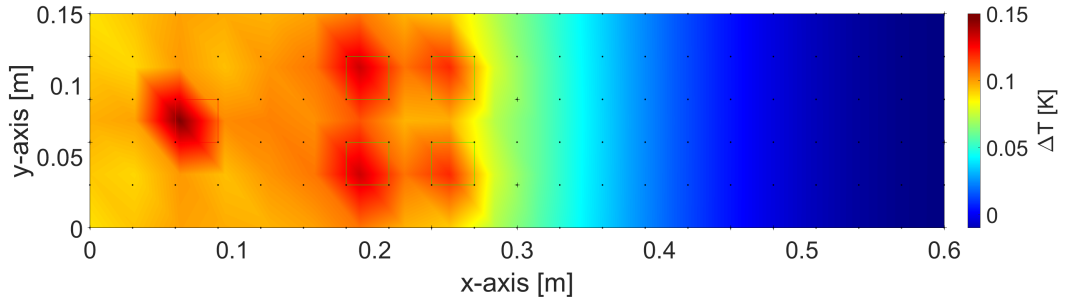

(c) Temperature difference between both meshs

Figure 3.6 Comparison of a temperature fields for different grid sizes, Matlab

A similar pattern emerges in the calculation of the steady-state temperature fields in the MATLAB simulation. For the coarser mesh depicted in Figure 3.6a, a temperature range of 9.66 °C to 12.31 °C is obtained, while the fourfold finer mesh, shown in Figure 3.6b, exhibits a temperature range of 9.64 °C to 12.49 °C. Notably, the maxima of the temperatures deviate by approximately 0.15 K more than the minima in both cases. Figure 3.6c depicts the temperature deviation between the two meshs, showing noticeable differences only around the HEs. On average, the nodal temperatures differ by only 0.05 K. Particularly in those parts of the plate, where the points to be controlled are located, almost no noticeable changes can be seen. The simplification in computational effort and meshing, given that the size of an element directly corresponds to the size of the HEs, leads to the utilization of the ostensibly coarser mesh

with an element size of 30 mm × 30 mm. The exemplary results shown here also illustrate that the differences between the solutions of the steady-state condition in Ansys and Matlab are minimal. Assuming, that the simulations in Ansys provide correct results, this confirms the use of the Matlab FEM model in this framework.

A detailed explanation of the setup of HEs already indicated here, which can be recognized as red or green squares in Figure 3.6, follows in Section 3.5.

3.3 Mounting and Support of the Test Object

The mechanical model must take into account that the structure under investigation must be supported in a certain way. The support of the aluminum plate chosen here must fulfill several conditions:

1. Even in zero gravity in space, the optical bench to be represented by the aluminum plate will not float freely in space, but will be attached to the satellite structure. Nevertheless, the structure must be able to expand freely during temperature changes without causing stresses and strains that would lead to damage. Since zero gravity cannot be simulated in laboratory tests, this must be taken into account in the mounting. The necessary theoretical basis for such a type of support is described in Section 3.3.1.

2. The approach presented here considers only radiation and heat conduction, but not convection, which would not exist in space either. The laboratory experiments must therefore take place in a vacuum chamber. Hence, the mounting must fulfill the conditions of vacuum suitability.

3. Since the plate will be filmed through a viewport from outside the vacuum chamber by a camera system that serves as a validation tool for the approach, it must be placed vertically, as shown in Figure 3.2, at a certain height and cannot lie on the table of the vacuum chamber. In addition, one fixed immovable point on the plate can serve as a reference for the camera system improving the repeatability and comparability of the displacement measurements. These conditions are fulfilled by the mounting described in Section 3.3.2.

4. The approach compensates for displacements due to changes in heat fluxes. To make these reproducible and quantifiable, a heat flux is introduced by HEs. Any other external heat flux on the aluminum plate must therefore be avoided. Hence, the mounting must be thermally decoupled from the plate as well as possible. The approach chosen for this purpose is explained in Section 3.3.2.

The listed conditions can be met by a specific type of kinematic couplings, the isostatic mounting.

3.3.1 Kinematic Coupling and Isostatic Mounting

Every rigid body possesses a limited number of independent DOF, three perpendicular translations and rotation, respectively, around the three perpendicular spatial axes. If a movement is contrained, the respective DOF becomes a degrees of constrain (DOC). The kinematic design is the way of selecting certain DOCs and allowing desired DOF without redundant constrains. A kinematic coupling is obtained, when every relative motion between two rigid bodies is contrained exactly once. Kinematic couplings are isostatic mounts of two bodies using exactly six contact points and their resulting nesting forces [44]. Kinematic couplings are widely used and have been intensively researched [44, 45, 46, 47, 48, 49].

One of the classic kinematic couplings, probably first described in the 19th century by William Thomson, who was known as Lord Kelvin and is thus the namesake of this type of mount [44, 45], can be seen in Figure 3.7. At point 3, a tetrahedral arrangement of edges constrains the contact element, shown here as a sphere, each of which is attached to a corner of the plate, in all translational DOF. At the second point, the sphere is then in a V-groove, allowing movement in the direction of the first mounting point and constraining it in the other two. Support 1 is simply a disk on which the sphere rests, so that the plate remains in the same plane defined by the previous two points and thus only one translational DOF is constrained. Because of the way the 6 DOF are constrained by the 3 points, this Kelvin mount is also called 3-2-1 configuration [45] or Tetrahedron-Vee-Flat coupling [44].

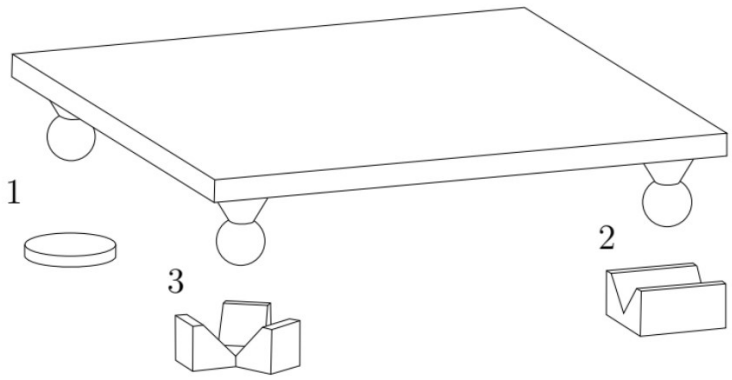

Figure 3.7 Classical Kelvin mounting [6]

The support necessary for the experimental setup is implemented with the Kelvin mounting. The description of the design and realization is given in the next Section.

3.3.2 Design of the Support

The support, which can be seen in Figure 3.7, must now be implemented according to the conditions formulated in Section 3.3. Initially, it must be considered that one surface of the plate must be filmed through a viewport by a camera system as an external validation instrument, which is described in detail in Section 3.4. For this purpose, the entire experimental setup must be placed at a height of approximately 400 mm within the TVC.

The necessary mounting system must be robust, easy to install, fully vacuum-compatible, as variable and adaptable as possible, and yet of the smallest possible cross-sectional area, so that the effects of radiation due to changes in view factors are minimal. Extruded aluminum profiles meet all the requirements and are also very inexpensive to purchase. The profiles were screwed together in a T-shape so that the planned Kelvin mount could be installed in one plane. The individual supports of the mount were modeled and 3D printed for test purposes before they were milled from one aluminum block each. The respective 3D models of the three support elements of the Kelvin mount can be found in Figure 3.8. Each support is provided with drill holes through which they are connected to the extruded aluminum profiles.

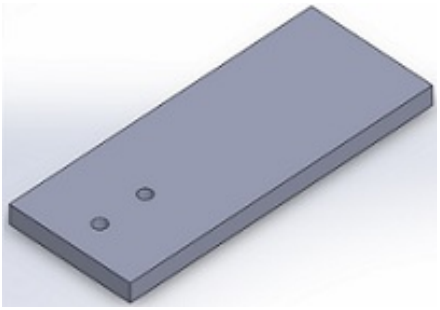

(a) Support 1: Plate

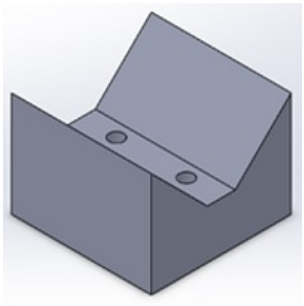

(b) Support 2: V-groove

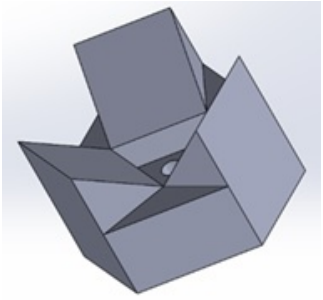

(c) Support 3: Tetrahedral

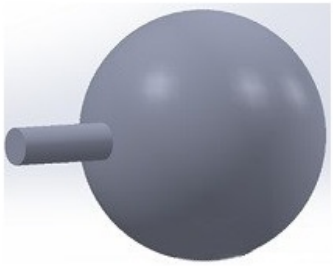

(d) Sphere as counterpart

Figure 3.8 Different supports of Kelvin mounting

As counterparts of the supports, as already shown schematically in Figure 3.7, spheres are used, which must be connected to the aluminum plate. To meet the conditions of thermal insulation, the spheres were milled from Teflon blocks and provided with a threaded pin at one end. Teflon, the commercial name for Polytetrafluoroethylene (PTFE), has many advantages. Its thermal conductivity of $0.25\,\mathrm{W\,m^{-1}\,K^{-1}}$ is about

500 times lower than that of aluminum [50]. Additional, unwanted heat input at the contact points on the plate by the Teflon spheres is thus reduced to a minimum. The static coefficient of friction μ_S of 0.19 is very low, which is why Teflon can slide very well on aluminum [51, 52]. Assuming that the weight of the aluminum plate including the sensors and actuators of approximately 1.6 kg is evenly distributed over both upper supports, a static friction of just 1.49 N would act in the V-groove support. While this friction is not negligible small and may, as experiments will show, potentially account for certain anomalies, it does not introduce a significant source of error. Due to the comparatively low weight of the plate, the strength of the Teflon spheres is sufficiently high so that they do not suffer any notches as a result of the mounting and the ability of the plate to expand freely with changes in temperature remains guaranteed. Through the pins, the balls are tightly screwed into holes, which were recessed in the two upper corners and the lower center of the plate. The length of the pins and position of the spheres were chosen so that the spheres lie in one plane, thus fulfilling the conditions of an isostatic mount. The 3D model of the spheres can also be seen in Figure 3.8. The mounting system made of the extrusions with the supports numbered according to the Kelvin conventions is shown in Figure 3.9.

Figure 3.9 Mounting system with supports of the isostatic mount

As a first approximation, both the aluminum rack and the spherical mountings themselves can be neglected for the model due to the thermal decoupling. Nonetheless, a slight heat flux will occur from the plate through the spherical bearings into the mount due to the temperature gradient. The heat flux density is dependent on the thermal conductivity of the material and the temperature gradient. However, the processes involved in heat transfer between two contacting bodies are considerably more complex and dependent on numerous parameters such as the thermal conductivity of both bod-

ies, the temperature difference, the size and roughness of the contact area, and other mechanical properties. As a result, there is no unified theory for calculating this heat transfer, and often, estimations based on empirical data in space technology are used [53]. For this simple test setup, in a first approximation, this heat flux is expected to be minimal and therefore not considered in the model. In the FEM analysis software Ansys, the absence of heat conduction at the contact surface caused a deviation of 0.1 K to 0.25 K in the calculation of the steady-state temperature field under various boundary conditions, depending on the setup and the settings. These values are in the range of the accuracy of the temperature sensor measurement. Based on the measured temperature ranging from approximately 9 °C to 15 °C for most of the experiments, this results in a relative error of 1 % to 2 %. Hence, the structure is modeled as symmetrical, even though it is not symmetrical in reality. This becomes evident in certain sensor measurements, particularly in the assessment of transfer functions (refer to Section 4.2). The influence of this model error on the accuracy and functionality of the framework is acceptable small.

All in all, the potential error caused by the mounting in the displacement measurement is very difficult to estimate but is almost certainly a great source of uncertainty in the entire setup and a primary target for improvements. The spherical bearing of the mounting must be perfectly fixed to the plate, preventing any relative displacement between them. However, because these bearings are made of PTFE for thermal decoupling, their stiffness is low, resulting in thermal expansions of the plate not necessarily leading to unrestricted expansion. Despite the low coefficient of friction, this also means that deformations of the plate are not entirely stress-free and hence reversible. Displacements will be measured in the low micrometer range. It can be assumed that deviations of 1 µm to 2 µm are possible due to the various simplifications indicated, which could result in a relative error of up to 20 % considering a measured displacement of 10 µm as reference. To demonstrate the functionality of the approach, it is compared with uncontrolled reference states. If the error introduced by the mounting is the same for all cases considered, the relative impact is minimal. For the comparison between simulation and experiment, however, greater deviations can occur, that might be attributable to the isostatic mounting.

3.4 Digital Image Correlation System

To measure the distortions of the plate, a speckle pattern is applied to the surface of the test object. In the experimental setup, the speckle pattern is realized by black color pigments sprayed on a white primer on the front side of the plate. Using a high-resolution camera and a DIC software, the change in gray levels of the speckle pattern is captured over time and the pixels of the camera images are precisely assigned to the local surface pattern of the black paint pigments [54]. Images acquired at certain intervals are analyzed using subpixel-accurate image correlation algorithms. From the

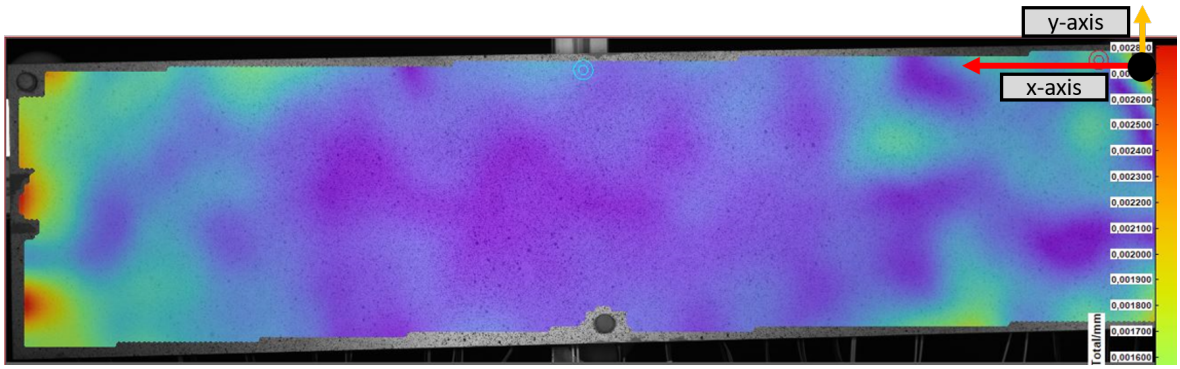

Figure 3.10 Coordinate system for displacement measurement with the DIC software

changes with time in the gray values of the speckle pattern relative to a reference state, the steady-state before the start of a test, the displacements in the image plane can be calculated to within approximately 1 µm. Within the image, this is done by defining a coordinate system whose origin is at the reference point of the isostatic mount. The temporal changes in the displacements of the points to be stabilized can be displayed and saved in the Istra4D software [41] as a contour plot, a 2D graph, or in tabular form. Contour and smoothing filters can be applied to improve the quality of the images. Figure 3.10 shows a screenshot of a recording made by this camera system. The origin of the reference coordinate system is placed in the far upper right corner of the test object within the recording. This is where the tetrahedral-shaped support of the isostatic mount is located, and thus the point that does not move translationally. The x-axis is defined along the upper edge of the plate, and the y-axis runs in extension of the right edge. As a result, the z-axis extends into the image plane. However, this is not relevant because one camera can only record displacements in the image plane. A second camera cannot be used due to the size of the viewport and the occurrence of reflections if it is not aligned parallel to the glass. The contour plot shown in the figure represents the displacements, the magnitudes of which can be read on the scale at the right edge. The region of interest to be evaluated must be marked before analysis, as well as many other analysis settings, to ensure that a sufficient number of pixels can be detected and grouped into clusters and facets so that they can be correlated with each other and with a reference image. The illumination of the test object is concentrated on the area where the points to be controlled are located. However, especially the peripheral areas are sometimes poorly resolved and result in larger deviations and errors. As can be seen in the figure, the lower part is not resolved, and the part of the support structure that does not have a speckle pattern is also unresolved. This may be related to both the lighting and the quality of the speckle pattern itself or inadequate clustering and facet formation within the software.

Since the color particles of the speckle pattern would easily detach from the surface in vacuum, the pattern is additionally protected by a PTFE sealant and thus made suitable for vacuum. Even though the connection of the color and the sealant to the

plate's surface is good due to heating and curing, it is not perfect. When the plate deforms, it is therefore assumed, in a first approximation, that the sealed color layer deforms in exactly the same way. The resulting discrepancies of this assumption are difficult to quantify as no reference values can be established. This could potentially have implications for the comparison between simulation and experiment. Nevertheless, it can be assumed that the effect remains consistent within an experimental series, making it negligible for the comparison between an uncontrolled reference case and a controlled case in the experiment. To provide a conservative and cautious estimate, a potential deviation between simulation and experiment due to the speckle pattern of around 1 µm will be assumed, resulting in a relative error of 10 % when leveraging the aforementioned 10 µm baseline here as well.

The camera is set up on a tripod outside the TVC, leveled and calibrated. Calibration is performed using a calibration target, which is a ceramic disc with a checkerboard pattern, with the corners and spatial orientation being captured by the camera. Since the DIC software contains information about the calibration target, calibration images of the target being placed in front of the test object are taken, defining the distance and relative orientation of the camera to this test object. In order to maintain this calibrated state of the camera, it must not be moved after calibration. Every vibration and even larger temperature fluctuations in the laboratory due to the time of day influence the measurement. The positioning including the viewing angle of the DIC system is shown in Figure 3.11.

Figure 3.11 DIC system in leveled condition on tripod

To be able to perform an imaging, the surface must be sufficiently illuminated. LEDs are positioned in the TVC for this purpose. A total of ten breadboards, each have 25 LEDs soldered onto them, are mounted on a fixture made of extruded aluminum

profiles. Each element can be individually aligned to ensure optimum illumination of the test object. The entire setup can be seen in Figure 3.12.

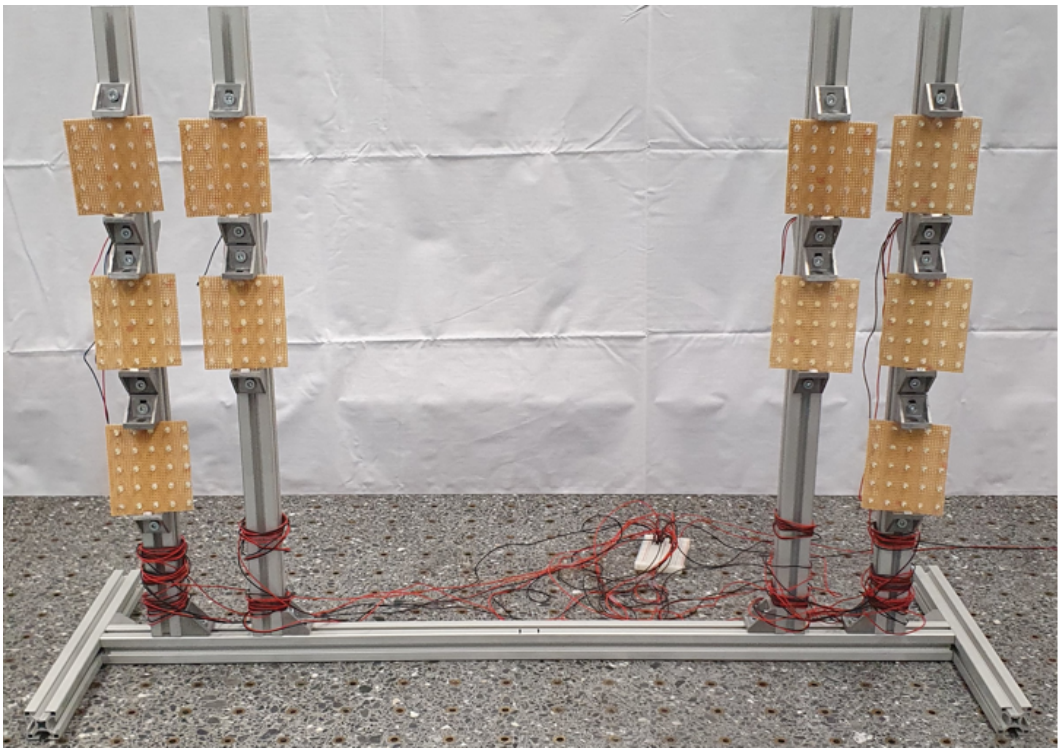

Figure 3.12 Support for the light fields

Finally, the fixture of the light fields was connected with the mounting system of the aluminum plate to form one total setup, which is shown in Figure 3.13.

The heat input from the permanent thermal radiation of the LEDs has a major influence on the radiation exchange of the structure and must not be neglected in continuous operation. The manufacturer's specifications of the LEDs used do not include information on their efficiency, but even the most efficient LEDs have an efficiency of only 50 %, which means that 50 % of the energy is emitted in the form of thermal radiation [55]. Since a simulation of this additional heat source is inaccurate and the parameters for the radiation influence change every time the light fields are readjusted, a light control was implemented to bypass a simulation and minimize the effects of additional heat radiation. Since the camera recordings are only carried out at a predefined interval, the light fields also only have to be switched on for this time. Therefore, the activation of the light fields is synchronized with the camera recordings of the DIC software, so that they are only switched on for 5 s. Assuming that an image is taken by the camera every 6 min, this results in an additional heat input to the experimental setup at 1.4 % of the runtime of the experiment. The 10 light fields are operated with a total output of 16 W. Even if it is assumed that the lighting is ideally directed onto the plate instead of omni-directional into the entire TVC, this results in a heat input per area of less than 100 $\mathrm{W\,m^{-2}}$ at 50 % efficiency. If only the steady-state operation

of the 4 control HEs is used for comparison, this results in a constant heat input per area of 2222 $\mathrm{W\,m^{-2}}$. Thus, this effect can be neglected in a first approximation.

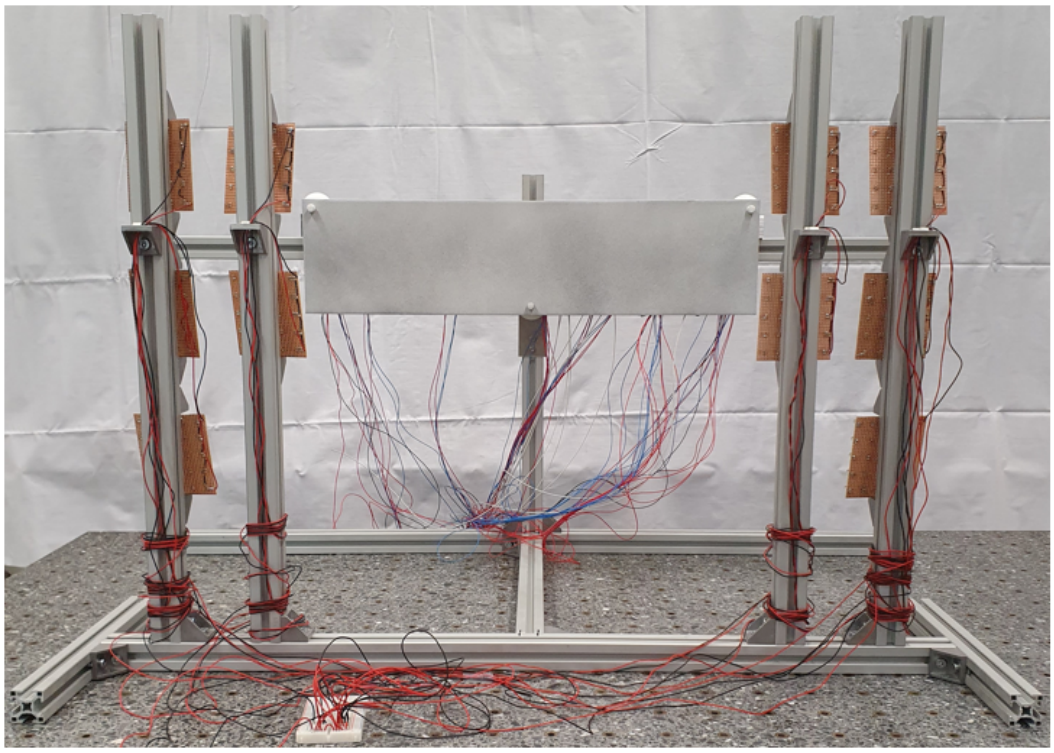

Figure 3.13 Setup of the mounting device with illumination

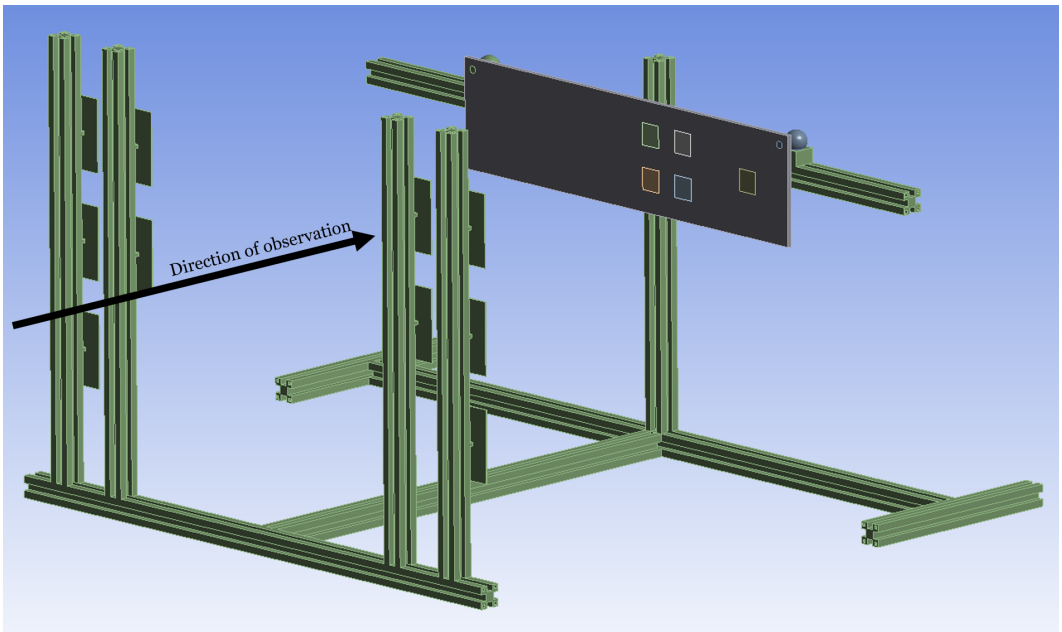

Figure 3.14 Model of the entire experimental setup

Figure 3.14 shows a model of the entire experimental setup, created with the Ansys FEM analysis software, which was also used to generate the FEM model of the alu-

minum plate, as well as the observation direction of the camera. The black coated vacuum chamber inner wall and the mounting table were used to model the uniform radiation background with an emissivity ε of 0.9. The model in Figure 3.14 clearly shows that a not insignificant part of the hemispherical radiation background - i.e., the view factors between the plate and the environment - would have to be represented by the aluminum rack and the light fields. Ansys modeling and simulations have shown that this area accounts for only under 10 % of the half-space. Although the emissivity of aluminum is much lower than that of the black coating of the vacuum chamber wall, due to heat conduction and radiation exchange, the temperature of the aluminium mounting at steady-state is equal to the temperature of the vacuum chamber wall. Therefore, the effects of the different radiation conditions on the temperature of the aluminum plate are negligible.

For the correlation process, calibration of the camera's position relative to the object to be measured is required. This calibration must be performed with the TVC bell open so that the aforementioned calibration target can be positioned in front of the setup. The calibration takes place under atmospheric conditions and without the presence of the TVC's viewport in front of the DIC system's lens. After closing the TVC bell, the experimental setup can move due to the evacuation of the atmosphere. Through the viewport, slight reflections and interferences, or disturbances due to water condensation on the inside or outside of the glass can occur, affecting the measurement resolution. However, comparative measurements in the laboratory under non-vacuum conditions have shown that the noise in the displacement measurements is at a comparable level. If the test object shifts during the evacuation of the TVC, and this positional change is permanent and constant, then the influence is also negligible, as each displacement measurement is performed relative to a reference state taken at the start of the experiment.

The camera is located outside the TVC since it is neither vacuum-compatible nor equipped with the necessary connections for installation inside the TVC. Consequently, it is exposed to the environmental conditions in the laboratory during the long runtime of the experiments. In particular, significant temperature fluctuations, which can reach up to 10 °C in the summer months in the laboratory without air conditioning, can affect the optics and the tripod to which the camera is attached. The smallest deformations or vibrations can thus influence the measurement if the position of the objective lens is shifted compared to the calibrated starting position. This process can either be gradual, resulting in a linear change in the displacement measurement, or it can occur suddenly, leading to a rapid change in this measurement that is beyond the measurement noise. However, a general quantification is also challenging at this point.

The camera system is probably the most critical component in the test setup and therefore the largest source of error for the measurement chain of the displacements. Measuring displacements in the micrometer range is inherently complex, delicate and

subject to various boundary conditions and factors that can affect and perturb it, as described in the course of this section. Despite all the inaccuracies and uncertainties, the DIC system provides the best option for non-contact strain measurement. Given that only small deformations in the range of 10 µm are expected due to the minor temperature differences, the accuracy specified by the manufacturer of 1 µm [54] already implies a potential error of 10 %. Since, as described in detail, there are many other influences on the measurement which, although small, are conceivable and which can hardly or not at all be quantified, a very conservative relative total error of 20 % appears realistic.

3.5 Experimental Design and Definition of System Parameters

As described in the preceding sections, many components of the experimental setup have an impact on the structure to be controlled, most of which are minor an can be neglected. In total, however, these simplifications ensure that, especially, the temperature field of the structure cannot be considered independently of the specific experimental setup. Deviations are therefore determined through tests and considered through different calibration processes. These include in particular the calibration of the sensors and actuators as well as the measuring and actuating chains so that they can be used correctly under the various conditions and test cases. Details regarding these steps can be found in Appendix B.

For the experimental validation, two points on the structure were selected, and their displacements in the x- and y-directions relative to a fixed point defined by the isostatic mount should be minimized. These two points should be distributed on the plate in such a way that their distance from each other is relatively large, making it easier to detect changes and to minimize measurement errors due to the maximized distance.

For an initial experimental setup to control the two selected points, four control HEs are symmetrically placed on the plate near the perturbation heat source. This also serves as an initial validation of the thermal behavior of the HEs and provides a correlation between the applied heating power and the measured temperature. Using HEs, only positive heat can naturally be introduced into the structure. Active cooling is not possible. However, to enable both positive and negative changes in heating power with the same elements, the HEs are operated at a certain power level in the steady-state condition, so that reducing the heating power or switching off the elements can simulate a negative heat flux and thus cool the structure below the steady-state temperature. Based on the positions of the HEs and the defined boundary conditions, the thermal steady-state solutions and the transfer functions can now be calculated.

The positions of the temperature sensors would have to be derived from the thermal transfer functions in the next step, which is described in detail later in this section. For an initial configuration aimed at verifying the thermomechanical transfer functions in addition to a first and simple controlled case, a wide distribution of sensors is pursued instead. Furthermore, by evenly distributing the heat input from the HEs, the formation of a uniform and symmetric temperature field is expected. Therefore, some sensors are placed at symmetric distances from the perturbation and control elements to validate the functionality of those HEs. All sensors have to be placed on the same side as the actuators due to the speckle pattern for DIC validation on the backside.

Figures 3.15 and 3.16 depict the experimental setup in the first configuration. In the first Figure, the positions of sensors and HEs are schematically illustrated. The red element represents the perturbation HE, while the four green-marked elements represent the control HEs. The crosses labeled with numbers 1 to 14 correspond to the positions of sensors on the plate. The two red dots labeled with numbers 1 and 2 represent the nodes to be controlled, which are located on the other side of the plate. The displacements in the x and y directions at these two locations are to be minimized by the control approach.

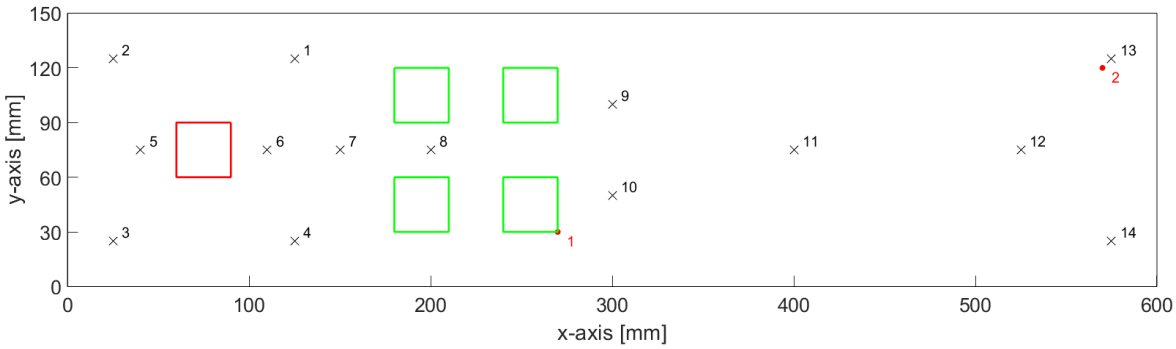

Figure 3.15 Sensor and heater position, configuration 1

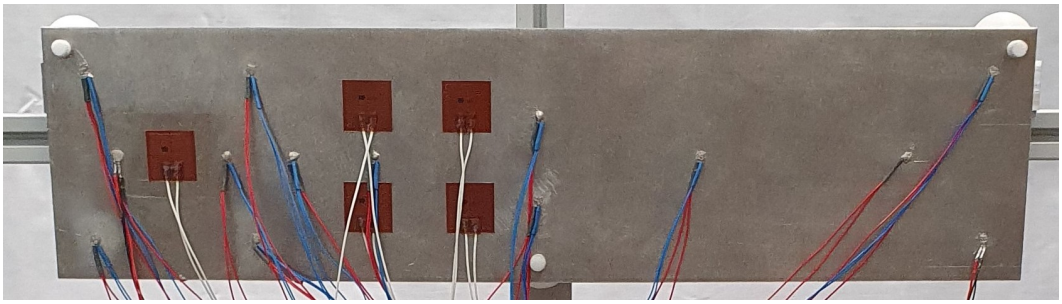

Figure 3.16 Test object, configuration 1

Once the configuration of the sensors and actuators was determined and the structure has been modeled via the FEM model, all the necessary components of the filter and controller approach can be calculated within the model. Before demonstrating the

control framework, the thermomechanical model is validated. In a first step, the thermal and thermo-optical properties of the structure are confirmed experimentally and calibrated to the model. The results of this validation can be found in Section 4.1. In a second step, the basic idea of the transfer functions is confirmed. Figure 3.17 illustrates the geometric representation of the thermal transfer function as a relation between the change in the heat flux q at any surface k in the FEM model of the structure to a change in temperature T at any node i of this FEM model.

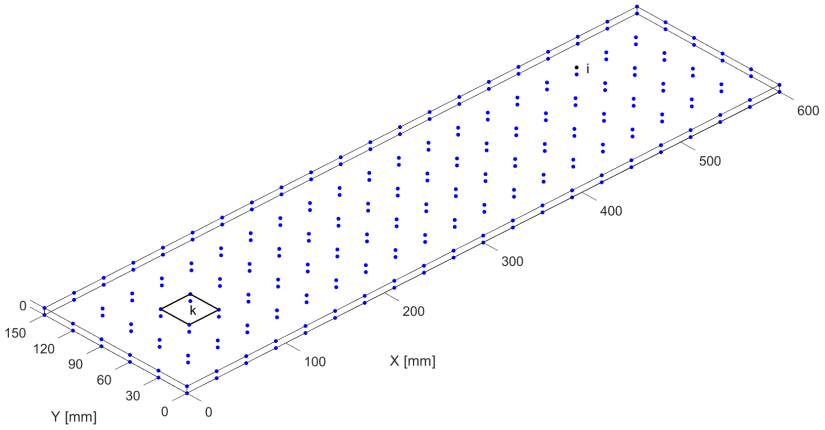

Figure 3.17 Geometric representation of thermal transfer functions in FEM model

The thermal transfer funtion H_{Tq} is calculated in the frequency domain s using the thermal FEM model of the structure and can be expressed as

$$H_{Tq}(s) = \frac{\delta T_i}{\delta q_k}. \tag{3.1}$$

The detailed derivations can be found in [6] and are shortly presented in Appendix A.1. The proof of the thermal transfer function is provided by a periodic variation with frequency s of the heat flux at one or more HEs. A simple perturbation was chosen because it allows to capture the relationships between the temperature field, the commanded heat fluxes and the displacements more clearly. Hence, through one HE a sinusoidal perturbation is simulated with an amplitude of 0.5 W and a period of 6 h, which corresponds to a frequency of 4.63×10^{-5} Hz fulfilling the requirement of low frequency changes. Lower frequencies associated with longer periods of 12 h or more were also simulated. For several reasons, a period of 6 h was chosen for the tests. Firstly, at lower frequencies, the modal weight is distributed over a smaller number of thermal modes, simplifying the reconstruction of the temperature field. This factor will be further discussed at the end of this section. Secondly, conducting numerous tests with periods of 12 h or more would require many weeks of testing time in the TVC, which is expensive, prone to wear, and hardly feasible due to usage capacities. Since no higher insights are expected from lower perturbation frequencies, focus was placed on this specific frequency. Due to the fact that a negative heating power would physically mean a cooling of the object, which cannot be represented by a HE, the perturbation

element already runs in steady-state with a power of 1 W. Thus, the perturbation is in a power range of 0.5 W to 1.5 W. The time course of the sinusoidal perturbation is shown in Figure 3.18.

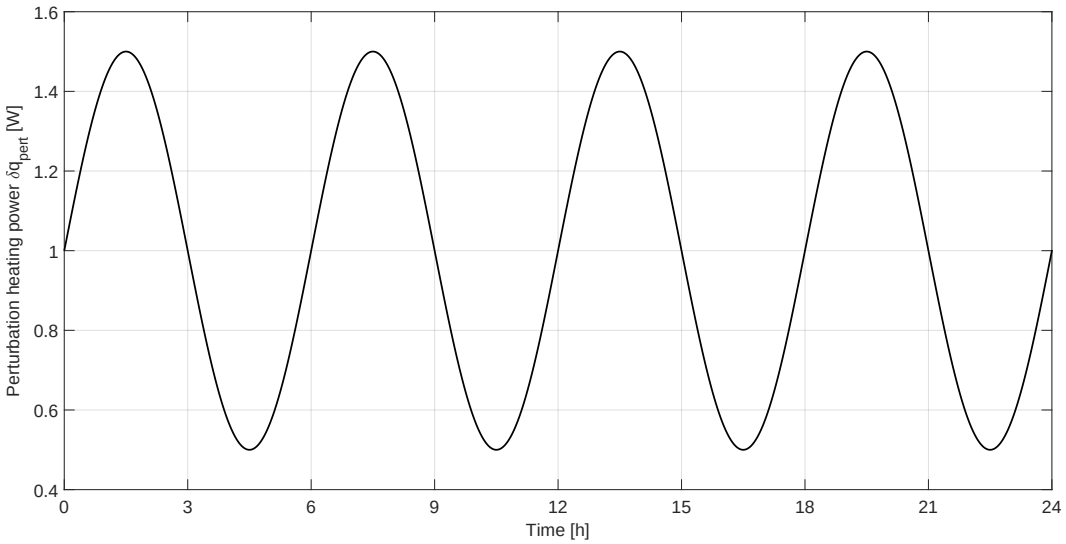

Figure 3.18 Time course of the sinusoidal perturbation

The validation of the thermal transfer functions can be found in Section 4.2

The effects of the sinusoidal perturbation are then controlled by the closed loop filter- and controller approach in the last step. The control HEs required for this must thus also enable heating and cooling simultaneously, so that these also have to be operated with a certain preset power in the steady-state case.

For this third and last step, the determination of the system parameters is required. These include setting the weighting matrices of the LQR and defining the covariance matrices of the Kalman filter.

The derivations of the equations for calculating all necessary components of the LQR as well as the Kalman filter are provided in detail in Appendix A.4.2. For a better understanding of the system parameters required for the design and configuration of the filter and controller, the most important correlations will be briefly described here.

A LQR is a common approach to control linear, discrete-time systems in space technology [56]. Figure 3.19 illustrates the principle of operation of the LQR as a block diagram, where δq_{pert} describes the change in the perturbation heat flux acting on the thermomechanical model, δq_c the change in the control heat flux as control input of the thermomechanical model, δT the change in the temperature as the output of the thermomechanical model and, simultaneously, the state-feedback to the LQR and δu the change in the displacement, that should ultimately be minimized.

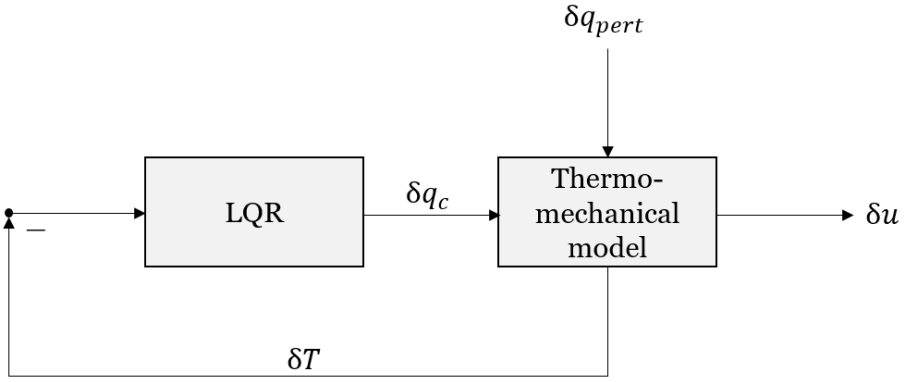

Figure 3.19 Block diagram LQR

The LQR is described by a linear controlled system defined by the state space and the quadratic cost function

$$J = \int_0^\infty \left(\{Y\}^2 + \rho_W \{U\}^2 \right) dt, \tag{3.2}$$

with Y being the output, U the control input and ρ_W a relative weight factor between input and output. A certain control input must be applied, so that the integrand in Equation 3.2 converges to zero and the integral becomes finite. This control input is given by the heat vector $\{\delta q_c\}$, so that

$$\rho_W \{U\}^2 = \rho_W \{\delta q_c\}^T [R] \{\delta q_c\} \tag{3.3}$$

with $[R]$ being a weight matrix between each control input with respect to the output. In this work, the control HEs describe this weight. As they are all treated equally, $[R]$ becomes a multiple of the identity matrix.

Based on Newton's 2$^{\text{nd}}$ law the equation of motion in matrix notation can be expressed as

$$[M_u^r]\{\delta \ddot{u}^r\} + [C_u^r]\{\delta \dot{u}^r\} + [K_u^r]\{\delta u^r\} = [F_T^r]\{\delta T\}. \tag{3.4}$$

The matrix $[M_u^r]$ represents the mass matrix, the matrix $[C_u^r]$ the damping matrix and the matrix $[K_u^r]$ the stiffness matrix, which can all be calculated from the FEM model via shape functions. Using $[F_T^r]$ on the right-hand side of the equation, a relationship is established between the temperature field and the forces acting as a result of thermal expansion. The index r stands for the reduced matrices and vectors due to the isostatic mount [45] in which 6 DOF are constrained at 3 points in the structure allowing a support of the structure while it can expand freely without arising stresses. As the displacement for those DOF is zero, the corresponding rows and colums in the mechanical matrices can be deleted.

If Equation 3.4 is reduced by the contributions of interia and damping, since perturbations of thermal origin can be regarded as quasi-static, the following is obtained by rearrangement

$$\{\delta u^r\} = [K_u^r]^{-1}[F_T^r]\{\delta T\} = [\mathcal{F}_T]\{\delta T\}. \tag{3.5}$$

Since only a few DOF are controlled, the outputs are reduced to the associated cells of the $\{\delta u^r\}$ vector. These reduced outputs $\{\delta u^r\}_{out}$ are then also reflected in the corresponding rows of $[\mathcal{F}_T]$ according to

$$\{\delta u^r\}_{out} = [\mathcal{F}_T]_{out}\{\delta T\}. \tag{3.6}$$

Based on Equation 3.6, the output Y of the cost function in Equation 3.2 can be calculated as

$$\{Y\}^2 = \{\delta u\}_{out}^T\{\delta u\}_{out} = \{\delta T\}^T[\mathcal{F}_T]_{out}^T[\mathcal{F}_T]_{out}\{\delta T\} = \{\delta T\}^T[Q]\{\delta T\}, \tag{3.7}$$

where $[Q]$ is the weight matrix assigning different weights to the cells of the $\{\delta T\}$. Substituting Equations 3.3 and 3.7 into the cost function 3.2 yields to

$$J = \int_0^\infty \left(\{\delta T\}^T[Q]\{\delta T\} + \rho_W\{\delta q_c\}^T[R]\{\delta q_c\}\right) dt. \tag{3.8}$$

The relativ weight factor ρ_W needs to be scaled to establish a certain ratio between the two weighting matrix $[R]$ and $[Q]$.

As shown and explained in the block diagram in Figure 3.19 the LQR feedback loop applies a proportional gain to the output, so that the control input $\{\delta q_c\}$ minimizes J. Using this gain matrix the control input can be calculated as

$$\{\delta q_c\}^t = -[K_{LQR}]\{\delta T\}^t. \tag{3.9}$$

$[K_{LQR}]$ is calculated in discrete-time by solving the algebraic Riccati equation [57] detailed in Appendix A.4.2. This Kalman gain matrix allows a change in the control heat to be calculated based on a temperature difference, so that the displacements at certain points in the structure are minimized.

One key factor in the design of this LQR is a good definition of those weighting matrices. Although there is no fixed rule or method to define and tune matrices $[Q]$ and $[R]$ properly, there exist a few methods to estimate them, like the *Bryson's rule* [58, 59]. Nevertheless, some trial and error, especially to determine the relative weight factor ρ_W between them, remains necessary. For the case presented in this work, almost all values in matrix $[Q]$ are in the range of 10^{-13} to 10^{-16} for the described initial estimation according to the mechanical model. Without scaling those values up, no control is possible and the displacements are not minimized. If the values are scaled

up too much, $[K_{LQR}]$ cannot be calculated due to singularities. If $[R]$ is not scaled in the same way, so that $[Q] \cdot [R] = 1$, the controller performance also deteriorates. For this reason, as a controller design, matrix $[Q]$ was scaled with 10^{15} and matrix $[R]$ with 10^{-15}. Those values are only valid for a specific configuration and might change for every setup.

The performance of the Kalman filter depends on how large the noise of the sensor measurements and the system noise of the model is. The respective noise is defined by covariance matrices and must describe the deviations of the model and the measurements from reality as accurately as possible in order to enable an optimal estimation of the system variables. The covariance matrices of the process noise $[Q_K]$ and the measurement noise $[R_K]$ are calculated according to

$$[Q_K] = [B_1^* \quad B_2^*] \begin{bmatrix} \sigma_1^2 & & \\ & \ddots & \\ & & \sigma_i^2 \end{bmatrix} [B_1^* \quad B_2^*]^T \tag{3.10}$$

$$[R_K] = \sigma_S^2 [I], \tag{3.11}$$

where σ_1^2 to σ_i^2 represent the variances of the respective control and perturbation HEs. Since identical HEs are used for both roles in this experimental setup and their variances are all modeled equally, the variance of a HE is denoted as σ_H^2. The matrices $[B_1^*]$ and $[B_2^*]$ are abbreviations for complex terms containing several FEM matrices from the thermal solution, which are generated by the prediction step in the Kalman filter. They are time-invariant and can be pre-calculated for every setup. Their derivations can be found in Appendix A.4.3. $[Q_K]$ remains constant over time as well. The measurement noise of the temperature sensor measurements, which is defined by the variance σ_S^2, determines the size of the covariance matrix $[R_K]$ via a multiplication with the identity matrix $[I]$, whose dimension corresponds to the number of nodes $n \times n$, as long as all sensors have the same level of noise. This assumption is valid in the demonstrated case because all temperature sensors are of the same design. The more accurately the variances of Equations 3.10 and 3.11 can be determined, the better are the improved estimates of the Kalman filter.

The standard deviation of the HEs σ_H and temperature sensors σ_S respectively, that enter into these matrices, depend on the particular system into which the Kalman filter is to be implemented. Although certain standard deviations are specified by the manufactures for the HEs and temperature sensors, other sources of error in the experimental setup also influence the performance of the filter, so that the actual values for the standard deviations do not correspond to those with the best results for the simulation of the approach or the actual experiment. Therefore, the fine-tuning and adjustment of these variables has an impact on the performance of the approach. This fine-tuning is performed empirically through trial and error of various values within

the simulation. It quickly becomes evident that the most significant improvements in displacements, along with the simultaneous minimization of the required control heating power, occur at standard deviation values close to those expected from the technical constraints.

For the first configuration, the HEs are modelled with a standard deviation of $\sigma_H = 0.02\,\mathrm{W}$, which corresponds to an accuracy of 2 % when applying 1 W to the heater. The temperature sensors have a manufacturer's accuracy of 0.1 K to 0.2 K [60], but this is further reduced by the DAS, cabling and the use of shunt resistors, which is explained in more detail in Appendix B.2, but improved again by means of calibration and filtering within the DAS. Therefore, the performance was simulated with different standard deviations between 0.075 K and 0.35 K and experimentally validated with values of $\sigma_S = 0.1\,\mathrm{K}$, $\sigma_S = 0.12\,\mathrm{K}$ and $\sigma_S = 0.18\,\mathrm{K}$.

Five test cases are conducted with this first configuration, which are listed in Table 3.2.

Table 3.2 Overview of the experimental test series, configuration 1

	Parameters	
Case	**Perturbation**	**Control**
1	sinusoidal 1 W ± 0.5 W	uncontrolled
2	sinusoidal 1 W ± 0.5 W	PCM
3	sinusoidal 1 W ± 0.5 W	control, $\sigma_H = 0.02\,\mathrm{W}$ and $\sigma_S = 0.18\,\mathrm{K}$
4	sinusoidal 1 W ± 0.5 W	control, $\sigma_H = 0.02\,\mathrm{W}$ and $\sigma_S = 0.12\,\mathrm{K}$
5	sinusoidal 1 W ± 0.5 W	control, $\sigma_H = 0.02\,\mathrm{W}$ and $\sigma_S = 0.10\,\mathrm{K}$

First, the perturbation HE is subjected to the sinusoidal perturbation, while the four control HEs remain at their power level of 0.6 W, which corresponds to the steady-state condition. This test case, referred to as the uncontrolled case, serves as a reference condition against which improvements in dimensional stability should be reached with this framework. This experiment is also used to demonstrate the thermal transfer functions. The results are presented in Sections 4.2 and 4.3.1.

The second test case represents the so-called Perturbation Compensation Method (PCM). If the perturbation is known exactly, the necessary control input for the control HEs can be calculated in advance, which ideally compensates for the displacements at the two points.

Analogous to the thermal transfer function, the thermomechanical transfer function establishes a relation between the change in heat flux q on a surface k and the change in displacement u of a node in one spatial direction j according to

$$H_{uq}(s) = \frac{\delta u_j}{\delta q_k}. \tag{3.12}$$

This transfer function H_{uq} derived in the frequency domain as well can be calculated purely from the FEM model. If the perturbation heat flux q acting on surface k is known, another heat flux can be introduced as a control at surface c to compensate for this perturbation, resulting in a displacement of 0 in spatial direction j. In the frequency domain, several transfer functions can be superimposed by simple addition. Hence, Equation 3.12 can be rearranged to

$$\delta u_j = [H_{uq}]_1 \delta q_k + [H_{uq}]_2 \delta q_c = 0. \tag{3.13}$$

This allows the calculation of the necessary control heat flux to ideally compensate the perturbation according to

$$\delta q_c = [H_{uq}]_2^{-1} [H_{uq}]_1 \delta q_k. \tag{3.14}$$

This derivation is considerably simplified. Details can be found in Appendix A.4.1. The results of this PCM validation can be found in Section 4.3.1. As the position of the HEs is not optimzied, the total power needed for the PCM is expected to be higher in this configuration than it might be for an improved setup.

In cases 3 to 5, different settings of the covariance matrices of the Kalman filter are tested. These matrices determine the extent to which the filter trusts the measurements or the model. The covariance of the process noise depends on the standard deviation of the HEs and is kept constant at $\sigma_H = 0.02\,\mathrm{W}$ for the conducted experiments. The covariance of the measurement noise is directly dependent on the standard deviation of the sensors σ_S. During the experimental preparation phase, various settings were simulated, and the best results with the smallest displacements were achieved for $\sigma_S = 0.18\,\mathrm{K}$. Since the variation of the covariance matrix of the measurement noise has a significant impact on the filter performance, additional standard deviations of $\sigma_S = 0.12\,\mathrm{K}$ and $\sigma_S = 0.10\,\mathrm{K}$ are considered in cases 4 and 5, respectively.

As described, the positions of the sensors and actuators in the first configuration of the experimental setup were chosen almost arbitrarily. For a second configuration, these placements will be improved to achieve better stabilization of the two points while requiring less control heating power.

In a first step, the positions of the control HEs are optimized for this purpose. The two nodes to be controlled in x- and y-direction remains the same. Again, one HE must be used for each degree of freedom. Each of these can only be placed on one side of

the plate, since the other side is covered with the speckle pattern for the DIC images. The artificial perturbation in the form of the perturbation HE is also predefined and remains the same. In the simulation of the closed loop filter and controller approach, brut-force [61] is now used to systematically try every possible position for each of the four control HEs, while the controller result is evaluated for the optimal positions of the temperature sensors in each case. Additional criteria are defined to reduce the computational cost. HEs should not be placed directly next to each other due to the wiring, nor should they be placed on or in close proximity to the isostatic mounts. For closer consideration, those distributions of the control HEs are then selected for which control of the two nodes with the lowest possible heating power and an improvement of the displacements by at least a factor of 4 compared to the uncontrolled case is possible in the presence of a perturbation with a specified frequency, in this case 4.63×10^{-5} Hz according to the period of 6 h.

The optimal positions of the temperature sensors are obtained by ranking the largest modal weights of each node. The sensors should be positioned in the FEM model at the locations where the thermal modes reach their maximum amplitudes. These modes originate from the modal expansion defining the temperature field by using the eigenvector matrix $[\phi]$ of the matrix containing the information of the thermal solution and the corresponding thermal modes $\{\tau\}$ according to

$$\{\delta T\} = [\phi]\{\tau\}. \tag{3.15}$$

Since the total temperature field $\{\delta T\}_n$ can be reconstructed for all nodes n with a sufficiently high accuracy from a reduced number of m modes with the highest weighting factors τ, only the corresponding rows and columns of the eigenvector matrix $[\phi]$ need to be evaluated. Thus, Equation 3.15 can be rewritten to

$$\{\delta T\}_n = [\phi]_{n\times m}\{\tau\}_m. \tag{3.16}$$

If the temperature is measured only at the s nodes, with always $s < n$, where a temperature sensor is mounted, Equation 3.16 can be expressed as

$$\{\delta T_{sensors}\}_s = [\phi]_{s\times m}\{\tau\}_m. \tag{3.17}$$

The number of sensors must be higher than the number of modes to sufficiently catch the changes in the temperature field due to uncertainties in the measurement, which makes the matrix $[\phi]$ non-square and therefore not invertible. However, the pseudoinverse $[\phi]^+_{m\times s}$ can be formed from the reduced matrix $[\phi]_{s\times m}$. Using this pseudoinverse, the least squares solution of the modal coordinate vector can be calculated as

$$\{\bar{\tau}\}_m = [\phi]^+_{m\times s}\{\delta T_{sensors}\}_s. \tag{3.18}$$

Substituting Equation 3.18 into 3.16, an estimation of the temperature field can be obtained by using

$$\{\delta\bar{T}\}_n = [\phi]_{n\times m}[\phi]^{+}_{m\times s}\{\delta T_{sensors}\}_s. \tag{3.19}$$

The solution of this pseudoinverse becomes impossible for sparsely filled matrices, if the number of sensors is less than 1.5 times the number of modes. In principle, the reconstruction of the temperature field improves as the number of sensors increases, but no significant effect could be achieved for the structure used here for up to 3 times the number of sensors. Only with a further increase in the number of sensors, the reconstruction becomes more accurate, albeit in a range that is still below the accuracy of the sensor measurement itself. However, using too many sensors runs counter to the basic idea of the approach. In [6] it was demonstrated that for low-frequency perturbations the majority of modal weight is distributed across a few thermal modes. The number of modes required for a sufficiently accurate reconstruction of the thermal field depends on various factors, such as the geometry, symmetry of the structure, and the positions of the points to be controlled. A general quantification of modes is not possible and must be adapted within the framework of designing the geometry and simulating the behavior of the structure. Ultimately, this also influences the total number of necessary sensors. Placing sensors exclusively at nodes where thermal modes have their highest amplitudes can, in some cases, lead to a significantly poorer reconstruction of the temperature field, e.g. because many nodes are located at the edge of the plate or concentrated in a certain area. In addition, it is also possible that the differences to the subsequent nodes with lower amplitude are only very small and therefore the distribution of the sensors over the entire geometry is more advantageous in the technical realization. Throughout the remainder of this section, this principle will be revisited and illustrated through an example.

In a final step, the sensor positions from the remaining cases are adapted for a technical realization. The sensors can also be placed only on one side of the plate, and neither on the edge nor directly on the HEs. Also an accumulation of many sensors in one area of the plate must be avoided for a better reconstruction of the temperature field, which significantly limits the selection of possible sensor positions. When using the same system parameters as for configuration 1 shown in Table 3.2, the best performance in terms of displacement stability, while minimizing the control heating power, was achieved when using the 10 thermal modes with the greatest weight and 18 temperature sensors to capture these modes. The resulting configuration is shown in Figures 3.20 and 3.21.

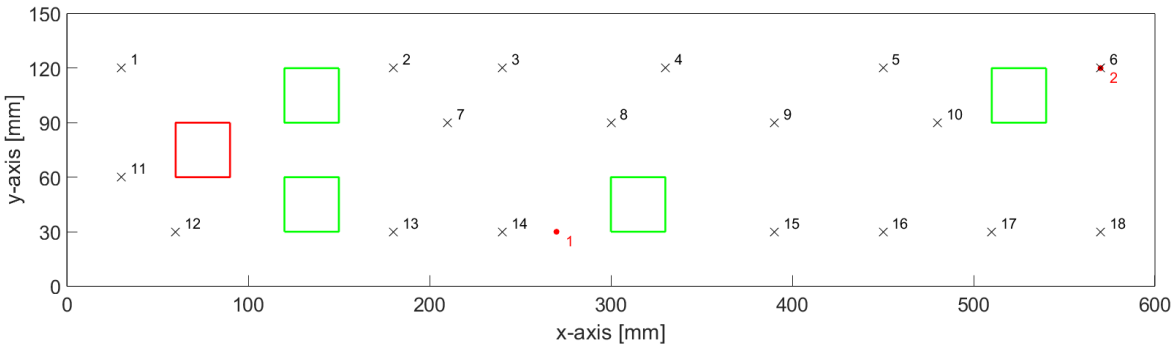

Figure 3.20 Sensor and heater position, configuration 2

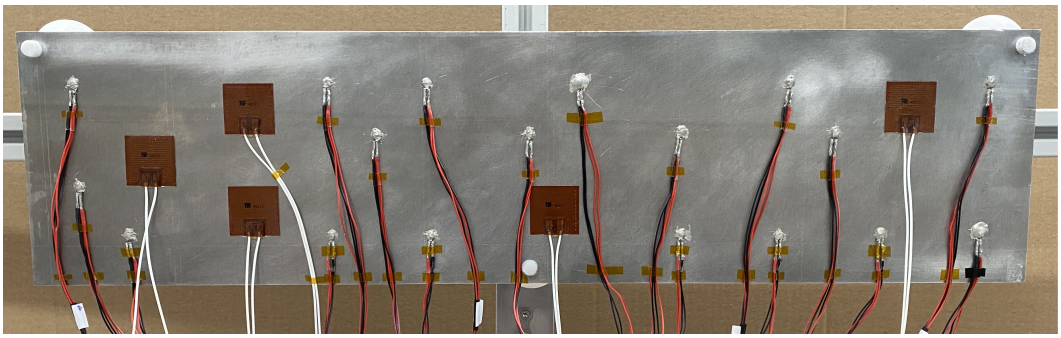

Figure 3.21 Test object, configuration 2

With this new configuration, an improvement compared to the initial configuration in terms of displacement reduction as well as necessary control heating power is expected. Moreover, two other types of perturbations will be examined: random perturbation and stepped perturbation. The randomly generated perturbation is achieved by superimposing five sinusoidal oscillations with the phases, amplitudes, and frequencies listed in Table 3.3, where each individual sinusoidal perturbation $\mathcal{P}_i(t)$ is calculated via Equation 3.20. The values were obtained using the built-in *rand* function in Matlab, which generates pseudo-random values within a given interval. The interval for the amplitude was set to [0,1], for the phase to [0,2π], and for the frequency exponent to [-6,-3]. The function of the total superimposed random perturbation $\mathcal{P}_{tot}(t)$ is calculated according to Equation 3.21. Finally, the total superimposed random perturbation is scaled to a maximum value of 1 W, so that the amplitude of the perturbation remains within the range of 0 W to 2 W.

Table 3.3 Parameters of the random perturbation

Parameters			
Perturbation $[\mathcal{P}_i]$	**Amplitude** $[\hat{y}_i]$	**Phase** $[\phi_i]$	**Frequency** $[f_i]$
$\mathcal{S}_1$	0.3014	3.6350	-3.1081
$\mathcal{S}_2$	0.7112	1.4909	-4.4040
$\mathcal{S}_3$	0.2217	2.8830	-3.7987
$\mathcal{S}_4$	0.1761	6.0513	-4.9848
$\mathcal{S}_5$	0.8934	3.4357	-5.2704

$$\mathcal{P}_i(t) = \hat{y}_i \sin(2\pi \cdot 10^{f_i} \cdot t + \phi_i) \qquad \text{with} \quad i \in [1,5] \tag{3.20}$$

$$\mathcal{P}_{tot}(t) = \sum_{i=1}^{5} \mathcal{P}_i(t) \tag{3.21}$$

Figure 3.22 shows the five sinusoidal oszillations individually, Figure 3.23 shows the resulting total perturbation from the superposition over a period of 48 h.

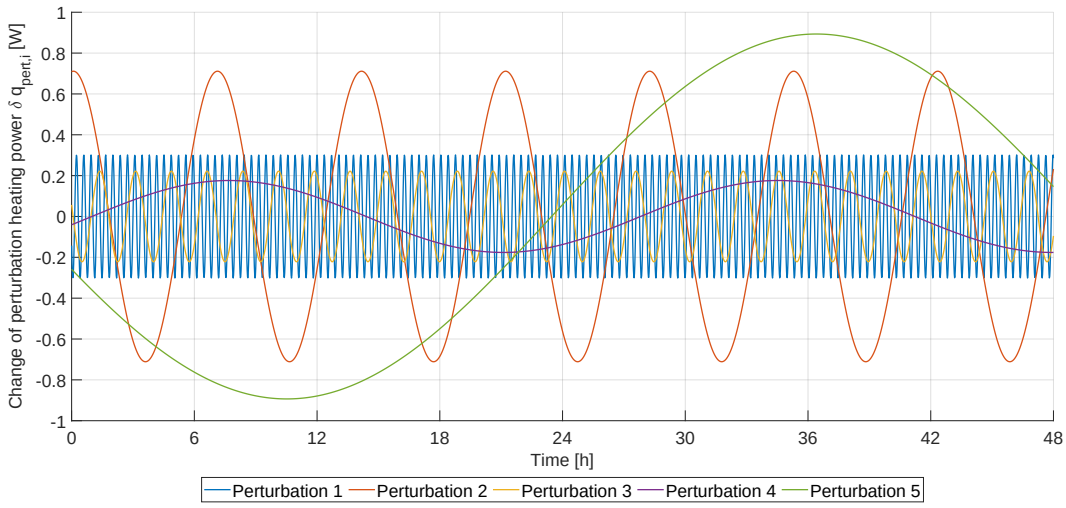

Figure 3.22 Time course of the perturbations $\mathcal{P}_i(t)$

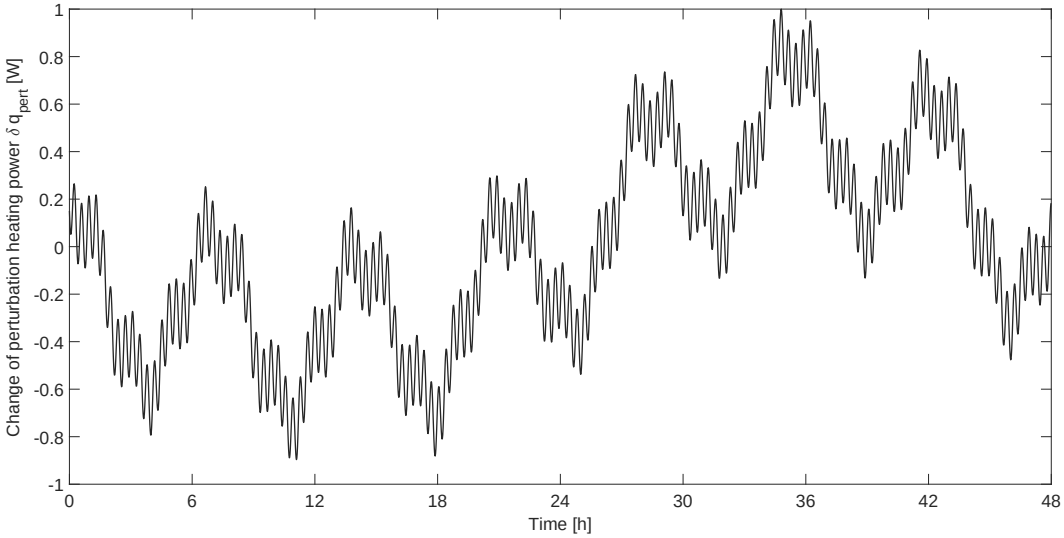

Figure 3.23 Time course of the random perturbation $\mathcal{P}_{tot}(t)$

The stepped perturbation is simulating a non-periodic perturbation. By changing the heating power in steps, it is possible to simulate the switching on and off of electrical devices that do not constantly dissipate energy. For this purpose, 8 steps were defined for a test with a running time of 24 h. The exact parameters can be taken from Table 3.4. Figure 3.24 shows the course of the change of the perturbation heating power, which is applied to the steady-state of 1 W.

Table 3.4 Stepped perturbation parameters

Step	Amplitude	Duration
1	0.75 W	6 h
2	0.25 W	6 h
3	0 W	1 h
4	-0.25 W	1 h
5	0 W	1 h
6	0.75 W	1 h
7	0 W	1 h
8	0.25 W	1 h

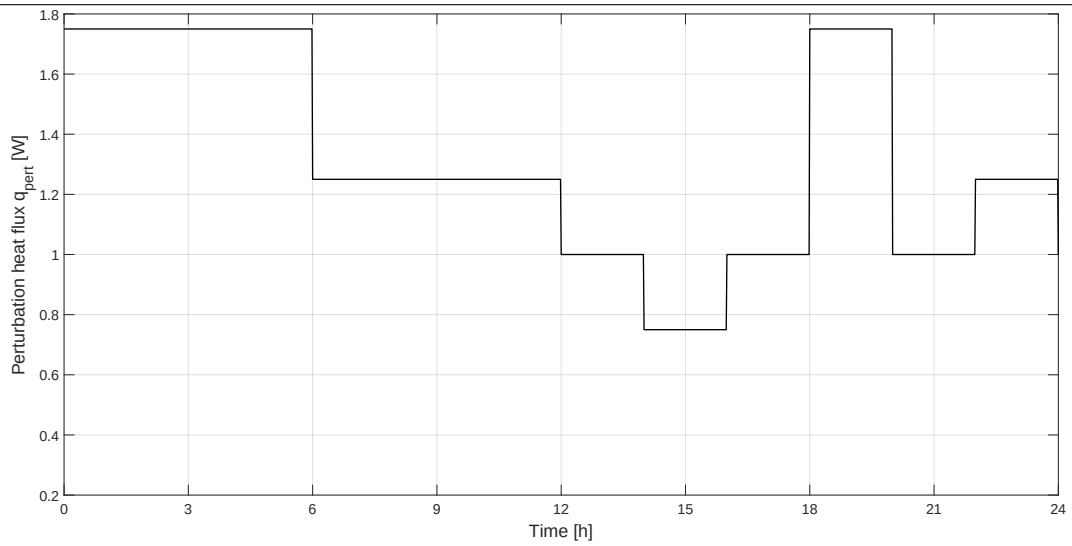

Figure 3.24 Time course of the stepped perturbation

Table 3.5 Overview of the experimental test series, configuration 2

Parameters		
Case	**Perturbation**	**Control**
1	sinusoidal 1 W ± 0.5 W	uncontrolled
2	sinusoidal 1 W ± 0.5 W	control, $\sigma_H = 0.02$ W and $\sigma_S = 0.10$ K
1	random	uncontrolled
2	random	control, $\sigma_H = 0.02$ W and $\sigma_S = 0.12$ K
3	random	control, $\sigma_H = 0.02$ W and $\sigma_S = 0.10$ K
1	stepped	uncontrolled
2	stepped	control, $\sigma_H = 0.02$ W and $\sigma_S = 0.12$ K
3	stepped	control, $\sigma_H = 0.02$ W and $\sigma_S = 0.10$ K

The test cases to be performed using this second configuration are listed in Table 3.5. First, the same sinusoidal perturbation as in the initial setup will be used to enable comparison. Various settings of the Kalman filter have also been tested. Due to the expected improved dimensional stability based on the simulations, the control HEs require lower power, resulting in them being operated at 0.5 W instead of 0.6 W in the steady-state condition. Consequently, the range of possible control heating power is reduced to 1 W. In the first configuration, the covariance of the process noise was kept unchanged by maintaining a constant standard deviation of the HEs. In the second configuration, simulations and experiments have also demonstrated that the best results can be achieved with this value. The variation of the standard deviation of the sensor

measurement has a greater impact on the system behavior. The optimal outcomes are likewise achieved here for values of $\sigma_S = 0.12\,\mathrm{K}$ and $\sigma_S = 0.10\,\mathrm{K}$. Therefore, for the second configuration, the system behavior for $\sigma_S = 0.10\,\mathrm{K}$ in case 2 is exemplified for the sinusoidal perturbation. Subsequently, the same experiments will be repeated with the random and stepped perturbation. To illustrate, the results for both standard deviations are presented for those perturbations.

Figure 3.25a shows the distribution of modal weights for the selected first 10 modes for the described sinusoidal perturbation with a period of 6 h. Over 95 % of the modal weight is distributed among these modes. Using the strongest 6 modes would still cover 93 % of the modal weight, resulting in a very good reconstruction of the temperature field. For comparison, the modal weights for perturbation periods of 48 h and 3 h are shown in Figures 3.25b and 3.25c, respectively. As the frequency decreases, the weight distributes slightly more towards the first modes, but 95 % of the total weight is still covered with the 10 strongest modes. With an increase in frequency, the weight noticeably spreads across other modes, allowing only 85 % of the total weight to be covered. However, since the approach is intended to compensate not only for sinusoidal perturbations whose frequency is known, but also for random perturbations whose frequency may be higher than that used for the sinusoidal perturbation, 10 modes are used. This ensures that the temperature field can be adequately reconstructed. The disadvantage of using a larger number of modes is the need to use more sensors.

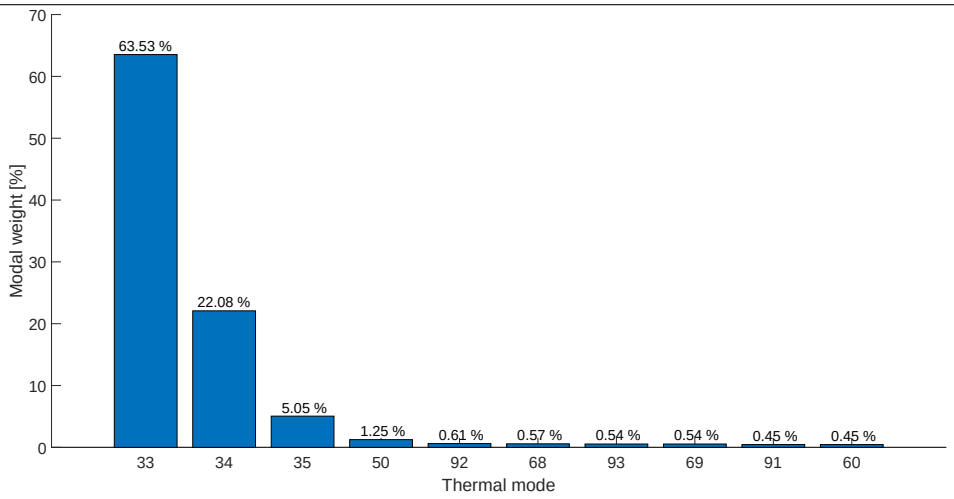

(a) Period 6 h

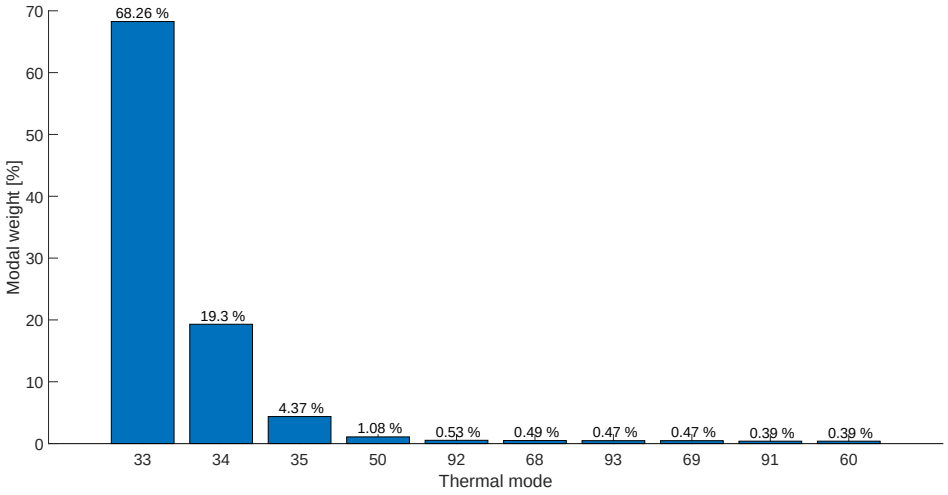

(b) Period 48 h

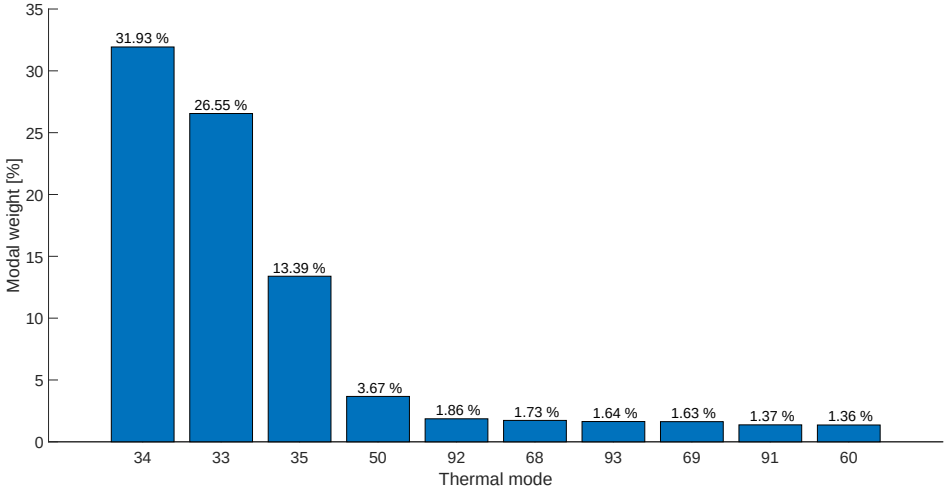

(c) Period 3 h

Figure 3.25 Modal weight distribution for a sinusoidal perturbation from the perturbation HE with different period durations

To illustrate the temperature field reconstruction, Figure 3.26 shows an exemplary of the strongest 4 thermal modes of the experimental setup for a sinusoidal perturbation with a period duration of 6 h. The linear combination of these modes and the 6 subsequent modes according to their modal weights would result in an overall temperature field with an accuracy of more than 95 %.

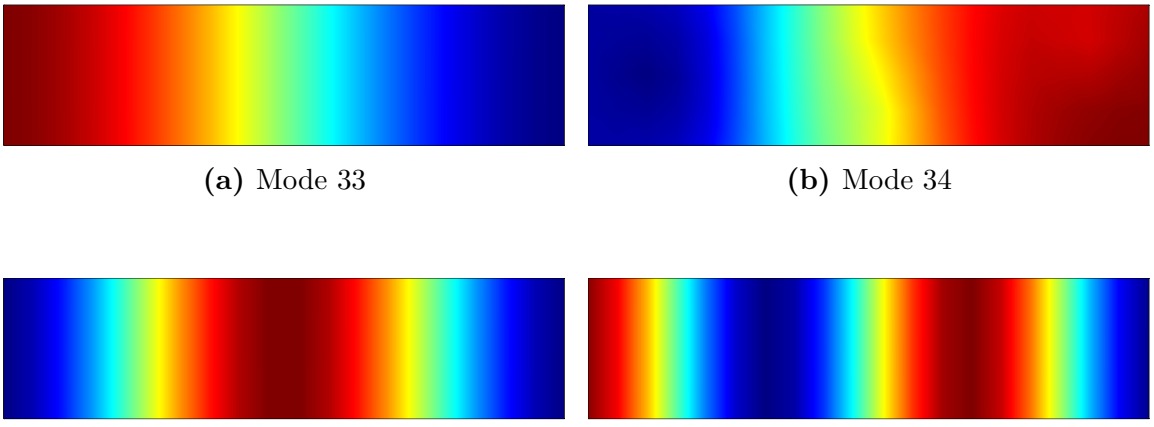

(a) Mode 33 **(b)** Mode 34

(c) Mode 35 **(d)** Mode 50

Figure 3.26 First 4 thermal modes describing the response to a sinusoidal perturbation from the perturbation HE with a period duration of 6 h

Figure 3.27 depicts the second configuration of the test setup with the positions of the 14 out of 18 best temperature sensors based on the maximum amplitude of the thermal modes. The remaining 4 sensors are on the backside of the plate, also all at the edge. Although theoretically, these positions should allow for the best reconstruction of the temperature field, they are technically challenging to realize. Moreover, due to the symmetry and simplicity of the structure, the difference in amplitudes in the respective nodes of the FEM model for a mode is extremely small. For example, for the strongest mode number 33, the largest amplitude is 0.063 48 K at node position 201, corresponding to sensor position 1 in Figure 3.27. The 50th largest amplitude is 0.062 41 K, only about 2 % lower. Thus, even with sensor placement at this corresponding node, there would be only a minor error in the reconstruction of the temperature field. Therefore, the described configuration, which excludes all technically impractical sensor positions, is not optimal, but the resulting error is also very small. In other cases, the deviation from the largest to the second-largest amplitude can already be 50 % or more. Such an evaluation must be carried out individually for each geometry and each changing perturbation for the points to be controlled, posing a significant effort in modeling and simulation.

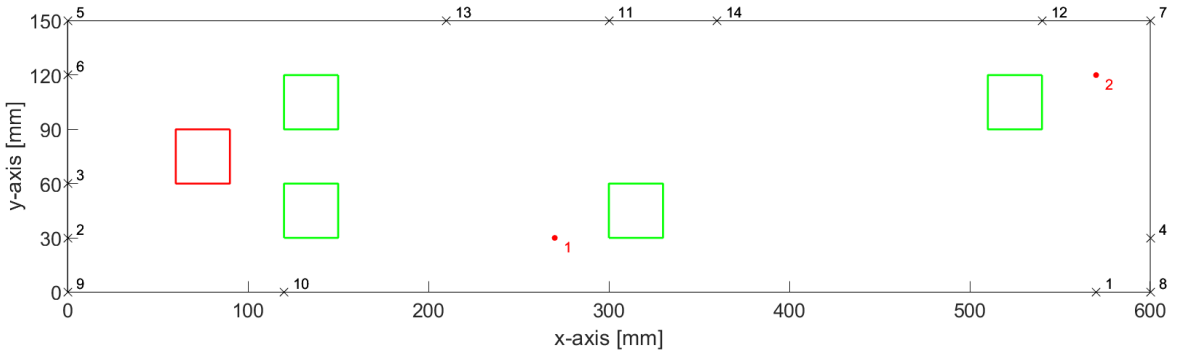

Figure 3.27 Optimal sensor positions, configuration 2

The principle of the thermal field reconstruction is illustrated in Figure 3.28 using various examples. For an inhomogeneous, steady-state condition where the perturbation heating element operates at 1 W and the 4 control elements each operate at 0.5 W, with a constant TVC temperature of 5 °C, Figure 3.28a depicts the temperature field based on all 252 known simulated ideal nodal temperatures. If the aforementioned 10 strongest thermal modes according to Figures 3.25 and 3.26 were combined linearly, this representation of the temperature field would result (apart from the deviation of just under 5 % due to the exclusion of the residual 242 modes). In case not all nodal temperatures are known, as in the experiment where only the temperatures measured by the sensors are available, the entire temperature field of the plate needs to be reconstructed using the modal transformation. The resulting recontructed temperature field is shown in Figure 3.28b. Upon visual comparison of these two representations, it becomes evident that the contour plots are not identical. The mean deviation of all nodal temperatures between the simulated overall solution and the modal-reconstructed solution is 0.024 K, with the absolute maximum deviation reaching 0.27 K. The modal reconstruction only works effectively when the sensors are positioned at locations in the model where they would measure the maximum amplitudes for the corresponding modes. However, due to the limited selection of positions available, the sensor configuration shown in this setup does not represent the optimum but rather a compromise solution adapted to the boundary conditions and restrictions, that were already discussed earlier in this section. Therefore, the thermal field reconstruction is not ideally achievable. However, the small mean deviation falls well within the accuracy of the sensors. The deviations are particularly large at the left edge of the plate, where higher temperatures are calculated by the reconstruction than are actually present.

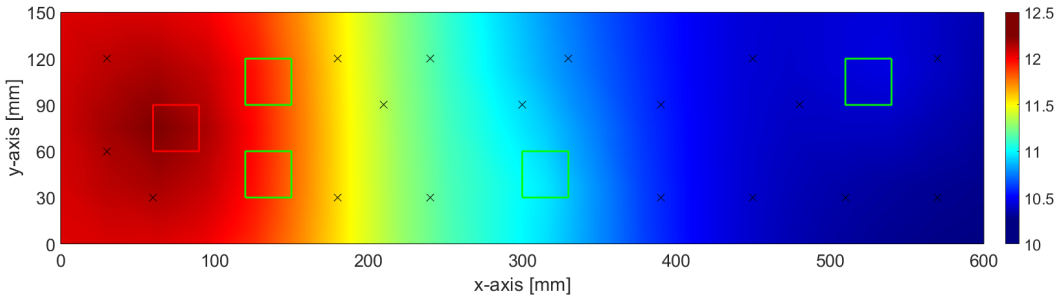

(a) Temperature field based on 252 simulated ideal nodal temperatures

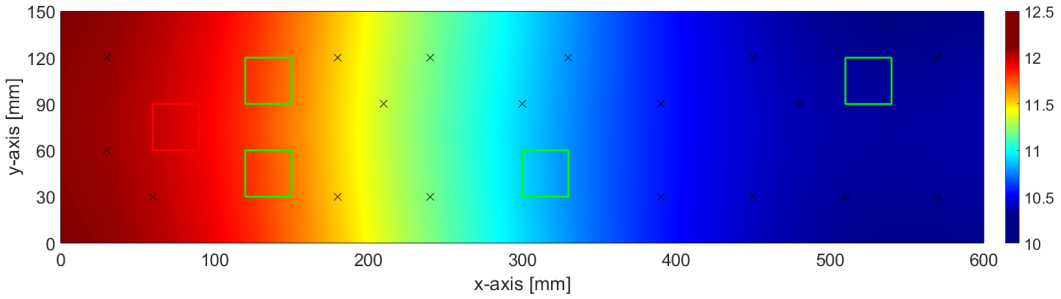

(b) Temperature field reconstruction based on 18 ideal sensors

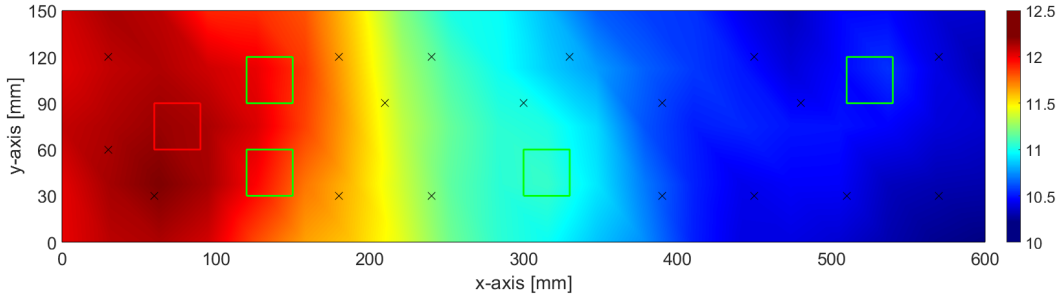

(c) Temperature field based on 252 simulated noisy nodal temperatures

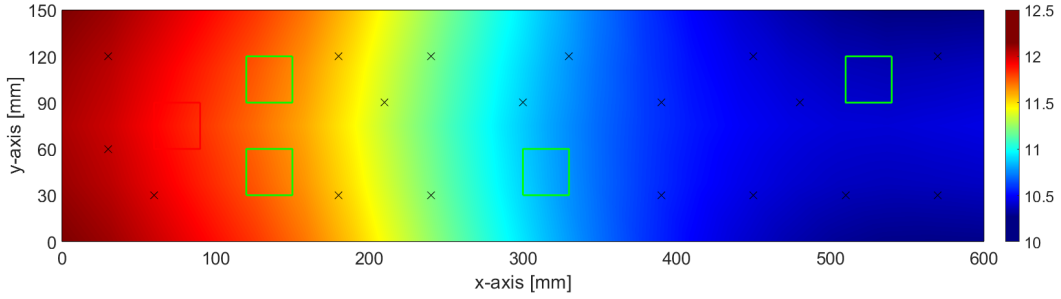

(d) Temperature field reconstruction based on 18 noisy sensors

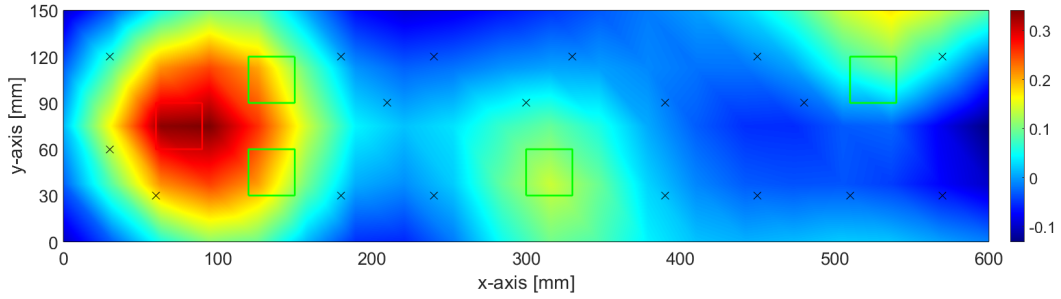

(e) Temperature difference between 252 simulated ideal nodal temperatures and the reconstruction based on 18 noisy sensors

Figure 3.28 Differences in temperature field representation

In this particular case, it should be noted that the thermal field reconstruction assumes the ideal, simulation-correct temperatures at the sensor positions. In the experimental setup, these measurements are noisy and subject to errors, which could further degrade the thermal field reconstruction. To illustrate this scenario, each simulated nodal temperature was offset with a normally distributed pseudo-random value in the range of [-0.2, 0.2] K. Figure 3.28c represents the temperature field based on all simulated noisy nodal temperatures, while Figure 3.28d reflects the result of the thermal field reconstruction based on the simulated noisy values at the sensor positions. In Figure 3.28c, the uneven and "spotty" temperature field due to the noisy nodal temperatures is clearly visible, while this effect is less pronounced in Figure 3.28d. The average difference between the temperature field based on 252 ideal simulated sensors and the reconstruction based on 18 noisy nodal temperatures are at 0.03 K, while the absolute maximum difference is at 0.37 K located around the perturbation HE. This indicates that the reconstruction using the modal transformation for noisy sensors leads to worse results compared to ideal sensors and deviates significantly for different locations. As this is just one example using a normally distributed pseudo-random offset, added to the simulated sensor positions, results can differ from simulation to simulation as well. This underlines the importance of adding a Kalman filter to correct for noisy measured values. Despite large local differences, the temperature difference in the right-hand area of the plate, in which the points to be controlled are located, is still very small. The deviation between the temperatures of those two nodes is only 0.03 K and therefore well within the accuracy of the temperature sensors. The temperature field reconstruction shows very good results in the area of the plate where fewer fluctuations occur due to the perturbation, which is the area of interest in this case. Hence, this method proves to be useful for comparing simulated nodal temperatures from the FEM model with experimental measurements based on just a few sensors.

To validate the approach, the simulations are compared with the experimental tests for both configurations presented in the course of this section with the corresponding system and test parameters. The simulated and experimental determined results are discussed in the following chapter.

3.6 Error Sources and Expected Accuracy

In this section, the potential sources of errors in the model, the experimental setup, and the measurement methods will be discussed, summarized and quantified, in order to accurately assess the results of the experiments. Some of the error sources are interrelated, so they can either amplify or diminish one another. Additionally, certain measurement errors can be corrected or even compensated for through the use of calibration, averaging, or filtering. However, to gain a comprehensive understanding, potential error sources mentioned in the course of this chapter are summarized in this section, regardless of whether they can be reduced or compensated for through countermeasures.

The specified percentage errors always refer to the respective property or physical quantity. The quantities to be measured or adjusted and relevant for the experimental setup are the displacements of the points to be controlled, the temperature of the plate, and the power of the control HEs. Since the presented approach aims to control displacements, the deviations resulting from possible sources of error are related to these displacements. Due to the linearization of the radiation terms (refer to the detailed mathematical derivations of the thermal model in Appendix A.1), it can be assumed in a first approximation that, for small temperature changes, the introduced heat behaves linearly with the temperature change. Furthermore, according to the thermomechanical transfer functions, the change in displacement depends linearly on the change in heat flux. Thus, all sources of error discussed in this chapter, in a first approximation, lead to a direct linear influence on the displacement measurement.

The first step is to categorise and differentiate the errors. Two groups are formed for this purpose: The errors in modelling, which occur due to simplifications and assumptions and thus lead to a deviation from reality, and the errors in carrying out the measurements on the experimental setup. Since the error estimation in this section should only provide a rough indication, for the sake of simplicity, the application of error propagation calculations or other methods of error analysis [62] is omitted.

Table 3.6 summarizes the expected inaccuracies and errors between the model and the real experimental setup. It is evident that despite the simple setup and coarse model, a quite accurate representation of the real setup can be achieved. This establishes the foundation for a functioning validation.

Table 3.6 Errors between model and experimental setup, referenced to a displacement of 10 µm in the temperature range of 9 °C to 15 °C

Error	**Expected impact**
Coarse FEM mesh	<1.5 %
Change in radiation by omitting the mounting system	<1 %
Heat conduction through contact surface of support	1 % to 2 %
Sum	below 5 %

Human-induced errors, caused by the operator during the preparation and execution of the experiment, can hardly be avoided completely. The sensors and actuators can only be mounted at their modelled positions with a certain degree of accuracy, the time-synchronous operation of the independent computer systems is carried out with a slight time lag and the calibration of the DIC system, including focusing of the camera and alignment of the light fields, is subjective to a certain degree. Due to the low-frequency perturbations, however, these inaccuracies do not lead to any significant error in the measurement of the displacements and are therefore estimated at less than 1 %.

The errors caused by measuring the temperature and controlling the HEs are described in detail in Appendix B.2. Most of these errors can be minimized or even compensated for through various procedures within data acquisition and further calibration steps. In addition, the Kalman filter is specially designed for processing temperature measurements. Nevertheless, a significant degree of uncertainty remains.

The isostatic mounting as well as the speckle pattern and the DIC system are expected to introduce the largest inaccuracies by far. These inaccuracies are non-correlative, thus not influencing or being influenced by other sources of error.

Table 3.7 summarizes the inaccuracies expected in the measurement.

Table 3.7 Errors in the execution of the experiments, referenced to a displacement of 10 µm in the temperature range of 9 °C to 15 °C

Error	**Expected impact**
Speckle pattern on the test object	10 %
Isostatic mounting	20 %
Instability of the PCU	<3 %
Temperature measurement∗	5 %
Heater control∗	10 %
DIC system	20 %
Humand-induced errors	<1 %
Sum∗	up to 70 %

∗Note: The expected errors in temperature measurement and heater control can be reduced using suitable methods (refer to Appendix B.2).

At first glance, a potential error of 70 % in the measurement of displacement might seem excessively large for successful validation. However, errors describing the expected deviations between simulation and experiment, behave to a large extent uniformly across all tests, ensuring a relative comparability. The possible sources of error listed here and their influence on the qualitative results of the tests are largely estimates and are only intended to provide a context for the evaluation of these results. Therefore, the error potential of up to 70 % is not considered negatively.

As described in this chapter, the measurement of displacements in the micrometer range is very complex and subject to many uncertainties. It is therefore expected that a comparison of simulated and measured displacements will lead to major deviations and that only the qualitative course of the measurements will match the simulations. However, as the measurements of the displacements should be consistent, comparable and repeatable, a reduction in the displacement will be measurable within the experiments through the use of the filter and controller framework. Therefore, in the following evaluation of the experiments, a clear division is made between the validation of the model and thus the usability of the approach itself and the achievable reductions in displacements through this approach within a series of experiments.

Chapter 4

Results and Discussion

The objective of this work is to experimentally validate the approach developed and simulated in [6] for compensating specific displacements in a satellite structure caused by changes in thermal boundary conditions. The presentation of the results is divided into two basic aspects: the validation of the theoretical model with respect to the experimental setup and the demonstration of the reduction of displacements by using this filter and controller framework compared to an uncontrolled reference state. Since similar or identical data (temperature and displacement measurements and the necessary control heating power) are often used for both aspects, a strict separation is not meaningful. Therefore, Sections 4.1 and 4.2 first present the validations of the thermal and thermo-optical properties listed in Section 3.2, as well as the thermal transfer functions detailed in Section 3.5. Section 4.3 then follows with the demonstration of the applicability of the closed-loop filter and controller approach based on the two configurations of the experimental setup described in Section 3.2 and various types of perturbations. A selection of test cases is described in detail, while others are briefly discussed or referred to in Appendix C.

4.1 Thermal and Thermo-optical Properties

The thermal conductivity values specified for the aluminum alloy used in the experimental setup range from $130\,\mathrm{W\,m^{-1}\,K^{-1}}$ to $160\,\mathrm{W\,m^{-1}\,K^{-1}}$[43]. It influences the difference between the maximum and minimum temperatures on the plate, as temperature equalization takes place more quickly or more slowly depending on the conductivity. The emissivity ϵ depends, among other things, on the composition, the surface properties and the degree of oxidation. Weighing these influences, an emissivity of 0.1 is initially assumed for the presented test setup, with literature values ranging between 0.08 and 0.3 [63]. In order to define these values for the model, a simplified experimental approach is performed: On the model side, different steady states with different heating elements in configuration 1 switched on are simulated at different power levels,

varying the thermal conductivity between $130\,\mathrm{W\,m^{-1}\,K^{-1}}$ to $160\,\mathrm{W\,m^{-1}\,K^{-1}}$ in steps of $5\,\mathrm{W\,m^{-1}\,K^{-1}}$ and the emissivity between 0.08 and 0.13 in steps of 0.002. The range for emissivity was chosen to be smaller than indicated in the literature because the surface of the structure is mirror-smooth and undamaged, thus expecting a value at the lower end of the range. The results obtained from those simulations are then compared with the actual measurements at the respective steady states. The greatest deviations occur with low or high emissivities in combination with a high thermal conductivity, at which the temperature on the plate becomes more homogeneous. All tested combinations have a maximum deviation of less than 5 %, still well within the expected accuracy discussed in Section 3.6. The smallest deviations of less than 0.1 K on average over the different steady states between model and measurement resulted from the combination of $\lambda = 130\,\mathrm{W\,m^{-1}\,K^{-1}}$ and $\epsilon = 0.098$. This accuracy is equivalent to an error of far less than 1 % when taking the different steady-state conditions with an overall temperature range of 27 °C to 32 °C as a reference. This temperature range is much higher than in all the contour plots shown up to this point, as in this case the speckle pattern was not yet applied to the front side of the aluminum plate, which greatly increases the emissivity.

After determining the emissivity of the aluminum alloy, the speckle pattern was applied to the front side of the plate. This resulted in a significant change in the emissivity of the largest radiating surface of the test setup. The same procedure for determining the emissivity of this plate side was therefore applied here as well, with the emissivity varied in the range from 0.85 to 1. The optimum for various inhomogeneous steady states with deviations less than 0.1 K or 1 % between model and experiment was found to be 0.93, when taking the different aforementioned steady-state conditions with an overall temperature range of 9 °C to 15 °C as a reference. The variation of the values for the conductivity has been repeated again, confirming the selected values once more. The procedure described here does not necessarily reflect the ideal approach. Rather, the simulation and experimental setup could be sensibly harmonized in this way. The values approximated from the literature could be confirmed and thus fixed for all subsequent experiments.

4.2 Thermal Transfer Functions

The thermal transfer function $H_{Tq}(s)$ was introduced in Section 3.5 and describes the frequency domain relationship between the temperature change δT at node i and the heat flux change δq on surface k according to Equation 3.1, which is presented once again for clarification

$$H_{Tq}(s) = \frac{\delta T_i}{\delta q_k}. \tag{4.1}$$

For low frequencies of the perturbation, utilizing a fraction of the total thermal modes is sufficient to reconstruct the thermal response of the system. In order to validate the thermal transfer function between the change in the heat flux at any surface related to the temperature change at any node, the leftmost heating element in cofiguration 1 is operated at a power level of 1 W in steady-state and subjected to a sinusoidal perturbation with an amplitude of 0.5 W and an oscillation period of 6 h, corresponding to a frequency of 4.63×10^{-5} Hz. In the steady-state condition, the control heating elements, which are necessary for the subsequent filter and controller framework, are operated at 0.6 W each. Their operation is not crucial for this test, but also not disruptive, as long as simulation and experiment are operated with the same parameters. In the FEM model, the thermal transfer function $H_{Tq}(s)$ is computed as a matrix based on several physical properties of the structure and the characteristics of the perturbation (refer to Appendix A.1 for more details on the derivation) . This matrix of transfer functions includes the temperature changes at all nodes of the FEM model due to the heat flux changes at all surfaces of the FEM model, represented as complex numbers. Equation 4.1 can be rearranged to

$$\delta T_i = H_{Tq}(s) \cdot \delta q_k, \tag{4.2}$$

whereas for k, the surface element corresponding to the perturbation HE on the aluminum plate is selected. Evaluating Equation 4.2 for this configuration and the given frequency at which the perturbation occurs results in the expected temperature changes for each node i in the model. Since the sensors are mounted at specific node positions, the responses for these nodes can be evaluated and compared with the measurements. The resulting temperature is also given as a complex number, which can be expressed in terms of phase and amplitude. The phase in seconds corresponds to the time delay between the occurrence of the perturbation and the response at the corresponding node of the model. Thus, in the experiment, the easiest way to determine the phase is to measure the time delay between the maximum or minimum heating power at the perturbation element and the maximum or minimum in the temperature measurement. If multiple occurrences of these maxima or minima are observed, the time interval should remain constant. Analogous to the phase, the amplitude describes the magnitude of the temperature difference between two successive maxima or minima. These values can be extracted from the temperature recordings. Figure 4.1 illustrates the temperature profile for a validation test as an example. The changes in temperature measurements also follow this sinusoidal variation in heating power. The time shift between the maxima of the heating power and the maxima of the temperature measurements becomes immediately evident. The closer a sensor is mounted to the perturbation, the smaller its phase shift compared to the sinusoidal oscillation of the heating power and the larger the temperature amplitude. This observed behaviour also corresponds to expectations, as the heat transport within the test structure is a time-dependent process.

Prior to the experiment, the effect of the change in heating power was simulated and the phase and amplitude of the response were determined for each sensor position.

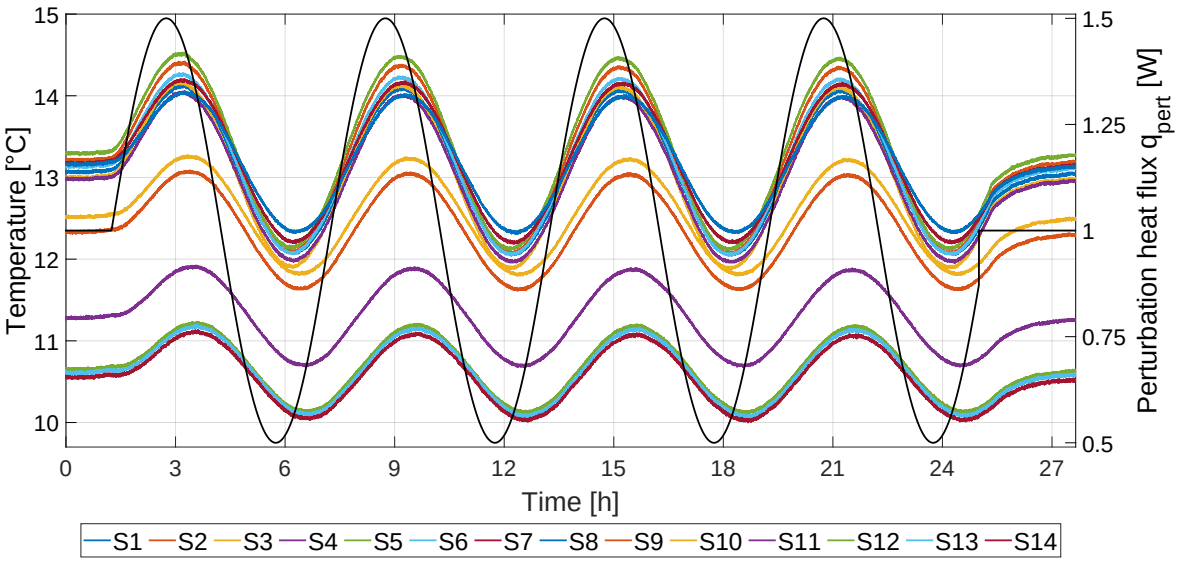

Figure 4.1 Temperature sensor plot for validation of H_{Tq} function

Table 4.1 and 4.2 compare the simulated values for phase shift and amplitude with the measured ones. The measured values for amplitude and phase represent the average of the 4 maxima and minima, that can be observed in Figure 4.1. The differences in these 4 measurements between minima and maxima, as in all other tests, were small and fluctuated around the calculated mean value, so that these differences can be adressed to measurement errors. If phases and amplitudes were to change in one direction during the course of the experiment - for example, increasing values of the maxima or shorter phases - this could be an indication of a faulty experimental setup, as the reversibility of the heat increase and decrease does not result in repeatable measurements. However, as the phases and amplitudes only fluctuate around a mean value, the experimental setup functions correctly as the temperature measurements are reversible and repeatable.

The average phase difference of all sensors are 0.55 %, whereas the average amplitude variations are 3.11 %. The measurement results for the phase deviation are particularly better than expected, considering the multitude of error sources and uncertainties in both the measurements and the model. The deviations in the amplitudes are highest for the sensors closest to the perturbation heating element, reaching up to 6.5 %. However, these deviations still fall within a very good range.

Table 4.1 Validation H_{Tq} function, phase shift

Phase shift				
Sensor	**simulated [s]**	**measured [s]**	**difference [s]**	**difference [%]**
S 1	1679.14	1696.17	17.03	1.01
S 2	1547.83	1552.33	4.50	0.29
S 3	1547.83	1562.50	14.67	0.95
S 4	1679.14	1712.83	33.69	2.01
S 5	1505.77	1499.00	6.77	0.45
S 6	1603.72	1599.33	4.39	0.27
S 7	1775.00	1773.83	1.17	0.07
S 8	1990.85	1981.67	9.18	0.46
S 9	2387.71	2385.00	2.71	0.11
S 10	2387.71	2389.17	1.46	0.06
S 11	2739.36	2733.67	5.69	0.21
S 12	3027.26	3021.83	5.43	0.18
S 13	3072.46	3054.33	18.13	0.59
S 14	3072.46	3060.33	12.13	0.40

The model assumes the plate to be perfectly symmetrical. This can be seen in the simulated values of symmetrically arranged sensor pairs. For example, S1 and S4, S2 and S3, and S9 and S10 in both tables exhibit the same model values. The evaluation of temperature profiles confirms the association between these symmetrically placed sensor pairs, although the measured values are never identical. This is due to the fact that exact symmetry is not achievable. On one hand, the sensors and heating elements are never precisely placed on the corresponding surfaces or nodes of the FEM model. On the other hand, the plate's structure is never perfectly homogeneous. The surface exhibits some macroscopic wear marks, and at a microscopic level, unavoidable defects are embedded in the structure. Furthermore, the thermal model does not consider the suspension and mounting device of the aluminum plate, which requires holes in the plate and affects the uniform radiation exchange with the surroundings. Although these influences are small and considered negligible, as discussed in Sections 3.2 and 3.3, their effects are small, but still noticeable here.

The absolute deviations of the phase shift are all in the order of a few seconds and not showing any correlation to the position of the sensors.

Table 4.2 Validation H_{Tq} function, amplitude

Amplitude				
Sensor	**simulated [K]**	**measured [K]**	**difference [K]**	**difference [%]**
S 1	2.13	2.00	0.13	6.50
S 2	2.35	2.27	0.08	3.52
S 3	2.35	2.21	0.14	6.33
S 4	2.13	2.01	0.12	5.97
S 5	2.41	2.33	0.08	3.43
S 6	2.23	2.15	0.08	3.72
S 7	1.96	1.94	0.02	1.03
S 8	1.74	1.67	0.07	4.19
S 9	1.41	1.40	0.01	0.71
S 10	1.41	1.40	0.01	0.71
S 11	1.20	1.17	0.03	2.56
S 12	1.07	1.05	0.02	1.90
S 13	1.05	1.04	0.01	0.96
S 14	1.05	1.03	0.02	1.94

The absolute deviations of the amplitude are larger than 0.1 K for just 3 sensors. The closer a sensor is located to the heating element, the larger the deviations between the model and reality, especially concerning the amplitudes. This can primarily be attributed to the introduced heat flux. In the model, this heat flux is uniformly distributed over the entire surface element and applied to the structure. In reality, this cannot be achieved by the heating element, as the heating wire pattern cannot generate a uniform heat flux. Therefore, the effects of this modeling are less noticeable at greater spatial distances from the heating element. Furthermore, it is noticeable that the measured values are consistently lower than the simulated values. This can also be explained by the fact that the support and isostatic mount are not considered in the model. These elements cause the average temperature on the plate to be lower due to heat losses through conduction.

The same test was performed for different configurations of switched-on HEs and power levels, frequencies, steady-state conditions and configurations. The variations between simulation and experiment were always below 0.6 % for phase and 4 % for amplitude, validating the functionality and useability of the transfer functions for the framework as well as a very good correlation between the model and the real experimental setup.

4.3 Closed Loop Filter and Controller Approach

In the following sections, various validation experiments for the two configurations previously described in detail are presented as exemplary cases. Two types of comparisons will always be drawn: firstly, the experimentally measured values will be compared with the respective model simulations. Secondly, different tested system parameters of the control framework will demonstrate the functionality of the approach in compensating for displacements by comparing these cases with an uncontrolled reference state. This analysis will focus on temperature measurements on the test object, the control heating power, and the displacements recorded by the DIC system. The factors used for these comparisons describe the ratio between the uncontrolled reference state and the controlled case.

4.3.1 Configuration 1

Section 3.5 already outlined the procedure for validating the framework using configuration 1. For the sake of clarity, the setup of sensors and actuators is shown again in Figure 4.2 and the evaluated test cases are listed in Table 4.3.

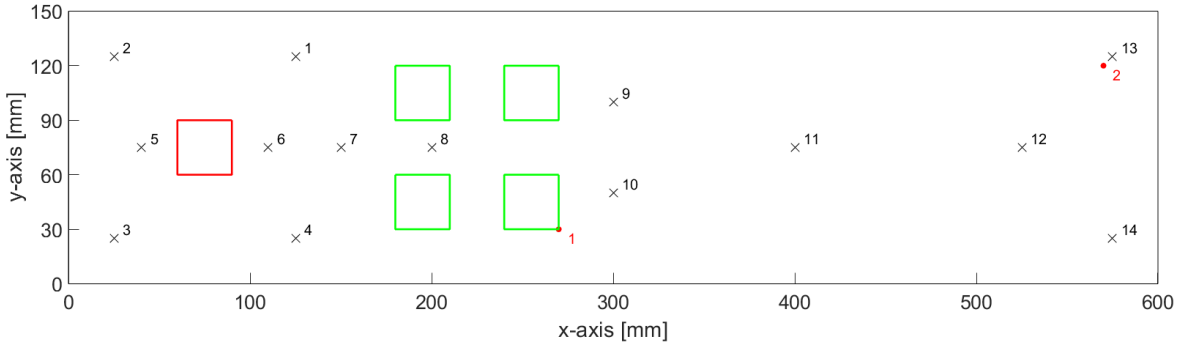

Figure 4.2 Sensor and heater position, configuration 1

Table 4.3 Overview of the experimental test series, configuration 1

	Parameters	
Case	**Perturbation**	**Control**
1	sinusoidal 1 W ± 0.5 W	uncontrolled
2	sinusoidal 1 W ± 0.5 W	PCM
3	sinusoidal 1 W ± 0.5 W	control, $\sigma_H = 0.02$ W and $\sigma_S = 0.18$ K
4	sinusoidal 1 W ± 0.5 W	control, $\sigma_H = 0.02$ W and $\sigma_S = 0.12$ K
5	sinusoidal 1 W ± 0.5 W	control, $\sigma_H = 0.02$ W and $\sigma_S = 0.10$ K

Figure 4.3 shows a chronological overview of the 5 experiments (indicated with the blocks) conducted over a period of approximately 15 days in one run. The red graph describes the average temperature of all sensors on the plate, the blue graph shows the average temperature of the TVC. Due to an instability in the temperature control of the PCU, it has to be switched off approximately every 4 days, which can be seen in the peaks. However, during the 5 experiments the system worked very stable.

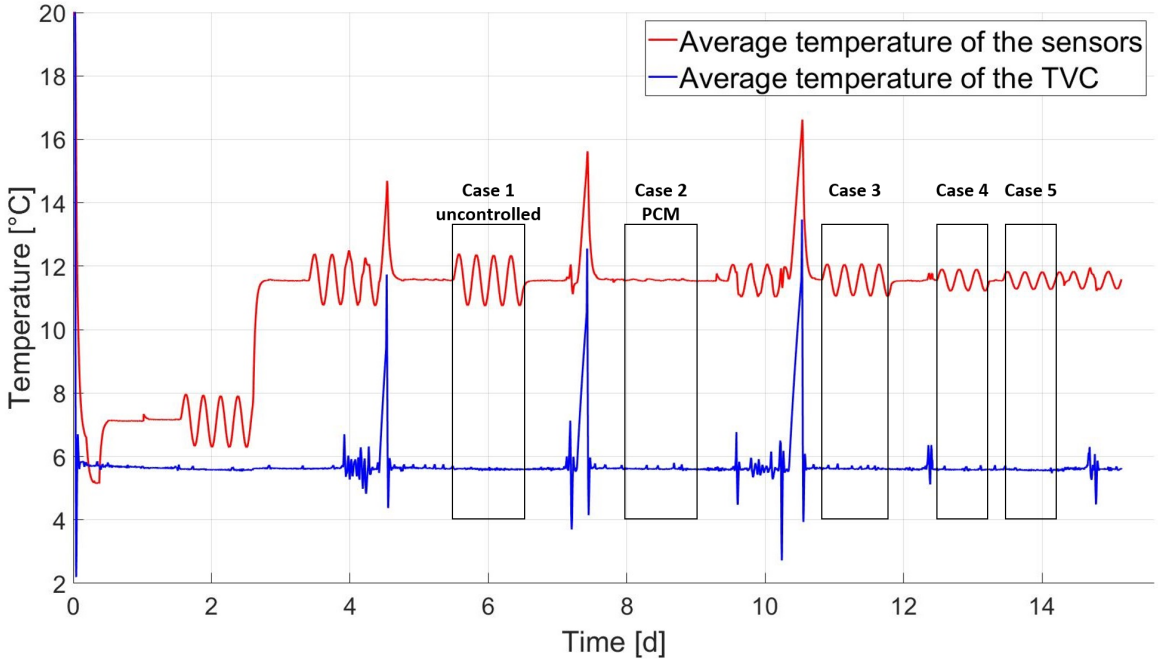

Figure 4.3 Overview of the test sequence for configuration 1

Figure 4.4 illustrates the simulated and experimentally determined temperature profiles for the uncontrolled reference state over a period of 24 h for a sinusoidal perturbation heat flux with a period of 6 h. In general, it can be observed that both profiles are qualitatively very similar. The sinusoidal perturbation is well reflected in the sinusoidal temperature fluctuations. The steady-state initial temperatures shown in the beginning of both plots are almost identical for nearly all sensors. The most obvious discrepancies arise from the fact that in the model, the effects of the perturbation on all symmetrically arranged sensors are identical (see Figure 4.2). Hence, the profiles of sensors S2 and S3 or S13 and S14 overlap, although differences of up to 0.15 K are measured in the experiment. This is due to the non-ideally symmetric temperature distribution resulting from losses through heat conduction at the isostatic mount, radiation influences from the aluminum rack, and not perfectly uniform heat input from the heating elements, as described in Sections 3.2 and 3.3. However, these effects can be compensated for through certain calibration steps (refer to Appendix B.2). Furthermore, it is clear that the temperature sensors placed very close to the perturbation heating element measure the largest amplitudes, approximately 1.2 K, while the sensors at the other end of the plate fluctuate by only about 0.5 K in amplitude. To establish

comparability with the subsequent test cases, the average temperature of all temperature sensors is computed, and their range, which is the maximum value minus the minimum value, is determined. This range amounts to 1.75 K for the uncontrolled reference case 1 in the simulation and 1.74 K in the experiment.

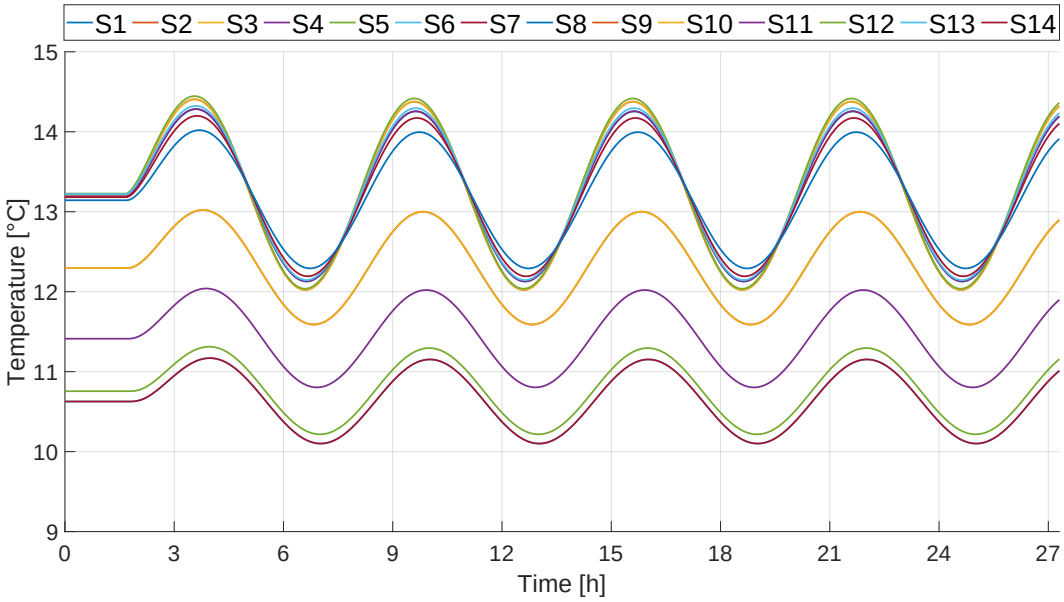

(a) Simulation

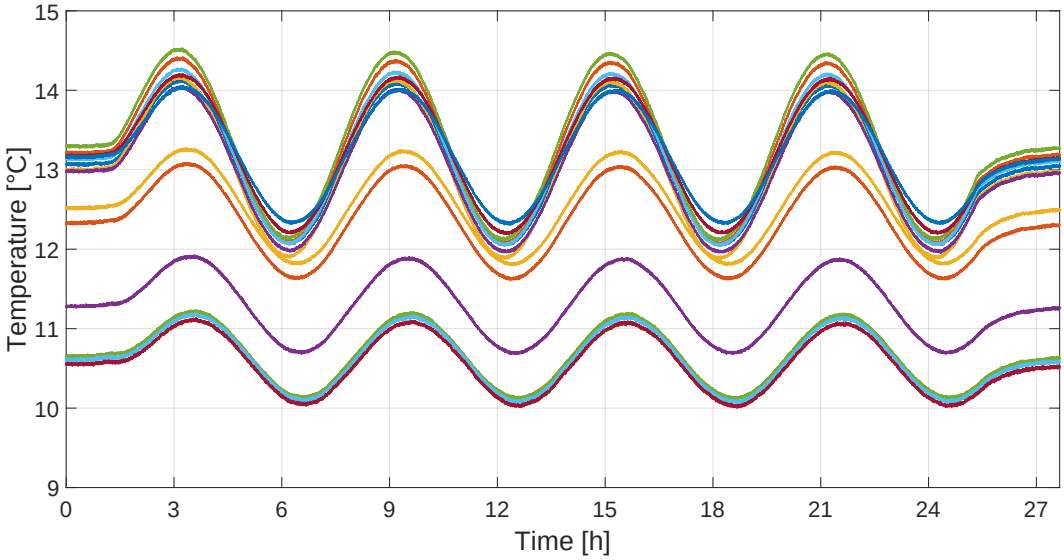

(b) Experiment

Figure 4.4 Uncontrolled case: Temperature sensor plot, configuration 1

Figure 4.5 depicts the displacements of the control points P1 and P2, due to the sinusoidal perturbation, with respect to the reference point of the isostatic mount and between the two points in the simulation. P1 is located at the lower edge of the plate near the center, resulting in a distance of approximately 0.31 m from the fixed reference point. The distance in the x-direction, at 0.27 m, is more than twice that in the y-direction, which is 0.12 m. Consequently, as expected, the displacement in the y-

direction is significantly less pronounced. The displacements can be roughly estimated using the CTE: assuming a value of $23.4 \times 10^{-6}\,\mathrm{K}^{-1}$ and a temperature change of approximately 1 K over a distance of 0.27 m or 0.12 m, displacements in the x- and y-directions of 6.3 µm and 2.8 µm, respectively, can be calculated. These values align with those in Figure 4.5a. In contrast, the displacements of P2 relative to the reference point are composed differently. Here, the distance in the x-direction is 0.57 m, but in the y-direction, it is only 0.03 m. Therefore, as expected, the displacement component in the y-direction appears to be almost 0, while displacements in the x-direction exceed 10 µm, as shown in Figure 4.5b. These values also match the rough estimation based on the CTE. Figure 4.5c results from the vectorial addition of the two points to each other. For the experimental validation, all three evaluations are now possible. To avoid duplication, only the displacement of point P2 relative to the reference point will be discussed below, as this should reveal the largest displacements in the x-direction, which can be best resolved by the DIC camera system. Due to the small expected displacements of the two points from each other, of up to just 4 µm, it is anticipated that an improvement through the approach can be difficult to visualize and validate since the values are within the resolution of the camera system, making a well-founded qualification challenging. Hence, the reference value for the displacement in the x- and y-directions is set at 22.06 µm and 0.75 µm, respectively. The total displacement in the simulation is then determined to be 21.34 µm through vectorial addition.

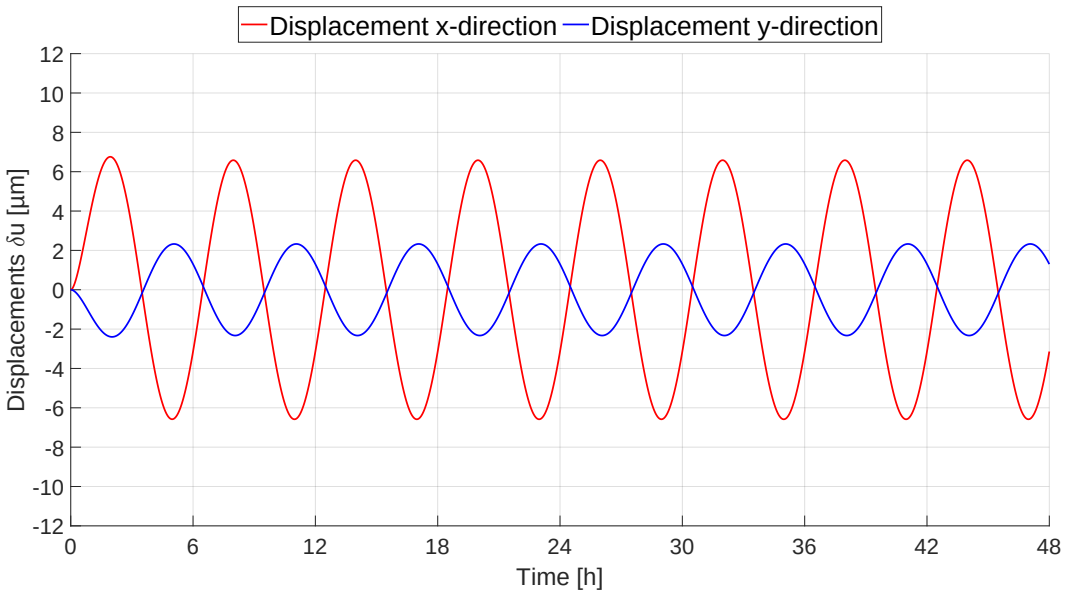

(a) Reference point to P1

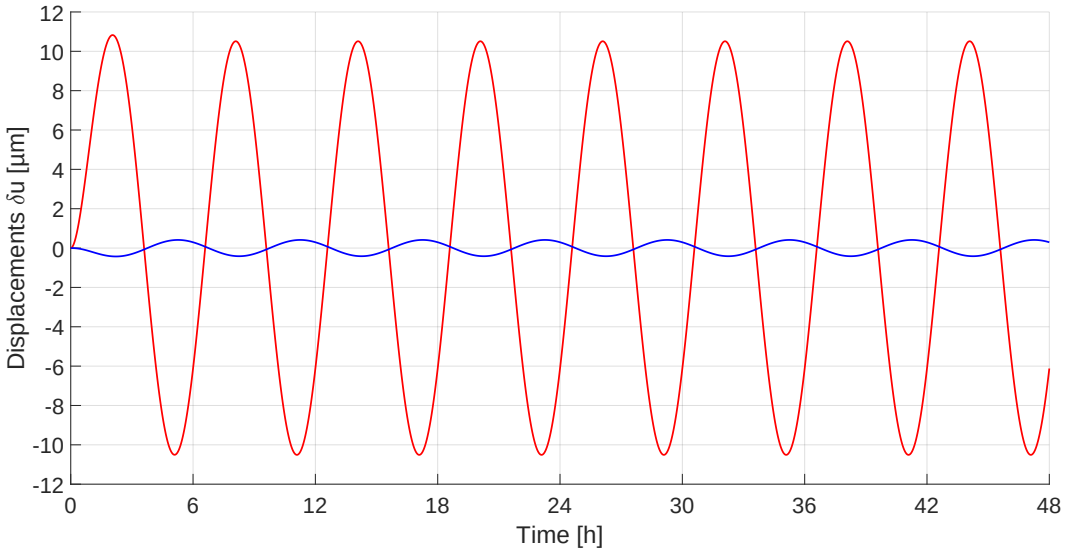

(b) Reference point to P2

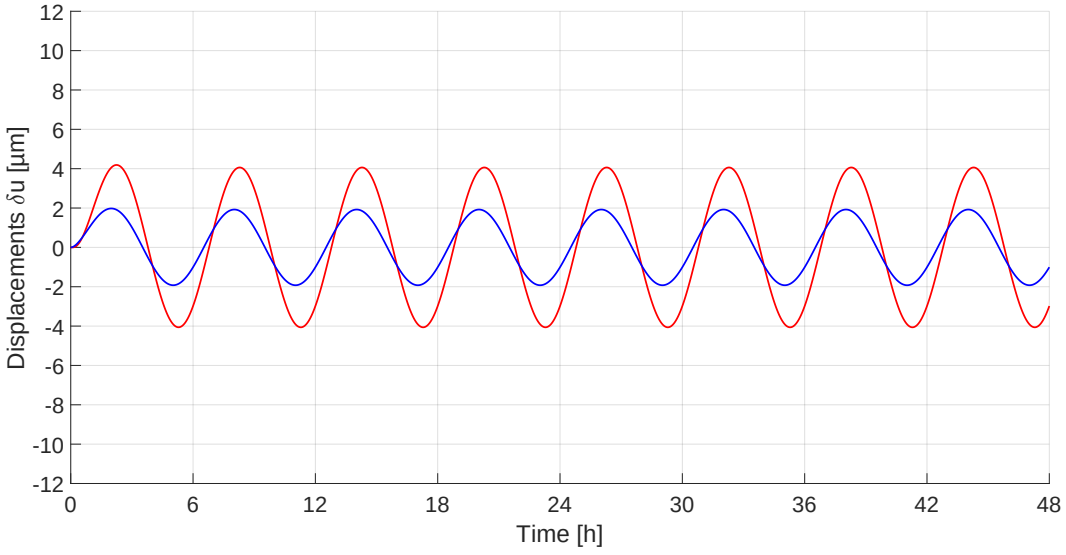

(c) P1 to P2

Figure 4.5 Uncontrolled case: Displacement plot, simulation, configuration 1

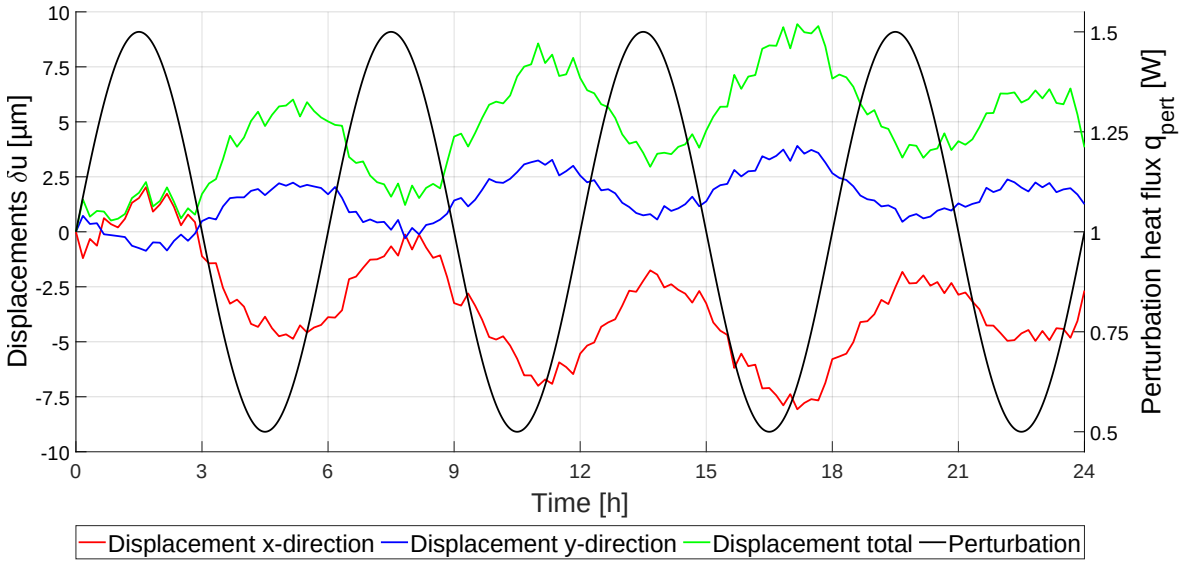

Figure 4.6 Uncontrolled case: Displacement plot, experiment, configuration 1

Figure 4.6 shows the corresponding displacements at point 2 relative to the reference point in x- and y-direction as well as in total. In order to be able to better classify the occurring fluctuations in the displacements, the perturbation is also plotted. The maxima of the shift in the x-direction occur about 40 min after the maxima in the heating power, which correlates with the transfer function as expected. As shown in section 3.4, the reference point for the evaluation of the displacements within the DIC software is located in the upper right corner of the plate on the isostatic mount, on which all three translational DOF are constrained. The x-direction points left along the edge of the plate. Consequently, increasing the heating power causes the plate to expand in the positive x-direction and negative y-direction. This can also be observed in Figure 4.6. Two facts in this plot seem unusual: First, the amplitude of the displacement is expected to be around 7 µm. This value is not reached here. Second, the sinusoidal fluctuations in the displacements should be around the zero line since expansion and contraction are reversible. The linear drift suggests that this reversibility cannot be ideally reflected by the isostatic mounting. This linear drift did not occur in every experiment but reflects the challenges associated with the isostatic mount on one side and the resolution of the camera system on the other side very well. The lack of reversibility could potentially be attributed to the friction between the mount and the Teflon counterpart, which has been explained in Section 3.3.2. The fact that displacements in micrometer range can be resolved at all is technically highly demanding. However, the qualtitative course is comprehensible and proves the basic functionality of the experimental setup, although the measured values are lower than those calculated in the simulation. The same evaluation was made for point 1 on the structure, located at the bottom centre of the plate. To avoid unnecessary duplications and to ensure comparability of the results, only the behavior at point 2 is evaluated in the following. Since it cannot be conclusively determined whether friction is the cause of

the drift and whether this drift results in a smaller amplitude of the perturbation than it would otherwise be, an alternative approach must be found to enable a qualitative comparison of the results. As visible sinusoidal changes in the displacements should not occur in controlled cases, the following comparison focuses on the differences between the absolute maxima and minima of the displacements during an experiment. These differences amount to 10.1 µm and 4.77 µm in the x- and y-directions, respectively, and 8.93 µm in the total displacement.

These measured values appear qualitatively correct, although they deviate significantly in amplitude from the values computed in the simulation. The displacement in the y-direction is noticeably pronounced, while the displacement in the x-direction is less significant. The specific causes of these discrepancies are difficult to assess. However, a combination of the previously mentioned sources of error in the isostatic mounting, the resolution of the camera system, and the overall error in the measurement method seems likely. If these errors occur in a similar manner in all experiments, the deviation between simulation and experiment is expected to remain similarly high. Nevertheless, an improvement in the displacements should be discernible within the experiments.

If the perturbation is known exactly, the necessary control input for the control HEs can be calculated in advance, which should ideally compensate the displacements at the two points. This case is referred to as the Perturbation Compensation Method (PCM). The mathematical derivations can be found in Appendix A.4.1. In the real experiment, a reduction of the displacement to 0 is not possible due to the resolution and uncertainties of the measuring instruments and the accuracy of the actuators. But theoretically, this case should yield a more significant improvement than any other case in which the control framework is employed. Figure 4.7 illustrates the applied control heating power of the four HEs. In this ideal case the heating elements 1 and 2, placed closest to the perturbation element, run with a phase shift of π with respect to the perturbation element and compared to heating elements 3 and 4 as well. The higher amplitude of the two elements closest to the perturbation source also appears plausible, as this is where the most significant influence on the overall temperature field is expected. In order to improve comparability between all test cases, the absolute values of the heating powers of all 4 control elements are summed. In the worst case, each element would utilize the maximum possible value range of $\pm 0.6\,\mathrm{W}$, so that the described comparative value would amount to $2.4\,\mathrm{W}$. In the case of PCM, this value results in $1.37\,\mathrm{W}$.

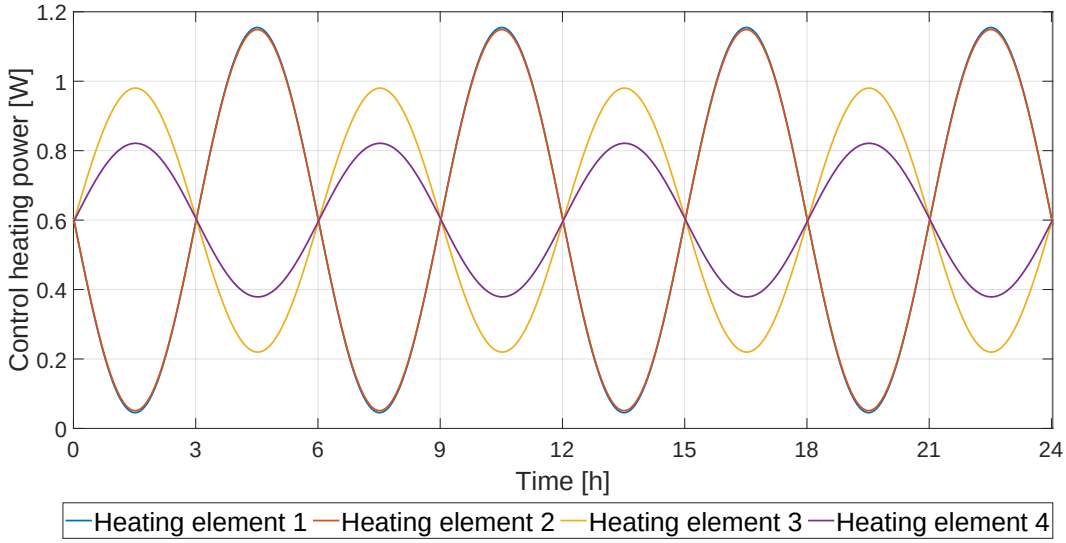

Figure 4.7 PCM case: Control heating power, configuration 1

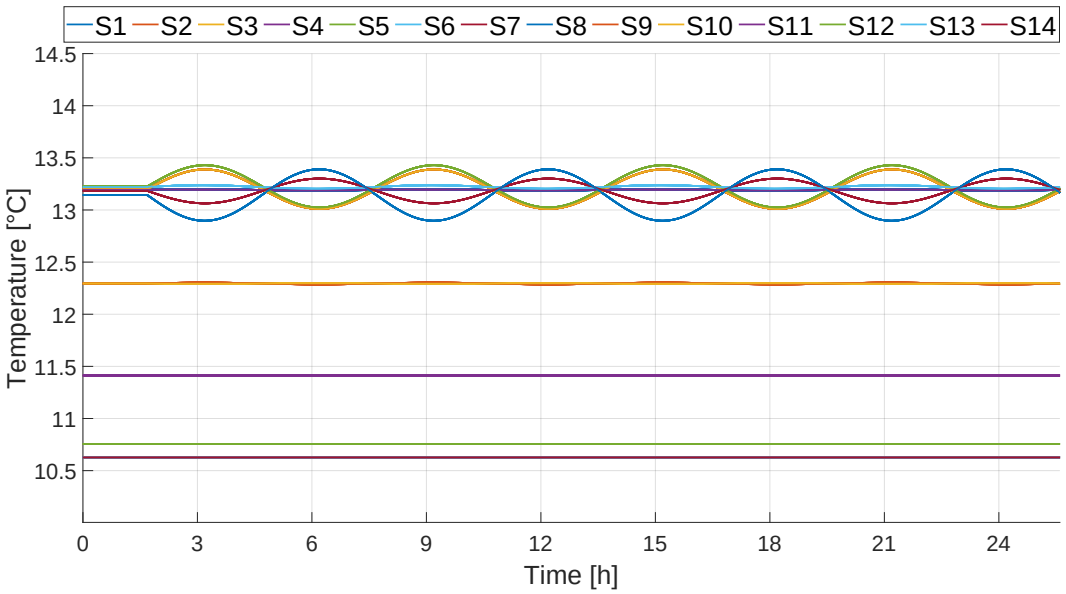

(a) Simulation

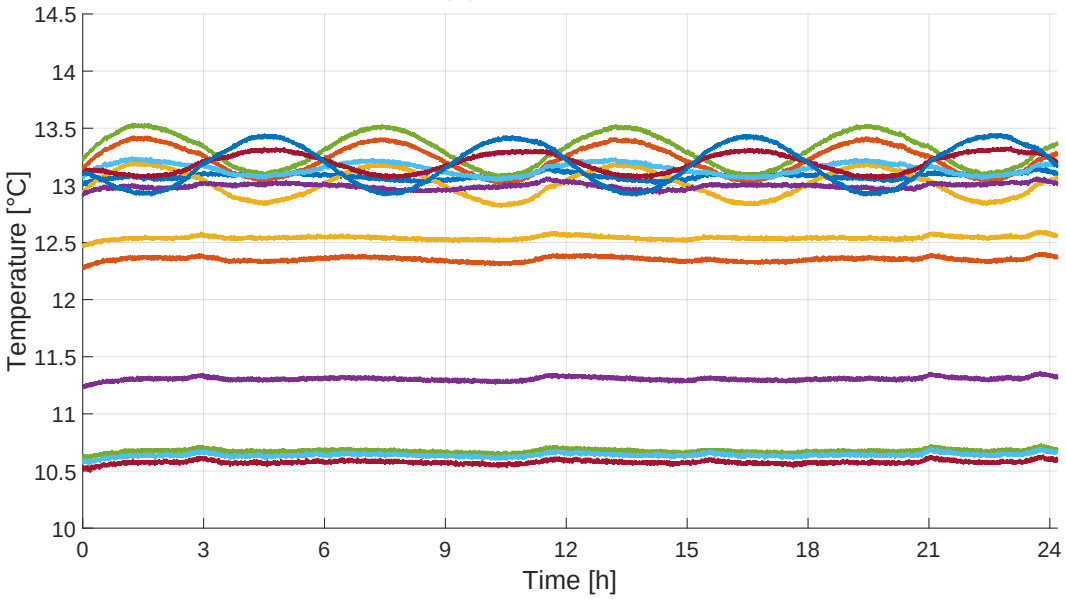

(b) Experiment

Figure 4.8 PCM case: Temperature sensor plot, configuration 1

The resulting temperature plots for both, simulation and experiment, are shown in Figure 4.8. Figure 4.8a shows the steady-state condition for a period of approximately 2 h before the start of the perturbation. During this time, the temperature measurements do not change at all. As in the first case, some sensor plots are overlapped which is why they seem to be missing. But especially when examining sensors S9 and S10, colored orange and yellow around 12.3 °C, slight differences become apparent. It is already evident at first glance that simulation and experiment are very similar, besides the timing difference. The temperature at the left end of the plate (sensors S9 to S14), where the heating elements are not located, remains almost constant and the curves of the sensors near the heating elements (sensors S1 to S8) are partially in phase

opposition, still showing the sinusoidal character of the perturbation. This results in an almost constant temperature when averaging all sensors, as it was already shown in Figure 4.3. However, the strongly damped effect of the sinusoidal perturbation is more pronounced in the experiment than in the simulation, where the maximum temperature amplitude is 0.25 K. If the average temperature range is compared, a value of 0.03 K is achieved in the simulation and 0.14 K in the experiment. This behavior is as expected, as inaccuracies in the sensors, actuators, and the experimental setup itself do not allow the simulated temperatures to precisely reflect the actual values.

The PCM reduces the displacement perfectly to a value of 0 for the points to be controlled, relative to each other and relative to the fixed corner of the isostatic mount.

Due to the nearly constant temperature at the left side of the plate measured from sensor S9 to S14, it is expected that the measured displacements are also close to zero. This assumption can be confirmed by evaluating the recorded image data. Looking at the displacement at point 2 shown in Figure 4.9, it is immediately apparent that the fluctuations are around the zero line, which falls within the order of magnitude of noise within the resolution of the camera and the basic experimental setup. It is noteworthy that the displacements vary only slightly and exhibit no correlation with the perturbation, which is also visible as a reference in Figure 4.9. For comparison, the difference between the smallest and largest displacement in the respective coordinate direction is formed for this case as well. This difference represents the value range in which the displacements fluctuate. These values result in approximately 2 µm and 3 µm for the x and y directions respectively. The total displacement can be reduced by a factor of 4, whereas the displacement in x-direction is reduced by factor of 3.

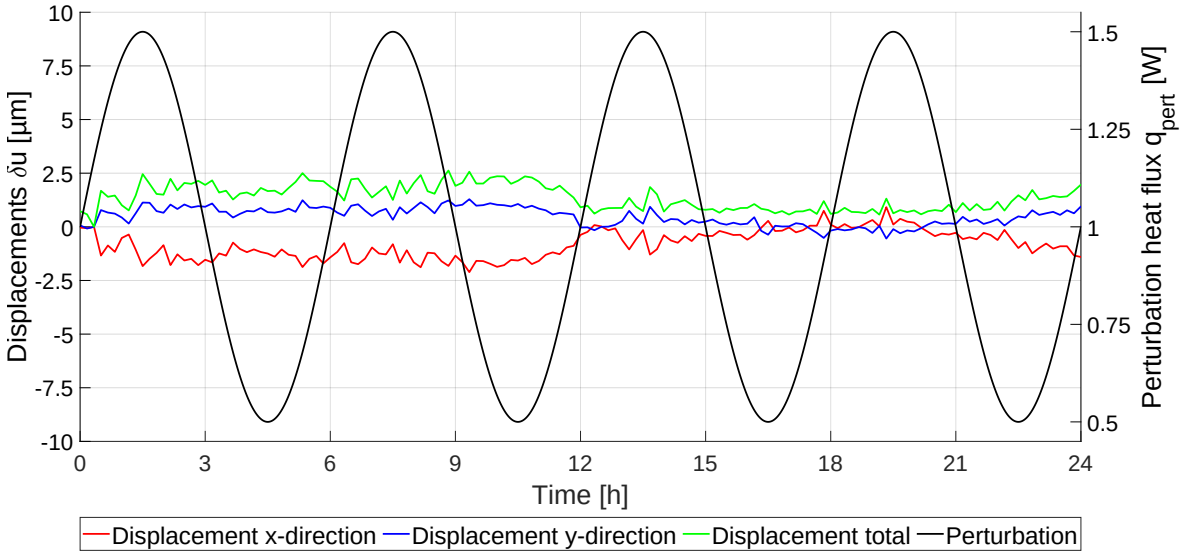

Figure 4.9 PCM case: Displacement plot, point 2, experiment, configuration 1

The compared values for the uncontrolled case 1 and the PCM case 2 are listed in Table 4.4.

Table 4.4 Comparison uncontrolled case 1 and PCM case 2 for a sinusoidal perturbation, configuration 1

Value	**Case 1**		**Case 2**		**Factor**	
	Sim.	**Exp.**	**Sim.**	**Exp.**	**Sim.**	**Exp.**
u_{total}	21.34 µm	8.93 µm	0 µm	2.23 µm	∞	4.01
u_x	22.06 µm	10.1 µm	0 µm	3.34 µm	∞	**3.02**
u_y	0.75 µm	4.77 µm	0 µm	1.97 µm	∞	**2.42**
$\Delta\bar{T}$	1.75 K	1.74 K	0.03 K	0.14 K	58.33	**12.43**
ΣQ_c			1.37 W	1.37 W		

For all subsequent controlled cases, the displacement is examined in relation to the uncontrolled case 1, both in simulation and in the experiment. If the improvements in displacements fall within the same range as those of the PCM presented in this case, it can be roughly assumed that these values represent the baseline noise of the DIC system. However, the improvement factors calculated subsequently do not account for this baseline noise.

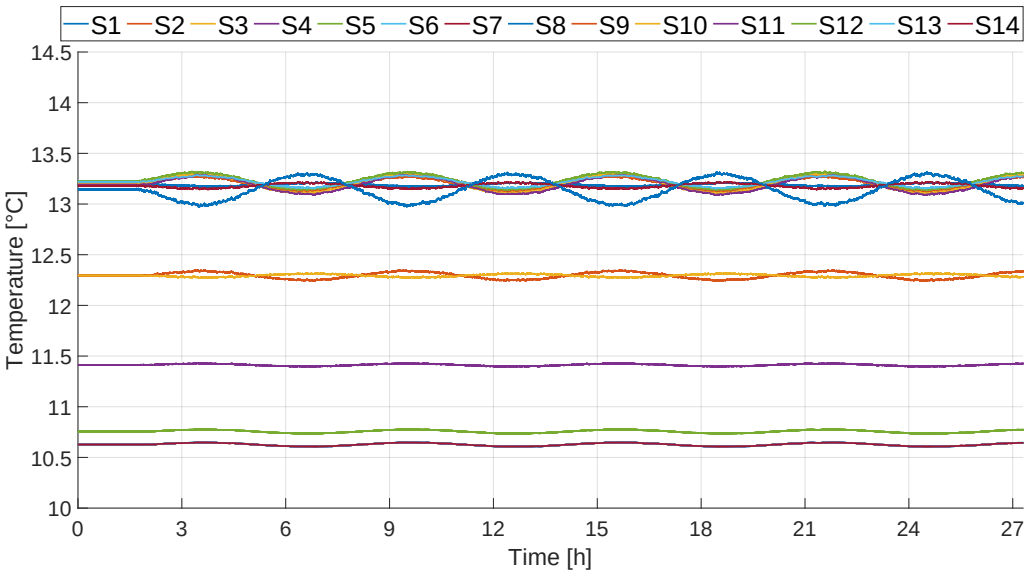

(a) Simulation, case 3: $\sigma_S = 0.18\,\mathrm{K}$ and $\sigma_H = 0.02\,\mathrm{W}$

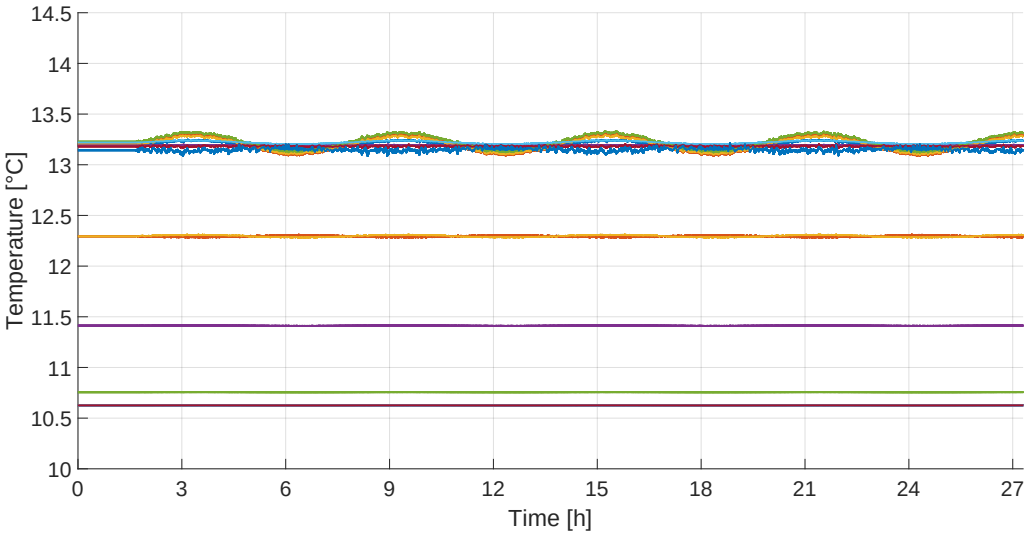

(b) Simulation, case 4: $\sigma_S = 0.12\,\mathrm{K}$ and $\sigma_H = 0.02\,\mathrm{W}$

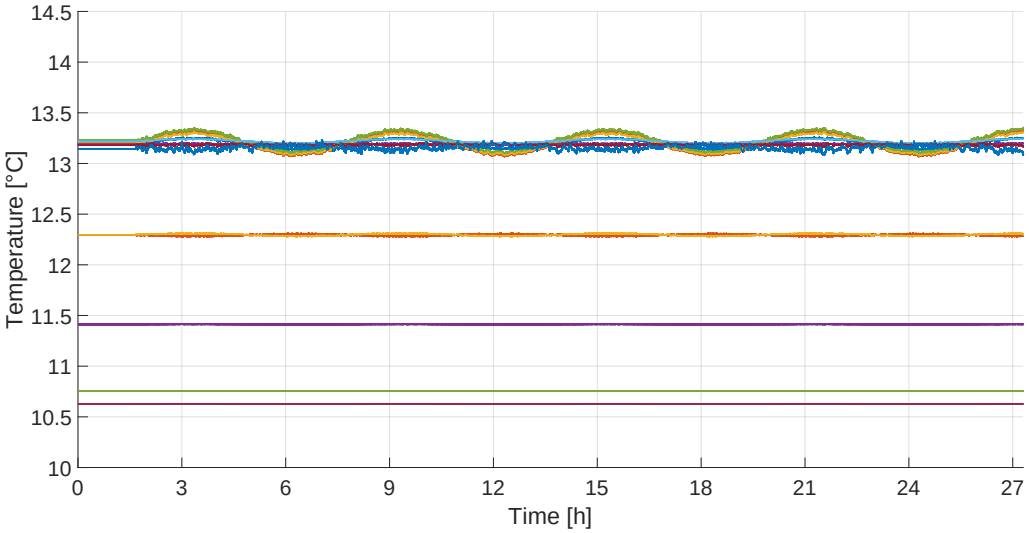

(c) Simulation, case 5: $\sigma_S = 0.10\,\mathrm{K}$ and $\sigma_H = 0.02\,\mathrm{W}$

Figure 4.10 Temperature sensor plots, controlled cases, simulation, configuration 1

Figure 4.10 shows a comparison of the simulated temperature plots for the 3 controlled cases with different standard deviations of the sensors ranging from $\sigma_S = 0.18\,\mathrm{K}$ in case 3 to $\sigma_S = 0.10\,\mathrm{K}$ in case 5. The sensors mounted close to the perturbation and control elements still show small sinusoidal amplitudes. As in the PCM case, some sensor curves have opposing phases, but the sinusoidal fluctuations are even smaller in all controlled cases shown in Figure 4.10. However, these amplitudes become more pronounced in the sensors positioned farther away from the HEs. The average temperature fluctuation in all 3 cases shown here is very low at 0.05 K to 0.06 K and as the standard deviation σ_S decreases, the sinusoidal fluctuation in the individual curves of the sensors decreases further and further.

Experimentally measured temperatures significantly deviate from the simulation, shown in Figure 4.11, as all sensors exhibit the sinusoidal pattern. Due to the aforementioned errors in the control of the PCU, the recording of the measurement data in cases 4 and 5 does not provide sufficient valid data for a period of 24 h, which is why the plots shown here are abbreviated. The basic correlations are nevertheless clearly recognizable.

The amplitudes, although lower than in the uncontrolled case 1, are only slightly reduced in all 3 plots. Essentially, substantial temperature fluctuations near the heating elements are not problematic since the points to be controlled are not located in this area. Nevertheless, especially in case 3 shown in 4.11a the fluctuations in sensors S9 to S14, with amplitudes of up to 0.4 K, are quite pronounced. The attenuation of the temperature curves increases with decreasing standard deviation, with the greatest reduction being observed between case 3 and the other two cases, while the changes between case 4 and case 5 are small. The mean temperature still fluctuates by 1.08 K in case 3, by 0.72 K in case 4 and by 0.59 K in case 5. This means that improvements by a factor of 1.61 to 2.95 are achieved compared to the uncontrolled case. While the temperature plots in the PCM case were still very similar, the temperature profiles between simulation and experiment differ very clearly in the three cases where the control framework was used.

The deviations can be explained by the commanded heating powers. While the HEs were controlled exactly with the simulated power in the case of the PCM, this is not happening here in the three controlled cases.

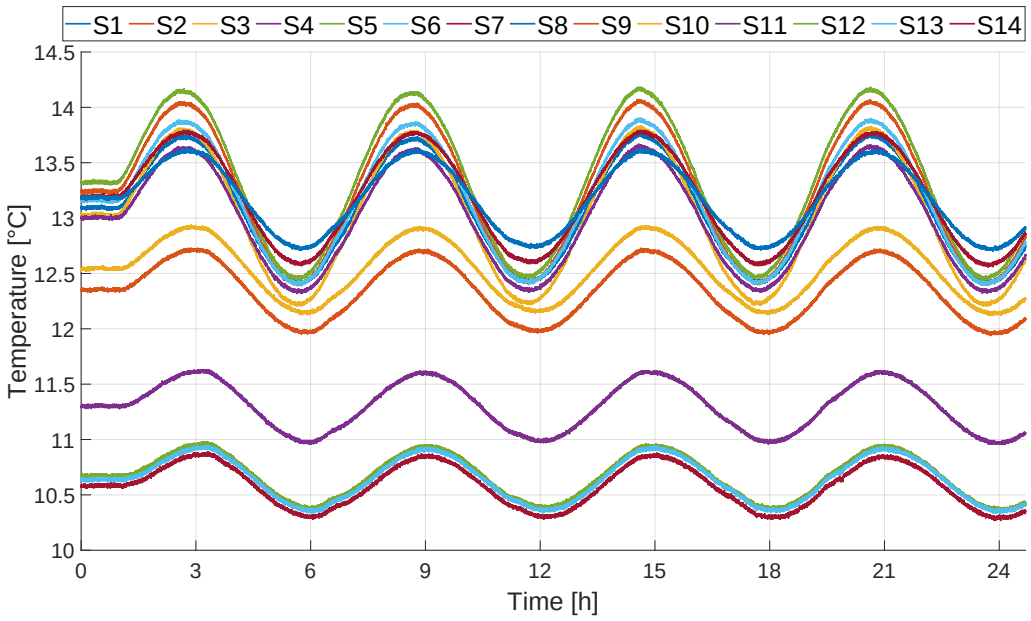

(a) Experiment, case 3: $\sigma_S = 0.18\,\mathrm{K}$ and $\sigma_H = 0.02\,\mathrm{W}$

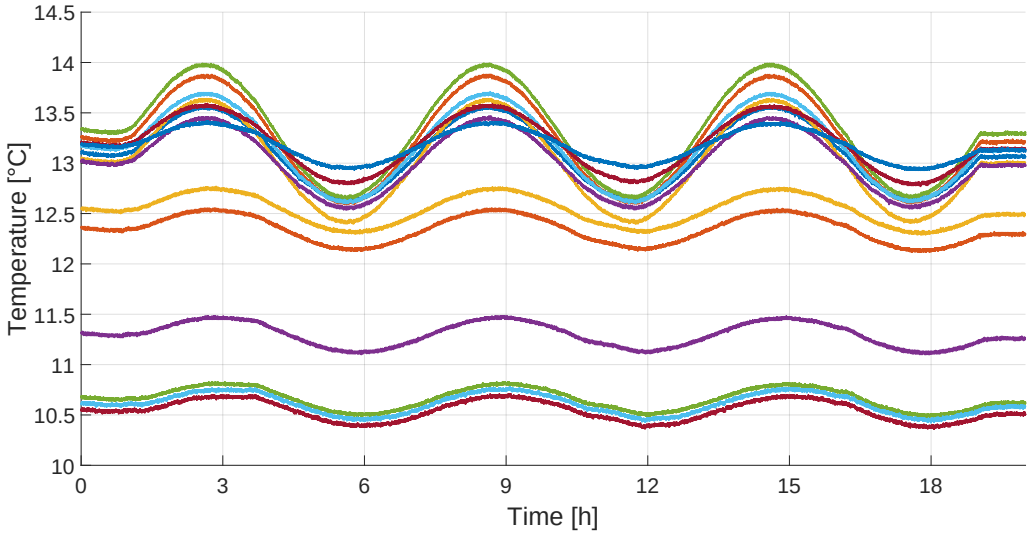

(b) Experiment, case 4: $\sigma_S = 0.12\,\mathrm{K}$ and $\sigma_H = 0.02\,\mathrm{W}$

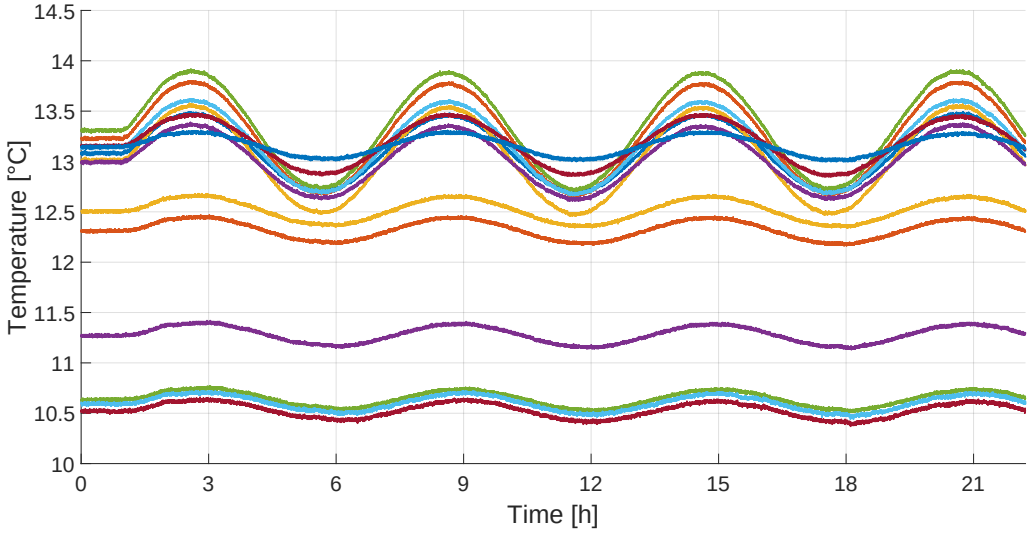

(c) Experiment, case 5: $\sigma_S = 0.10\,\mathrm{K}$ and $\sigma_H = 0.02\,\mathrm{W}$

Figure 4.11 Temperature sensor plots, controlled cases, experiment, configuration 1

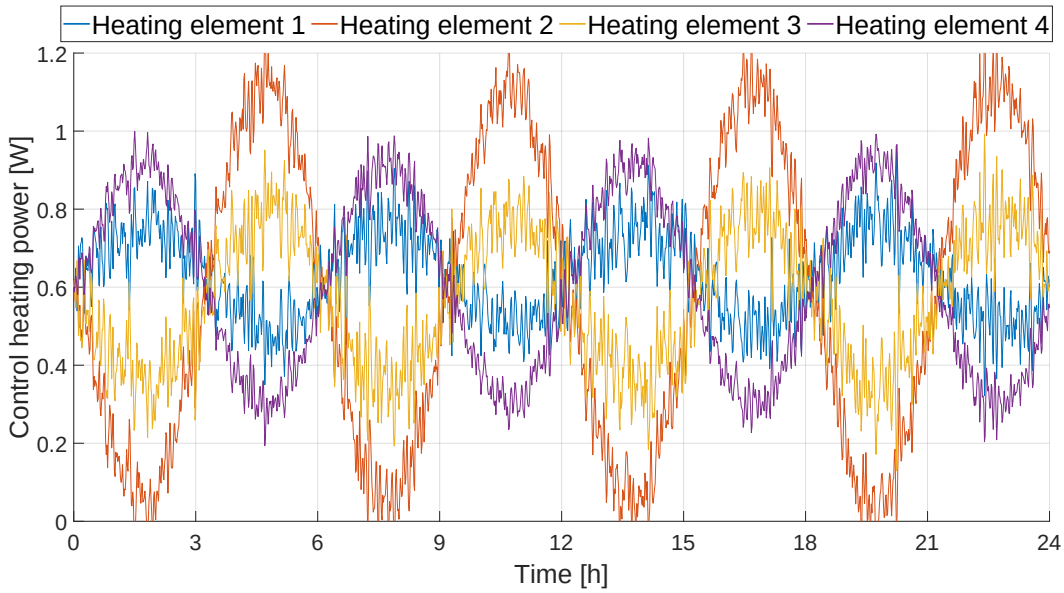

(a) Simulation

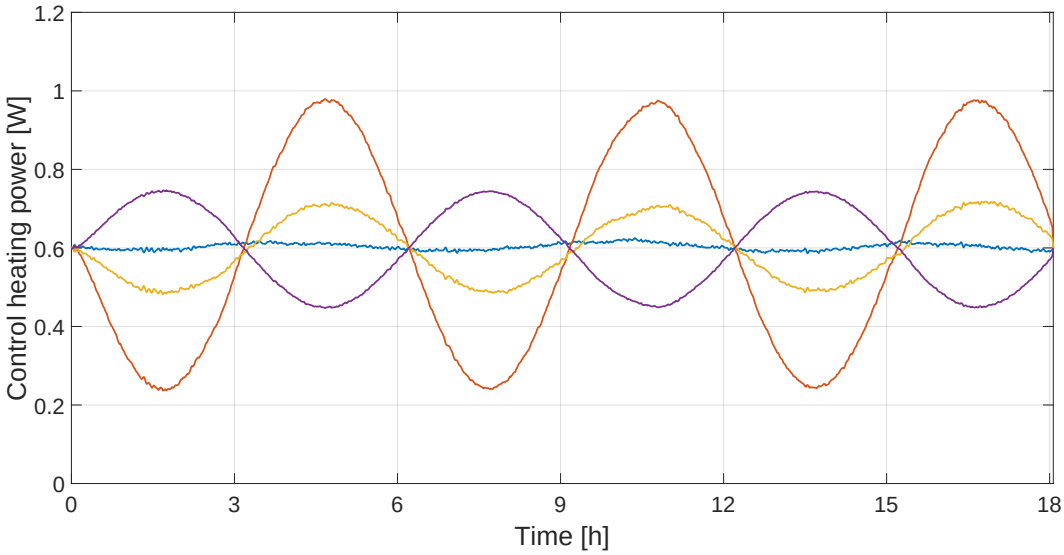

(b) Experiment

Figure 4.12 Controlled case 4 with $\sigma_S = 0.12\,\mathrm{K}$ and $\sigma_H = 0.02\,\mathrm{W}$: Control heating power, configuration 1

Figure 4.12 shows the comparison between simulated and actually commanded heating power, as an example for case 4 with a standard deviation of $\sigma_S = 0.12\,\mathrm{K}$. The curves are very similar in all 3 cases, whereby the amplitudes of the heating power of the individual heating elements increase as the standard deviation of the sensors decreases. The maximum in case 3 for heating element 2 is at $\pm 0.4\,\mathrm{W}$ and in case 5 it is already in the maximum usable range of $\pm 0.6\,\mathrm{W}$ defined by the steady-state condition, in which each element runs with $0.6\,\mathrm{W}$. The control heating power plots of cases 3 and 5 can be found in Figures C.1 and C.2, respectively, in Appendix C.

It is notable that the control heating powers commanded in the experiment are almost half the magnitude of those predicted in the simulation. Lower control heating power

consequently leads to reduced temperature stabilization. In the simulation, the maximum absolute sum of the control heating power amounts to 1.11 W in case 3, 1.61 W in case 4 and 1.85 W in case 5, while in the experiment, only 0.48 W, 0.65 W and 0.74 W respectively are utilized.

The simulated control heating powers exhibit significant noise, which can be attributed to the use of discretely determined simulated temperature measurements taken at one-second intervals. In the experiment, due to the low frequency of the perturbation, a new control input is commanded to the voltage sources only every 30 s, and the mean of the temperature measurement over the last 10 s is used to additionally filter out noise. Therefore, the profile of the control heating powers in Figure 4.12b appears less noisy in the experiment.

The cause of the discrepancy between simulated and actually commanded heating power has not been conclusively identified. The reconstruction of the temperature field based on the 14 sensors used in this configuration is not ideal, as the sensor positions were not optimized. The positioning of the HEs was also carried out without optimizing for the perturbation. With the approach presented here, optimal results for improving the displacements cannot be achieved if these optimizations have not taken place. This can also be seen in the following figures when the displacements are considered. Possibly, due to the "wors" positioning of the sensors, the effect of individual measurement errors and inaccuracies is greater, so that the HEs command lower values than they actually should according to the simulation, since the system parameters set in those cases here attribute a rather high weight to the measurements. However, the use of other system parameters yielded to even poorer results in the simulation and experiment, which is why those are not discussed here. In Configuration 2 in section 4.3.2, however, there will be a significant improvement with regard to the heating power used, which is why a large contribution from the non-optimized sensor and HE positions is assumed at this point.

Even in the simulation, the control heat is significantly lower compared to the PCM case, which is why the expected improvement in the displacements is also lower. This behavior can be seen in Figure 4.13, which shows a comparison of the displacements in the x-direction of point 2 between the uncontrolled case and the 3 controlled cases with different system parameters. Since the uncontrolled case and the PCM case have already shown that the displacements in the y-direction are significantly lower and the control will also be worse due to the level of base noise of the measurement, the focus here is only on the x-direction as an example. Even for case 3 with a standard deviation of $\sigma_S = 0.18\,\mathrm{K}$, the improvement is just at a factor of less than 2 in the simulation. It is therefore quite evident that despite substantial temperature stabilization, only a minor enhancement in displacement is anticipated in the simulation. Due to the low control heating power, the displacement fields also have larger values compared to the PCM case 2.

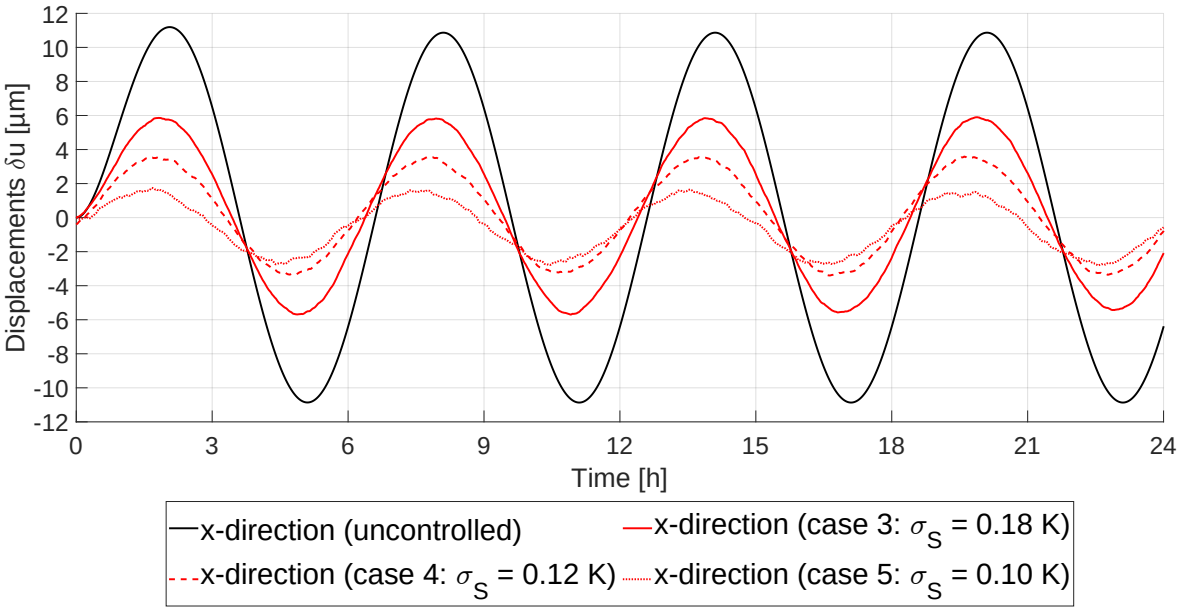

Figure 4.13 Comparison of simulated displacements of point 2 in x-direction for uncontrolled vs. controlled cases, configuration 1

However, as the standard deviation decreases, the displacements in the x-direction also decreases significantly, until in case 5 the improvements have reached a factor of 4.31. It can also be seen that a certain phase shift occurs. The maxima and minima of the displacements in the controlled cases occur earlier than in the uncontrolled case, while these maxima and minima extend slightly in time. A similar behavior could already be observed in Figure 4.12, but less pronounced. The time offset in reaching the respective maxima and minima in the individual heating powers of the HEs is therefore reflected in the maxima and minima in this plot. Nevertheless, the displacements still fluctuate relatively evenly around the zero line in the 3 controlled cases. A further reduction in the standard deviation of the sensors does not lead to any further improvement in the displacements compared to case 5, but the necessary control heating power increases far outside the possible range of $\pm 0.6\,\mathrm{W}$, which is why these cases are not considered further here.

Although the total displacement is calculated in the experiments by the DIC software, this is only the result of the vectorial addition of the components in the x and y directions, which is why it is not shown in the simulation here nor in the subsequent plots in the experiment.

The comparisons of the resulting displacements of point 2 in the x and y directions for the 3 controlled cases are shown in Figure 4.14.

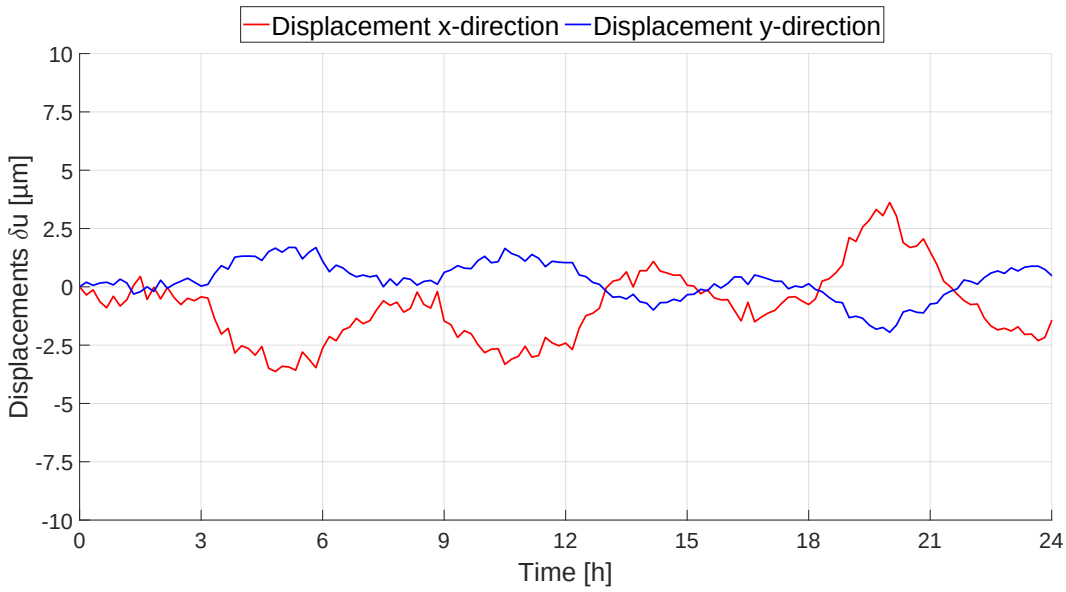

(a) Experiment, case 3: $\sigma_S = 0.18\,\mathrm{K}$ and $\sigma_H = 0.02\,\mathrm{W}$

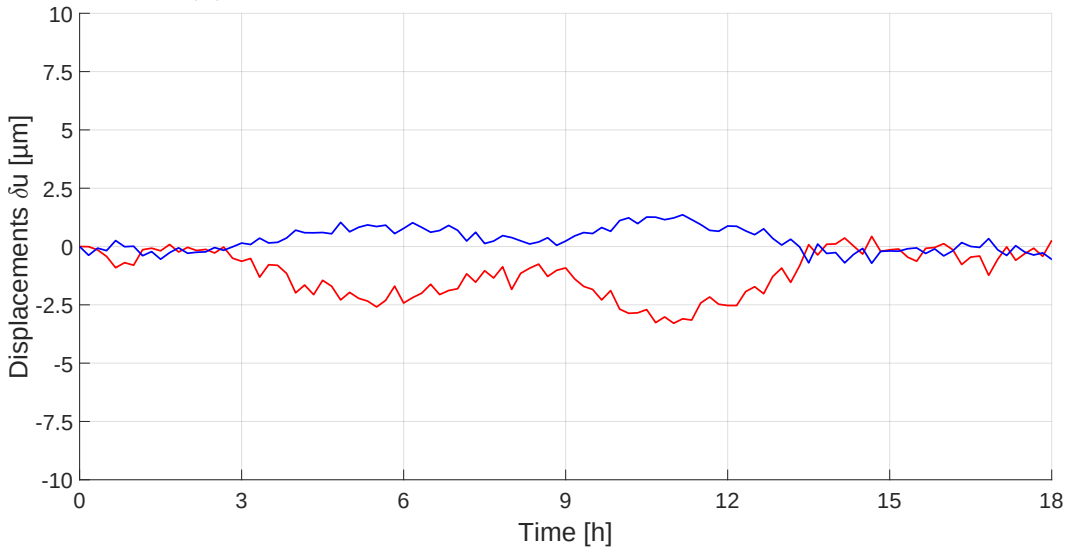

(b) Experiment, case 4: $\sigma_S = 0.12\,\mathrm{K}$ and $\sigma_H = 0.02\,\mathrm{W}$

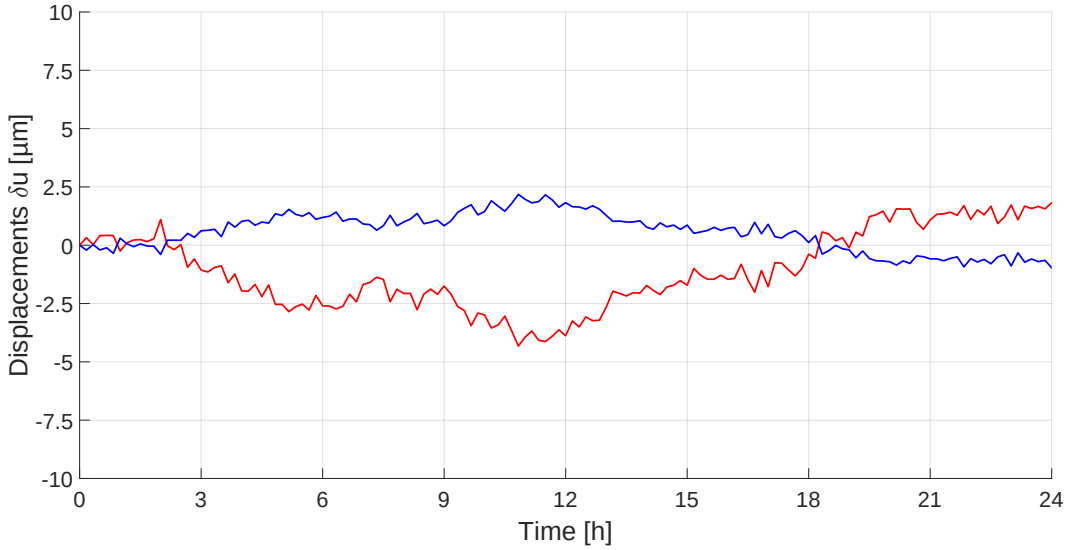

(c) Experiment, case 5: $\sigma_S = 0.10\,\mathrm{K}$ and $\sigma_H = 0.02\,\mathrm{W}$

Figure 4.14 Displacement plots, controlled cases, experiment, configuration 1

Due to the aforementioned errors in the control of the PCU, only shorter time periods are available for the measurements of the displacements in cases 4 and 5. The sinusoidal course of the perturbation can still be seen in the displacements in x and y direction, especially in case 3. The correlation with the perturbation becomes less pronounced as the standard deviation decreases. However, the amplitude of the displacement has decreased slightly compared to the uncontrolled case by a factor of 1.3 in x- and y-direction when comparing the value ranges in case 3 in Figure 4.14a. An increasing improvement can also be achieved in the experiment with decreasing standard deviation. However, the best values for a displacement improvement in the x and y directions with factors of 1.93 and 1.88 respectively are already achieved here in case 4 with $\sigma_S = 0.12\,\mathrm{K}$. This demonstrates that reducing the standard deviation of the sensors, that is, shifting the weight towards the measurements, is associated with an improvement in displacement stability while simultaneously increasing the required control heating power. However, an optimum for case 4 already appears to have been reached in the experiment, even if the best results in the simulation are obtained in case 5.

Nevertheless, the experimentally determined values significantly deviate from the simulated values once again. The reversibility of displacement, which is expected in the case of sinusoidal variation of heating power, is notably dampened here.

Interim Conclusion and Results

Table 4.5 summarizes the various values examined in the course of this section. Once again, it is clear that the greatest improvements in the displacements are achieved in case 4 in the experiment, while this is achieved in case 5 in the simulation. Nevertheless, the factors of just under 2 achieved in the improvement of the displacements by utilizing this approach are clearly below the PCM with a factor of 3.

Table 4.5 Comparison uncontrolled case 1 and controlled cases 3, 4 and 5 for a sinusoidal perturbation, configuration 1

	Experiment				**Simulation**			
	u_x µm	u_y µm	$\Delta\bar{T}$ K	ΣQ_c W	u_x µm	u_y µm	$\Delta\bar{T}$ K	ΣQ_c W
Case 1	10.1	4.77	1.74		22.06	0.75	1.75	
Case 3	7.25	3.64	1.08	0.48	11.79	0.43	0.05	1.11
(Factor)	**(1.39)**	**(1.31)**	**(1.61)**		**(1.87)**	**(1.74)**	**(35)**	
Case 4	5.24	2.54	0.72	0.65	7.78	0.24	0.06	1.61
(Factor)	**(1.93)**	**(1.88)**	**(2.42)**		**(2.84)**	**(3.13)**	**(29.2)**	
Case 5	6.33	3.15	0.59	0.74	5.12	0.17	0.06	1.85
(Factor)	**(1.60)**	**(1.51)**	**(2.95)**		**(4.31)**	**(4.41)**	**(29.2)**	

The first proof of the framework for active structural stabilization could be performed using a basic experimental setup. Assuming that a structure is already in thermal equilibrium and passively stabilized, it is possible to react to a change in this thermal equilibrium by selectively introducing thermal power. While the simulations by [6] show improvements of a factor of around 20 to 100 compared to the uncontrolled case, this could not be achieved with this rudimentary model without optimization, neither in the simulation nor in the experiment. Nevertheless, it could be shown that by appropriate choice of the parameters for the Kalman filter and the LQR, improvements compared to an uncontrolled reference case are possible and provable with this approach within the simulation and experiment.

The choice of the Kalman filter parameters, as expected, has a crucial impact on the functionality of the approach. These values can only be determined through prior estimates based on the technical characteristics of sensors and actuators. However, it has already been demonstrated that simulation and experiment sometimes deviate significantly, making it seemingly inevitable to determine the values purely empirically through experimentation. Various values for standard deviations were tested in the simulations, including those that deviate far from technical practicability. It has been shown that, beyond the absolute values, the relationship between the two standard deviations becomes more relevant. In the simulation, values of $\sigma_S = 0.1\,\mathrm{K}$ and $\sigma_H = 0.02\,\mathrm{W}$ have proven to be optimal, and for this initial configuration, the best results were achieved with values of $\sigma_S = 0.12\,\mathrm{K}$ and $\sigma_H = 0.02\,\mathrm{W}$ in the experiment. Since there was no optimization of the positioning of actuators or sensors for this initial configuration, it is expected that an improvement, along with a reduction in the necessary control heating power, will be achieved for the enhanced setup in configuration 2, despite the rudimentary nature of the experimental setup itself. Especially the expected improvements in displacements, which were lower in simulation with factors of 2 to 4 than expected, should increase significantly in an optimized and revised configuration. However, the measurability and resolution are naturally limited by the DIC system. This can be particularly observed in the small displacements in the y-directions due to the geometry of the test structure. However, this is not modified for the second configuration to maintain comparability.

4.3.2 Configuration 2

As previously described in Section 3.5, the second configuration of the experimental setup was improved in terms of the positioning of sensors and actuators. The points on the structure to be controlled, which are also nodes in the model, as well as the position and amplitude of the perturbation, remained unchanged. Based on the thermo-mechanical model and the modal transformation, as well as the reconstructibility of the temperature field through sensor measurements, the positions of the sensors and actuators for this setup were revised. They still do not represent an optimum due to technical constraints (e.g., no heating elements at locations of the isostatic mount, no sensors inside the structure or on the back of the plate), which led to many potential positions being excluded in advance. Furthermore, the identification of these improved positions was achieved not through a mathematical optimization method, like nonlinear programming with evolutionary algorithms [64], but by systematically testing all possibilities through a brute-force approach [61]. This is feasible with this simplified model; however, the computational effort for systematically exploring all possibilities increases exponentially with larger structures or finer meshing. In addition to validating the previously used sinusoidal perturbation, the approach will also be validated for random and stepped perturbations. In contrast to the first configuration, in this case, the displacements between the two points to be controlled relative to each other are evaluated for all types of perturbations and test cases, allowing for a slightly better assessment of changes and improvements in stability in the y direction.

An overview of the test cases has been presented in Section 3.5 and is reiterated here for clarity and comprehensibility in Table 4.6. Again, each case of the framework is compared to an uncontrolled reference state and compared to the simulations.

Table 4.6 Overview of the experimental test series, configuration 2

	Parameters	
Case	**Perturbation**	**Control**
1	sinusoidal 1 W ± 0.5 W	uncontrolled
2	sinusoidal 1 W ± 0.5 W	control, $\sigma_H = 0.02\,\mathrm{W}$ and $\sigma_S = 0.10\,\mathrm{K}$
1	random	uncontrolled
2	random	control, $\sigma_H = 0.02\,\mathrm{W}$ and $\sigma_S = 0.12\,\mathrm{K}$
3	random	control, $\sigma_H = 0.02\,\mathrm{W}$ and $\sigma_S = 0.10\,\mathrm{K}$
1	stepped	uncontrolled
2	stepped	control, $\sigma_H = 0.02\,\mathrm{W}$ and $\sigma_S = 0.12\,\mathrm{K}$
3	stepped	control, $\sigma_H = 0.02\,\mathrm{W}$ and $\sigma_S = 0.10\,\mathrm{K}$

Since the positions of the sensors and HEs are important for understanding the evaluation of the different cases and the corresponding correlations, the schematic representation of the experimental setup in configuration 2, which was presented in detail in Section 3.5, is shown again here in Figure 4.15. HE 1 (top) and 2 (bottom) are located directly next to the perturbation HE (red), while HE 3 is located in the middle of the plate and HE 4 on the right. The number of sensors has been increased to 18. Sensors S1, S11 and S12 are located in the immediate vicinity of the perturbation element on the left-hand side of the plate and should in most cases display approximately the same and the highest temperatures compared to all other sensors.

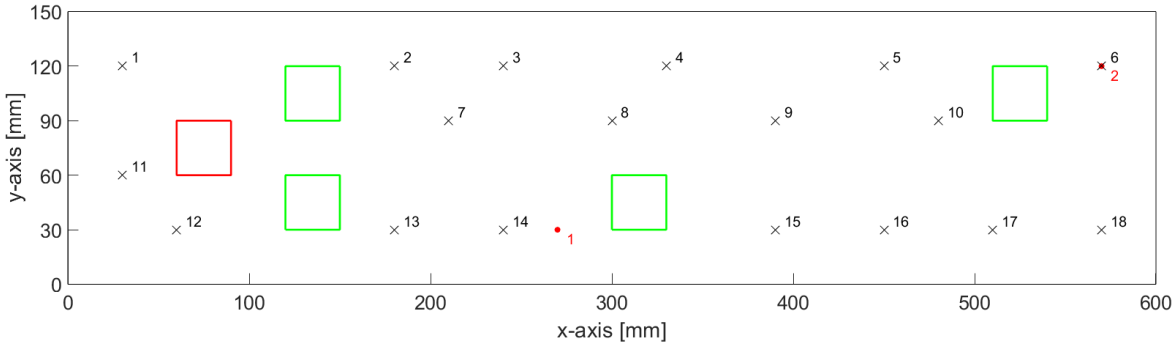

Figure 4.15 Sensor and heater position, configuration 2

4.3.2.1 Sinusoidal Perturbation

Since in the first configuration, the parameter settings of $\sigma_S = 0.18\,\mathrm{K}$ and $\sigma_H = 0.02\,\mathrm{W}$ showed the smallest improvements and this is also expected according to simulations for configuration 2, this case is not evaluated. The PCM is also omitted for this configuration, as no new insights are expected from it. Since the results of the experiments with the standard deviations of $\sigma_S = 0.12\,\mathrm{K}$ and $\sigma_S = 0.10\,\mathrm{K}$ differ only slightly, the results with $\sigma_S = 0.10\,\mathrm{K}$ are presented here exemplary.

The fundamental behavior of the uncontrolled system can be compared to that of configuration 1. Since the control HEs are only operated at 0.5 W instead of 0.6 W in the steady-state, the overall temperature of the structure is also lower in this condition in configuration 2. The sensors are now arranged differently on the plate, which has changed the fluctuation in the average temperature to 1.55 K. The sinusoidal pattern of the perturbation heating power can once again be clearly observed in the simulated sensor values in Figure 4.16a. There is a temperature difference of about 2 K between the sensors closest and furthest from the perturbation HE in the steady-state condition. Simulation and experiment align qualitatively in their behavior. Sensor S7 exhibited higher noise during the test series, likely due to an imprecise solder joint or a loose connection, as visible in Figure 4.16b. However, this had little influence on the controller's functionality due to averaging and filtering. The deviation in the fluctuation of the average temperature between simulation and experiment is slightly greater in this test series compared to configuration 1. Nevertheless, with a value of

1.44 K in the experiment, this deviation is still small. This can be partially attributed to a slight error in the control of the perturbation heating element when transitioning from the steady-state condition to the perturbation operation, which is evident in the slight temperature drop in the beginning of the measurements of sensors S1, S11, and S12, which are closest to the perturbation HE, as shown in Figure 4.16b. Additionally, unusual fluctuations in temperature measurements are observed in the diagram after approximately 10 h and 22 h, attributed to malfunctions in the PCU, which could not ensure a stable ambient temperature within a small range throughout the entire operating time. Therefore, errors and unusual fluctuations are occasionally observed in the subsequent course; some experiments are also shortened in their duration.

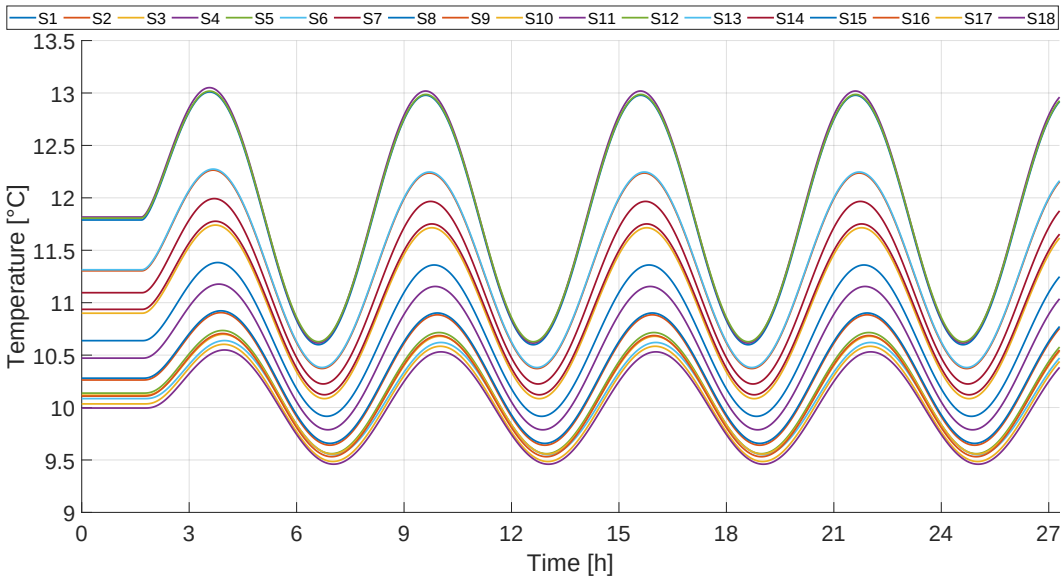

(a) Simulation

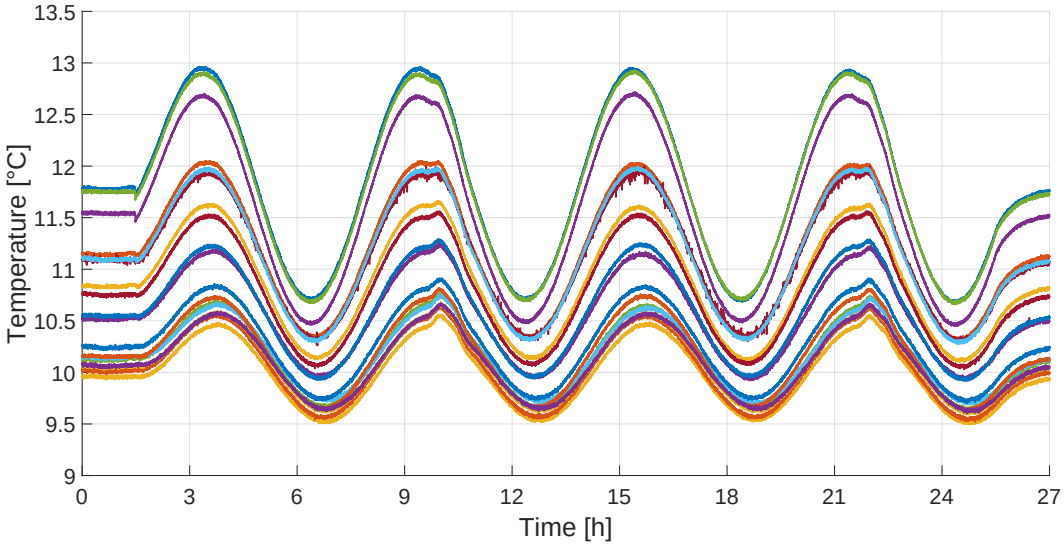

(b) Experiment

Figure 4.16 Uncontrolled case: Temperature sensor plot, sinusoidal perturbation, configuration 2

The displacements of the points to be controlled relative to the reference state are directly proportional to the changes in heating powers. Since only the reference state has changed, but not the fluctuations relative to it, in the case of the sinusoidal perturbation, the uncontrolled displacements are also identical, as shown in Figure 4.17a. Since, as described earlier, the displacements of the two control points relative to each other are considered, the absolute values are lower due to the shorter distance between those two points. In the experiment in Figure 4.17b, the sinusoidal fluctuations are once again clearly visible. The drift observed in the first configuration is also present here, indicating that the complete reversibility of the displacements may not be achieved. Nevertheless, all displacement values are within the range calculated by the simulation, which poses a significant improvement in comparison to the first configuration. The total displacement is not considered here, as this is not calculated in the simulation and only results from the vectorial addition of the components in the x and y directions.

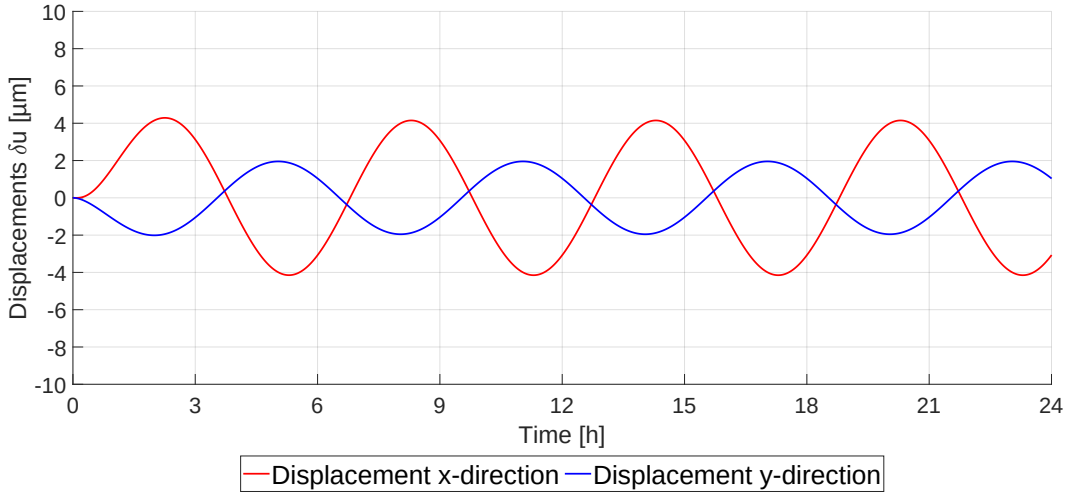

(a) Simulation

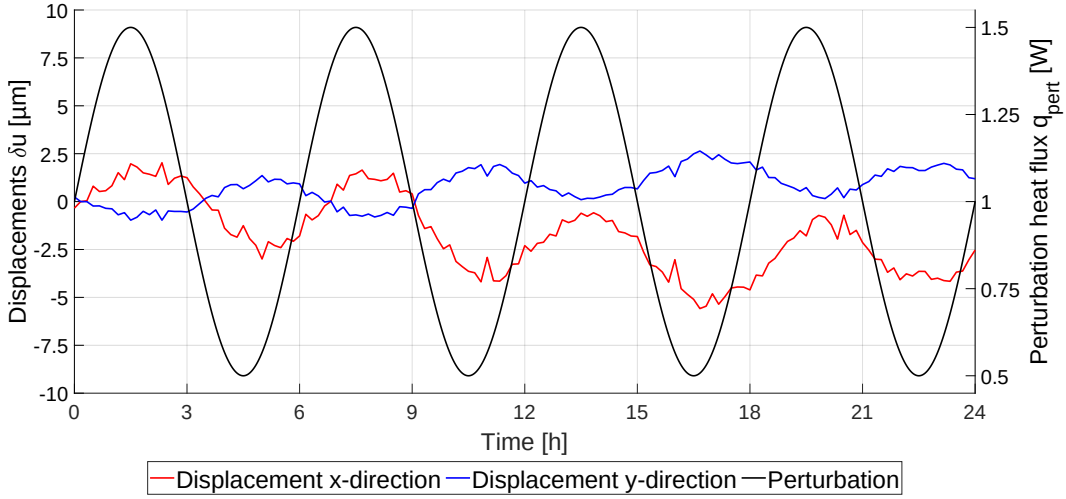

(b) Experiment

Figure 4.17 Uncontrolled case: Displacement plot, sinusoidal perturbation, configuration 2

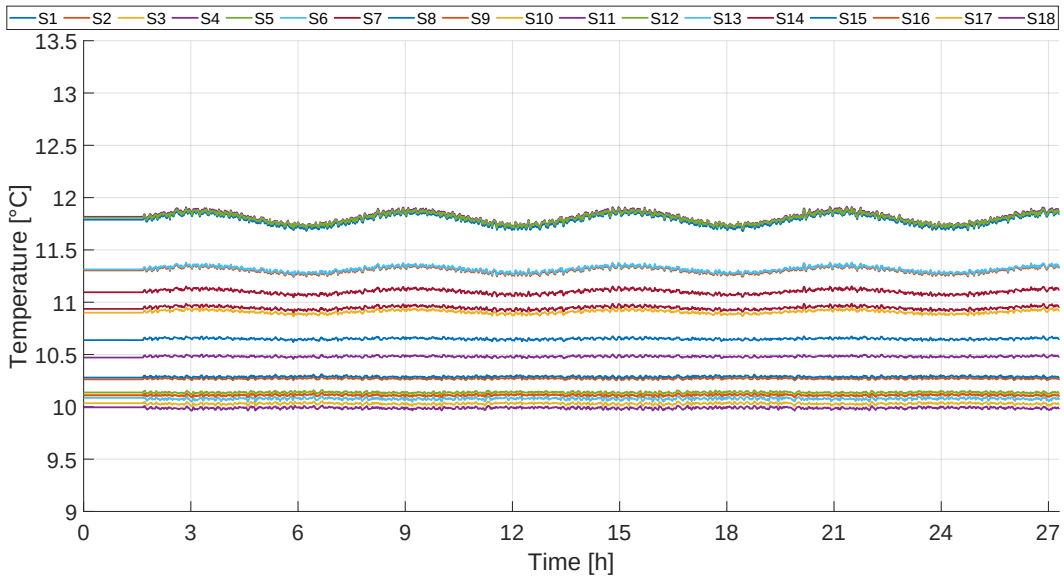

(a) Simulation

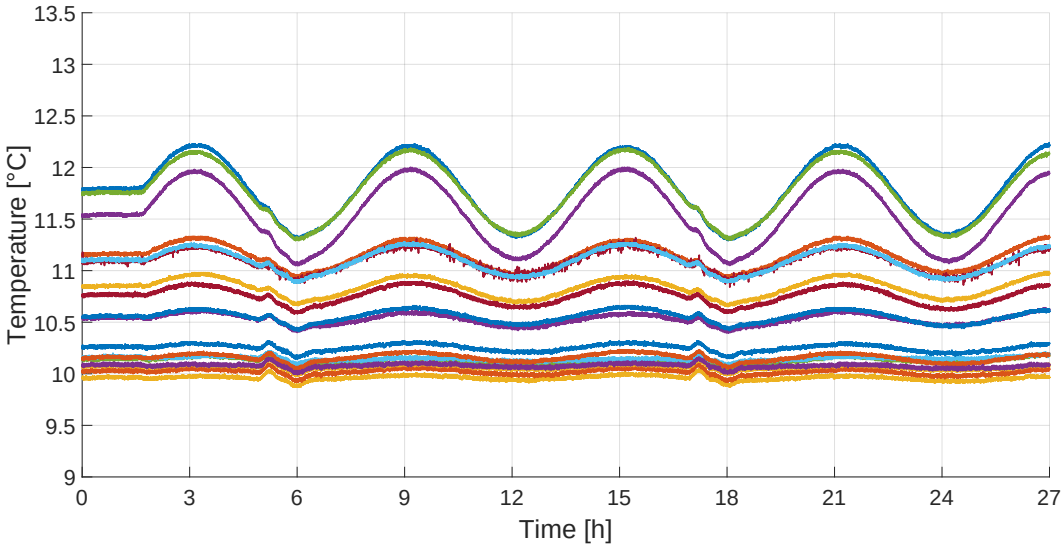

(b) Experiment

Figure 4.18 Controlled case 2 with $\sigma_S = 0.10\,\mathrm{K}$ and $\sigma_H = 0.02\,\mathrm{W}$: Temperature sensor plot, sinusoidal perturbation, configuration 2

For the controlled case, the system parameters of $\sigma_S = 0.10\,\mathrm{K}$ and $\sigma_H = 0.02\,\mathrm{W}$ are set for the Kalman filter. Figure 4.18 compares the temperature profiles for simulation and experiment. Even the simulation of temperature measurements clearly demonstrates the extent of temperature fluctuation damping. For the average temperature, it is 0.08 K, representing an improvement of nearly a factor of 20 compared to the uncontrolled case. However, as observed in the experiments with configuration 1, this damping is significantly lower in the experiment. The fluctuations in the average temperature remain at 0.32 K, which still signifies a more than fourfold improvement. The slight fluctuations in the temperature sensor profiles, especially at a time of 6 h and 18 h in this plot, are due to fluctuations in the PCU. These periodically occurring

fluctuations and irregularities in the radiation background influence temperature measurement and thus also affect the command of the control heating power. The reason for the lower temperature damping lies in the lower control heating power used in the experiment compared to the simulation. As Figure 4.19 shows, the sum of these values in the experiment is only 0.48 W instead of 0.86 W as in the simulation. Furthermore, the qualitative trends are very similar and exhibit the previously described peculiarities due to the malfunctions in the PCU. But, this shows, that the controller reacts to those fluctuations, attempting to compensate for the changing environmental conditions. As with configuration 1, the difference between the simulated and actually commanded control heating power for the sinusoidal perturbation is pronounced.

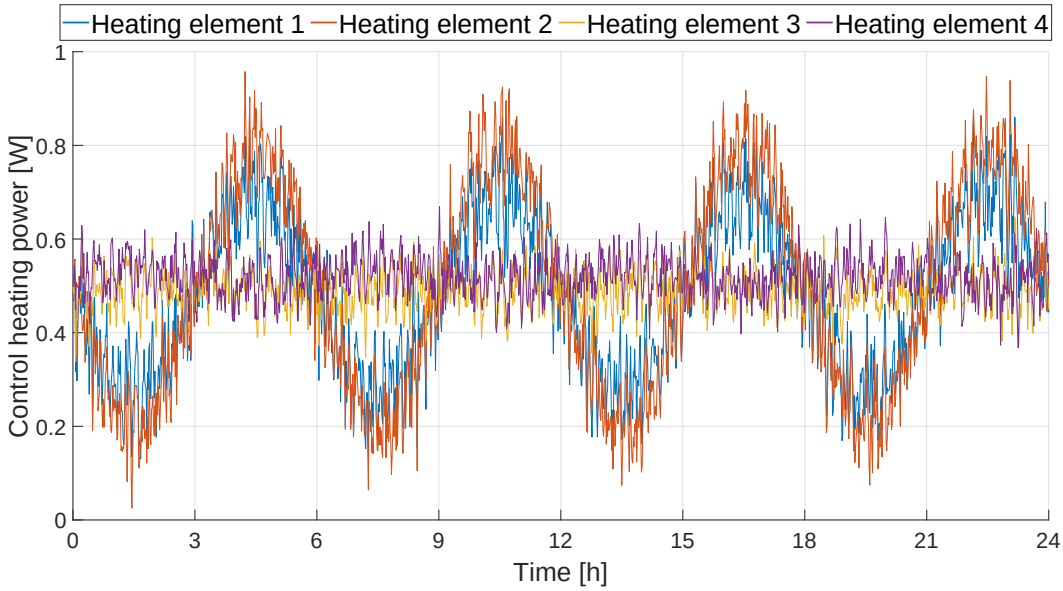

(a) Simulation

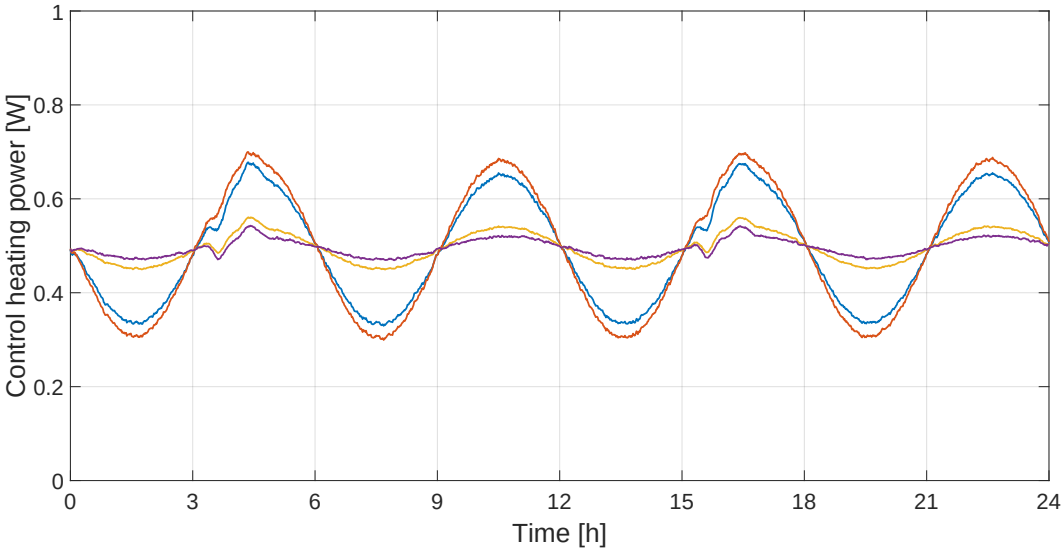

(b) Experiment

Figure 4.19 Controlled case 2 with $\sigma_S = 0.10\,\mathrm{K}$ and $\sigma_H = 0.02\,\mathrm{W}$: Control heating power, sinusoidal perturbation, configuration 2

Even though the simulation suggests an improvement in displacement by a factor of 9 to 15, this is not achievable in this experiment with this configuration as well. The displacement increases linearly in magnitude in all spatial directions up to 18 h after the start of the test before decreasing again. It is worth noting that sinusoidal fluctuations are no longer visible. Nevertheless, these trends, which are independent of the perturbation, represent an unexpected and challenging error. Once again, the total displacement is not shown here. While in the simulation a displacement of ±4 µm is reached in the x direction in the uncontrolled case, the value range for this displacement in the controlled case in the experiment is still 5 µm. The displacement in the y direction is also still very high at almost 2.5 µm in the experiment. Considering the entire duration of the experiment, improvements in the displacements of only a factor of approximately 1.5 are achieved.

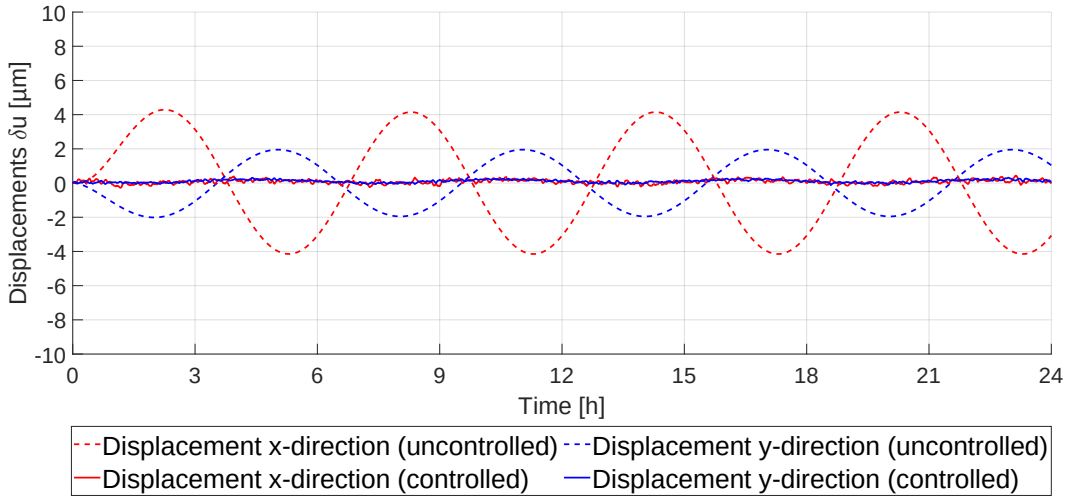

(a) Simulation

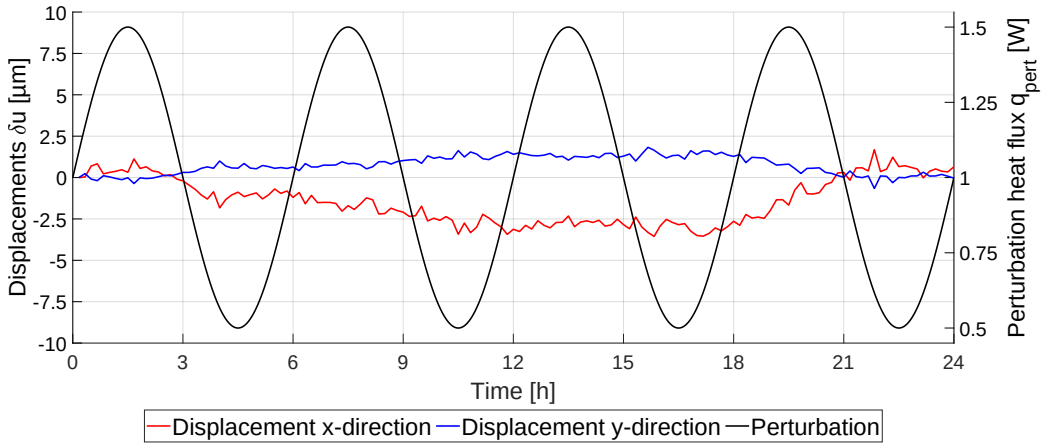

(b) Experiment

Figure 4.20 Controlled case 2 with $\sigma_S = 0.10\,\mathrm{K}$ and $\sigma_H = 0.02\,\mathrm{W}$: Displacement plot, sinusoidal perturbation, configuration 2

Interim Conclusion and Results

Table 4.7 compares the values of all discussed parameters for simulation and experiment in this controlled case to the uncontrolled reference case 1.

Table 4.7 Comparison uncontrolled case 1 and controlled case 2 with $\sigma_S = 0.10\,\mathrm{K}$ and $\sigma_H = 0.02\,\mathrm{W}$ for a sinusoidal perturbation, configuration 2

Value	**Case 1**		**Case 2**		**Factor**	
	Sim.	**Exp.**	**Sim.**	**Exp.**	**Sim.**	**Exp.**
u_x	8.44 µm	7.61 µm	0.73 µm	5.24 µm	11.56	**1.45**
u_y	3.96 µm	3.61 µm	0.41 µm	2.49 µm	9.66	**1.45**
$\Delta\bar{T}$	1.55 K	1.44 K	0.08 K	0.32 K	19.38	**4.5**
ΣQ_c			0.86 W	0.48 W		

The improvement in the positioning of sensors and actuators did not result in a significant enhancement of the displacements for the sinusoidal perturbation in the experiment, but in the simulation. However, this nearly equivalent performance is nevertheless accompanied by a reduction in the required control heating power by 50 % to 60 % compared to configuration 1. It can therefore be assumed that this saving is due to the optimization of the positions of the HEs. Furthermore, it must be noted that the optimization steps of the positioning of sensors and actuators took place under the influence of the random perturbation, which is explained in the following section. This randomly generated perturbation has a higher amplitude, which has a direct influence on the positioning of the HEs. The base frequency of the perturbation influences the weighting of the thermal modes and thus the selection of the sensor positions. However, the base frequency of the random perturbation is the same as for the sinusoidal perturbation. Only the final selection of the sensor positions, for which the technical feasibility is also evaluated, took place in the simulations on the basis of this random perturbation. This could be an explanation for the fact that the actual simulated values of the control heating powers are not commanded, as the sensor measurements were not carried out at the ideal positions for this perturbation.

The experiments with this setup have also been conducted for other system parameters. However, a very similar result has consistently been observed. The improvements in temperature stability were clearly visible, with simulations showing improvements by a factor of up to 20, depending on the selected parameters, while in experiments, a factor of almost 5 could be achieved. However, in all experiments, the displacement only improved slightly by a factor of approximately 1.5, reaching nearly the same level as in the first configuration. A slight linear drift can be observed in the measurements of the displacements in most of the experiments, but the sinusoidal profile of the perturbation is no longer visible in the plots. Whether this behavior can be explained by

the measurement accuracy of the DIC system, such as fluctuations in laboratory temperature due to day-night cycles, or by the friction of the isostatic mounting, cannot be conclusively determined. Many experiments have been conducted in the summer months, where the temperature fluctuated significantly between day and night in the laboratory. Some of the linear changes observed in displacement measurements correspond to the day-night cycles the camera system was exposed to. This may have had an impact on the optics or the stability of the camera tripod. An indicator that this behavior of the displacements can be attributed to an error in the measurement is the fact, that mostly no abnormal temperature fluctuations or control heater activations occurred during these time periods. However, since there is no air conditioning available in the laboratory to prevent these temperature fluctuations, and the experiments typically run for several days, a comparison measurement under different environmental conditions was not possible and feasable. Thus, a validation of this theory cannot be provided. Doubling the period duration of the perturbation to 12 h to increase the reversibility of the temperature change has also shown no differences in other experiments, which is why these cases are not further presented here.

Nevertheless, it can be concluded that optimizing the positions of sensors and actuators due to the reduction in control heating power still has a demonstrable and measurable positive effect.

4.3.2.2 Random Perturbation

In the following three cases, the behavior of the system exposed to a random perturbation is demonstrated. This perturbation now spans a duration of 48 h and consists of 5 sinusoidal perturbations with random phase, amplitude, and frequency. The sum of these individual perturbations is then normalized to a range of 0 W to 2 W, so that the perturbation has a maximum amplitude of 1 W around the steady-state condition, in which the perturbation HE operates at 1 W, and the four control heating elements each operate at 0.5 W. Due to the higher amplitude in the perturbation, higher temperatures are expected compared to the sinusoidal perturbation shown in the previous cases. Case 1 represents the uncontrolled reference state for this random perturbation.

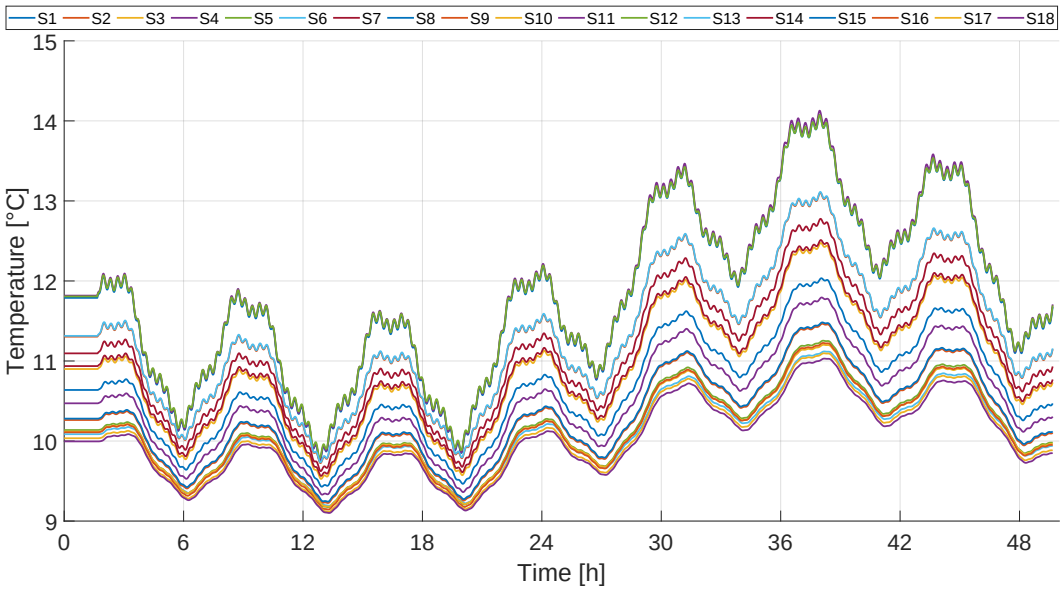

(a) Simulation

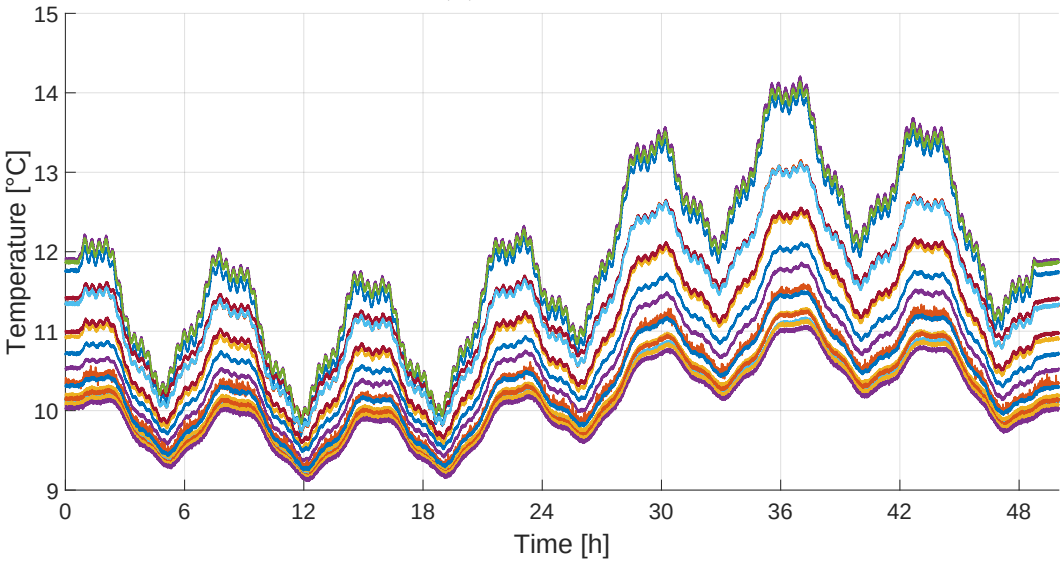

(b) Experiment

Figure 4.21 Uncontrolled case: Temperature sensor plot, random perturbation, configuration 2

Figure 4.21 depicts the temperature profiles in simulation and experiment. Again, it is evident that the profiles are very similar, demonstrating a strong correspondence between the model and the experimental setup. In this case, the range of uncontrolled temperatures is significantly larger, reflecting the broader range of perturbation heating power. The temperatures span from 9 °C to 14 °C, with the range of the average temperature being 2.76 K in the simulation and 2.79 K in the experiment.

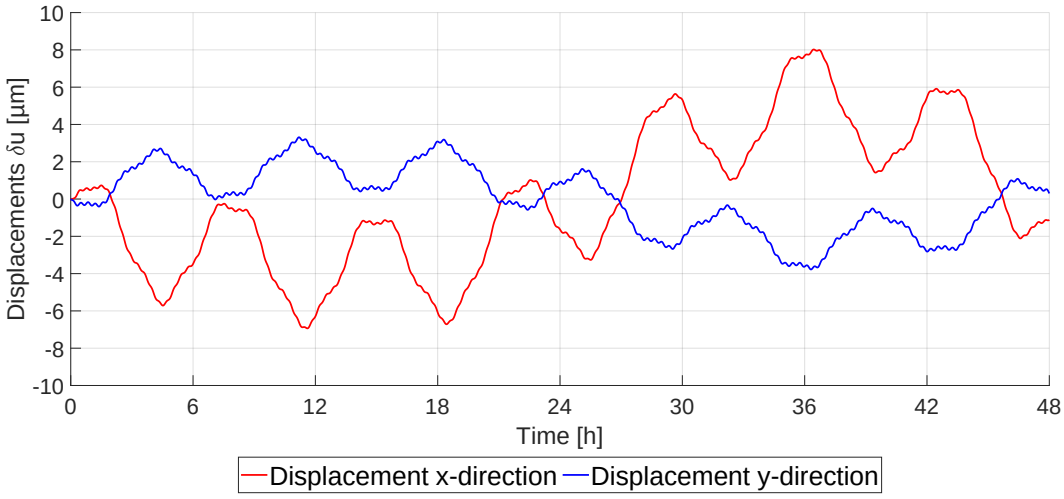

(a) Simulation

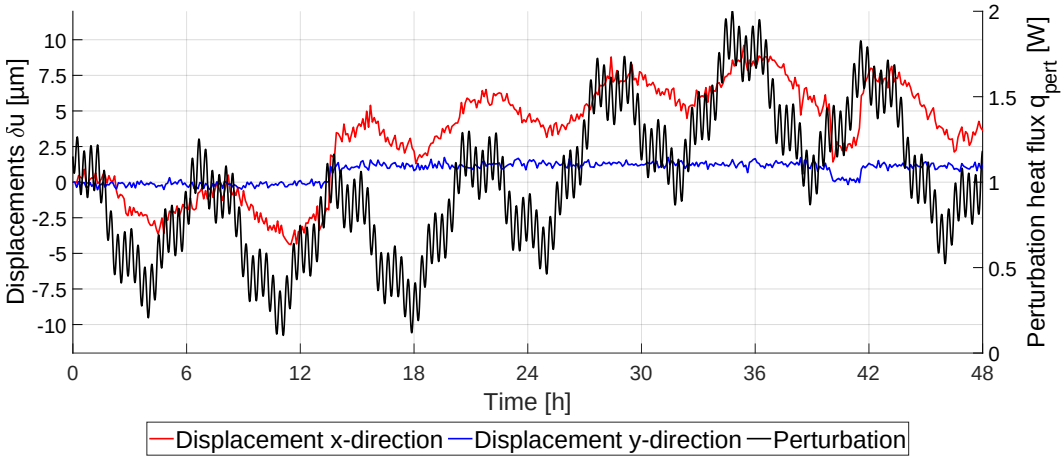

(b) Experiment

Figure 4.22 Uncontrolled case: Displacement plot, random perturbation, configuration 2

Figure 4.22 shows the displacements between the two points to be controlled. It is evident that the displacements in x-direction are more than 2 times larger in magnitude than those in y-direction in the simulation, as expected due to the geometry of the structure. The displacements clearly follow the perturbation. This results in a maximum range of 14.96 µm and 7.09 µm for displacements in the x and y directions, respectively. In the experiment, the perturbation can also be observed in the x-direction. Unfortunately, this visibility of the perturbation is entirely lost in the y-direction displacement, which shows again the limited resolution of the camera system. At approximately 13 h, 40 h, and 42 h after the start of the test, there is a jump in these displacements, which could support the theory of friction in the spherical bearings of the isostatic mount, already previously mentioned in the cases of the sinusoidal perturbation. No temperature jumps occur at these points, making it difficult to identify practically relevant causes for this behavior. Therefore, aside from measurement errors, the most probable explanation is a flawed experimental setup. Particularly, the

jump that occurs around 13 h leads to a disproportionately large increase in x-direction displacement. A permanent shift in the course of the displacement is created, so the oscillations no longer occur around the zero line. Unlike in previous experiments, this shift is not linear. This observation reinforces the theory of an erroneous mounting. The individual sinusoidal fluctuations, which had an amplitude of 4 µm to 6 µm in the uncontrolled case, are strongly attenuated in the experiment, but can still be easily recognized apart from the described times with faulty jumps. As with previous experiments, however, after correcting for drift or jumps, the displacement in the x-direction show a reduced amplitude in the experiment. When comparing the range of the displacement, 13.99 µm for x-direction are well in line with the simulation. The measured value for the displacement in y-direction is 2.28 µm.

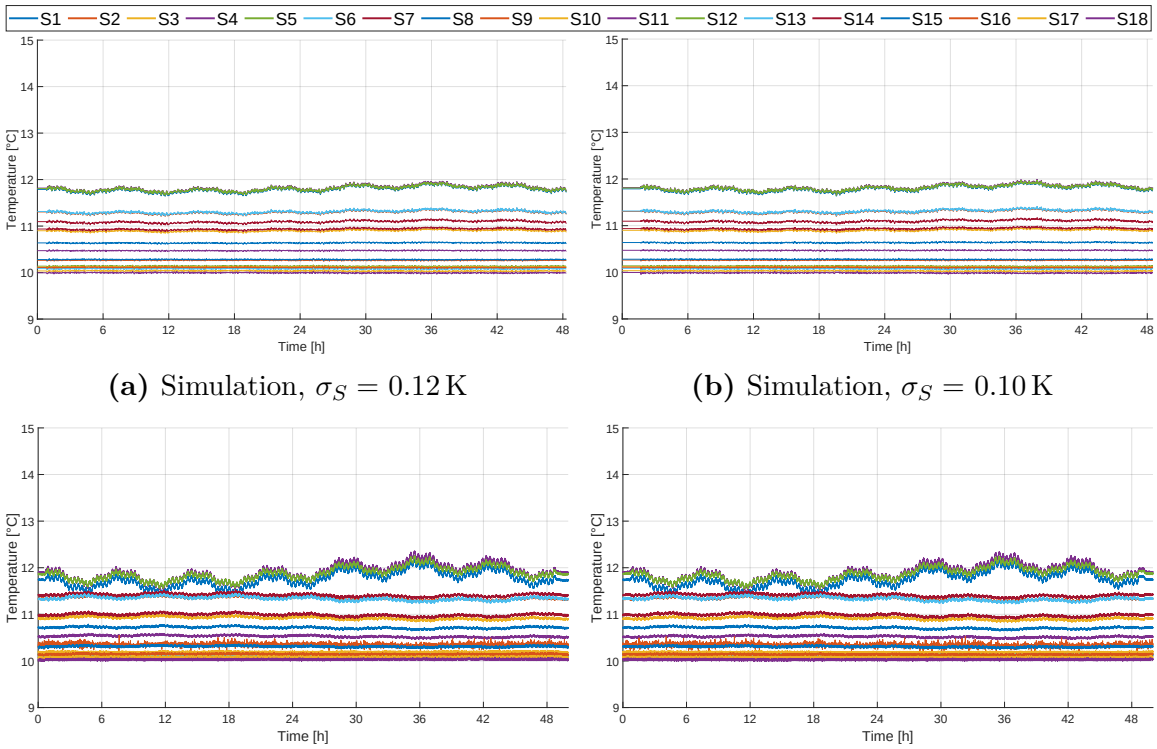

(a) Simulation, $\sigma_S = 0.12\,\mathrm{K}$ **(b)** Simulation, $\sigma_S = 0.10\,\mathrm{K}$

(c) Experiment, $\sigma_S = 0.12\,\mathrm{K}$ **(d)** Experiment, $\sigma_S = 0.10\,\mathrm{K}$

Figure 4.23 Temperature sensor plots, comparison simulation and experiment, controlled cases 2 and 3, random perturbation, configuration 2

Since the best results for the sinusoidal perturbation were achieved for standard deviations of $\sigma_S = 0.12\,\mathrm{K}$ and $\sigma_S = 0.10\,\mathrm{K}$, the evaluation of the random perturbation also focuses on these two cases. The temperature curves are very similar in both cases and almost correspond to the simulated curves. They are therefore shown together in Figure 4.23. Only in the experiment, the sensor values of S1, S11, and S12, which are located at the far-left area of the plate close to the perturbation element, fluctuate slightly more and reveal the course of the random perturbation. All other sensor measurements are very well damped in the experiment as well. In general, it can already be observed that this damping is significantly stronger than in previous experiments with

the sinusoidal perturbation. The maximum temperature fluctuation range is 0.10 K in the simulation and 0.09 K to 0.10 K in the experiment, even though the perturbation profiles are more pronounced in the experiment. Due to averaging, the slightly worse curves in the experiment are compensated for. The improvements, by a factor of 30 compared to the uncontrolled reference state, are significantly greater than in previous experiments.

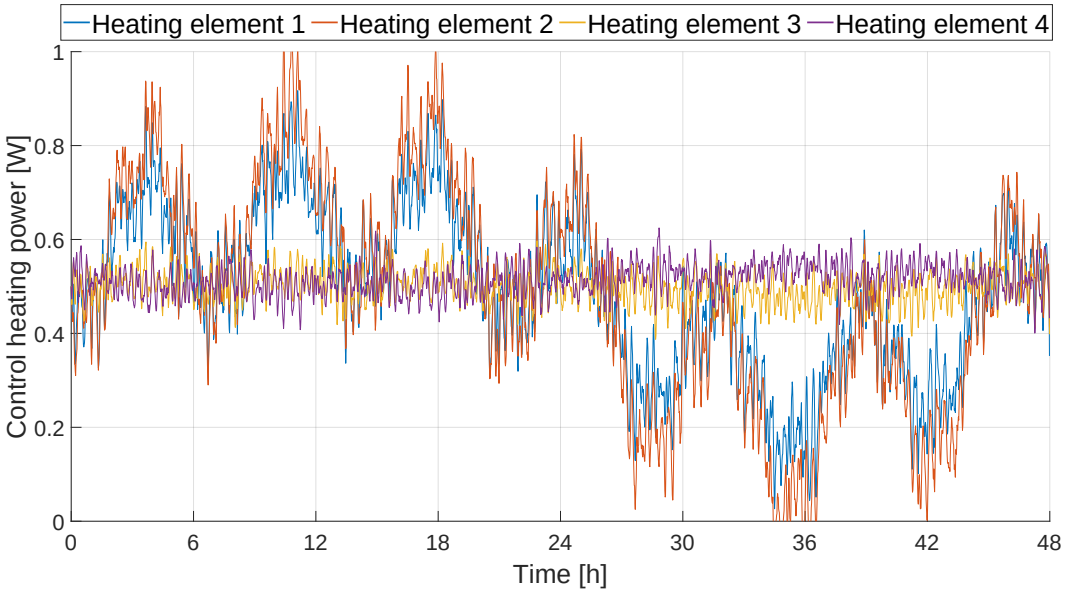

(a) Simulation

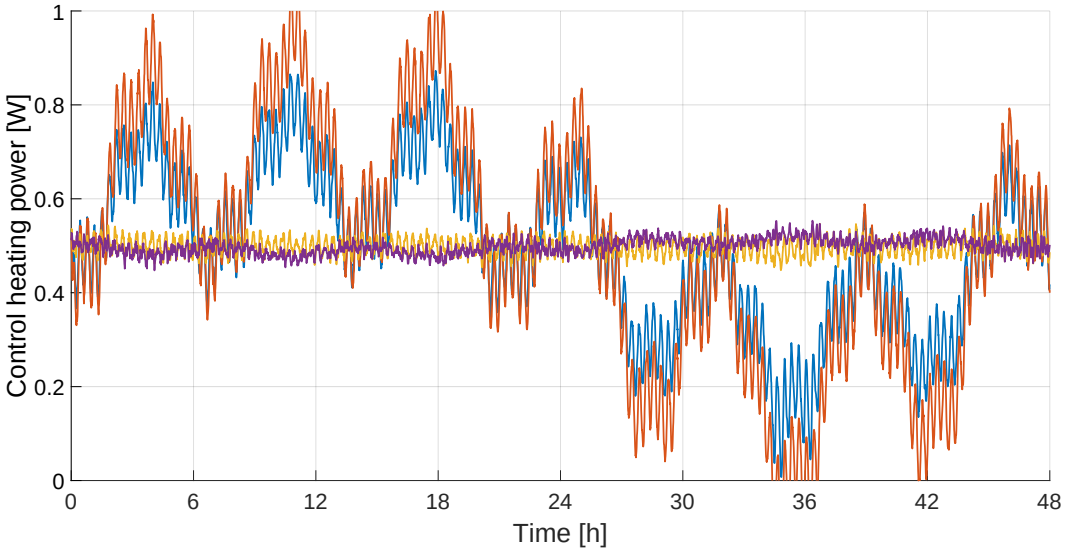

(b) Experiment

Figure 4.24 Controlled case 2 with $\sigma_S = 0.12\,\mathrm{K}$ and $\sigma_H = 0.02\,\mathrm{W}$: Control heating power, random perturbation, configuration 2

When examining the control heating power in Figure 4.24, the consistency between the experiment and simulation is confirmed. Here, the profiles are almost identical, and the value ranges are very close, with 1.20 W in the simulation and 1.23 W in the experiment. In the simulation, a few values for HE 2 are outside the allowable range of ± 0.5 W. This was assessed as non-critical in the simulation because in previous experiments, the range was not fully utilized in the experiment. Due to averaging when commanding a new control input every 30 s in the experiment, those peaks outside the allowable range are mostly smoothed out. The revision and improvement of the positions of sensors and actuators appear to have ensured that the simulated values are indeed executed as commanded for this random perturbation. The system seems to react more as expected for a random perturbation than for a sinusoidal perturbation. It is also interesting to note that HEs 3 and 4 appear to have a minimal effect on stabilization and are almost unnecessary for these points to be controlled in this configuration. However, they must still be present for the solvability of the linearized system of differential equations of the filter and controller approach. Since the course of the control heating power for case 3 with $\sigma_S = 0.10$ K is almost identical, the corresponding comparison can be found in Figure C.3 in Appendix C.

The resulting displacements for the controlled case 2 with $\sigma_S = 0.12$ K and $\sigma_H = 0.02$ W are presented in Figure 4.25. According to the simulation, the framework improves the displacements by factors of 11 to 13, depending on the spatial direction, reducing them to a value of around 1 µm. Substantial improvement is also achieved in the experiment. The perturbation is no longer discernible in the displacement, which is at approximately 3 µm for the x-direction, nearly four times better than in the uncontrolled case. Even in the y-direction an improvement of factor 2 can be reached. These results represent the best improvements achieved so far and once again demonstrate that the approach functions effectively despite the basic setup.

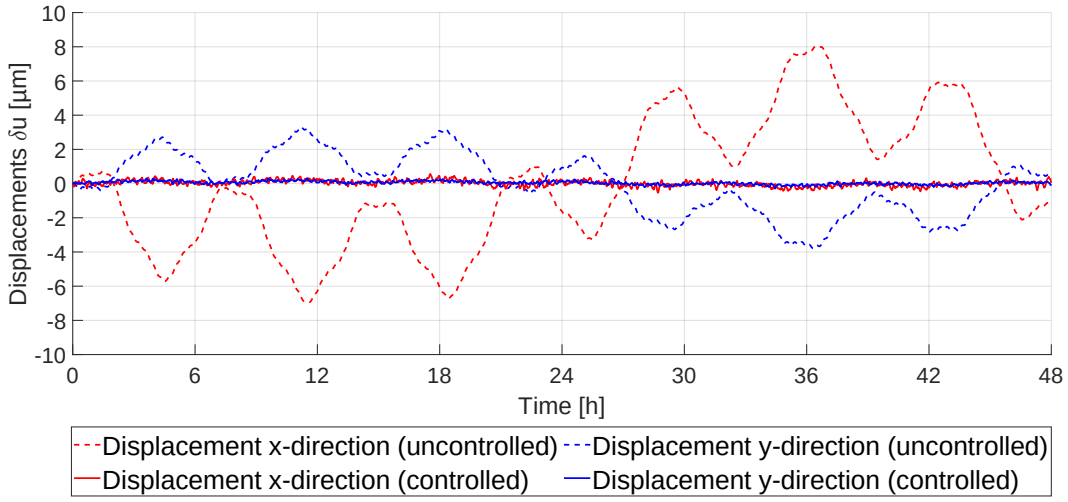

(a) Simulation

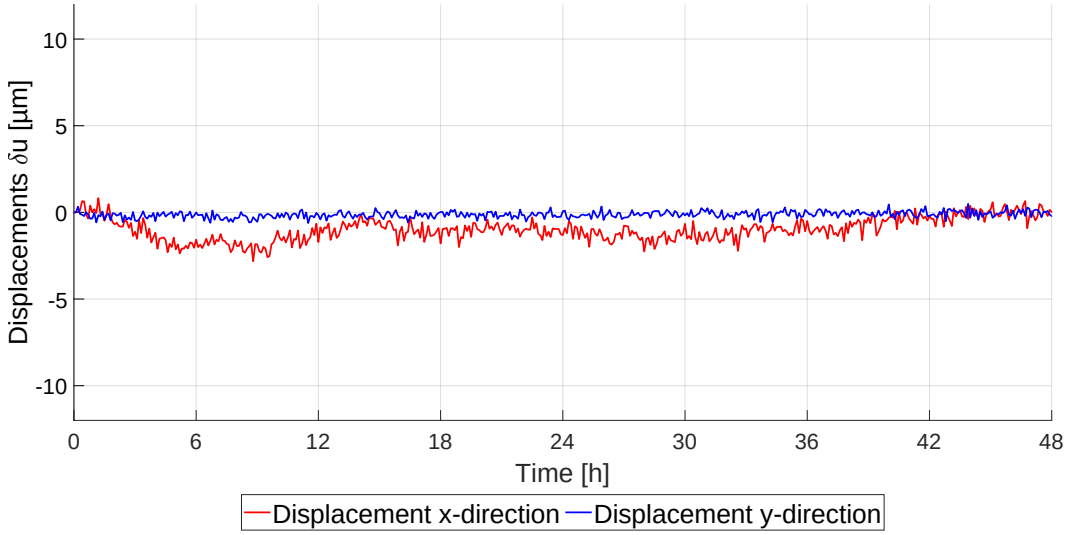

(b) Experiment

Figure 4.25 Controlled case 2 with $\sigma_S = 0.12\,\mathrm{K}$ and $\sigma_H = 0.02\,\mathrm{W}$: Displacement plot, random perturbation, configuration 2

The displacements for the controlled case 3 with $\sigma_S = 0.10\,\mathrm{K}$ and $\sigma_H = 0.02\,\mathrm{W}$ are shown in Figure 4.26. In the simulation, these displacements are improved to below 1 µm, which is slightly better than in the other presented controlled case, resulting in factors of approximately 12 to 16, depending on the spatial direction. In the experiment, it is immediately noticeable that there is a significant jump in displacements after approximately 22 h of runtime. Since there is no temperature jump, no significantly abnormal behavior in the control heating power at that time and the displacements before and after this jump remain at a nearly constant level, it can be assumed that this is caused by an error in the data acquisition or due to the experimental setup. When considering the entire duration of the experiment, due to this jump, there are only improvements of approximately a factor of 2. However, when examining the two subperiods in which the displacements are very stable and only slightly fluctuate separately, significantly higher improvements of a factor of 6 or even 7 are achieved.

This demonstrates that without this obvious measurement error, the approach, even in the experimental implementation, has the most significant effect for these system parameters. While temperature and control heating power are almost identical in the controlled cases 2 and 3, the resulting displacements in the simulation and in the experiment are more significantly reduced for this controlled case using the system parameters $\sigma_S = 0.10\,\mathrm{K}$ and $\sigma_H = 0.02\,\mathrm{W}$.

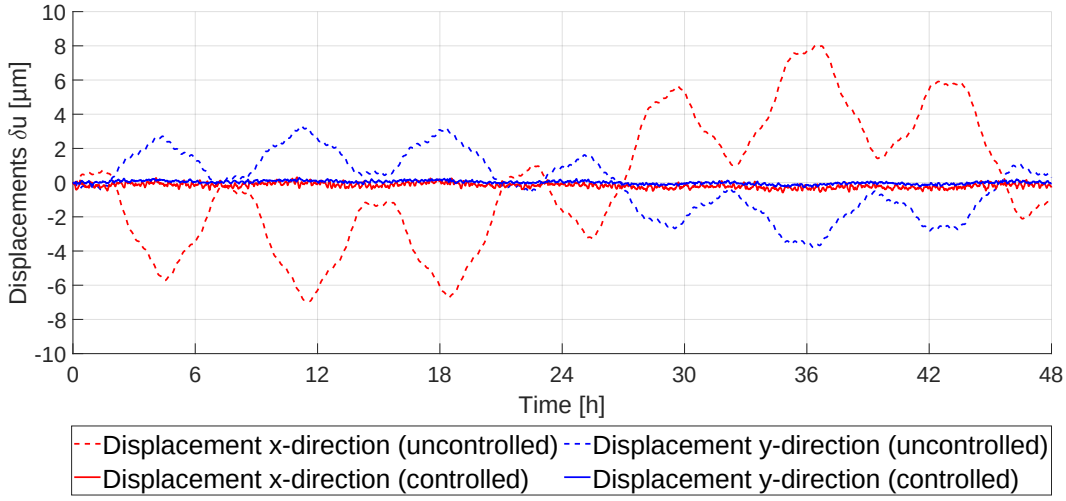

(a) Simulation

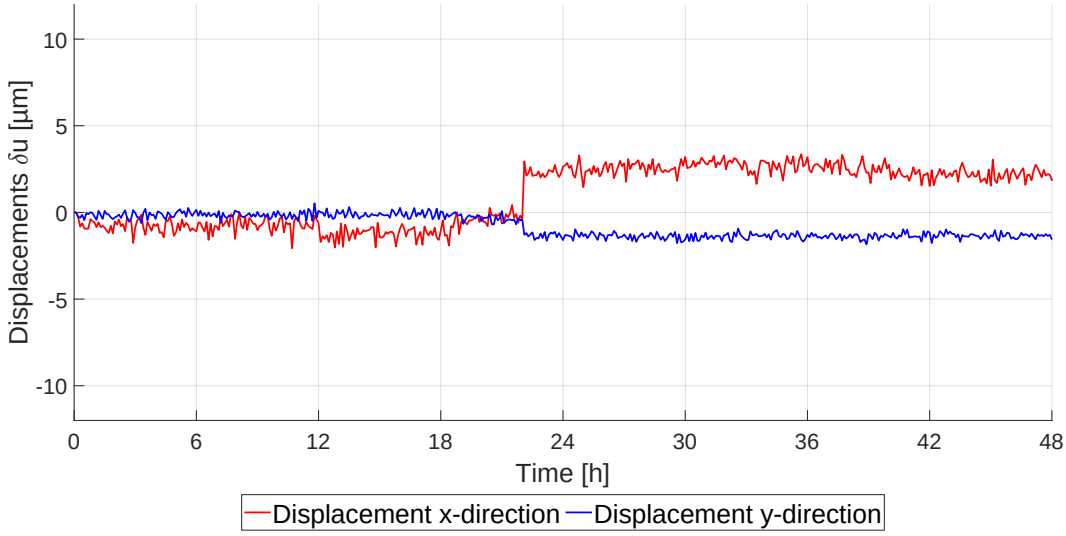

(b) Experiment

Figure 4.26 Controlled case 3 with $\sigma_S = 0.10\,\mathrm{K}$ and $\sigma_H = 0.02\,\mathrm{W}$: Displacement plot, random perturbation, configuration 2

4.3.2.3 Stepped Perturbation

In the following section, the results of an experimental series with a stepped perturbation are presented. This is intended to demonstrate that even a sudden and constant difference in perturbation heating power, which can be caused, for example, by energy dissipation from switching on or off an electric device producing lost heat, can be adequately compensated for by the filter and controller framework. The uncontrolled case

1 serves as the reference state for the two subsequent experiments with active control, using the system parameters previously employed in the other tests.

Figure 4.27 illustrates the temperature profiles for the uncontrolled case. It is immediately apparent that simulation and experiment are nearly identical within the range affected by the perturbation. The slight deviations in the individual sensor measurements in the experiment compared to the model can also be explained here by assuming a symmetrical test setup, which is not present in reality. The maximum range of fluctuation in the mean temperature in both simulation and experiment is 1.88 K.

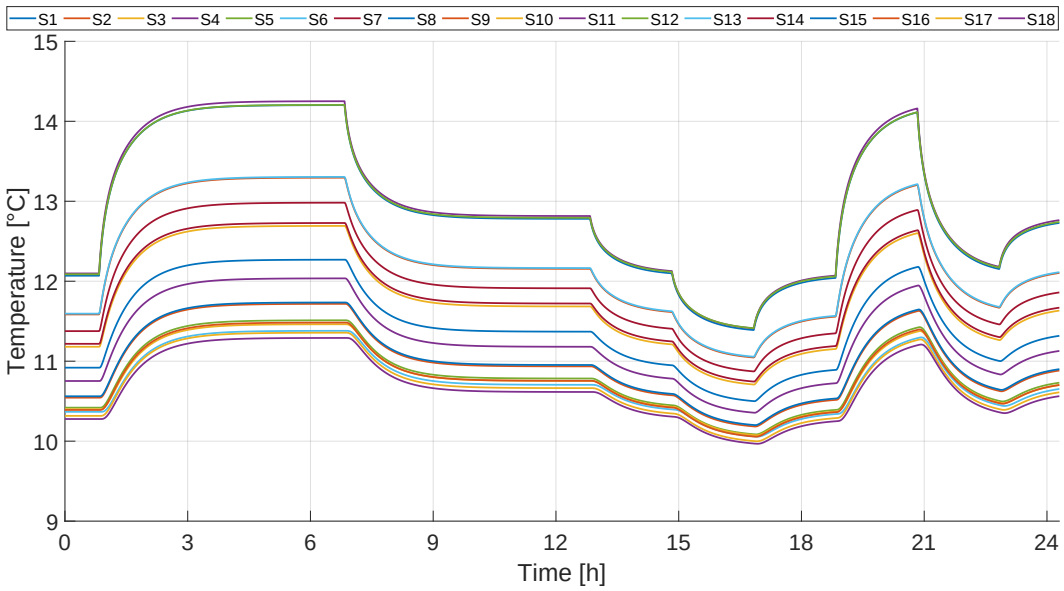

(a) Simulation

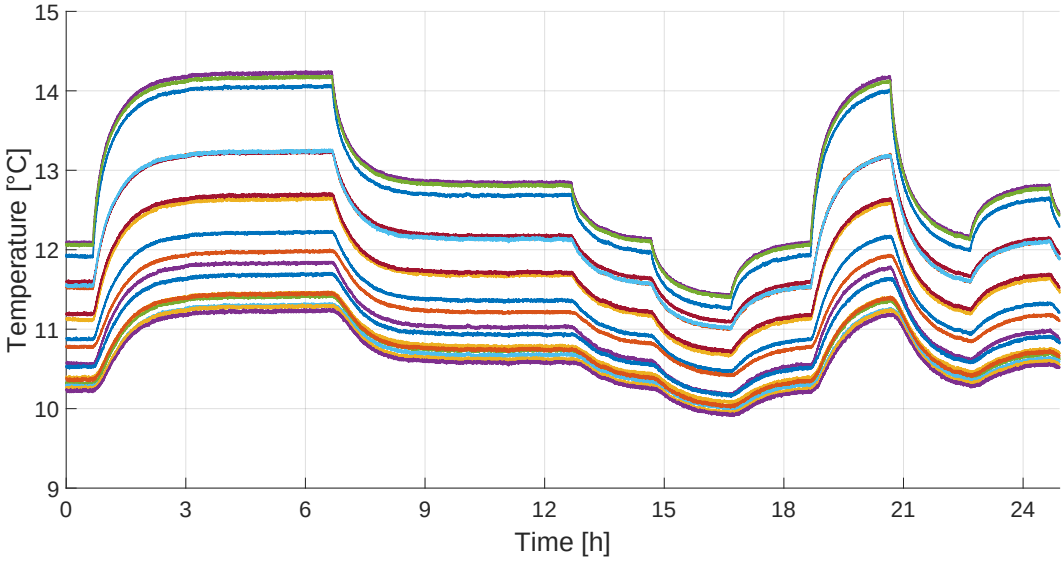

(b) Experiment

Figure 4.27 Uncontrolled case: Temperature sensor plot, stepped perturbation, configuration 2

Figure 4.28 displays the displacement trends in both simulation and experiment. The uncontrolled displacement between the two points reaches a maximum range of 10.29 µm in the x-direction and 4.72 µm in the y-direction. The behavior of the perturbation can be effectively traced in the patterns of the uncontrolled displacement in the model, particularly the transient response. Magnitude-wise, the displacement in the x-direction is approximately twice as large as that in the y-direction. This is in accordance with the roughly doubled distance in this direction due to isotropic heat source induced uniform deformation.

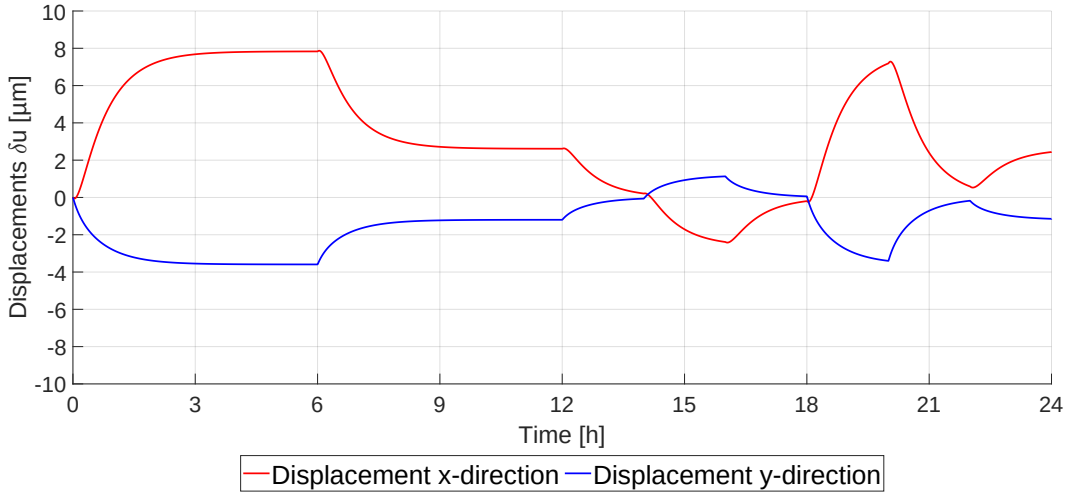

(a) Simulation

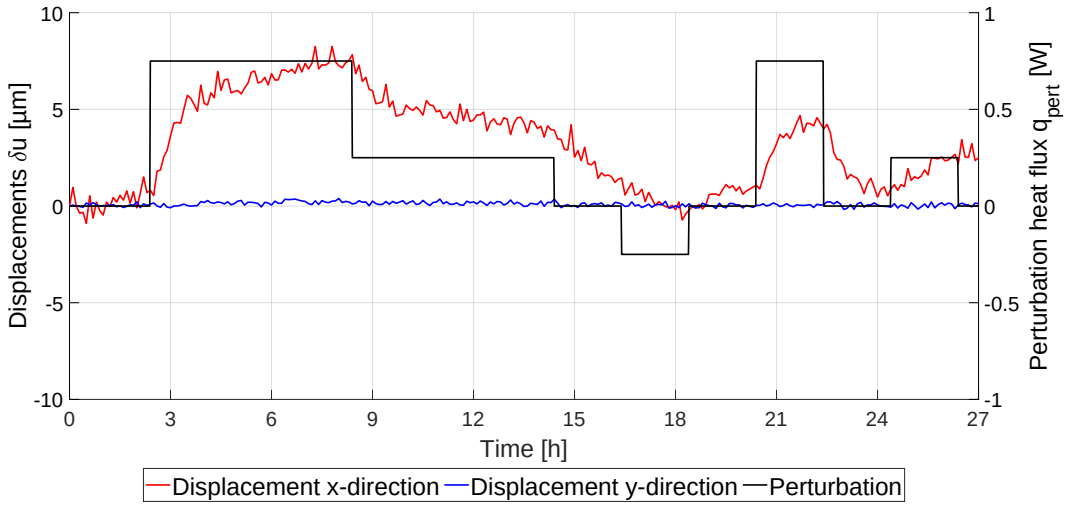

(b) Experiment

Figure 4.28 Uncontrolled case: Displacement plot, stepped perturbation, configuration 2

In Figure 4.28b, the initial steady-state condition is also visible in the experimental displacement, which is why the duration of the test is slightly longer than displayed in the simulation. During these additional 3 h runtime in the beginning, all values in all spatial directions fluctuate only minimally within the measurement noise and the DIC system's resolution. The displacement in the x direction increases as soon as the

perturbation takes effect, reaching its maxima roughly around the same time as predicted in the model. Afterward, the perturbation diminishes, and the displacements decrease again, albeit less abruptly and more slowly compared to the simulation. This could also be attributed to friction caused by the isostatic mounting in this case. The range in which the perturbation is below the steady-state power level in the experiment does not lead to a significant negative displacement in the x direction. This, too, can be explained by the lack of reversibility due to the isostatic mount. Otherwise, the displacement trends in the x direction closely resemble the simulation. The range of values for the displacement in the x direction is 9.14 µm, only slightly below the simulation's value. The displacements in the y direction on the other hand, as observed in previous experiments, are barely discernible in this case with a value range of 0.57 µm and remain nearly unchanged throughout the entire experiment within the measurement noise. Therefore, no conclusions about stabilization in this spatial direction can be drawn and no improvement is expected for the controlled cases.

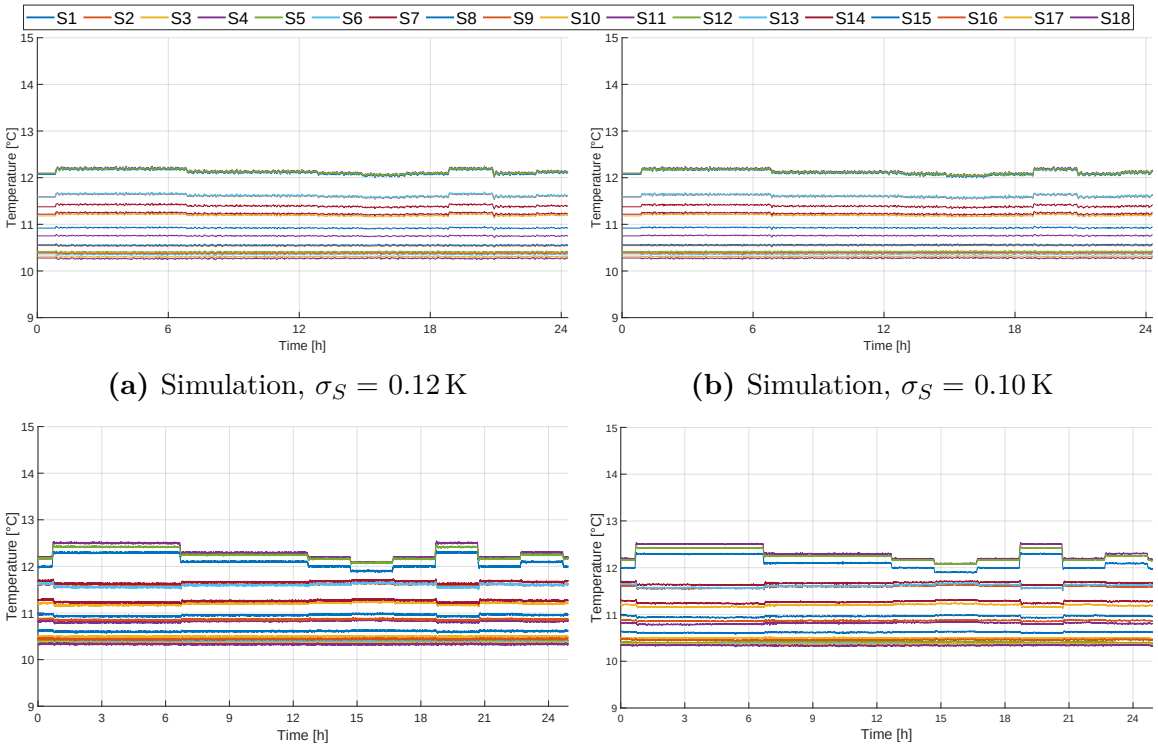

(a) Simulation, $\sigma_S = 0.12\,\mathrm{K}$ **(b)** Simulation, $\sigma_S = 0.10\,\mathrm{K}$

(c) Experiment, $\sigma_S = 0.12\,\mathrm{K}$ **(d)** Experiment, $\sigma_S = 0.10\,\mathrm{K}$

Figure 4.29 Temperature sensor plots, comparison simulation and experiment, controlled cases 2 and 3, stepped perturbation, configuration 2

Figure 4.29 shows the comparison of simulated and experimentally determined temperatures for the two controlled cases. Both, the simulations and the experiments, are almost identical in each case without any major difference. In the simulated temperature profile in Figures 4.29a and 4.29b, the damping is highly pronounced, to the extent that the stepped perturbation is barely discernible. In the corresponding experiment,

this perturbation is somewhat more pronounced, but still significantly attenuated compared to the uncontrolled case. The fluctuation in the average temperature are between 0.08 K in the simulation and 0.10 K in the experiment, which is approximately 20 times better than in the uncontrolled case in both instances.

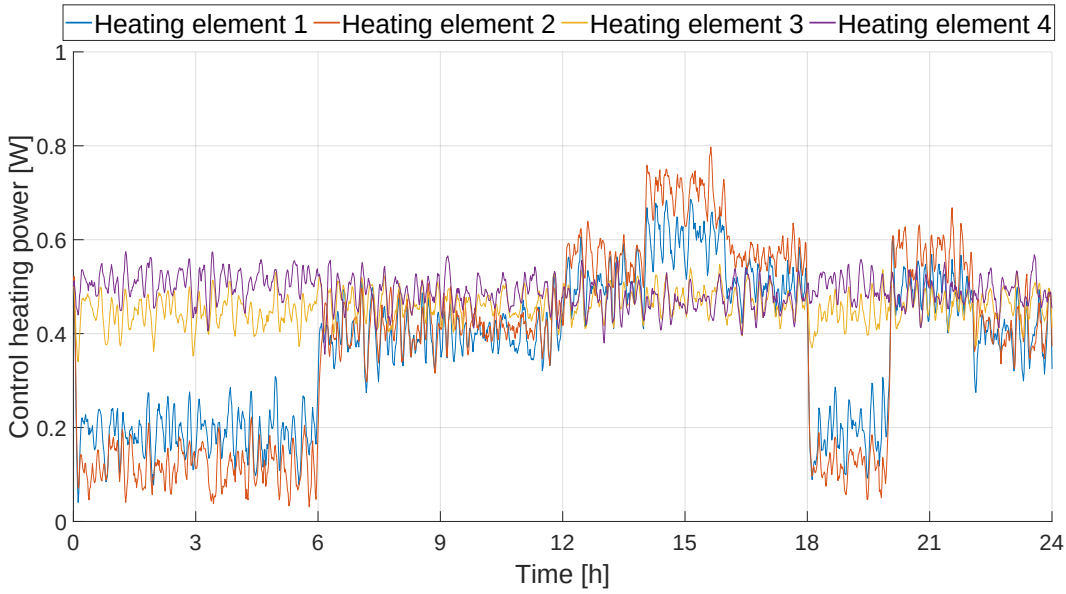

(a) Simulation

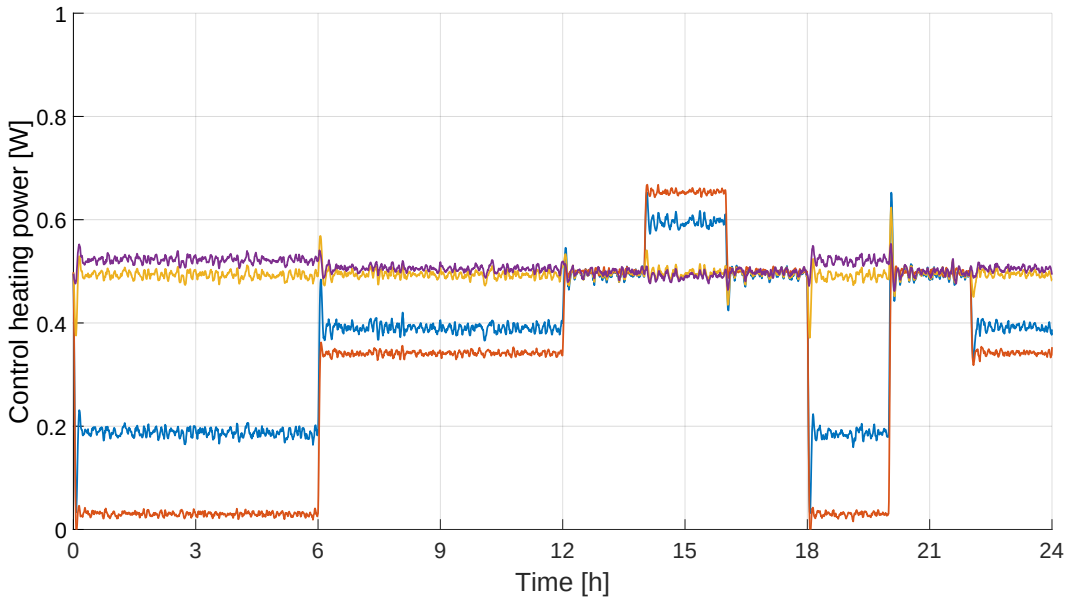

(b) Experiment

Figure 4.30 Controlled case 2 with $\sigma_S = 0.12\,\mathrm{K}$ and $\sigma_H = 0.02\,\mathrm{W}$: Control heating power, stepped perturbation, configuration 2

The control heating profiles also distinctly reveal the perturbation's influence, as seen in Figure 4.30, exemplary for controlled case 2 with $\sigma_S = 0.12\,\mathrm{K}$. Here as well, the contributions of HEs 3 and 4 are relatively small compared to the other two elements. While the heating profiles in the simulation exhibit more noise, in the experiment,

they are notably more uniform but at the same level. When examining the range of the summed control heating powers, both cases are at 1.11 W. This indicates that the improved positioning of sensors and actuators leads to a significantly better utilization of the available control heating power and these values are highly comparable. It is also interesting to note that the strong gradient in the temperature measurement of the sensors closest to the perturbation heating source leads to an immediate response, with the heating elements being commanded to operate at a significantly different level within a few steps, effectively within a few minutes. The system reacts very dynamically to rapid changes, with only minor overshoots occurring. The behavior of the HEs in the other controlled case is identical and can be found Figure C.4 in Appendix C.

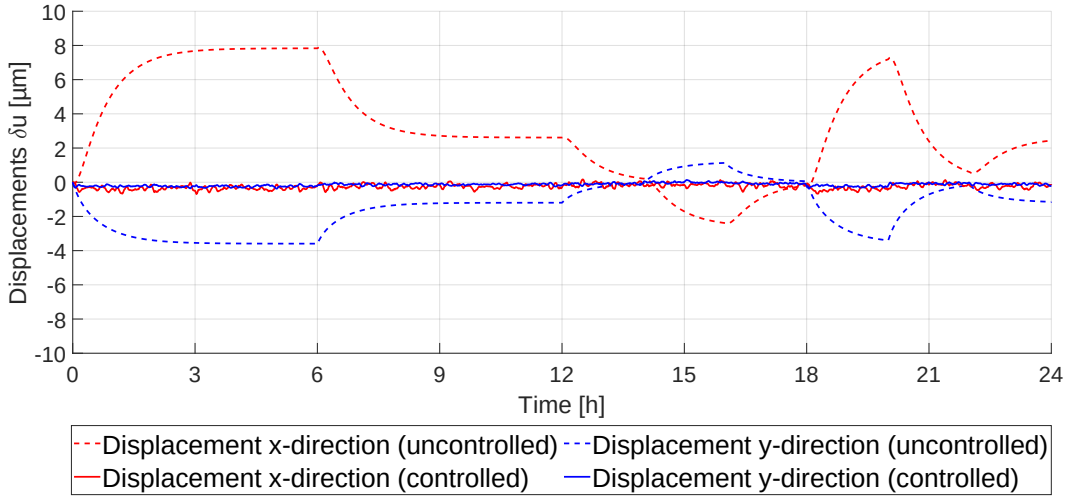

(a) Simulation

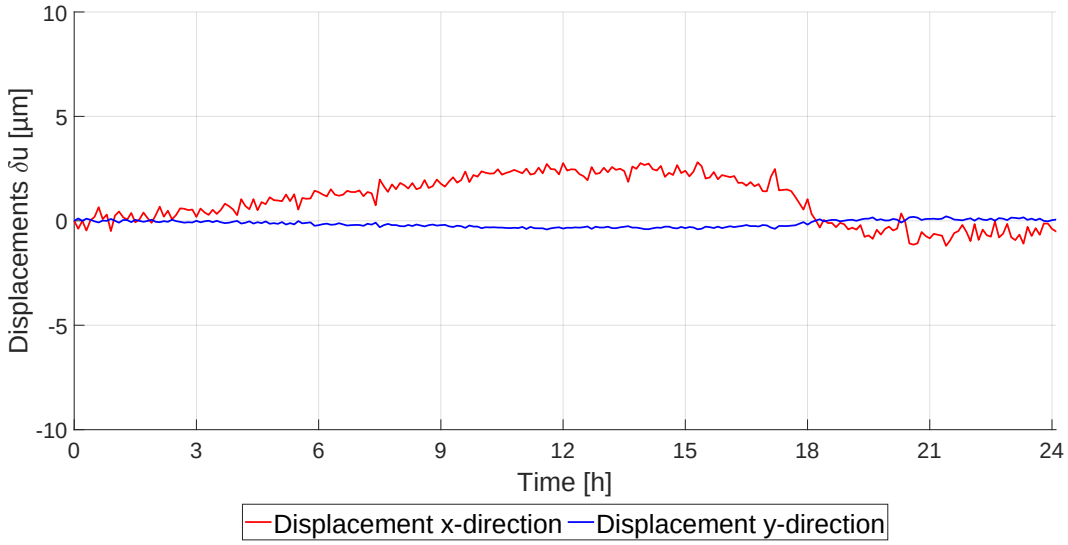

(b) Experiment

Figure 4.31 Controlled case 2 with $\sigma_S = 0.12\,\mathrm{K}$ and $\sigma_H = 0.02\,\mathrm{W}$: Displacement plot, stepped perturbation, configuration 2

The resulting displacements for controlled case 2 with $\sigma_S = 0.12\,\mathrm{K}$ are depicted in Figure 4.31. According to the simulation, the displacements in the x direction should

decrease by a factor of almost 12 to 0.87 µm, while the displacement in the y direction decreases by a factor of 9. Figure 4.31a also illustrates that all values fluctuate only slightly around the zero line. In the experiment, a significant improvement is also evident. However, it is noticeable that the displacement in the x direction gradually, but steadily, increases up to a point 15 h after the start of the experiment and then decrease again. The range of displacement in the x-direction is 4.00 µm, which is less than half the size of the uncontrolled case. Nevertheless, this linear increase is abnormal and hardly explainable, as it does not correspond to the temperature profils or the control heating power. The displacement in the y direction is near 0 and not relevant. Due to the long duration of the linear increase, the possible explanation of the temperature fluctuations occurring in the laboratory due to day-night cycle also does not appear to be appropriate. Nevertheless, control improves stability in this case as well, altaugh to a smaller amount.

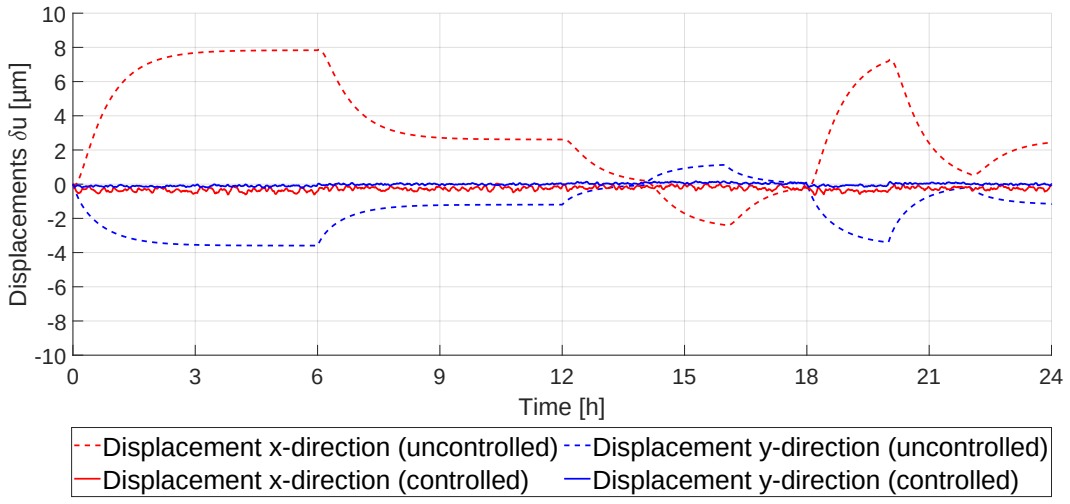

(a) Simulation

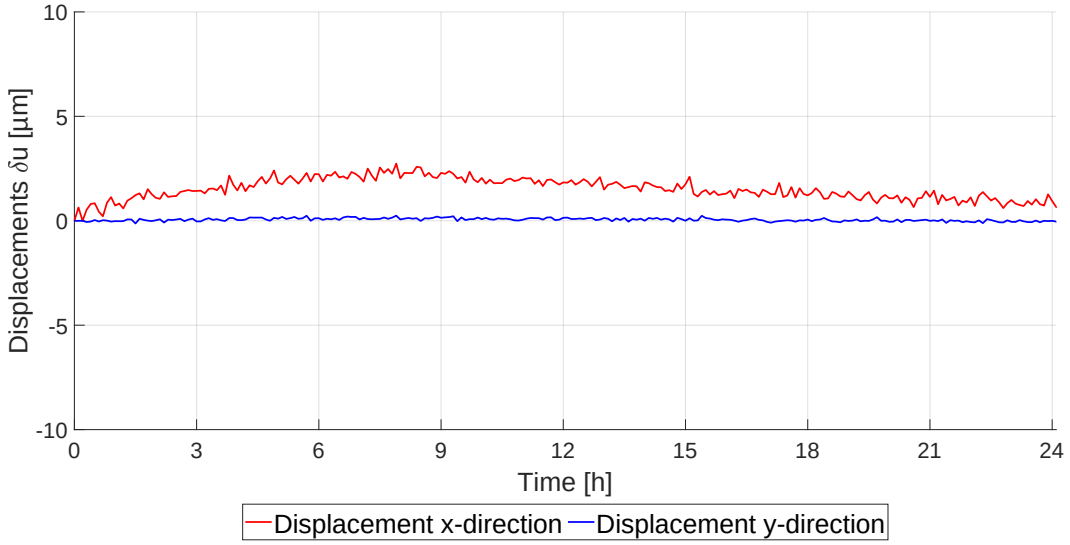

(b) Experiment

Figure 4.32 Controlled case 3 with $\sigma_S = 0.10\,\mathrm{K}$ and $\sigma_H = 0.02\,\mathrm{W}$: Displacement plot, stepped perturbation, configuration 2

Figure 4.32 depicts the results of the second controlled case regarding the displacement. The reduction of the displacements in both directions is slightly better in the simulation than in the previous case, reaching factors of around 11 to 14, respectively. In the experiment, a significant improvement is also evident, although the displacement in the x direction shows a similar linear increase compared to the previous case. However, this time, the increase aligns better with the perturbation in terms of timing, but it is significantly damped compared to the uncontrolled reference state. Once again, the displacement in the y direction is negligible and shows no improvement.

Interim Conclusion and Results

Table 4.8 summarizes the tests performed for configuration 2 with random and stepped perturbations. As before, both simulation and experiment are shown in comparison as well as the controlled cases 2 and 3 compared to the uncontrolled case 1. The factors refer to the improvement of the controlled cases compared to the uncontrolled case. For both types of perturbations, the strongest improvements are shown in the simulation in case 3 with the system parameters $\sigma_S = 0.10\,\mathrm{K}$ and $\sigma_H = 0.02\,\mathrm{W}$. The factors in the experimental validation are significantly smaller than in the simulation, but the clearest improvements are shown in case 3 as well.

Table 4.8 Comparison of uncontrolled case 1 and controlled cases 2 and 3 for random and stepped perturbation, configuration 2

		Experiment			**Simulation**		
		u_x µm	u_y µm	$\Delta\bar{T}$ K	u_x µm	u_y µm	$\Delta\bar{T}$ K
Random	**Case 1**	13.99	2.28	2.79	14.96	7.09	2.76
	Case 2	3.64	1.11	0.09	1.10	0.62	0.10
	(Factor)	**(3.84)**	**(2.05)**	**(31)**	**(13.60)**	**(11.44)**	**(27.60)**
	Case 3	5.42∗	2.37∗	0.10	0.90	0.57	0.10
	(Factor)	**(2.58)**∗	**(0.96)**∗	**(27.90)**	**(16.62)**	**(12.44)**	**(27.60)**
Stepped	**Case 1**	9.14	0.57	1.88	10.29	4.72	1.88
	Case 2	4.00	0.63	0.10	0.87	0.51	0.08
	(Factor)	**(2.29)**	**(0.90)**	**(18.80)**	**(11.83)**	**(9.25)**	**(23.50)**
	Case 3	2.74	0.37	0.09	0.71	0.43	0.08
	(Factor)	**(3.34)**	**(1.54)**	**(20.89)**	**(14.49)**	**(10.98)**	**(23.50)**

∗Note: Due to the error that occurred around 22 h after the start of the experiment in case 3 of the random perturbation, the results of this analysis are distorted. If only the first part of the test up to the error is considered, the displacements in the x and y directions decrease to 2.33 µm and 1.22 µm, respectively. This would result in improvements of factors 6.01 and 1.87, respectively. Considering only the second part after the error, even smaller displacements of 1.89 µm, and 0.92 µm are observed for the two directions, leading to improvement factors of 7.4 and 2.48, and thus, more significant improvements than in all considered cases.

The experiments described here have demonstrated that the approach, with the selected system parameters, effectively improves the displacements of the two points to be controlled for both random and stepped perturbations. Changes in thermal boundary conditions due to heat conduction typically occur periodically or entirely randomly, albeit within a certain range. This range can be estimated in preparation for a mission. The simulations and experiments presented, which depict random and stepped perturbations, precisely represent these scenarios. Hence, direct application to a real-world scenario is feasible.

In various experiments, the displacement between the two points to be controlled could be reduced by a factor of 4 or even better compared to an uncontrolled reference state, with the required control heating power consistently falling within the technically feasible range. As described at the outset, the limitations of the experimental setup prevent achieving greater improvements, just as the accuracy and resolution of the DIC system does. Nevertheless, the achieved improvements are significant, and the results here demonstrate that the approach already functions effectively even with a basic experimental setup.

Unlike with the sinusoidal perturbation, where larger discrepancies occurred between the simulated temperatures and control heat inputs, respectively, and the values actually measured or commanded in the experiment, these are very similar in all cases for the two kinds of perturbations. Therefore, it can be inferred that the model seems to reflect reality very well. Consequently, the effectiveness of the approach can be considered very high. However, significant differences between simulation and experiment regarding the displacements do occur. These errors, which are attributed to the experimental setup itself, the isostatic mounting, or the DIC system, are nevertheless present in a similar manner in all experiments, allowing for their comparison and thus confirming the achieved improvements. Based on the temperature profiles and commanded heat inputs, which are almost as expected, it can be assumed that the displacements are actually compensated for more strongly and effectively.

The definition of the system parameters σ_S and σ_H has the greatest effect on the system behavior. Increasing the standard deviation of the control heating elements generally results in greater noise in the commanded control heating powers and higher absolute values of this power, which significantly exceed the permissible range of $\pm\, 0.5\,\mathrm{W}$. This, in turn, reduces the displacements in the simulation to a similar level but introduces significantly more noise. Reducing the standard deviation of the sensors has the same effect on the temperature measurements, which are given higher importance by the filter. This also impacts the control heating power, causing it to fluctuate more and fall outside the permissible range. On the other hand, if the standard deviation of the sensors is increased too much, measurement noise is amplified, and the filter places more weight on the model-based estimation. Since this estimation is also subject to errors, it leads to poorer compensation of the displacements and an increasing need for

control heating power. In the experiments, the two right-hand HEs 3 and 4 were barely controlled at all throughout all the tests. Their heating power fluctuated only slightly around the steady-state power. In the simulations, their contribution was greater, albeit only slightly. The presence of the two HEs is essential for the mathematical determination of the system. However, it would be possible to improve the approach at this point if these two HEs were only operated at 0 W in the steady-state condition in simulation and experiment and their use was ultimately dispensed with completely in the experiment. The effect on the stability of the temperature and the displacements would probably be small, but in terms of a technical realization of the approach, power could be saved. The issue of redundancy also plays a role here, which is discussed in more detail in section 5.4.

The optimal values for the system parameters are found near the technically plausible ranges. The optimization of these parameter settings must consider not only the best possible reduction of displacements but also the reduction in the required control heating power. However, this process is device-specific and structure-dependent and must therefor be tailored individually for each case, setup and source of perturbation.

Chapter 5

Technical Implementation and Potential Improvements

The results detailed in the previous chapter have demonstrated that the approach proposed in [6] to reduce thermally induced displacements could be experimentally validated. The observed discrepancies between simulation and real experiments can be improved by enhancements in the experimental setup, particularly the isostatic mount, sensor and actuator systems, and their modeling. However, a limiting factor for quantifying the improvement remains the DIC system as an external validation instrument, whose accuracy could only be marginally enhanced. Nevertheless, the structure used to demonstrate the approach will not be employed in this manner on a satellite for in-orbit validation. Therefore, additional aspects need to be considered for the technical implementation of the approach, some of which will be discussed below. These include:

1. Choice of structural material: Instead of a simple plate made of an aluminum alloy, an optical bench in real-world applications will be constructed from ceramics, which exhibit significantly better passive stability. Additionally, the use of composite materials or other additively manufactured structures is conceivable and likely. The choice of the structural material and the factors to be considered in this regard are discussed in Section 5.1.

2. Choice of sensor technology: In addition to traditional temperature sensors, which were used in this work to determine the pointwise surface temperature, the use of fiber optic sensors, such as FBGs, is particularly sensible, especially for composite materials or additively manufactured structures. This is addressed in Section 5.2.

3. Choice of actuator technology: As emphasized multiple times throughout the work, the use of heating elements allows for targeted heating but not cooling of the structure. To represent cooling, the heating elements must be operated in the

steady-state reference condition with continuous power, so reducing this power can simulate cooling. This represents an immense energy consumption that must be avoided in a real application on a satellite due to the limited available power. Therefore, Section 5.3 examines the use of Peltier elements, which theoretically can do both, heat and cool.

For the technical implementation, especially in space applications, redundancy plays a crucial role. Therefore, this aspect should also be taken into account when using sensors and actuators. In addition to the use of other actuators, an improvement in performance with a simultaneous reduction in control heating power could be achieved by employing a higher number of heating elements. Moreover, this offers the mentioned advantage of redundancy in case of a heating element failure, and the positioning of other heating elements in different locations of the structure could better respond to unforeseen perturbations. This will be addressed in Section 5.4. In conclusion, Section 5.5 demonstrates the redundancy of sensor measurements by modifying two test cases, that were already utilized in Section 4.3, in such a way that certain sensor measurements are not available. The resulting behavior of the filter-controller system is then examined.

5.1 Choice of Structural Material

In this work, a simple, cost-effective, and easily simulated and modeled aluminum alloy was used as the structural material. Due to the relatively large CTE, it was possible to detect larger deformations and displacements with the DIC system for the small temperature changes for which the approach is applicable. As evident in Chapter 4, due to the rectangular shape of the plate, an improvement in the displacement of the points to be controlled in the vertical y-direction is hardly detectable, as the uncontrolled displacements in this spatial direction are already very small. To detect displacements in this direction, a square geometry could be chosen, although limited in size as well by the viewport of the TVC. However, this would come at the expense of the very good detectability of the approach for the horizontal x-direction. Since the use of a different geometry would not yield fundamentally new insights, it was not pursued in this work.

In general, two different possible paths can be pursued with the presented approach: firstly, already passively highly stable structures, such as a ceramic in an optical bench, can be additionally stabilized, allowing, for example, highly precise sensors or instruments for scientific experiments to be more precisely aligned. Secondly, a simpler, more cost-effective, or less complex and possibly lighter structure could be used, which is stabilized by this active control so that the requirements for dimensional stability are achieved. Depending on the application and mission specifications, either option might be feasible. The advantage of the active control approach is that it is independent of

material and geometry. Only the characterization of the physical properties of the selected structure needs to be sufficiently well-known to be simulated in a mathematical model.

Due to the accuracy of the sensors and actuators as well as the resolution of the DIC system, the validation of the approach with a ceramic, e.g. Zerodur [42], as different structural material was omitted in this work, as the uncontrolled deformations and displacements of the reference points on the structure would already be so small that expected improvements would lie within the measurement noise and error tolerance. When modeling a different structure, particular attention must be paid to the thermo-optical properties, which can change significantly at the points where sensors and actuators are applied.

The combination of the validated approach with already passively very stable structures promises the greatest potential. Additionally, a combination with Phase-Change Materials (PCMs), briefly introduced in Section 2.1, is possible. Paraffin embedded in an additively manufactured lattice structure has a specific melting temperature precisely matched to the temperature at which a structure should be maintained for steady-state operation. If there is additional heat input due to changed thermal boundary conditions, such as the thermal cycle in an orbit, it causes the paraffin to melt. Only when the paraffin is melted does further heat input lead to a temperature increase. When the structure cools, for example, during the eclipse phase, the paraffin solidifies before the structure can cool below the melting temperature of the paraffin [24, 25]. For example, in [65], it was investigated how strong the passive thermal stabilization of the alignment of a star tracker for different paraffins in different orbits and thus different frequencies of changes in thermal boundary conditions can be compared to a case without the use of PCMs. Thus, a much more uniform temperature distribution could be achieved, and the stability and alignment accuracy of the star tracker could be improved by 25 % to 69 %, depending on the orbit and application [65]. However, this approach has limitations due to its additional weight because of the paraffin, increased complexity, and the very limited field of application. For the selection of paraffin, the expected equilibrium temperature must be modeled very accurately. If this deviates too much from the modeling in real-world orbital applications, the use of PCMs is ineffective. Another limitation occurs once all the paraffin has melted or, conversely, solidified, and thus, no more heat energy can be absorbed or released into the structure, and the external heat flux continues to act. At this point, the active control of the approach presented here could ideally intervene and take effect as soon as the PCMs has reached its limit. In this way, the disadvantage of the high energy consumption of the presented approach could also be circumvented.

In addition to PCMs, in Section 2.1, the use of meta-material as passive dimensional control has been hinted at and is taken up again in Section 5.3.

5.2 Choice of Sensor Technology

In satellite construction and space applications, TCs for temperature measurement, and less commonly, RTDs are predominantly used. There are only minor differences in the fundamental measurement principle, as well as the required wiring and data acquisition [26, 66, 67]. The Pt-100 sensors used here are detailed in Appendix B.2.1. Although this choice is optimal for the approach presented in this work due to its ease of use, cost-effectiveness, and flexible application, the selection of sensors for a real-world application, such as on the Athene-1 satellite within the SeRANIS project [13], may differ. In addition to the classical measurement of pointwise surface temperature using TCs or RTDs, the use of IR cameras or fiber-optic sensors is possible. IR cameras have the advantage of measuring the temperature field of an entire surface. However, their resolution and accuracy are low. Typically, the latter is only about 10 K, and even for specifically calibrated systems, it is at most 2 K to 3 K, which is insufficient for the approach. The use of fiber-optic sensors, on the other hand, could be an alternative. Therefore, the use of Fiber Bragg Gratings (FBGs) in particular will be discussed here.

FBGs are fiber optical sensors consisting of refractive index modulations embedded in a single-mode or multi-mode fiber at equidistant intervals [29, 68, 69]. The refractive index modulation reflects a specific wavelength of light known as the Bragg wavelength. The distance and periodic variation of the refractive index determine the reflected wavelength [30]. Figure 5.1 illustrates how the light travels through the optical fiber, reflecting only the Bragg wavelength through the modulation inside. The remaining part of the spectrum is transmitted through the fiber. Any external perturbation leading to changes in the structure causes shifts within the modulation.

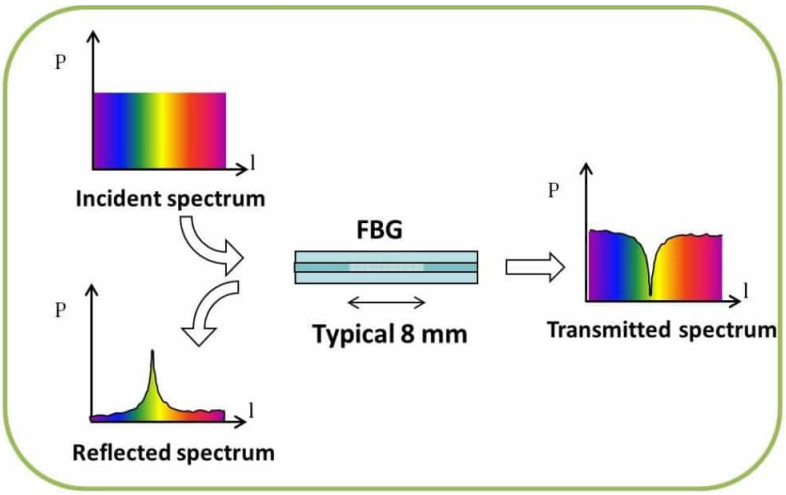

Figure 5.1 Operating principle of FBG [70]

Figure 5.2 demonstrates how a change in refractive index n and the period of the refractive index Λ alters the reflected wavelength. Both temperature and strain can influence these values, allowing a calibrated interrogator to evaluate shifts within the Bragg wavelength [70].

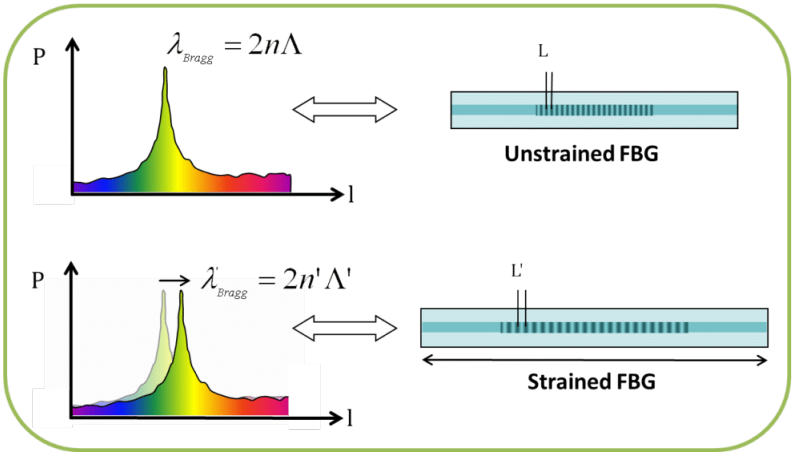

Figure 5.2 FBG response as function of strain[70]

Such an interrogator generates a light spectrum through an integrated light source, typically a laser. They also record the reflected wavelengths and convert them into an electrical signal. The accuracy of temperature or strain measurement depends on the fiber and the resolution of the interrogator. Different Bragg gratings of varying periods can be incorporated into a single fiber, enabling multiple measurement points. However, it is essential to ensure that the corresponding reflection peaks do not overlap. This requires a prior estimation of the expected changes in temperature or strain to design the measurement points. Depending on the design, an interrogator can handle multiple fibers with different Bragg gratings at once.

This clearly illustrates the three major advantages of using FBGs: numerous measurement points at arbitrarily selectable intervals and distributions, simultaneous determination of temperature and strain, and the possibility of integrating the fiber directly into the additively manufactured structure or composite material. However, the disadvantages, especially for space applications, are significant.

As part of the Piezoelectric Assisted Smart Satellite Structure (PEASSS) project by the European Space Agency (ESA), a CubeSat was launched in 2017, serving as a technology demonstrator on which novel smart structures were tested. This includes a piezoelectrically actuated smart panel for aligning a star sensor on an optical bench made of a fiber-reinforced composite material, into which 2 optical fibers with FBGs for temperature and strain measurements were incorporated [69, 71, 72]. Figure 5.3 shows the PEASSS CubeSat within laboratory environment.

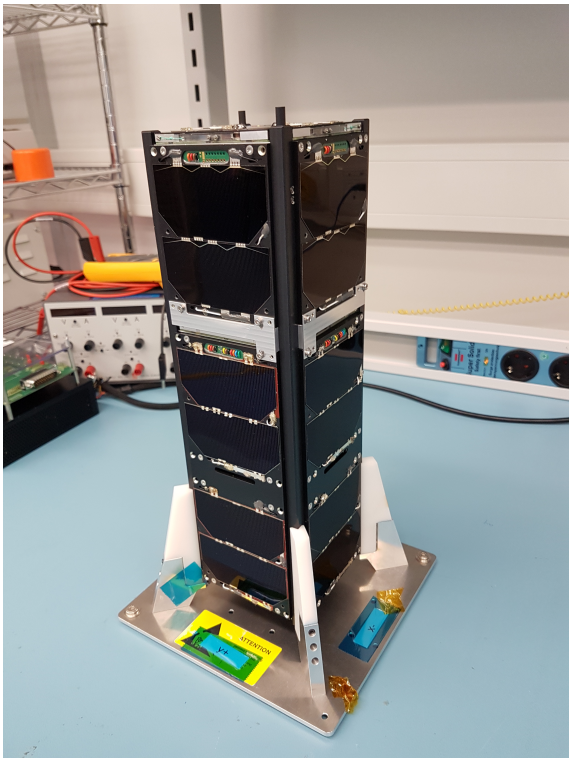

Figure 5.3 PEASSS satellite [73]

With the PEASSS satellite, the fundamental usability of FBGs and piezoelectric actuators in space was demonstrated with rudimentary equipment and relatively coarse accuracy. FBGs are inherently vacuum-compatible and can easily be deployed under space conditions, but commercially available interrogators for generating laser light and measuring wavelength shifts are not vacuum-compatible [69]. The greatest challenge lies in designing a space-compatible interrogator with low weight and size, low power, and the highest possible accuracy and stability. Within the PEASSS project, such an interrogator was developed that can operate on a CubeSat [69]. Figure 5.4 shows this interrogator. The requirements for wavelength repeatability were below 12 pm, corresponding to a temperature measurement resolution of approximately 1 K. Through tests, a repeatability of 3.5 pm was determined, allowing for significantly better measurement accuracy. Depending on various factors, interrogator technology can provide repeatability of up to under 0.1 pm, enabling temperature measurements that are orders of magnitude more accurate than those obtained through TCs or RTDs.

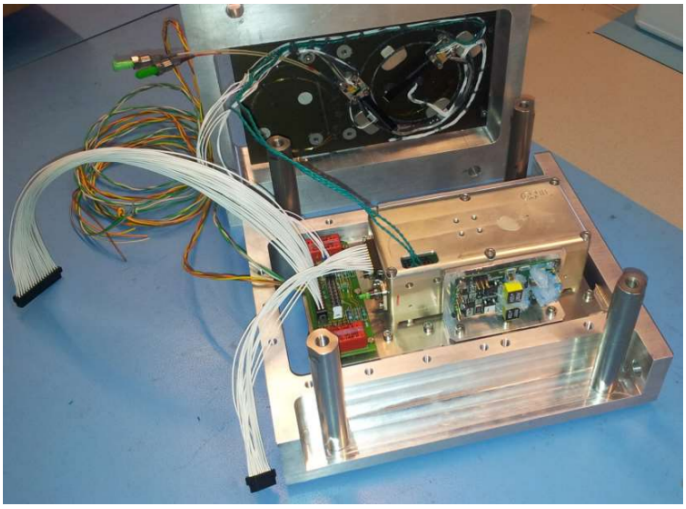

Figure 5.4 PEASSS interrogator [72]

The use of this technology for deployment in the SeRANIS project on the ATHENE-1 satellite [13] would be possible and meaningful. Testing could not be conducted in the context of this work due to the high acquisition costs of a commercially available interrogator, the necessary manufacturing processes for the structure, the lack of connections for testing in the TVC, as well as long delivery times and complicated procurement routes.

5.3 Choice of Actuator Technology

If the structure to be controlled, as described in Section 5.1, is additively manufactured, certain components or sections could be replaced by meta-materials. These design materials, created, for example, by the combination of two metals with different CTE, can be connected to elements with a negative CTE and serve as a kind of actuator [74, 75]. If there is an increase in thermal power, the meta-material contracts and can thus compensate for the expansion of another material connected to the meta-material. However, the use of such material as an actuator in the context of this work would not be expedient, as it requires thermal energy for targeted activation, which would need to be provided by a heating element or similar means.

One of the most significant drawbacks of the presented and validated approach is the use of heating elements. While they have the advantages of high efficiency, direct conversion of electrical power to heat, easy installation, and controllability through DC voltage sources, their major disadvantage lies in the fact that they can only produce heat. However, since both cooling and heating are required for the approach, a trick is employed by operating the heating elements at a certain power in the steady state, so reducing this power corresponds to cooling the structure. This, in turn, has the advantage that cooling power can also be easily generated in the same way. However, the continuous operation of the heating elements results in extremely high energy

consumption, limiting their usability in real applications on a satellite. Therefore, investigating alternatives is necessary. The use of Peltier elements (PEs) could eliminate this disadvantage.

A PE is an electrical device that harnesses thermoelectric effects to either function as a heat pump, absorbing heat on one side and emitting it on the other (Thermoelectric Cooler (TEC)), or act as a generator, converting a temperature difference between the two sides into an electrical voltage (Thermoelectric Generator (TEG)). Thermoelectric effects describe the interaction between thermal energy and electrical energy and are divided into three phenomena: the Seebeck, Peltier, and Thomson effects [76].

The Seebeck effect describes the generation of an electrical voltage between the junctions of two dissimilar electrical conductors when subjected to a temperature gradient. The reverse of this effect is the Peltier effect, which states that at the junction of two dissimilar electrical conductors, heat is either absorbed or emitted when a current flows through them. The Thomson effect describes the absorption or emission of heat by charge carriers moving with or against a temperature gradient. In PEs, this effect has little influence.

A thermocouple is the smallest unit within a PE. In this structure, a p-type and a n-type doped semiconductor are electrically connected in series via copper bridges. However, due to their different thermal orientations, they are thermally connected in parallel, as shown in Figure 5.5. Multiple thermocouples, connected between two ceramic plates, form a PE. The shape and size of PE can be scaled and adapted to meet specific requirements. When a current flows through the PE, heat is absorbed at the cold side (CS) and released at the hot side (HS) of the PE.

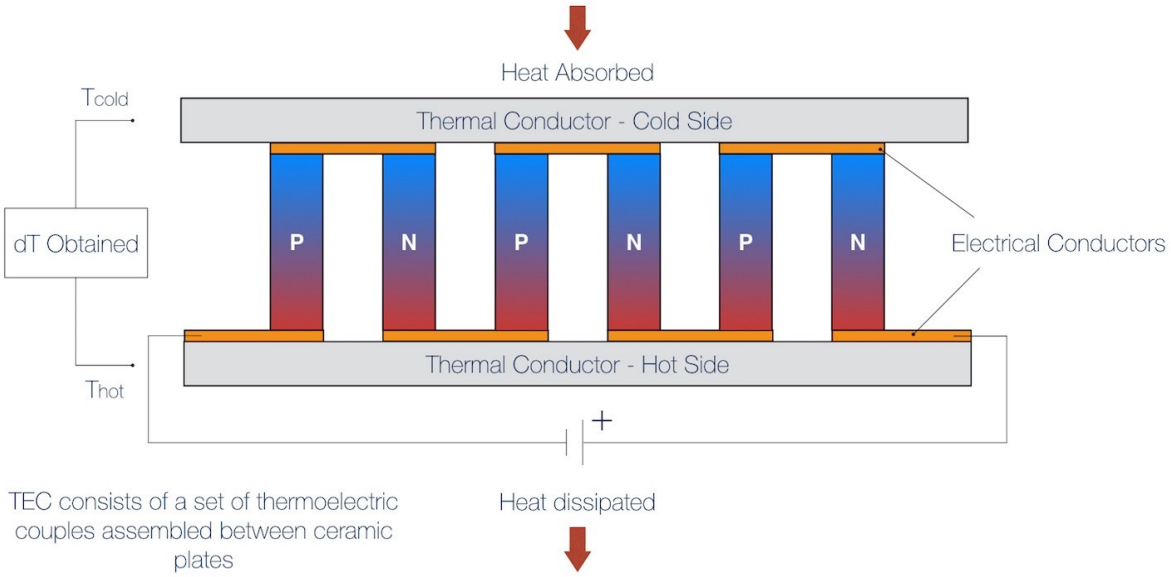

Figure 5.5 Thermoelectic Cooler [35].

A remarkable property of PEs is their ability to reverse the temperature gradient by reversing the polarity of the applied DC voltage. Typically, PEs have designated hot and cold sides. The HS can be identified by the soldered cable connections, which are intended to prevent the Joule heating from the connection cables from entering the CS. Besides this detail, there is no difference in the thermal behavior of the PE when the current direction is reversed. The thermal state when a PE is reversed can be observed in Figure 5.6, which represents the steady states of a PE for both polarities of the applied voltage, but not the dynamics during the transition from one state to another. A ΔT between CS and HS is established and maintained with a constant current. When the current direction is reversed from this state, the same ΔT will re-establish, but the temperature gradient will be in the opposite direction. The temperature difference between CS and HS is limited by the maximum current.

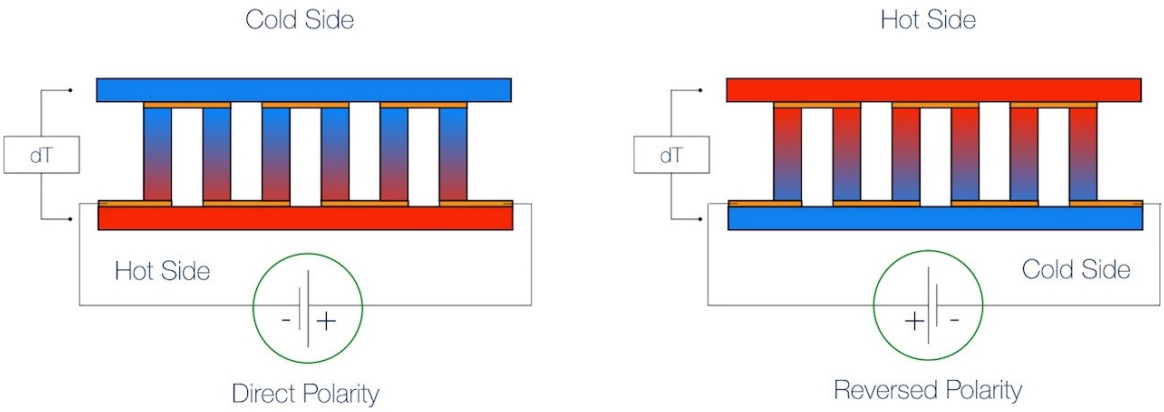

Figure 5.6 Temperature curve when reversing the polarity of a Peltier element [35]

Figure 5.7 shows a cross-sectional view of a PE, illustrating the three-dimensional arrangement of the legs. PEs are available in various shapes and can be scaled as needed.

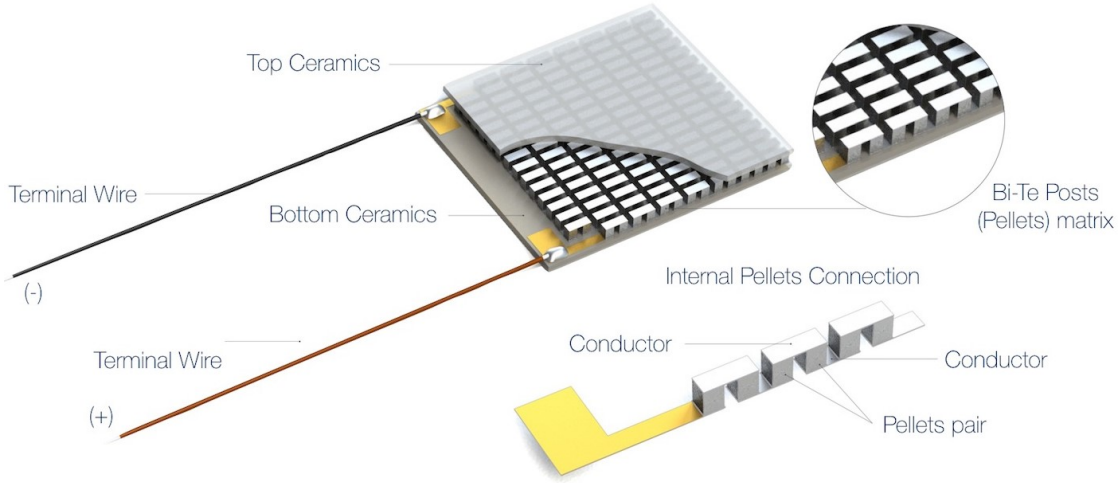

Figure 5.7 Sectional view of a Peltier element [35]

PEs have no moving parts, require no cooling fluids, occupy a small footprint with low weight, exhibit high reliability, and operate on direct current. However, their disadvantages include relatively low efficiency and higher costs [77]. Both the assembly and the control are more complex, as is the modeling, because there is no direct correlation between electrical power and resulting heating power. The necessary coefficients of the thermoelectric effects are experimentally challenging to determine, electrical resistance is not constant, and the temperature difference between both sides affects efficiency. Low efficiency is the primary reason why PEs are typically used in specialized applications, where efficiency only plays a subordinate role. PEs can generate heat flows with both positive and negative signs, depending on the direction of the current flow. Unlike classic resistance heating elements, PEs thus do not have to be operated continuously, which could mean significant energy savings.

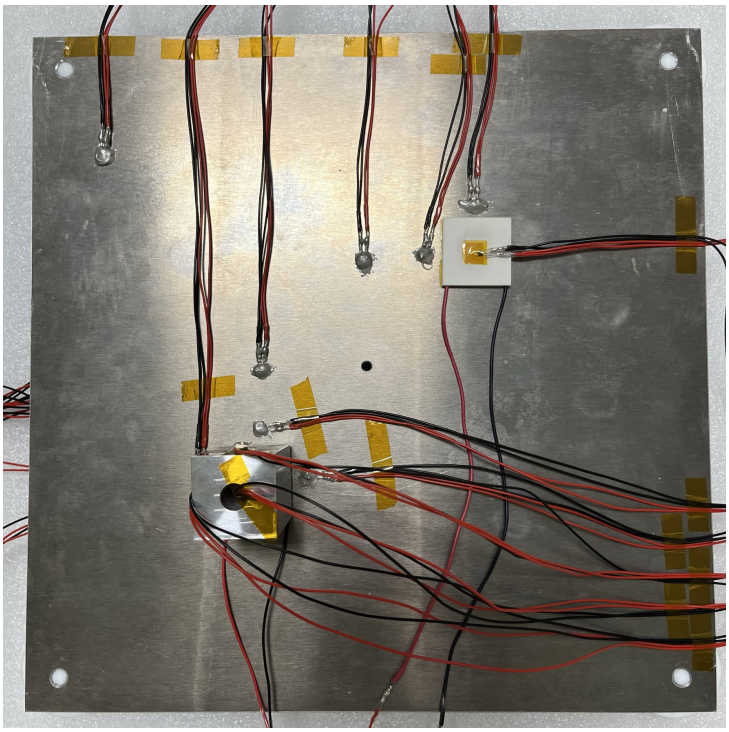

(a) Base plate

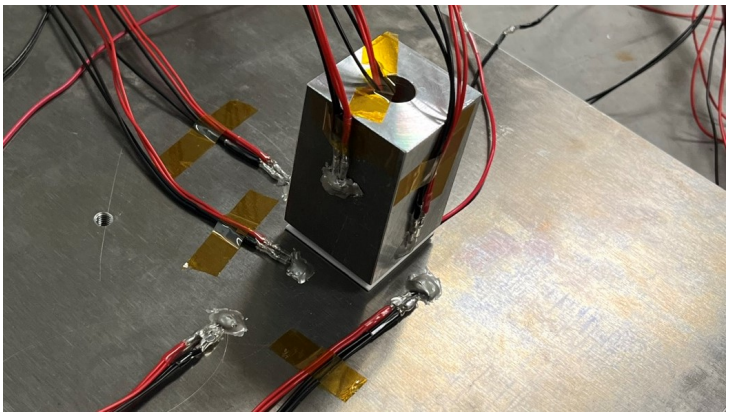

(b) PE with aluminum alloy block

Figure 5.8 Test setup for PE [12]

To test the feasibility of using PEs for this approach, a simple experimental setup, shown in Figure 5.8, was developed to test the basic properties [12]. The basis of the experimental setup is a base plate made of the same aluminum alloy used in the structural stabilization tests, on which two PEs and a total of 18 Pt-100 temperature sensors are attached. One of the PEs (TEC1) is equipped with only one temperature sensor on the back (Figure 5.8a top right). On the back of the second PE (TEC2), a block made of the same aluminum alloy as the base plate is attached (Figure 5.8a bottom left and Figure 5.8b). The temperature sensors measure the temperatures of both sides of the PEs, the temperatures in the attached block, and temperatures at various points on the base plate. The temperature acquisition is intended to capture the absorption or emission of heat in the form of temperature changes. The recording of measurement data is analogous to the experimental setup of the structural stabilization tests.

The control of the PEs is done through MATLAB. Each DC voltage source connected to a PC regulates the required current for one PE. Using a two-channel relay and an Arduino microcontroller, the reversal of the applied voltage to the PE is switched. The magnitude and sign of the heat flow in the PEs can thus be controlled. The voltage, current, and electrical power values of the entire circuit with the respective PE are also recorded using the DC voltage sources.

The PE, which is attached to the base plate without the block, should simulate the case in which a heating element is replaced by a PE without modifying the experimental setup at all. Heat is absorbed or released from the base plate. The exposed side of the PE can only exchange heat with the environment through radiation.

The PE to which the block is attached on the back is in heat exchange with both the block and the base plate and can transport heat from one body to the other. The attached block can store significantly more heat than the ceramic plate of the PE. It should be noted, however, that the volume and mass ratio between the base plate and the block is approximately 16:1, and the block changes its temperature much more strongly when the same amount of heat is exchanged.

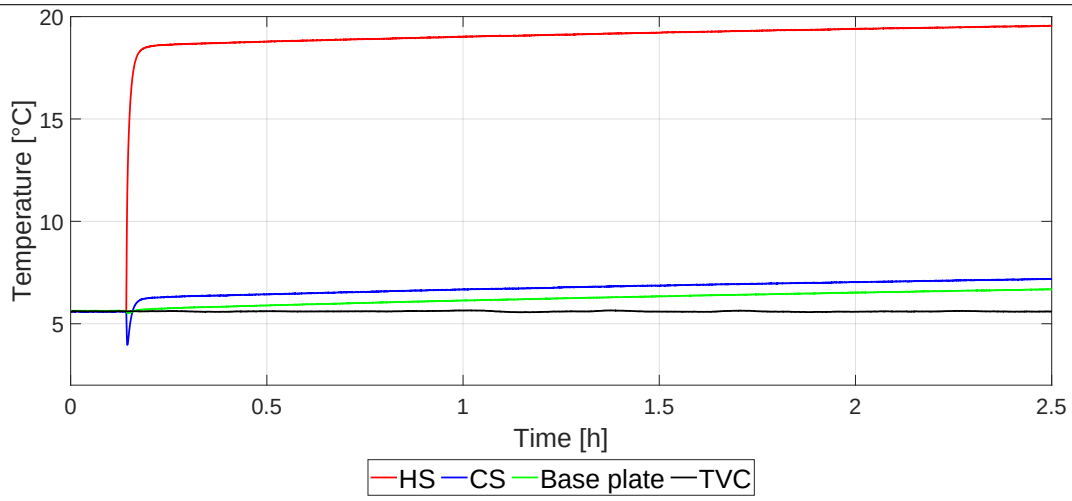

(a) Total plot

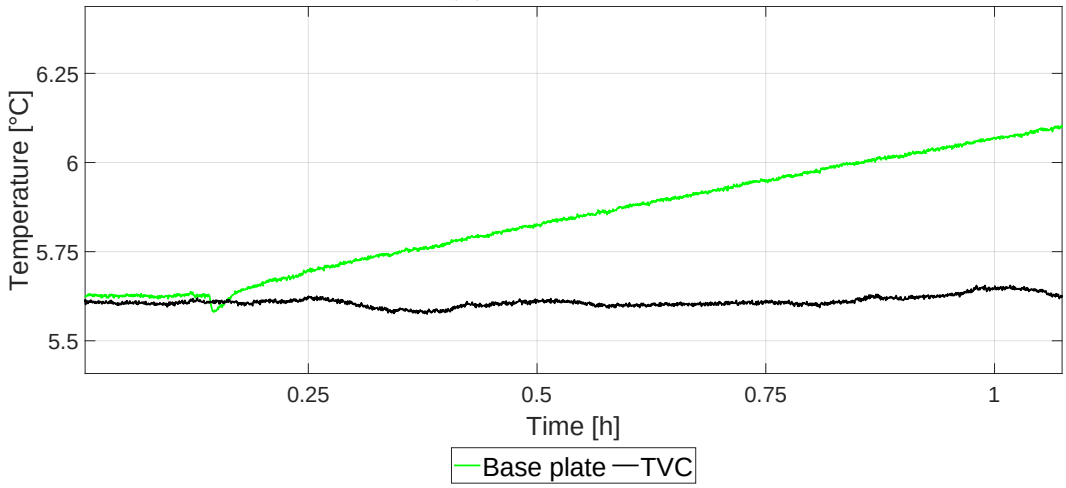

(b) Start of the test, temperature base plate

Figure 5.9 TEC1 temperature plot, $I = 0.25\,\mathrm{A}$ [12]

Figure 5.9 illustrates temperature profiles during the operation of TEC1 with a constant current of 0.25 A. In this configuration, the PE is polarized so that the CS is located on the base plate, while the HS is exposed to radiative exchange with the surroundings. As shown in Figure 5.9a, upon switching on the power supply, a rapid temperature difference ΔT between the two sides of the PE is established. The red temperature curve in Figure 5.9a represents the HS, and the blue curve represents the CS. This ΔT remains approximately constant throughout the experiment. At the beginning of the experiment, there is a heat flow from the CS to the HS, causing a temporary sharp drop in the CS temperature and the buildup of the ΔT. With increasing ΔT, the heat transport between HS and CS also increases, reaching the Peltier heat flow at the maximum temperature difference. From this moment, just a few minutes after the start of the experiment, the entire Peltier heat flow is required to maintain this ΔT, and no more heat transport from the base plate to the HS through the PE occurs.

Figure 5.9b demonstrates that the temperature of the base plate can be lowered briefly.

However, a few minutes later, no more heat is absorbed from the base plate, and the base plate, in turn, is heated due to Joule's heat flow. Using a PE in this configuration essentially functions as a heating resistor with very poor efficiency and cannot effectively replace the existing heating elements. The main reason for this is the low thermal capacity of the top side of the PE and inadequate radiation, leading to a rapid temperature difference between the two sides of the PE, preventing further heat absorption from the base plate.

Figure 5.10 depicts the temperature evolution around TEC2 for the same PE settings. The block attached to the HS significantly increases the thermal capacity on this side. As a result, the temperature difference between the two sides of the PE establishes more slowly, allowing a heat flow from the base plate for an extended period. Consequently, the base plate can be cooled for an extended duration, as indicated in the diagram. However, the resistance of the PE also contributes to the generation of a Joule heat flow, leading to a linear temperature increase. The ΔT between the two sides of the PE is of the same magnitude as with TEC1, but it establishes much later. Despite the relatively small thermal capacity of the block compared to the base plate due to the mass ratio, the cooling effect can only be sustained for a short period before the entire system warms up due to the described thermoelectric effects.

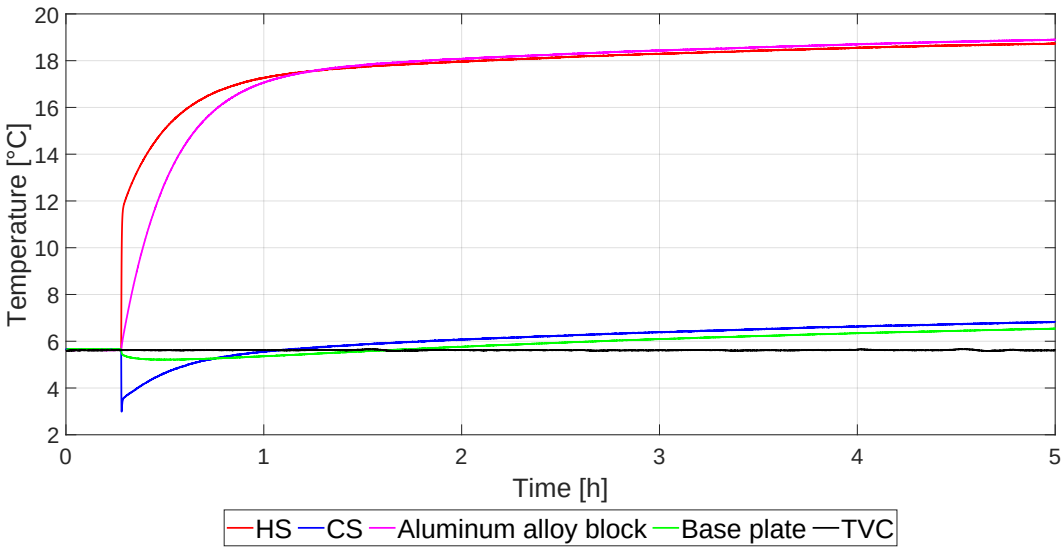

Figure 5.10 TEC2 temperature plot, $I = 0.25\,\mathrm{A}$ [12]

This effect becomes more pronounced when reversing the polarity of the PE and attempting to cool the block instead. In Figure 5.11, temperature profiles of the base plate and the aluminum alloy block are shown. When used as a cooler (Figure 5.11a), heat is transported from the base plate to the block. The block changes its temperature much faster than the base plate, which has a mass 16 times larger. The base plate can only be cooled to a limited extent since the maximum temperature difference between the two sides of the PE is reached relatively quickly, and thereafter, Joule heating leads to a linear temperature increase.

With reversed polarity (Figure 5.11b), the block is cooled. The same heat flux results in a significant cooling of the block due to the previously described mass ratio. Consequently, the block is maintained at a temperature below the reference temperature of the TVC throughout the entire experiment. The linear increase in both temperatures due to the described thermoelectric effects is also evident here.

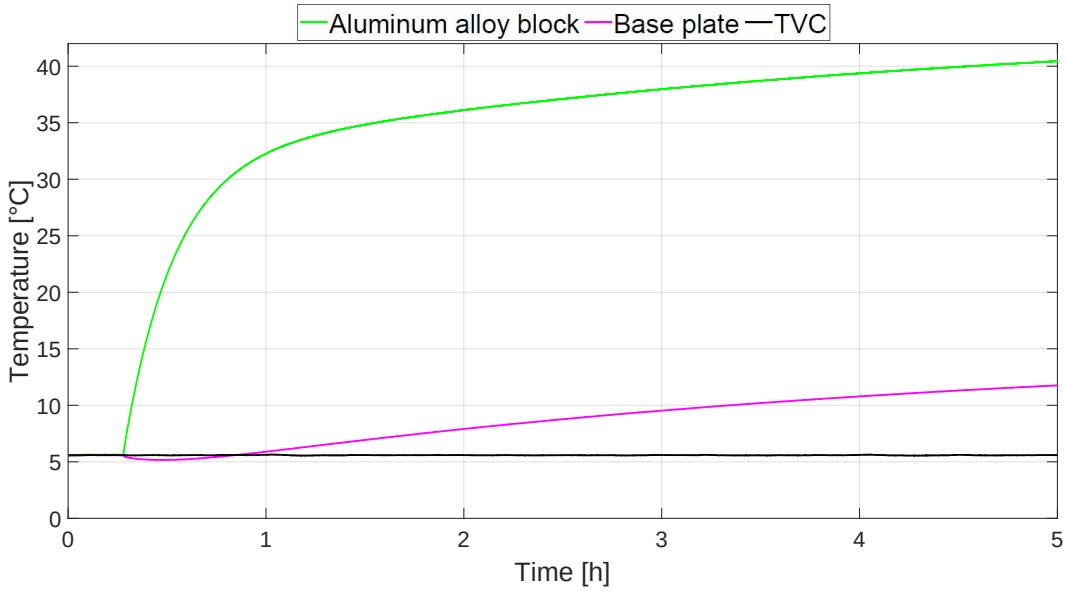

(a) Polarity as cooler

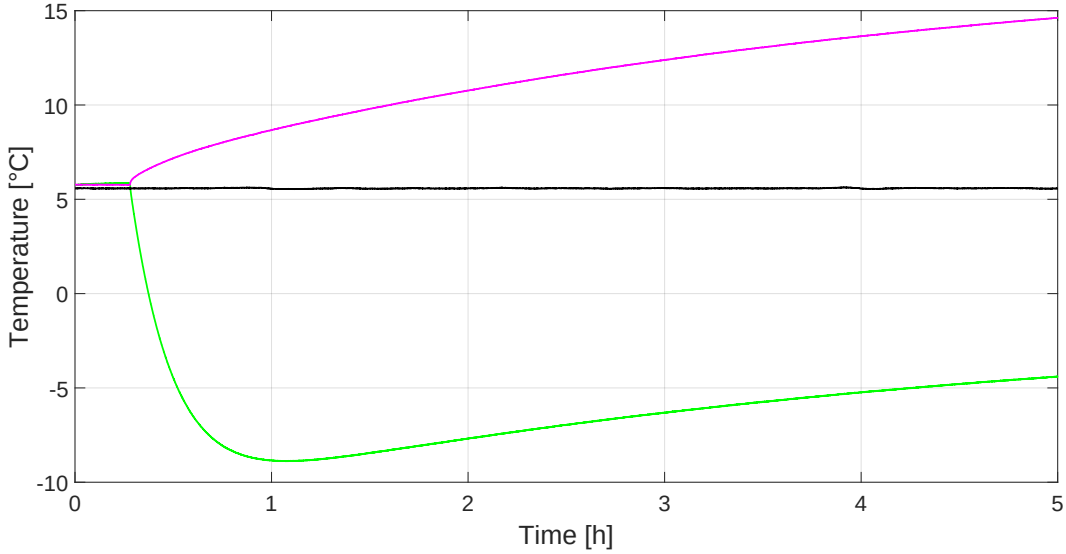

(b) Polarity as heater

Figure 5.11 TEC2 temperature plot, $I = 0.50\,\mathrm{A}$ [12]

Fundamentally, both positive and negative heat fluxes were generated and demonstrated using the PE. However, several aspects need to be considered to employ PEs as alternative actuators.

While the Joule heat flux as constant perturbation when operating PEs is quadratically dependent on the current, the Peltier heat flux is linearly dependent on the current.

This perturbation can be reduced by distributing the required heat flux among multiple PEs. In the structural stabilization approach, a FEM model's surface element must be equipped with a control heating element, determining the size of the heating element for the FEM model. Substituting this with PEs would require them to be very small, representing many PEs as one heating element. This significantly increases the demands on control, wiring, and thus the complexity of the setup.

The second aspect to be considered is the heat flux generated by the temperature difference between the two sides of the PE. This heat flux opposes the Peltier heat flux and can become a zero-sum with it, if the temperature difference becomes too large. This perturbing factor is reduced by appropriate heat dissipation. As seen in Figure 5.11, the much smaller block can be cooled more effectively than the larger base plate. Therefore, the object to be influenced must be connected to the PE through a heat sink with a much larger heat capacity. This keeps the heat sink's temperature more constant, and the heat flux in or out of the object to be influenced can be better regulated. If the temperature difference is kept permanently very small, the Peltier heat flux can continuously absorb or emit heat from or to an object.

For use in structural stabilization, an experimental setup with the highest possible coverage of PEs should be designed, where the free side of the PEs is connected, stress-free, to a heat sink that keeps its temperature as constant as possible. However, this poses significant challenges to the setup.

5.4 Number of Heating Elements

Adding two more control heating elements to a total of six requires only a minor adjustment of the mathematical model, when minimizing the cost function in Equation 3.8. Furthermore, there is no change in the modeling and simulation of the approach necessary.

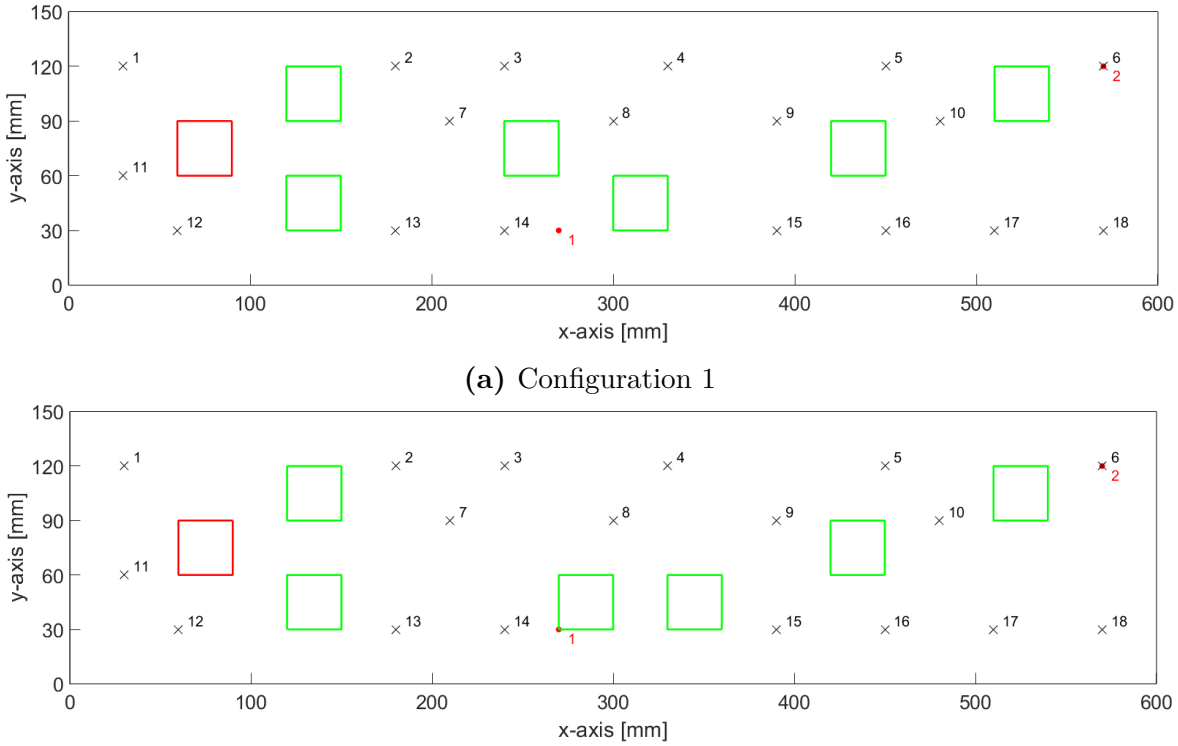

(a) Configuration 1

(b) Configuration 2

Figure 5.12 Possible configurations of the extended setup [12]

The sensor positions, improved for configuration 2 in Section 3.5, need not be altered for the new configuration with six control elements, as long as the origin of the perturbation remains unchanged. To ensure comparability of results, the perturbation source and the points on the structure to be controlled are not modified. All possible positions of the heating elements are systematically explored using a brute-force approach [61], similar to the steps described in Section 3.5. Configurations with the greatest improvements in displacements compared to their respective uncontrolled reference states for the three types of perturbations described in Section 3.5, while simultaneously minimizing the total control heating power, are identified. The two best configurations meeting these criteria are depicted in Figure 5.12. The perturbation heating element is marked in red, and the control heating elements are marked in green. The positions of the 18 temperature sensors correspond to the black-bordered nodes of the FEM model and remain unchanged, as do the two reference points to be controlled, represented by the red-marked nodes. Both configurations differ only in the positions of the two middle heating elements. Since configuration 1 differs only in the position of the two additional

elements from the one previously presented in Section 3.5, it is selected for experimental validation [12].

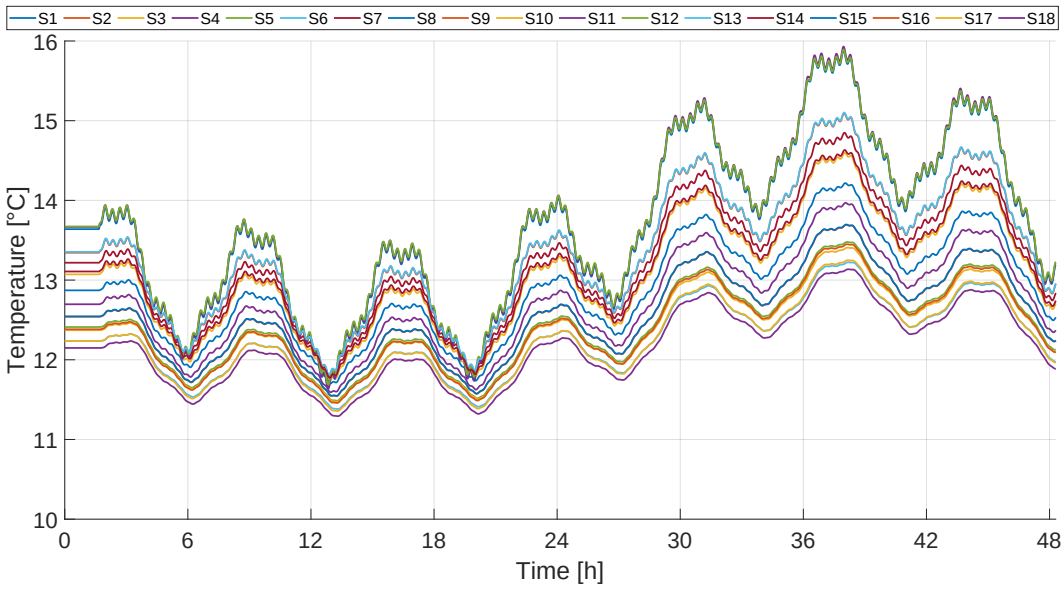

(a) Simulation

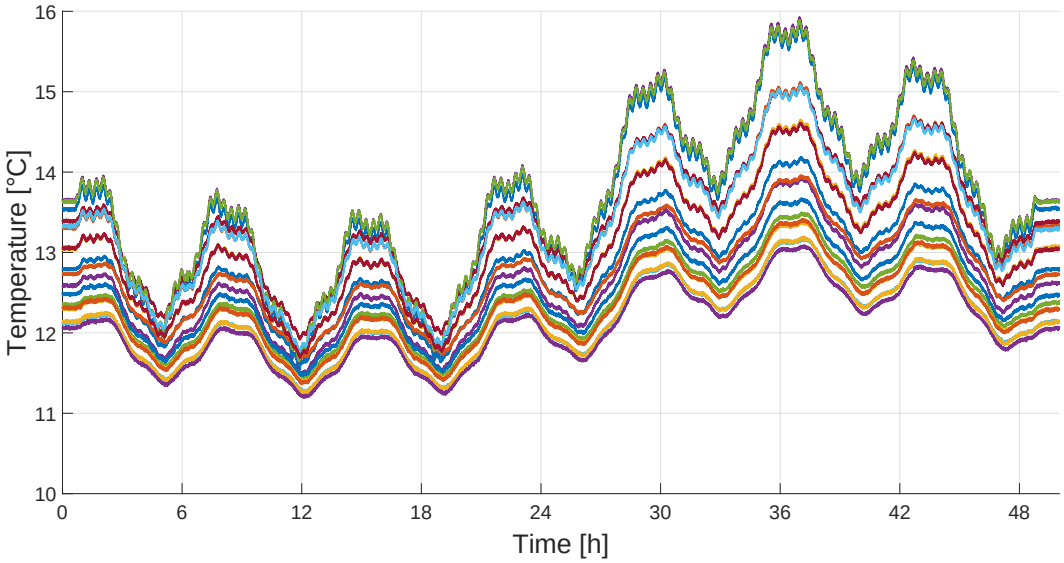

(b) Experiment

Figure 5.13 Temperature sensor plot, uncontrolled case, configuration 6 heaters

With this selected configuration, the same test series, as described in Section 3.5 for the configuration with 4 control heating elements, are conducted with different types of perturbations. The results of these test series are generally very similar, so only one experiment will be presented here as an example. For this purpose, the same random perturbation of $\pm$ 1 W is applied to the perturbation heating element over an experimental period of 48 h. For the Kalman filter system parameters in the controlled case, $\sigma_T = 0.12\,\mathrm{K}$, and $\sigma_H = 0.02\,\mathrm{W}$ are considered. Again, comparisons between the uncontrolled reference state and the controlled state, both with each other and with the respective simulation, will be made [12].

In Figure 5.13, temperature profiles of all 18 sensors in the uncontrolled system are depicted. In the simulation, the maximum temperature amplitude $A_{T,max}$ is ± 2.15 K at Sensor 11, which is closest to the perturbation heating element. The minimum temperature amplitude $A_{T,min}$ is ± 0.91 K at Sensor 18, which is farthest from the perturbation. The simulated profile is comparable to previous results, but all temperature data are about 1.5 °C higher due to the additional steady-state heating power of 1 W from the two additional heating elements, each operated at 0.5 W in steady-state. The fluctuation of the average temperature in the simulation is 2.68 K. The experimentally determined uncontrolled temperature profile is very comparable to the simulation, with a slightly higher fluctuation of the average temperature at 2.74 K.

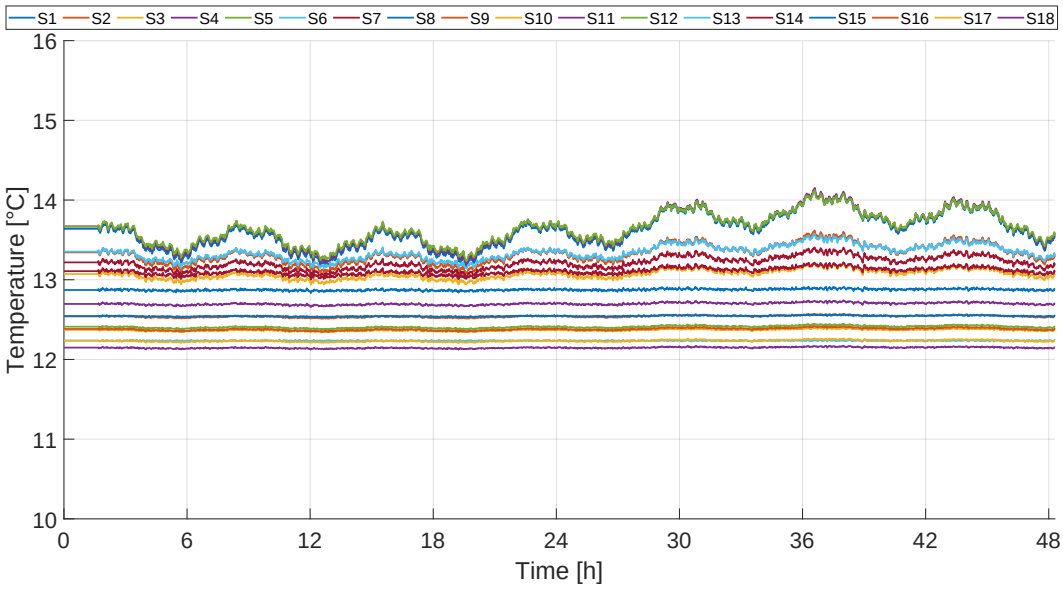

(a) Simulation

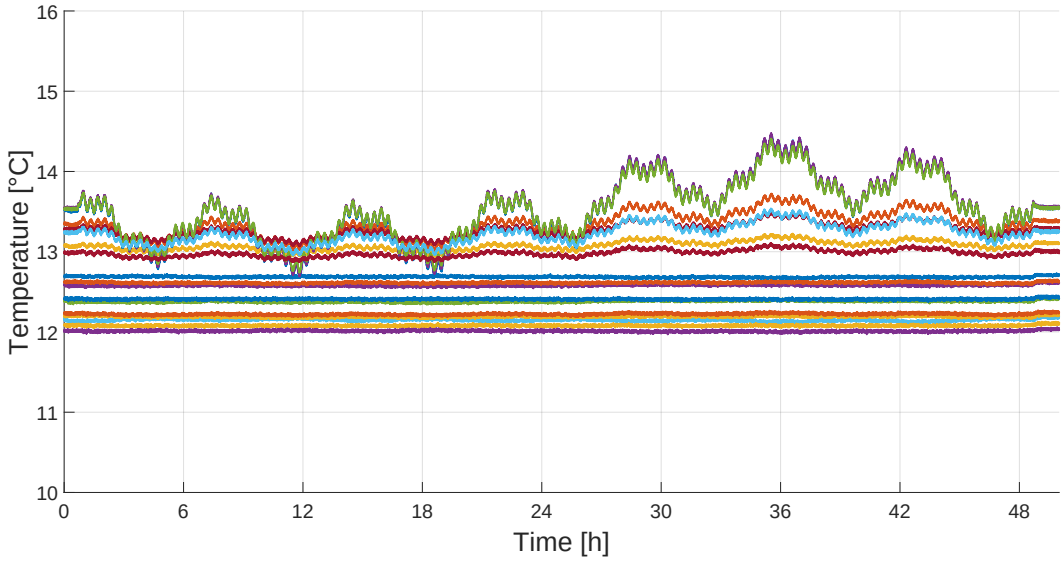

(b) Experiment

Figure 5.14 Temperature sensor plot, controlled case, configuration 6 heaters

In the controlled case, illustrated in Figure 5.14, fluctuations in the temperature measurements in both simulation and experiment are still noticeable in the sensors close to the perturbation heating element, while in all other sensors, no significant fluctuations can be recorded. However, it is observed that the fluctuations are slightly higher than in the experiments with 4 heating elements. This effect was observed in all experiments in this configuration. Nevertheless, this is generally not problematic, as despite significant temperature fluctuations at selected locations in the structure, excellent stabilization of the points to be controlled can still be achieved. The fluctuation of the average temperature in the simulation is 0.28 K, and in the experiment, it is 0.41 K.

Looking at the displacements of the points to be controlled in Figure 5.15 yields a differentiated picture. In the simulation of the uncontrolled case, the course of the perturbation is well traceable. The displacements in the x-direction are again significantly more pronounced than in the y-direction. The range of the displacements in the x- and y-directions decreases due to the filter and controller approach from 14.33 µm and 6.91 µm to 0.69 µm and 1.11 µm, respectively, by similar factors as in the cases presented in Section 4.3.2 for configuration 2 with 4 control HEs. In the experiment, however, the improvements in the controlled case compared to the uncontrolled reference state are significantly smaller. In the uncontrolled case, the displacements are similar to those in Section 4.3.2, with the course of the x-directional displacement being poorer in the second 24 h half of the experiment due to low fluctuation. The course of the displacement in the controlled case is more damped, yet linear increases and decreases are noticeable in the front and rear parts of the experiment, up to $\pm$ 5 µm. Similar deviations are found in almost all experiments, regardless of the type of perturbation, making an assessment of the performance of this configuration more challenging. The ranges of the displacements in both cases and the factors of improvement are lower compared to previous tests and provided in Table 5.1.

Finally, Figure 5.16 shows the required control heating powers for simulation and experiment. They are very similar here as well. However, it is noticeable that the individual heating powers of the control elements are actually lower than shown in Section 4.3.2. In those tests individual peaks outside of the allowed range were regularly found in that configuration, whereas in this configuration, the peaks are about 0.2 W lower, corresponding to a reduction of 40 %. The ranges here are slightly below the values of the configuration with 4 heating elements, with 1.05 W in the simulation and 1.15 W in the experiment. In the previous configuration, 0.3 W could be saved at 2 heating elements in each case, allowing the necessary ranges to still be used. Here, with 3 elements, 0.2 W and with the remaining 3 elements, even 0.4 W could be saved compared to the used 0.5 W steady-state. Thus, this configuration could be operated with a 0.2 W lower total power in steady-state heating.

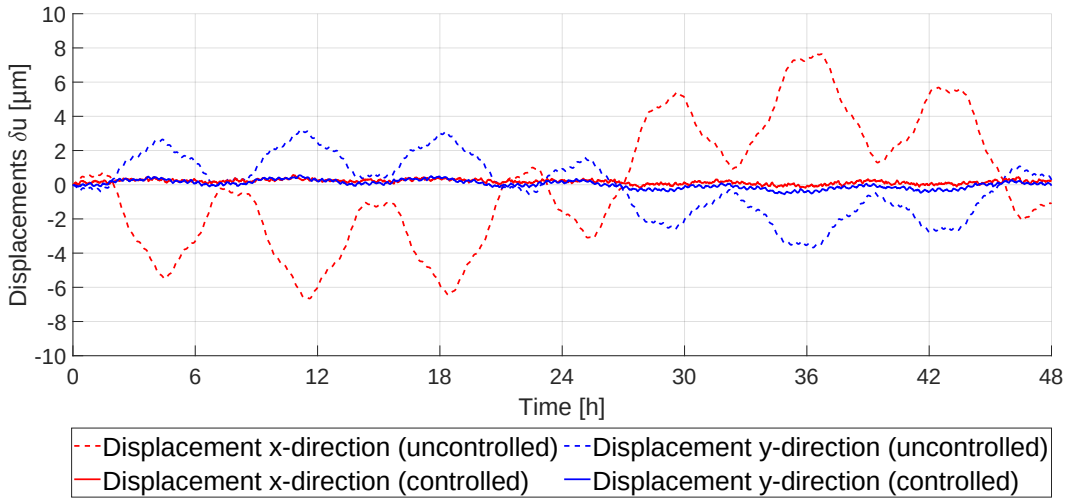

(a) Simulation

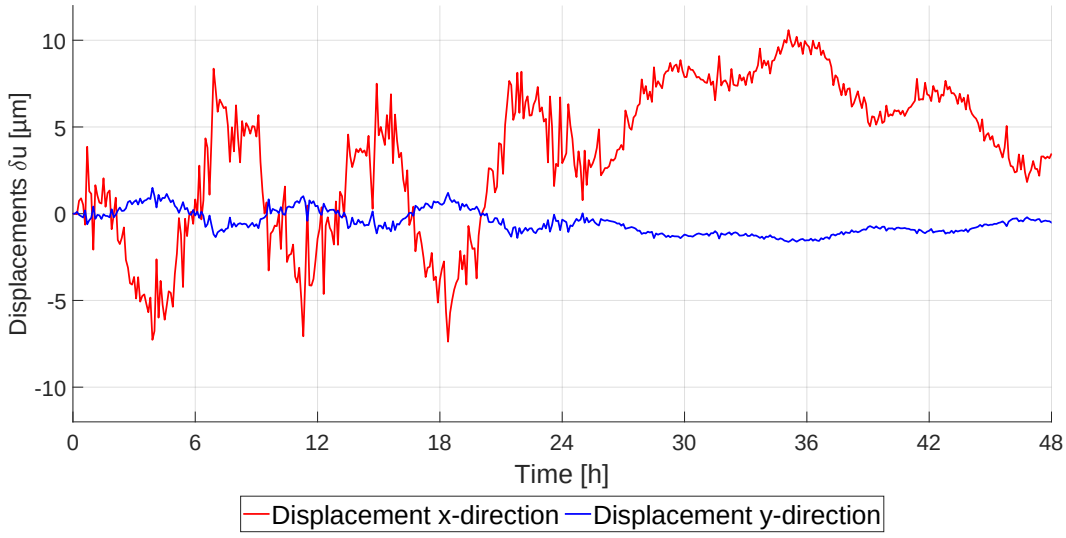

(b) Experiment (uncontrolled case)

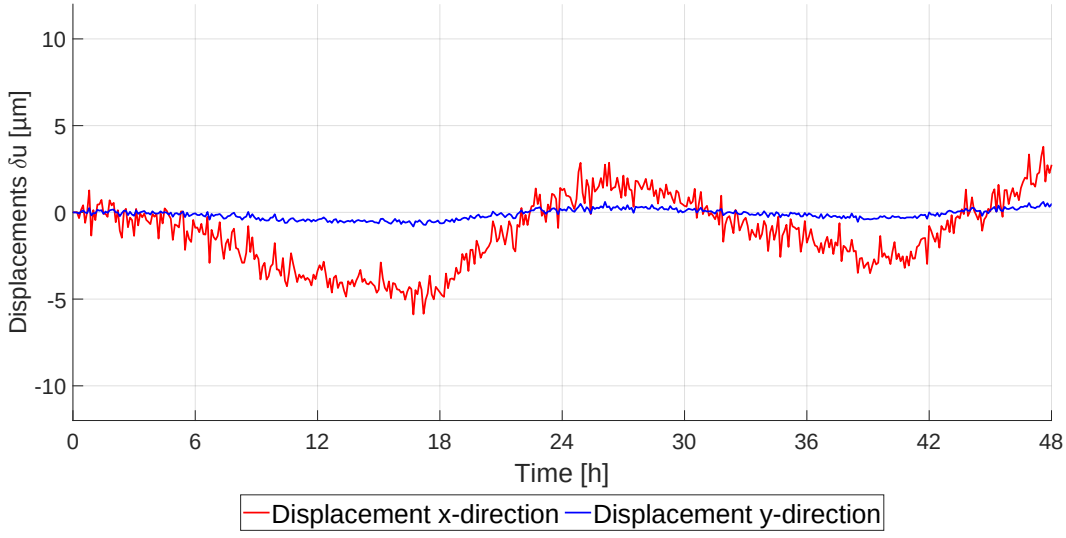

(c) Experiment (controlled case)

Figure 5.15 Displacement plots, configuration 6 heaters

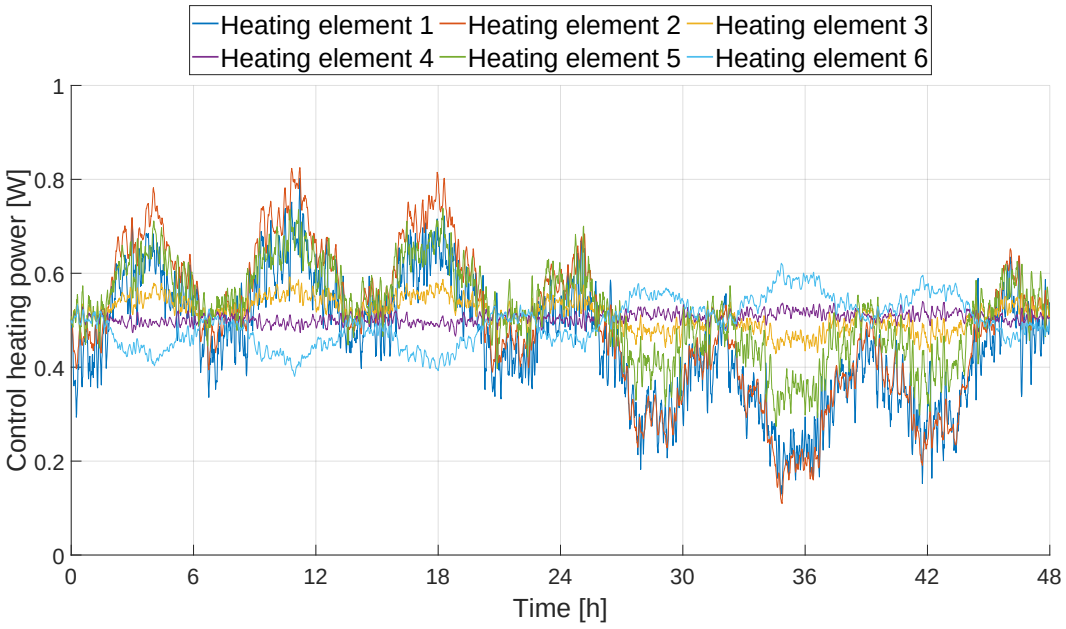

(a) Simulation

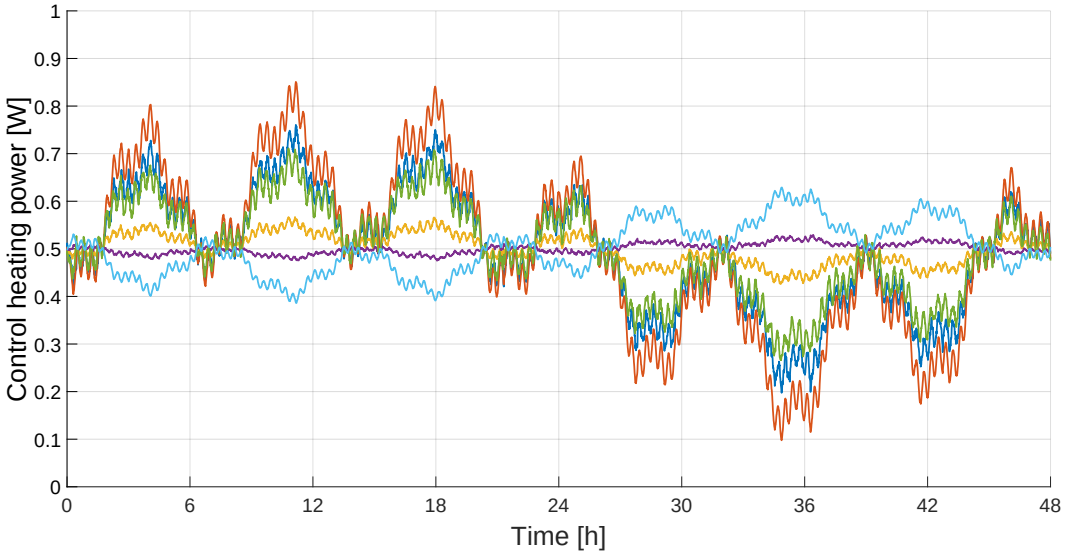

(b) Experiment

Figure 5.16 Control heating power, configuration 6 heaters

Table 5.1 summarizes the comparison made in this section between the uncontrolled and controlled case for the configuration with 6 HEs.

Table 5.1 Comparison of uncontrolled and controlled cases for 6 heater configuration

Value	**Uncontrolled**		**Controlled**		**Factor**	
	Sim.	**Exp.**	**Sim.**	**Exp.**	**Sim.**	**Exp.**
u_x	14.33 µm	17.96 µm	0.69 µm	9.67 µm	20.77	**1.86**
u_y	6.91 µm	3.12 µm	1.11 µm	1.42 µm	6.23	**2.20**
$\Delta\bar{T}$	2.68 K	2.74 K	0.28 K	0.41 K	9.57	**6.68**
ΣQ_c			1.05 W	1.15 W		

The improvements in displacements with factors around 2 and temperature stabilization with factor 6 for this configuration are slightly worse, both in simulation and experiments compared to the several cases investigated with 4 control HEs. However, achieving the desired reduction in control heating power while ensuring redundancy remains a consideration. Therefore, the use of an overdetermined system, i.e., the use of more control elements than there are degrees of freedom to control, is still noteworthy.

The evaluation of the tests with 4 HEs has shown that under certain circumstances the control contribution of some HEs is so minimal that they are barely or not at all commanded. This effect was also particularly evident in this configuration in HE 5. To ensure redundancy for technical implementation, it is sensible to use a larger number of HEs than it would be necessary for the DOFs to be controlled. However, it has also been shown that these can serve primarily as cold redundancy. An individual adaptation of the mathematical model in the event of the failure of one or more HEs can be relatively straightforward. Stabilization of the displacements remains thus possible, albeit to a lesser extent.

5.5 Effect of Temperature Sensor Failure

In Section 3.5, the selection of sensor positions and the influence of the number of sensors on mode selection and thermal field reconstruction were discussed. Although the ratio of the number of sensors to thermal modes varies for each geometry and location of the perturbation, a good initial estimate and rule of thumb should be that at least 1.5 times as many sensors as modes are needed. The number of required modes depends on the distribution of modal weights and is primarily influenced by the frequency of the perturbation. For the experimental setup used in configuration 2, 18 sensors were employed to adequately represent the 10 modes with the highest modal weight. Since the temperature field should still be reconstructed with fewer sensors, in various scenarios 2 or 3 sensors were randomly removed in the simulation. Maintaining consistent system parameters as in Section 4.3.2, an improvement in displacements was achieved in each case, which was only slightly worse than when using 18 sensors or required slightly more control heating power. These results were also confirmed in the experiments. As an example, Table 5.2 compares the uncontrolled case from Section 4.3.2.2 with a controlled case using the system parameters $\sigma_S = 0.10\,\mathrm{K}$ and $\sigma_H = 0.02\,\mathrm{W}$, where 2 sensors, S6 and S11 (refer to Figure 3.20), were not considered. It can be observed that, particularly, the averaged temperature fluctuations remain unchanged, and the required control heating power remains nearly the same. The improvements in the displacements of the controlled points range from factors of 10.74 to 13.85 for the simulation and 1.93 to 3.44 for the experiment at comparable levels.

Table 5.2 Comparison uncontrolled and controlled case with $\sigma_S = 0.10\,\mathrm{K}$ and $\sigma_H = 0.02\,\mathrm{W}$, random perturbation, 16 sensors

Value	**Uncontrolled**		**Controlled**		**Factor**	
	Sim.	**Exp.**	**Sim.**	**Exp.**	**Sim.**	**Exp.**
u_x	14.96 µm	13.99 µm	1.08 µm	4.07 µm	13.85	**3.44**
u_y	7.09 µm	2.28 µm	0.66 µm	1.18 µm	10.74	**1.93**
$\Delta\bar{T}$	2.76 K	2.79 K	0.11 K	0.11 K	25.09	**25.36**
ΣQ_c			1.23 W	1.25 W		

This indicates that for the chosen configuration, good results can be achieved even with a smaller number of sensors. On the other hand, especially in the application in a real flight experiment, redundancies in temperature measurement can be easily established. If one or more sensors fail, the mathematical model of the structure can be adjusted, and the affected sensors can thus be bypassed.

Chapter 6

Conclusions and Outlook

The main objective of the present work has been the experimental demonstration and validation of an approach for active stabilization of displacements in a structure arising from changing thermal boundary conditions. The results presented in this work indicate that the theoretical approach, validated through simulations, provides an adequate means of significantly reducing the displacements of selected points on a structure compared to an uncontrolled reference state through controlled application of heating power. Thus, the main goal has been achieved.

To validate the theoretical approach in an experimental laboratory setup, a test setup has been designed. Various components are required for this setup, which must be vacuum-compatible for use in a thermal vacuum chamber (TVC).

An aluminum alloy has been chosen as the structural material, configured as a rectangular plate suspended in a thermal vacuum chamber with a specially designed isostatic mount attached to a frame structure. In situations where a structure is intended to undergo minimal deformation due to temperature changes, as it is the case with optical benches for highly precise measuring instruments, materials with low coefficients of thermal expansion and high stiffness are employed. Glass ceramics, such as Zerodur, meet these criteria and are commonly used in the aerospace industry. However, due to the high cost of such ceramics, their demanding processing requirements, and the need for substantial deformations under minimal temperature changes for the purposes of the experiments conducted here, a metal structure has been selected. The isostatic mount has been designed using a classical Kelvin mount, allowing the structure to expand freely without stress during temperature changes. The front surface of the structure has been equipped with an artificial speckle pattern, enabling the measurement of displacements of this pattern due to deformations resulting from changes in thermal boundary conditions using an external camera system. This camera systen allows validation by quantifying the displacements through digital image correlation.

The sensor and actuator strategy required for the approach has been implemented using temperature sensors and heating elements attached to the back side of the plate. In particular, precise temperature measurement poses a significant challenge in space applications. Sensors embedded in or attached to the structure measure their own temperature with a certain level of accuracy. Since, under vacuum conditions, heat transfer from the structure to the sensor relies solely on conduction and thermal radiation, an optimal thermal connection must be ensured, while maintaining unchanged radiative properties. The most precise results have been achieved using special Pt-100 sensors, affixed with highly conductive, silver-based thermal adhesive. Kapton heating foils as actuators offer advantages such as high efficiency, straightforward modeling in simulation, and easy control with direct current power sources, available in various sizes and tailored geometries.

Concurrently with the design of the test setup, the mathematical model of the approach has to be adjusted for use in a real experiment to enable the comparison of the behavior of the structure with the digital twin. Subsequently, in the simulation, the filter and controller parameters could be adjusted to achieve the best possible improvement in the displacement of the points to be controlled, while minimizing the required control heating power. These parameters have been implemented in the experiment, and the resulting outcomes were compared with those of the simulation.

Through simulation and modeling of the test setup, it has been demonstrated that both the mounting of the plate and the isostatic support itself have a negligible impact on the steady-state temperature equilibrium of the system. Therefore, these factors can be approximated as negligible for the structural model and compensated for by calibrating the temperature sensors within the operating temperature range. To make the pertubations of the thermal equilibrium state reproducible for the tests, another heating element has been positioned on the structure, capable of representing different types of perturbations by operating at different power levels. Various configurations and setups with different perturbations and filter and controller parameters have been tested during this work, with some being examined and discussed in detail.

Before the functionality of the closed-loop filter and controller approach can be demonstrated, preliminary experiments are required to test, calibrate, and align the sensors and actuators with the model of the test setup. In conjunction with this, the thermal and thermo-optical properties of the structure, which are only available within a certain range based on literature values or influenced by the characteristics of the surface, have been determined. Subsequently, the thermal transfer functions, which form the basis of the mathematical approach, could be validated in the second step. These transfer functions represent a relation between applied heat and resulting temperature change as a function of the frequency of the heat change and can be calculated in the FEM model of the structure based on thermal conductivity, heat capacity, and emissivity of the surface. If a heat change acts on one or more surface elements in the FEM model

of the structure, and its frequency and amplitude are known, the temperature change at each node of the model can be represented as a complex number. This, in turn, can be converted into an amplitude and frequency, indicating the delay and strength with which the temperature changes at each point in the structure due to these perturbations. The response to a sinusoidal change in heating power is thus a sinusoidal temperature change, with maxima and minima occurring with a determinable time delay. The amplitude of this change and the phase of the maxima or minima at the locations in the model where temperature sensors are attached have been compared with actual measurements. For various configurations of heating elements operated with this sinusoidal perturbation and various positions of the temperature sensors, deviations between simulation and experiment averaged at most 0.6 % for phase and 4 % for amplitude. This places all values within the expected measurement accuracy and tolerance, thus demonstrating the practicality of the transfer functions in the frequency domain. In a third step, the first proof of the closed-loop filter and controller approach for active structural stabilization could be performed using the first configuration of the experimental setup.

For this purpose, the perturbation heating element has been subjected to the same sinusoidal perturbation used to demonstrate the transfer functions. The amplitude of the perturbation of 0.5 W generates temperature differences large enough to cause measurable displacements in the aluminum alloy, yet remain small enough to preserve the validity of all mathematical simplifications made, such as the linearization of radiation terms or the neglect of transient terms during Laplace transformation into the frequency domain. The perturbation period of 6 h is long enough to enable modal transformation, yet short enough to allow for numerous tests with different settings within the limited laboratory capacities when using the TVC. In this configuration, the 14 temperature sensors represent the minimum number required to utilize the ten strongest thermal modes for the reconstruction of the entire temperature field mathematically. In the Kalman filter, a continuous adjustment occurs between the temperature values calculated by the model and the actual measured values. The variation of the covariances of the measurement and process noise through variation of the standard deviations of the sensors and actuators influences how strongly the filter weights measurement and model in this comparison. Various combinations and settings have been tested throughout this work. The combinations of $\sigma_S = 0.12\,\mathrm{K}$ and $\sigma_H = 0.2\,\mathrm{W}$, as well as $\sigma_S = 0.10\,\mathrm{K}$ and $\sigma_H = 0.2\,\mathrm{W}$, have emerged as the optimal system parameters in simulations and experiments, where the displacements are most effectively compensated, with the lowest required control heating power. Thus, improvements of up to a factor of 4.4 compared to the uncontrolled reference state have been achieved in simulation, and improvements of up to a factor of 2.8 have been achieved in experiments.

In this approach, each degree of freedom is controlled by one control element. However, in the first configuration, it has been found that 2 heating elements have only a minor contribution to the total power, which is related to the limited control in the y-direction of the two reference points. Due to the geometry of the plate, the distance between the two selected points in the longitudinal direction (x-axis) is significantly greater, making the displacements occurring here much more significant in the uncontrolled case. Due to the uncertainties and inaccuracies of the model, complete compensation of the displacements is not possible. This is illustrated by the perturbation compensation method (PCM), where the contribution of all 4 control elements is pronounced. If the acting perturbation is fully known, the necessary heat power for the ideal compensation of this perturbation can be calculated mathematically using the transfer functions. This method has also been experimentally demonstrated. The temperature fluctuations measured therein have approximately been at the level of the simulated ranges beforehand. While in the simulation, the resulting displacements are fully compensated, displacements of 2 µm to 3 µm remain in the experiment. In a rough estimation, it can thus be assumed that this remainder represents the noise or the measurement accuracy with which the DIC system can be reliably used. Considering this fact, the actually achieved improvements in the displacements are even greater; they are simply not fully resolvable with this system.

For highly stable satellite structures, especially optical benches or laser terminals, a possible improvement of the displacement stability by a factor of 3, as proven with this experimental setup, is already good and could ensure that necessary requirements are met in the first place.

In this first configuration the achieved improvement factors are lower than expected, since the positions of the control heating elements and sensors for the location of the perturbation as well as the points to be controlled have not been optimized. Based on these results, a second configuration of the experimental setup has been designed with the same plate made of an aluminum alloy, with the positions of the perturbation element and the points to be stabilized unchanged. The positions of the temperature sensors have been determined based on the maximum amplitudes of the 10 thermal modes with the greatest modal weight and adjusted to be technically feasible for mounting onto the plate. The selection of the positions of the control heating elements has been made in such a way that the displacements of the two points could be reduced by the greatest possible factor while requiring the least amount of control heating power.

The aim of this optimized configuration is not only to better compensate for displacements during a sinusoidal perturbation but also to investigate behavior under random and stepped perturbations. The random perturbation is build through superposition of 5 sinusoidal perturbations with different phases, frequencies, and amplitudes, subsequently normalized to the range of 0 W to 2 W, and remained the same across all experiments for comparability. The stepped perturbation, in which the heating power

is abruptly changed at different time intervals, represents the switching on and off of energy-dissipating devices. Various system parameters have been simulated and experimentally investigated for both types of perturbations, with the parameters identified in the first configuration proving most effective for both cases.

In the simulation as well as the experiment, the displacement stability during the sinusoidal perturbation remaines unchanged due to the improved experimental setup. However, it has been observed that the improved heater positions required, on average, 50 % to 60 % less control power to achieve the same results. This suggests that operating the control heaters in the steady state could be reduced to a much smaller value, as only a narrower range of heating power is needed. The approach has been proved significantly more effective in compensating for random perturbations. Here, improvement factors of around 12 have been achieved in simulation for both spatial directions of the points to be controlled. While these improvements can not be achieved in the experiment due to the high baseline noise of the DIC system, the achieved improvements ranging from factors of 2 to 6 relative to the reference state represent a significant success, depending on the system parameters. Similar improvements have been observed in simulation and experiment for the stepped perturbation, demonstrating that not only periodic and slowly acting perturbations but also abrupt changes within a certain range are compensable.

Based on the results of the various experimental series, it can be summarized that the theoretical approach to active structural stabilization through targeted heat input could be experimentally demonstrated. Thus, the research question underlying this work has been answered.

To implement the approach in a flight test onboard a satellite, many boundary conditions need to be considered, some of which have been explicitly investigated. In addition to the choice of the specific structural material, which is usually determined or prescribed by the application, the appropriate sensor and actuator strategy is crucial. Therefore, redundancies in the use of sensors and actuators have been additionally investigated. As long as the minimum number of sensors required for reconstructing the temperature field is not undercut, the failure of individual sensors can be considered unproblematic. Adding two more control heater elements has not reduced the overall control heating power or further increased displacement stability. However, these redundancies enable better responses to perturbations that may deviate from the current model. Furthermore, entirely different sensor and actuator strategies have been analyzed or tested. Fiber optic sensors have been explored as a promising method for temperature measurement, especially in additively manufactured structures or fiber composite materials. These sensors offer the advantage of measuring temperature simultaneously at multiple points with a single fiber optic cable embedded in the structure. The main drawback of this approach is that control heater elements must be continuously operated in the system's steady state to simulate cooling by shutting

down these elements. To circumvent this issue, Peltier elements have been tested as actuators, which can both actively cool and heat depending on the direction of current flow. However, their low efficiency and the ability to effectively dissipate heat on the other side of the Peltier element when cooling the structural side pose new and significant challenges to the approach.

The potential errors arising from the rudimentary experimental setup, the isostatic mount, and especially the DIC system as an external validation tool have strongly influenced the results of the experiments. Originally, the approach has been developed to further improve an already passively highly stabilized structure. The aim has been to reduce displacements to less than 1 µm to 3 µm, well into the sub-micrometer range. Deformations at these levels can essentially only be determined punctually using certain laser measurement methods. Therefore, the demonstration in this work has been provided using an aluminum alloy, where the uncontrolled deformations are already significantly larger. Nevertheless, the accuracy of the DIC system of 1 µm to 2 µm, which can be even worse, as some experiments have shown, is a limiting factor. Potential improvements within this measurement noise cannot be resolved. Despite the fact that the simulated and experimentally determined temperature profiles and control heating powers are nearly identical, especially for random and stepped perturbations, there remain some significant differences in determining displacements due to these uncertainties.

Thus, the technical implementation of the approach and the experimental setup allow for some improvements and recommendations for further work.

Depending on the previously discussed improvements in the experimental setup and the selection of a different validation system, the next step could involve testing a different geometry or structure, possibly in conjunction with a different type of passive structural stabilization. Meta-materials or PCMs, mentioned earlier in this work, are potential candidates for such investigations. By combining the active method presented here with passive methods, even more realistic test conditions for in-orbit validation could be achieved. If fiber optic sensors, such as FBGs, are embedded into such an additively manufactured structure, the method of comparison measurement presented in Section 5.2 can be used to directly measure not only temperatures but also displacements. This can serve as both another validation method of the approach and a means to change the mathematical model of the framework, allowing for direct measurements of displacements to determine the overall deformation of the structure.

In the approach presented here, only changes due to heat conduction and thermal radiation are considered, which is plausible for an application on a satellite under vacuum conditions, which is why all tests are conducted in a TVC. However, an additional adjustment of the mathematical model to account for convection could also be possible, in case the approach should be demonstrated for ground conditions without using a TVC. Since modeling free convection can become nonlinear and thus very complex, one possi-

bility would be to add forced convection. Initial experiments with a small wind tunnel have already been conducted and investigated during this work. However, it should be noted that due to the air flow, which can also be linearized and thus considered in the form of transfer functions, a very rapid and steady temperature equalization occurs on the structure. Any temperature gradients that produce different deformations in the structure, which are easier to detect, are therefore dampened, further complicating validation.

Furthermore, instead of a heating element to simulate changes in boundary conditions, the deliberate changes through thermal radiation on a surface of the structure could also be investigated. This could be realized, for example, by a solar simulator. However, since the institute's TVC has only one viewport that is transparent to wavelengths in the optical spectrum, this approach has not been pursued here because this viewport is needed for validation using the DIC system. However, if this validation is done in another way, this viewport can be used for the solar simulator. This would enable another, more realistic tests of the approach.

The objective of this dissertation has been to validate the approach developed and simulated in [6]. Therefore, a deliberate decision was made to avoid modifying the underlying mathematical models, despite the potential improvements that certain adjustments might bring. For example, instead of using hexahedral elements as the dominant elements in the FEM modeling, shell elements could have been used, which are particularly suitable for small thickness-to-length ratios of an element, as in the case of the plate used here. A typical LQR has been employed as controller for this framework. At this point, another MIMO approach (e.g. PID) might yield better results. Instead of using more HEs than necessary according to the number of DOFs, as it has been discussed and evaluated in Section 5.4 to achieve redundancy or reduce the required overall performance, an entirely different approach could be considered. In this alternative approach, rather than controlling each DOF individually, a global requirement for the displacements as a whole would be controlled. This would lead to the need for fewer HEs than DOFs to be controlled, which could significantly reduce complexity, especially in structures with many such DOFs, although it would likely result in lower stabilization compared to the current approach. Depending on the type of criteria and boundary conditions (available power on the satellite for controlling the HEs, positioning constraints due to structural limitations), a reduction in stability might be acceptable.

In cases where periodic perturbations of the thermal boundary conditions repeatedly affect the system, such as those caused by the orbit or the cyclical activation of payloads dissipating heat, the approach presented here could be augmented by a deep learning algorithm. This algorithm would evaluate the effectiveness of the stabilization improvements achieved by the approach in each cycle, thereby generating optimization options.

Bibliography

[1] European Space Agency, ESA Books, ed. *PLATO: Revealing habitable worlds around solar-like stars, Definition Study Report*. 2017. URL: https://platomission.files.wordpress.com/2018/05/plato2-rb.pdf.

[2] R. Lindberg et al. "Preliminary results on the internal assessment study of the ESA Cosmic Vision mission PLATO". In: *Instruments, Methods, and Missions for Astrobiology XI*. Ed. by R. B. Hoover, G. V. Levin, A. Y. Rozanov, and P. C. Davies. SPIE Proceedings. SPIE, 2008, 70970F. DOI: 10.1117/12.793353.

[3] R. P. Kornfeld et al. "GRACE-FO: The Gravity Recovery and Climate Experiment Follow-On Mission". In: *Journal of Spacecraft and Rockets* 56.3 (2019), pp. 931–951. ISSN: 1048-5104. DOI: 10.2514/1.A34326.

[4] L. Buinhas, K. Frankl, H. Linz, and R. Förstner. "IRASSI infrared space interferometer: Formation geometry and relative dynamics analysis". In: *Acta Astronautica* 153 (2018), pp. 394–409. ISSN: 00945765. DOI: 10.1016/j.actaastro.2018.02.005.

[5] E. Ferrer, L. Buinhas, and R. Förstner. "System Design and Thermal Stability Analysis for the IRASSI Infrared Space Interferometer". In: *AIAA SPACE 2016*. Reston, Virginia: American Institute of Aeronautics and Astronautics, 9132016. ISBN: 978-1-62410-427-5. DOI: 10.2514/6.2016-5496.

[6] E. Ferrer Gil. "Framework for active stabilization of thermomechanical distortions in space structures". Dissertation. Neubiberg: Universität der Bundeswehr München, January 2019.

[7] R. Förstner and E. Ferrer Gil. "Method for thermomechanically stabilizing an apparatus, control unit, thermomechanical control system, and apparatus". EP 3502711 (A1). 2019.

[8] F. Möller, J. Grundhöfer, L. Maschino, A. Schmidt, and R. Förstner. "Initial validation of a closed loop filter and controller approach for active stabilization of thermomechanical distortions". In: *73rd International Astronautical Congress (IAC) Paris, France, 18th - 22nd September 2022*.

[9] F. Möller, J. Grundhöfer, L. Maschino, A. Schmidt, and R. Förstner. "Initial validation of a closed loop filter and controller approach for active stabilization of thermomechanical distortions". In: *Acta Astronautica* 213 (2023), pp. 90–101.

ISSN: 00945765. DOI: 10.1016/j.actaastro.2023.08.041. URL: https://www.sciencedirect.com/science/article/pii/S0094576523004472.

[10] F. Möller, T. Essig, S. Holzhauer, and R. Förstner. "Experimenteller Nachweis eines Ansatzes zur aktiven Strukturstabilisierung von Satellitenstrukturen gegenüber zufälligen Störungen der thermalen Randbedingungen mittels eines geschlossenen Filter- und Regleransatzes". In: *DLRK 2022 proceedings: Deutscher Luft- und Raumfahrtkongress (DLRK) 2022, Dresden, Germany*. Dresden: Deutsche Gesellschaft für Luft- und Raumfahrt (DGLR), 2022.

[11] F. Möller, T. Essig, S. Holzhauer, and R. Förstner. "Experimental demonstration of a method to actively stabilize satellite structures against random perturbations of thermal boundary conditions using a closed-loop filter and controller approach". In: *CEAS Space Journal* (2023), pp. 1–18. ISSN: 1868-2510. DOI: 10.1007/s12567-023-00514-y. URL: https://link.springer.com/article/10.1007/s12567-023-00514-y.

[12] F. Möller, E. Franzen, S. Holzhauer, and R. Förstner. "Modellierung, Analyse und Erprobung von Sensor- und Aktuatorstrategien für die aktive Strukturstabilisierung". In: *DLRK 2023 proceedings: Deutscher Luft- und Raumfahrtkongress (DLRK) 2032, Stuttgart, Germany*. Deutsche Gesellschaft für Luft- und Raumfahrt - Lilienthal-Oberth e.V., Bonn, 2023. DOI: 10.25967/610249. URL: https://publikationen.dglr.de/?tx_dglrpublications_pi1%5bdocument_id%5d=610249.

[13] J. Bachmann et al. "SeRANIS: In-Orbit-Demonstration von Spitzentechnologie auf einem Kleinsatelliten". In: *Deutscher Luft- und Raumfahrtkongress (71., 2022, Dresden)*. 2022.

[14] E. G. Wolff. *Introduction to the dimensional stability of composite materials*. Lancaster, PA: DEStech Publications, 2004. ISBN: 9781615830978.

[15] B. P. Dolgin, J. Moacanin, and T. P. O'Donnell. "Theoretical limits of dimensional stability for space structures". In: *Optomechanics and Dimensional Stability*. Ed. by R. A. Paquin and D. Vukobratovich. SPIE Proceedings. SPIE, 1991, p. 229. DOI: 10.1117/12.48859.

[16] H. D. Baehr and K. Stephan. *Wärme- und Stoffübertragung*. Berlin, Heidelberg: Springer Berlin Heidelberg, 2010. ISBN: 978-3-642-05500-3. DOI: 10.1007/978-3-642-10194-6.

[17] F. Zhang, L. Liu, X. Lv, Y. Liu, and J. Leng. "Properties of Smart Adaptive Composite Materials". In: *Smart composite coatings and membranes*. Ed. by M. F. Montemor. Woodhead Publishing series in composites science and engineering. Amsterdam, Boston, and Cambridge: Elsevier/WP Woodhead Publishing, 2016, pp. 3–31. ISBN: 9781782422839. DOI: 10.1016/B978-1-78242-283-9.00001-4.

[18] J. Jortner and N.S. Priya. "Applications of Carbon/Carbon Composites". In: *Comprehensive composite materials II*. Ed. by A. Johnson, C. Soutis, P. W. Beaumont, and C. H. Zweben. Vol. 5. Amsterdam, Boston, and Heidelberg: Elsevier, 2017, pp. 421–436. DOI: 10.1016/B978-0-12-803581-8.10101-8.

[19] W. Z. Hai Nguyen and Hiroshi Mutsuyoshi. “Hybrid Polymer Composites for Structural Applications”. In: *Hybrid Polymer Composite Materials*. Ed. by Vijay Kumar Thakur, Manju Kumari Thakur and Asokan Pappu. Cambridge: Woodhead Publishing, 2017, pp. 35–51. ISBN: 978-0-08-100785-3.

[20] M. Askari et al. “Additive manufacturing of metamaterials: A review”. In: *Additive Manufacturing* 36 (2020), p. 101562. ISSN: 22148604. DOI: 10.1016/j.addma.2020.101562. URL: https://www.sciencedirect.com/science/article/pii/S2214860420309349.

[21] W. Cai and V. Shalaev. *Optical Metamaterials: Fundamentals and Applications*. New York, NY: Springer New York, 2010. ISBN: 978-1-4419-1150-6. DOI: 10.1007/978-1-4419-1151-3.

[22] A. A. Zadpoor. “Mechanical meta-materials”. In: *Materials Horizons* 3.5 (2016), pp. 371–381. ISSN: 2051-6347. DOI: 10.1039/C6MH00065G.

[23] D. G. Gilmore. *Spacecraft Thermal Control Handbook: Volume I: Fundamental Technologies*. 2. ed. Vol. 1. El Segundo, Calif.: The Aerospace Corporation, 2002. ISBN: 188498911X.

[24] D. Wild, J. Schrezenmeier, M. Czupalla, and R. Förstner. “Thermal Characterization of additive manufactured Integral Structures for Phase Change Applications”. In: (2020). URL: http://ttu-ir.tdl.org/handle/2346/86394.

[25] D. Wild, M. Czupalla, and R. Foerstner. “Modeling, Prediction and Test of Additive Manufactured Integral Structures with Embedded Lattice and Phase Change Material Applying Infused Thermal Solutions (ITS)”. In: (2021). URL: https://ttu-ir.tdl.org/handle/2346/87104.

[26] D. Döring, P. J. Hein, and C. Spiessberger. “Temperature measurements in thermal-vacuum tests for spacecraft qualification – possibilities for infrared thermography”. In: *e-Journal of Nondestructive Testing* 22.02 (2017). URL: https://www.ndt.net/search/docs.php3?id=20682.

[27] F. Bernhard. *Handbuch der Technischen Temperaturmessung*. Berlin, Heidelberg: Springer Berlin Heidelberg, 2014. ISBN: 978-3-642-24505-3. DOI: 10.1007/978-3-642-24506-0.

[28] R. Kashyap. *Fiber Bragg gratings*. 2nd ed. Optics and photonics. Burlington, MA: Academic Press, 2010. ISBN: 9780080919911. URL: http://www.sciencedirect.com/science/book/9780123725790.

[29] K. O. Hill and G. Meltz. “Fiber Bragg grating technology fundamentals and overview”. In: *Journal of Lightwave Technology* 15.8 (1997), pp. 1263–1276. ISSN: 07338724. DOI: 10.1109/50.618320.

[30] S. J. Mihailov. “Fiber Bragg grating sensors for harsh environments”. In: *Sensors (Basel, Switzerland)* 12.2 (2012), pp. 1898–1918. DOI: 10.3390/s120201898.

[31] S. Katzir. *The Beginnings of Piezoelectricity: A Study in Mundane Physics*. Vol. 246. Dordrecht: Springer Netherlands, 2006. ISBN: 978-1-4020-4669-8. DOI: 10.1007/978-1-4020-4670-4.

[32] K. Hoffmann. *An introduction to stress analysis and transducer design using strain gauges*. HBM Test and Measurement, 2012. URL: https://www.hbm.com.

[33] Telemeter Electronic GmbH. Ed. by Telemeter Electronic GmbH. Donauwörth, 2021. URL: https://telemeter.info/de/temperaturmanagement/heizfolien/heizfolien/kapton-heizfolien (visited on 01/02/2024).

[34] A. Kohlhase, R. Schlitt, and J. Doyé. "Thermalkontrolle". In: *Handbuch der Raumfahrttechnik*. Ed. by W. Ley, K. Wittmann, and W. Hallmann. München: Carl Hanser Verlag GmbH & Co. KG, 2019, pp. 299–333.

[35] A. Hoferichter; TEC Microsystems. *Thermoelectic Coolers Introduction - the Basics*. 2023. URL: https://www.tec-microsystems.com/faq/thermoelectic-coolers-intro.html (visited on 05/26/2024).

[36] E. H. Anderson and N. W. Hagood. "Simultaneous Piezoelectric Sensing/Actuation: Analysis And Application To Controlled Structures". In: *Journal of Sound and Vibration* 174.5 (1994), pp. 617–639. ISSN: 0022460X. DOI: 10.1006/jsvi.1994.1298.

[37] S. Kaliszky et al. *Smart Structures*. Vol. 429. Vienna: Springer Vienna, 2001. ISBN: 978-3-211-83681-1. DOI: 10.1007/978-3-7091-2686-8.

[38] D.-X. Li and R. Xu. "Optimal Design and Control of Smart Space Structures: A Memetic Evolution Approach". In: *IEEE Intelligent Systems* 29.1 (2014), pp. 40–46. ISSN: 1541-1672. DOI: 10.1109/MIS.2013.26.

[39] H. S. TZOU, H.-J. LEE, and S. M. ARNOLD. "Smart Materials, Precision Sensors/Actuators, Smart Structures, and Structronic Systems". In: *Mechanics of Advanced Materials and Structures* 11.4-5 (2004), pp. 367–393. ISSN: 1537-6494. DOI: 10.1080/15376490490451552.

[40] D. Huber; Huber Kältemaschinenbau AG. *Betriebsanleitung: Unistat® 930w*. 2024. URL: https://www.huber-online.com/fileadmin/user_upload/huber-online.com/download_center/Betriebsanleitungen/BAL_Unistat_Standard_DE.pdf (visited on 05/26/2024).

[41] Dantec Dynamics. *Digital Imagine Correlation System (Q-400) with ISTRA-4D*. 2024. URL: www.dantecdynamics.com/solutions/digital-image-correlation-dic/ (visited on 05/26/2024).

[42] F. Heinricht; SCHOTT AG. *ZERODUR® Zero Expansion Glass Ceramic*. 2024. URL: https://www.schott.com/en-sg/products/zerodur-p1000269/downloads (visited on 05/26/2024).

[43] R. Gleich; Gleich Aluminiumwerk GmbH. *Produktdatenblatt EN AW 7075 Aluminium Walzplatte*. 2024. URL: https://gleich.de/de/produkte/en-aw-7075 (visited on 05/26/2024).

[44] Kruis, Johannes Richard Cornelis Geerit. *Design, analysis, testing and applications of two-body and three-body kinematic mounts*. 2016. DOI: 10.5075/EPFL-THESIS-7005.

[45] L. C. Hale and A. H. Slocum. "Optimal design techniques for kinematic couplings". In: *Precision Engineering* 25.2 (2001), pp. 114–127. ISSN: 01416359. DOI: 10.1016/S0141-6359(00)00066-0.

[46] C. H. Schouten, P. Rosielle, and P. Schellekens. "Design of a kinematic coupling for precision applications". In: *Precision Engineering* 20.1 (1997), pp. 46–52. ISSN: 01416359. DOI: 10.1016/S0141-6359(97)00002-0. URL: https://www.sciencedirect.com/science/article/pii/S0141635997000020.

[47] A. H. Slocum and A. Donmez. "Kinematic couplings for precision fixturing — Part 2: Experimental determination of repeatability and stiffness". In: *Precision Engineering* 10.3 (1988), pp. 115–122. ISSN: 01416359. DOI: 10.1016/0141-6359(88)90029-3. URL: https://www.sciencedirect.com/science/article/pii/0141635988900293.

[48] J. C. Maxwell. *The Scientific Papers of James Clerk Maxwell*. Cambridge University Press, 2011. ISBN: 9781108015387. DOI: 10.1017/CBO9780511710377. URL: https://www.cambridge.org/core/books/scientific-papers-of-james-clerk-maxwell/6C1B3B403BBCBC9B5CBB72256F09127F#.

[49] A. J. Hart, A. H. Slocum, and P. Willoughby. "Kinematic coupling interchangeability". In: *Precision Engineering* 28.1 (2004), pp. 1–15. ISSN: 01416359. DOI: 10.1016/S0141-6359(03)00071-0. URL: https://www.sciencedirect.com/science/article/pii/S0141635903000710.

[50] A. de Rooij. *SPACEMATDB - Space Material DataBase*. URL: https://www.spacematdb.com/spacemat/datasearch.php?name=PTFE (visited on 05/26/2024).

[51] Auer Kunststofftechnik GmbH Co. KG. *Werkstoffdatenblatt Polytetrafluorethylen (PTFE)*. Ed. by Auer Kunststofftechnik GmbH Co. KG. 2023. URL: http://www.auer-kunststofftechnik.de/pdf/Datenblatt%20PTFE.PDF (visited on 04/17/2023).

[52] T. Axsom. *Teflon (Polytetrafluoroethylene) PTFE and the Coefficient of Friction*. 2023. URL: https://www.fictiv.com/articles/teflon-polytetrafluoroethylene-ptfe-and-the-coefficient-of-friction (visited on 05/26/2024).

[53] W. Ley, K. Wittmann, and W. Hallmann, eds. *Handbuch der Raumfahrttechnik*. 5th ed. München: Carl Hanser Verlag GmbH & Co. KG, 2019. DOI: 10.3139/9783446457232.fm. URL: http://dx.doi.org/10.3139/9783446457232.fm.

[54] R. Lichtenberger. *Q-400 Bildkorrelation*. Ed. by LIMESS Messtechnik und Software GmbH. Krefeld, 2021. URL: https://www.limess.com/de/produkte/q400-bildkorrelation#documents-downloads (visited on 01/02/2024).

[55] D. Polle; DIAL GmbH. *Effizienz von LEDs*. Lüdenscheid, 2024. URL: https://www.dial.de/article/effizienz-von-leds-die-hoechste-lichtausbeute-einer-weissen-led/ (visited on 05/26/2024).

[56] E. Lavretsky and K. A. Wise. *Robust and Adaptive Control: With Aerospace Applications*. Advanced Textbooks in Control and Signal Processing. London: Springer, 2013. ISBN: 9781447143956. DOI: 10.1007/978-1-4471-4396-3. URL: http://dx.doi.org/10.1007/978-1-4471-4396-3.

[57] J. Lunze. *Regelungstechnik 2*. Berlin, Heidelberg: Springer Berlin Heidelberg, 2010. ISBN: 978-3-642-10197-7. DOI: 10.1007/978-3-642-10198-4.

[58] A. E. Bryson and Y.-C. Ho. *Applied optimal control: Optimization, estimation and control*. Rev. print. A Halsted Press book. Washington, DC: Hemisphere Publ, 1975. ISBN: 0470267747.

[59] G. F. Franklin, J. D. Powell, and M. L. Workman. *Digital control of dynamic systems*. 3. ed., reprinted with corrections. Half-Moon Bay, CA: Ellis-Kagle Press, 2014. ISBN: 0979122619.

[60] Heraeus. *Platin-Temperatursensor in Dünnschichttechnik*. Ed. by Heraeus. 2024. URL: https://cdn-reichelt.de/documents/datenblatt/B400/M422_DE.pdf (visited on 05/26/2024).

[61] H. Lohninger. *Fundamentals of Statistics: Optimization Methods - Brute Force Approach*. 2024. URL: http://www.statistics4u.com/fundstat_eng/cc_optim_meth_brutefrc.html (visited on 05/26/2024).

[62] D. Hofmann. "Analyse und Korrektur systematischer, zufälliger und grober Meßfehler". In: *Handbuch Meßtechnik und Qualitätssicherung*. Vieweg+Teubner Verlag, Wiesbaden, 1983, pp. 183–210. DOI: 10.1007/978-3-663-14093-1_10. URL: https://link.springer.com/chapter/10.1007/978-3-663-14093-1_10.

[63] A. Howard; Omega Engineering GmbH. *Emissionsfaktoren: Technische Hintergrundinformationen*. URL: https://www.omega.de/techref/pdf/ti1008-emissionsfaktoren.pdf (visited on 05/26/2024).

[64] T. Bäck. *Evolutionary Algorithms in Theory and Practice*. Oxford University Press, 1996. ISBN: 9780195099713. DOI: 10.1093/oso/9780195099713.001.0001.

[65] D.-S. Kohlberger, D. Wild, S. Kasper, and M. Czupalla. "Modeling and Analyses of a Thermal Passively Stabilized LEO/GEO Star Tracker With Embedded Phase Change Material Applying the Infused Thermal Solutions (ITS) Method". In: (2021). URL: https://ttu-ir.tdl.org/items/2f1aa3e8-2dcd-4c71-ac96-5ca37196268d.

[66] E. K. Ungar and S. E. Wright. *Temporary Thermocouple Attachment for Thermal/Vacuum Testing at Non-Extreme Temperatures*. Ed. by Thermal & Fluids Analysis Workshop 2017, NASA/Johnson Space Center. 2017. URL: https://tfaws.nasa.gov/wp-content/uploads/TFAWS2017-AT-20-Presentation.pdf (visited on 05/26/2024).

[67] R. Dunwoody et al. "Thermal Vacuum Test Campaign of the EIRSAT-1 Engineering Qualification Model". In: *Aerospace* 9.2 (2022), p. 99. DOI: 10.3390/aerospace9020099.

[68] Chaluvadi V Naga Bhaskar, Subhradeep Pal, and Prasant Kumar Pattnaik. "Recent advancements in fiber Bragg gratings based temperature and strain measurement". In: *Results in Optics* 5 (2021), p. 100130. ISSN: 2666-9501. DOI: 10.1

016/j.rio.2021.100130. URL: https://www.sciencedirect.com/science/article/pii/S266695012100078X.

[69] P. M. Toet, M. P. Maniscalco, R. A. J. Hagen, H. C. Hakkesteegt, and J. Lugtenburg. "Miniature and low cost fiber Bragg grating interrogator for structural monitoring in nano-satellites". In: *International Conference on Space Optics – ICSO 2014*. Ed. by B. Cugny, Z. Sodnik, and N. Karafolas. SPIE, 10/6/2014 - 10/10/2014, p. 190. ISBN: 9781510616158. DOI: 10.1117/12.2304250. URL: https://www.spiedigitallibrary.org/conference-proceedings-of-spie/10563/2304250/Miniature-and-low-cost-fiber-Bragg-grating-interrogator-for-structural/10.1117/12.2304250.full.

[70] E. Linder. *FBG Principle*. Ed. by FBGS Technologies GmbH. 2024. URL: https://fbgs.com/technology/fbg-principle/ (visited on 05/26/2024).

[71] D. Rockberger and H. Abramovich. "Piezoelectric assisted smart satellite structure (PEASSS): an innovative low cost nano-satellite". In: *Active and Passive Smart Structures and Integrated Systems 2014*. Ed. by W.-H. Liao. SPIE Proceedings. SPIE, 2014, p. 905714. DOI: 10.1117/12.2045002.

[72] H. Oosterling. *Final Report Summary - PEASSS (Piezoelectric Assisted Smart Satellite Structure)*. 2017. URL: https://cordis.europa.eu/project/id/312216/reporting/de (visited on 05/26/2024).

[73] E. Kulu. *PEASSS (PiezoElectric Assisted Smart Satellite Structure)*. 2023. URL: https://www.nanosats.eu/sat/peasss (visited on 05/26/2024).

[74] E. Buchmann et al. "A Unit Cell with Tailorable Negative Thermal Expansion Based On a Bolted Additively Manufactured Auxetic Mechanical Metamaterial Structure: Development and Investigation". In: *Proceedings of the Munich Symposium on Lightweight Design 2021*. 2021, pp. 198–211. URL: https://www.springerprofessional.de/en/a-unit-cell-with-tailorable-negative-thermal-expansion-based-on-/23341898 (visited on 05/26/2024).

[75] E. Buchmann, I. Prestes, B. Musil, and P. Höfer. "Design and Investigation of a Thermoelastic Actuator with Tailored Unidirectional Thermal Expansion and Stiffness using Mechanical Metamaterials and Joule Heating Activation". In: Springer Vieweg, Cham, 2023, pp. 1–14. DOI: 10.1007/978-3-031-33758-1_1. URL: https://link.springer.com/chapter/10.1007/978-3-031-33758-1_1.

[76] S. Z. Jia. "Waste energy harvesting in sustainable manufacturing". In: *Sustainable Manufacturing Processes*. Elsevier, 2023, pp. 231–256. ISBN: 9780323999908. DOI: 10.1016/B978-0-323-99990-8.00014-X.

[77] D. Zhao and G. Tan. "A review of thermoelectric cooling: Materials, modeling and applications". In: *Applied Thermal Engineering* 66.1-2 (2014), pp. 15–24. ISSN: 13594311. DOI: 10.1016/j.applthermaleng.2014.01.074.

[78] J. T. Katsikadelis. *Dynamic Analysis of Structures*. Academic Press, 2020. ISBN: 0128186445. URL: https://www.sciencedirect.com/science/book/9780128186435.

[79] P. Steinke. *Finite-Elemente-Methode: Rechnergestützte Einführung*. 5., bearb. und erg. Aufl. Berlin: Springer Vieweg, 2015. ISBN: 3642539378. DOI: 10.1007/978-3-642-53937-4.

[80] M. Jung and U. Langer. *Methode der finiten Elemente für Ingenieure*. Wiesbaden: Springer Fachmedien Wiesbaden, 2013. ISBN: 978-3-658-01100-0. DOI: 10.1007/978-3-658-01101-7.

[81] G. P. Nikishkov. *Introduction to the finite element method*. Aizu-Wakamatsu, Japan, 2009. URL: https://citeseerx.ist.psu.edu/document?repid=rep1&type=pdf&doi=d3fc5d5051cb464be2e4238f18ddf54d40576ddb (visited on 05/26/2024).

[82] D. Jackèl. *Grafik-Computer: Grundlagen, Architekturen und Konzepte computergrafischer Sichtsysteme*. Berlin and Heidelberg: Springer, 1992. ISBN: 978-3-662-07546-3. DOI: 10.1007/978-3-662-07546-3. URL: http://dx.doi.org/10.1007/978-3-662-07546-3.

[83] A. Quarteroni, R. Sacco, and F. Saleri. *Numerische Mathematik 2*. Springer-Lehrbuch. Berlin, Heidelberg and s.l.: Springer Berlin Heidelberg, 2002. ISBN: 9783642561917. DOI: 10.1007/978-3-642-56191-7. URL: http://dx.doi.org/10.1007/978-3-642-56191-7.

[84] R. Marchthaler and S. Dingler. *Kalman-Filter: Einführung in die Zustandsschätzung und ihre Anwendung für eingebettete Systeme*. Lehrbuch. Wiesbaden: Springer Vieweg, 2017. ISBN: 9783658167271.

[85] G. Ludyk. *Theoretische Regelungstechnik 2: Zustandsrekonstruktion, optimale und nichtlineare Regelungssysteme*. Springer-Lehrbuch. Berlin and Heidelberg: Springer, 1995. ISBN: 9783642793912. DOI: 10.1007/978-3-642-79391-2. URL: http://dx.doi.org/10.1007/978-3-642-79391-2.

[86] N. Assimakis and M. Adam. "Kalman Filter Riccati Equation for the Prediction, Estimation, and Smoothing Error Covariance Matrices". In: *International Scholarly Research Notices* 2013 (2013). DOI: 10.1155/2013/249594. URL: https://www.hindawi.com/journals/isrn/2013/249594/.

[87] R. Förstner. "Thermalhaushalt von Satelliten, Apparatives Praktikum Raumfahrttechnik - Versuch 1". Vorbereitungsskriptum. Neubiberg: Universität der Bundeswehr München, 2023.

[88] Deutsches Kupferinstitut. *Produktdatenblatt Kupfer*. Ed. by Deutsches Kupferinstitut. 2019. URL: https://www.kupferinstitut.de/wp-content/uploads/2019/11/Cu-ETP.pdf (visited on 05/26/2024).

[89] innovatek OS GmbH. *Data sheet - Properties and technical information: innovatek High Silver Thermal adhesive*. Ed. by innovatek OS GmbH. 2022. URL: https://www.webshop-innovatek.de/media/pdf/81/e7/fb/Datenblatt-High-Silver-W-rmeleitkleber-Englisch.pdf (visited on 05/26/2024).

[90] S. Messlinger. *Zur Temperaturmessung mit Platin-Widerstandsthermometern und Prema 5017 DMM*. Ed. by Universität Bayreuth. Bayreuth, 2013. URL: https://epub.uni-bayreuth.de/43/1/tmeas-dossier.pdf (visited on 05/26/2024).

[91] N. A. Fishwick, K. A. Smith, and J. A. R. Perez. *Lessons Learned from Thermal Vacuum Testing of LISA Pathfinder over three system level Thermal Tests*. 45th International Conference on Environmental Systems, 2015. URL: https://ttu-ir.tdl.org/handle/2346/64502?show=full.

[92] I. GW Instruments. *INSTRUNET DATA ACQUISITION*. 2023. URL: http://www.gwinst.com/index.html (visited on 05/26/2024).

[93] F. Puente León. *Messtechnik: Grundlagen, Methoden und Anwendungen*. Berlin: Springer Vieweg, 2019. ISBN: 3662597667.

[94] J. Hilsmann; measX GmbH & Co. KG. *DASYLab: Allroundsoftware für die Messtechnik*. 2024. URL: https://www.measx.com/de/produkte/software/dasylab (visited on 05/26/2024).

[95] J. Titus. "Engineers warm up to IR vision". In: *EDN* (2007). URL: https://www.edn.com/engineers-warm-up-to-ir-vision/ (visited on 05/26/2024).

[96] D. K. Singh, S. Donovan, E. R. Pardyjak, and T. J. Garrett. "A differential emissivity imaging technique for measuring hydrometeor mass and type". In: *Atmospheric Measurement Techniques* 14.11 (2021), pp. 6973–6990. DOI: 10.5194/amt-14-6973-2021.

[97] W. Weissgerber. *Elektrotechnik für Ingenieure 1: Gleichstromtechnik und Elektromagnetisches Feld. Ein Lehr- und Arbeitsbuch für das Grundstudium*. 8th ed. Vieweg + Teubner, 2009. ISBN: 978-3-8348-047. URL: https://link.springer.com/content/pdf/10.1007/978-3-8348-9246-1.pdf (visited on 05/26/2024).

[98] M. Papageorgiou, M. Leibold, and M. Buss. *Optimierung*. Berlin, Heidelberg: Springer Berlin Heidelberg, 2012. ISBN: 978-3-540-34012-6. DOI: 10.1007/978-3-540-34013-3.

Appendix A

Mathematical Framework for Active Structural Stabilization

Within the following subsections, the mathematical derivations of the thermal and mechanical problems are briefly explained. The detailed calculation paths can be taken from [6].

The FEM represents a numerical solution method for various types of problems that can be described as partial differential equations. Such a method must be applied if the component to be calculated is complex, so that analytical solutions do not achieve sufficient accuracy. The technical problem for a certain area of interest is therefore divided into finite small subtasks (elements), in which a sufficient accuracy of the solution can thus be achieved. These elements are represented by simple geometric shapes, such as triangles or rectangles in the two-dimensional domain or cubes, cuboids, pyramids or tetrahedra in the three-dimensional domain. Each of these elements is bounded by nodes at the corners, as well as edges and surfaces on the outside. Physical properties, such as temperature or displacement, are assigned to the nodes of the elements and interpolated by simple shape functions for the entire solid or surface element. The continuous field problem thus becomes a finite-dimensional equivalent problem by applying the FEM [78, 79, 80]. Lumped Parameter Method (LPM) is often chosen to solve thermal problems, as in the ESATAN program commonly used for aerospace industry. However, this method has its limitations in the description of mechanical problems, which is why the FEM is used in the presented approach for the combination of the thermal and mechanical problem [6, 80].

A.1 Thermal Model

The thermal model has been derived in [6] and is presented here briefly for clarification. Following the Galerkin method [81] the thermal problem for all the finite elements can be combined to

$$[C]\{\dot{T}\} + [K]\{T\} = \{R_q\}, \tag{A.1}$$

where $[C]$ is the square thermal capacity matrix, $[K]$ is the conductivity matrix, $\{T\}$ is a column vector containing the nodal temperatures and $\{R_q\}$ the heat flux vector on the elements surfaces. Next, Equation A.1 must be extended to include modeling of radiative exchange with the environment. The radiative transfer is modeled as a boundary condition of the FEM model by describing it in terms of an external heat flux acting on the external surfaces i of the elements. For this purpose, the assumption is made that the external surfaces of the elements are isothermal. In the mathematical definition of the heat flux, a distinction is made between radiation leaving the surface and radiation arriving at the surface. The heat flux of a surface element can then be calculated using the radiosity method [82] to obtain an equation for the heat flux of all surfaces according to

$$\{q_{rad}\} = [D_s]\{T_s\}^4 + \{S\}T_e^4 \tag{A.2}$$

with

$$\begin{aligned} [D_s] &= \sigma_{SBC}([I] - [F])([I] - ([I] - [\epsilon])[F])^{-1}[\epsilon] \\ \{S\} &= \sigma_{SBC}(([I] - [F])([I] - ([I] - [\epsilon])[F])^{-1}([I] - [\epsilon])\{F_e\} - \{F_e\}) \end{aligned} \tag{A.3}$$

just through the surface temperature $\{T_s\}$, the environmental temperature $\{T_e\}$, the view factor matrices $[F]$ containing the view factors between each two surface elements and $\{F_e\}$ containing the view factors between each surface element and the environment as well as the emissivity matrix $[\epsilon]$ and the Stefan-Boltzmann constant σ_{SBC}. Transforming the surface temperatures $\{T_s\}$ into nodal temperatures $\{T\}$ by applying a correlation matrix that takes into account that each surface is considered isothermal and, hence, the average of the four nodal temperatures, it is possible to express the radiation heat flux as a function of those nodal temperatures and incorporate it into Equation A.1 with $[R_r]$ as a matrix based on the surface integration at each radiating surface. Rewriting the heat flux vector $\{R_q\}$ as the product of a matrix $[R_q]$ build through the FEM shape functions and a load vector $\{q\}$, the system of equations for the solution of the thermal problem is expressed as

$$\begin{aligned} [C]\{\dot{T}\} + [K]\{T\} &= [R_q]\{q\} + [R_r]\{q_{rad}\} \\ \{q_{rad}\} &= [D]\{T\}^4 + \{S\}T_e^4. \end{aligned} \tag{A.4}$$

The approach presented in [6] solves this system of equations in the frequency domain, which is common in the field of thermal analyses in highly precise space missions such as Laser Interferometer Space Antenna (LISA). The prerequisite is that the system can be linearized around the equilibrium state, which is only valid for small temperature changes. Since this approach shall be applied to an already passively well stabilized structure, no large fluctuations in the temperature field and thus displacements are to be expected. The thermal transfer functions obtained from this linearization are validated experimentally (refer to Section 4.2). Introducing the equilibrium states

$$\{T\} = \{T_{eq}\} + \{\delta T\}, \tag{A.5}$$

$$\text{and} \quad \{q\} = \{q_{eq}\} + \{\delta q\} \tag{A.6}$$

and taking into account, that

$$\{T\}^4 = (\{T_{eq}\} + \{\delta T\})^4 = \{T_{eq}\}^4 + 4[T_{eq}]^3\{\delta T\} \tag{A.7}$$

due to linearization and the neglect of all terms proportional to $\{\delta T\}^2$ and higher, Equation A.4 results in

$$\begin{aligned}[C]\{\dot{T}_{eq}\} + [C]\{\delta\dot{T}\} + [K]\{T_{eq}\} + [K]\{\delta T\} - [R_r][D]\{T_{eq}\}^4 \\ - 4[R_r][D][T_{eq}^3]\{\delta T\} = [R_q]\{q_{eq}\} + [R_q]\{\delta q\} + [R_r]\{S\}T_e^4.\end{aligned} \tag{A.8}$$

With the equilibrium conditions

$$\{\dot{T}_{eq}\} = 0 \tag{A.9}$$

$$\text{and} \quad [K]\{T_{eq}\} - [R_r][D]\{T_{eq}\}^4 = [R_q]\{q_{eq}\} + [R_r]\{S\}T_e^4 \tag{A.10}$$

Equation A.8 is simplified to

$$[C]\{\delta\dot{T}\} + [K]\{\delta T\} - 4[R_r][D][T_{eq}^3]\{\delta T\} = [R_q]\{\delta q\}. \tag{A.11}$$

Premultiplying by $[C]^{-1}$ from the left and using the abbreviations

$$[H_T] = [C]^{-1}([K] - 4[R_r][D][T_{eq}^3]), \tag{A.12}$$

$$[H_q] = [C]^{-1}[R_q] \tag{A.13}$$

the changes of the temperature field depend on the changes of the heat fluxes according to

$$\{\delta\dot{T}\} + [H_T]\{\delta T\} = [H_q]\{\delta q\}. \tag{A.14}$$

In order to obtain a transfer function between changes in heat fluxes and changes in temperature, a modal transformation is applied to the temperature vector using the eigenvector matrix $[\phi]$ and eigenvalue diagonal matrix $[\lambda]$ of matrix $[H_T]$ to get the

modal coordinates

$$\{\tau\} = [\phi]^{-1}\{\delta T\}. \tag{A.15}$$

Using this coordinate transformation on Equation A.14 and premultiplying $[\phi]^{-1}$ leads to

$$[\phi]^{-1}[\phi]\{\dot{\tau}\} + [\phi]^{-1}[H_T][\phi]\{\tau\} = [\phi]^{-1}[H_q]\{\delta q\}. \tag{A.16}$$

Note, that $[\phi]^{-1}[\phi] = [I]$ and $[\phi]^{-1}[H_T][\phi] = [\lambda]$, which are both diagonal matrices. Hence, Equation A.16 simplifies to

$$[I]\{\dot{\tau}\} + [\lambda]\{\tau\} = [\phi]^{-1}[H_q]\{\delta q\}. \tag{A.17}$$

By taking the Laplace transform of the time dependent variables it is possible to solve Equation A.17 after the modal transformation for $\{\tau(s)\}$, with $s = j\omega$ being the complex frequency parameter, as follows

$$\{\tau(s)\} = (s[I] + [\lambda])^{-1}[\phi]^{-1}[H_q]\{\delta q(s)\}. \tag{A.18}$$

Evaluating this linear relation between the modal coordinates $\{\tau\}$ and the heat flux results in a transfer function between the temperature change at node k and the heat flux change at surface l, that can be calculated as

$$H_{Tq}(s) = \frac{\delta T_k}{\delta q_l} = \sum_{j=1}^{N} \phi_{kj} \frac{A_{jl}}{s + \lambda_j}, \tag{A.19}$$

with A_{jl} being the value at cell jl of matrix $[\phi]^{-1}[H_q]$ and N being the modal truncation from the total number of thermal modes n_n, when the frequency s of the fluctuation is lower than 10^{-4} Hz. In that case, the thermal response can already be reconstructed from a small subset of nodes with sufficient accuracy. In [6] was shown, that the thermal field can be reconstructed with an accuracy of more than 99 % when using those 8 thermal modes out of 1000 with the highest thermal weight. The transfer function can be evaluated for a given frequency at which the perturbation occurs and for any combination of nodes and elements within the FEM model. Hence, it is possible to obtain the temperature response at any node given a heat flux at any element. This fundamental relation has been proven by experiments and presented in Section 4.2.

A.2 Mechanical Model

Analogous to the thermal model, the mechanical model was also derived in [6]. Based on Newton's 2nd law the equation of motion in matrix notation can be expressed as

$$[M_u^r]\{\delta\ddot{u}^r\} + [C_u^r]\{\delta\dot{u}^r\} + [K_u^r]\{\delta u^r\} = [F_T^r]\{\delta T\} \tag{A.20}$$

following the same transient analysis in the frequency domain with respect to an equilibrium state. The changes in displacement in all three spatial directions relative to the stationary displacement field are defined by vector $\{\delta u\}$. The matrix $[M_u^r]$ represents the mass matrix, the matrix $[C_u^r]$ the damping matrix and the matrix $[K_u^r]$ the stiffness matrix, which can all be calculated from the FEM model via shape functions. Using $[F_T^r]$ on the right-hand side of the equation, a relationship is established between the temperature field and the forces acting as a result of thermal expansion. Since the focus of the approach presented in [6] is on the pure distortion of a structure due to changes in the thermal boundary conditions, certain DOF in the structure must be constrained to allow free expansion as it would be the case on a satellite. This free-floating condition can be realized when only constraining 6 DOF corresponding to the rigid body motion. Hence, an isostatic mount needs to be implemented within the model. The index r stands for the reduced matrices and vectors due to that isostatic mount [45] in which 6 DOF are constrained at 3 points in the structure. As the displacement for those DOF is zero the corresponding rows and colums in the mechanical matrices can be deleted. The principles of isostatic mounts and kinematic couplings and how the isostatic mount is realized in this work is explained more detailed in Section 3.3.

After premultiplying Equation A.20 by $[M_u^r]$ and introducing the same modal representation as presented before the eigenvector matrix $[\vartheta]$ and eigenvalue matrix $[\gamma]$ of matrix $[M_u^r]^{-1}[K_u^r]$ can be obtained to get the modal coordinates

$$\{\eta\} = [\vartheta]^{-1}\{\delta u^r\}. \tag{A.21}$$

As the damping matrix in the model is build as a linear combination of the mass matrix and the stiffness matrix, it is possible to build a diagonal matrix expressed by

$$[\zeta] = [\vartheta]^{-1}[M_u^r]^{-1}[C_u^r][\vartheta]. \tag{A.22}$$

Taking again the Laplace transform for the time dependent variables and introducing them in Equation A.20, the resulting expression can be solved for $\{\eta(s)\}$ as

$$\{\eta(s)\} = (s^2[I] + s[\zeta] + [\gamma])^{-1}[\vartheta]^{-1}[M_u^r]^{-1}[F_T^r]\{\delta T(s)\}. \tag{A.23}$$

From Equation A.23, a transfer function can again be derived which establishes a relationship between temperature change at node k and resulting displacement change

at node i according to

$$H_{uT}(s) = \frac{\delta u_i}{\delta T_k} = \sum_{j=1}^{M} \vartheta_{ij} \frac{B_{jk}}{s^2 + \zeta_j s + \gamma_j}, \tag{A.24}$$

where B_{jk} represents the value at cell jk of matrix $[\vartheta]^{-1}[M_u^r]^{-1}[F_T^r]$. In this transfer function, the summation runs up to M mechanical modes after the truncation from the total number of mechanical modes $3n_n$ has been applied similarly to the thermal model. The applicability of this transfer function is shown in Section 4.2.

A.3 Thermomechanical Model

Equation A.19 represents the thermal transfer function between the temperature change at node k and the heat flux change at surface l. Equation A.24 gives a similar relation between temperature change at node k and resulting displacement change at node i for the mechanical representation. By combining those two relations a thermomechanical transfer function can be obtained between the displacement change at node i and the heat flux change at surface l, expressed as

$$H_{uq}(s) = \frac{\delta u_i}{\delta q_l} = \sum_{k=1}^{N} \frac{\delta u_i}{\delta T_k} \frac{\delta T_k}{\delta q_l} = \sum_{j=1}^{M} \sum_{k=1}^{N} \vartheta_{ij} \frac{C_{jk}}{s^2 + \zeta_j s + \gamma_j} \frac{A_{kl}}{s + \lambda_k}, \tag{A.25}$$

with C_{jk} being the value at cell jk of matrix $[\vartheta]^{-1}[M_u^r]^{-1}[F_T^r][\phi]$. Furthermore, due to the low frequency of thermal perturbations, the mechanical behaviour of the structure can be seen as quasi-static. Hence, Equation A.25 simplifies after the removal of the inertia and damping terms resulting in

$$H_{uq}(s) = \frac{\delta u_i}{\delta q_l} = \sum_{j=1}^{M} \sum_{k=1}^{N} \vartheta_{ij} \frac{C_{jk}}{\gamma_j} \frac{A_{kl}}{s + \lambda_k}. \tag{A.26}$$

A.4 Control Framework

The fully derived thermomechanical model of the FEM structure can be used to minimize displacements at specific nodes of that structure. The first and direct approach is to compensate a known perturbation. For this, amplitude, frequency, phase and the location of the perturbation must be precisely describable. Thus, the deformation of the structure can be calculated in the FEM model, so that the necessary control heat input can be determined directly. This approach, called perturbation compensation method, is described in Section A.4.1. In general, however, only the location of the perturbation is known, all other components are random. Therefore, sensors are necessary to measure the displacements directly or indirectly, so that a control loop can be used to calculate the necessary heat input to compensate for the corresponding

displacements. This approach, as well as the necessary modeling of the sensors and actuators, is described in Section A.4.2. In order to improve noisy measurements a Kalman filter is added as discribed in Section A.4.3. The controller responsible for calculating the required heat control input and the Kalman filter are then combined with the FEM model to develop a closed-loop formulation presented in Section A.4.4.

All derivations and approaches are taken from [6]. Nevertheless, there are many modifications in the theoretical model for the simulation, which will be discussed in more detail. Furthermore, for the experimental verification of the method, a model is needed which is able to process real measured values and to provide control outputs. The experimental model is therefore compared to the simulation model and described separately.

A.4.1 Perturbation Compensation Method

Considering the fact, that the thermomechanical transfer function obtained in Equation A.26 gives a relation between the displacement change at node i and the heat flux change at surface l all displacement changes for all nodes in the FEM model can be computed for a known heat flux change. The main advantage in the frequency-domain solution is that the influence of several heat flux changes can be described independently by a separate thermomechanical transfer function in each case. Thus, the overall response in form of a displacement results as a superposition of individual changes. This fact can be used to apply control heat fluxes in such a way that displacements at certain nodes can be canceled. Mathematically, this is simply equivalent to solving a system of linear equations. Based on Equation A.26, the displacement change δu_i at node i due to the heat flux change δq_l at surface l can be calculated as

$$\delta u_i = [H_{u_i q_l}]_s \delta q_l. \tag{A.27}$$

By adding a control heat flux δq_c at another surface of the FEM model and the corresponding thermomechanical transferfunction with respect to node i the total change in the displacement results in

$$\delta u_i = [H_{u_i q_l}]_s \delta q_l + [H_{u_i q_c}]_s \delta q_c. \tag{A.28}$$

The necessary control heat flux, which cancels the displacement at node i, can thus be calculated as

$$\delta q_c = [H_{u_i q_c}]_s^{-1} [H_{u_i q_l}]_s \delta q_l. \tag{A.29}$$

This Single Input Single Output (SISO) system, in which the displacement change for only one DOF is canceled using one control heat flux change, can be extended as desired for controlling several DOF impacted by several perturbation heat fluxes leading to a MIMO system. It is important to note, that for each DOF to be controlled one control heat flux is required.

For the experimental verification of this approach, a sinusoidal change of the heating power is introduced into the structure by a perturbation element in the further course of the work, where amplitude, frequency and phase as well as the location of the perturbation are known for the PCM. The evaluation for this case can be found in Section 4.3.1.

A.4.2 Optimal Control Method

Each DOF to be controlled in the structure requires one control element on one surface element of the FEM model. A differentiation between perturbation elements ($pert$) and control elements (c) is made in equation A.14 resulting in

$$\{\delta\dot{T}\} + [H_T]\{\delta T\} = [H_c]\{\delta q_c\} + [H_{pert}]\{\delta q_{pert}\}. \tag{A.30}$$

The dimensions of the matrices $[H_c]$ and $[H_{pert}]$ correspond to those of matrix $[H_q]$ and are build from the specific columns of that matrix. From equation A.30 the properties of a MIMO system can be derived, in which the heat fluxes represent the input variables and the temperature of the nodes within the FEM model are the output variables. Since the MIMO system is subsequently to be extended by an observer, which processes discrete-time measured values and passes them on to the control loop, equation A.30 must be discretized. The transformation from a continuous-time system to a discrete-time system can be done using a finite difference approximation. A common scheme for integration with respect to time is the Θ method [83], which is applied to equation A.30 resulting in

$$\begin{aligned}\frac{\{\delta T\}^{t+\Delta t} - \{\delta T\}^t}{\Delta t} = &- [H_T](\Theta\{\delta T\}^{t+\Delta t} + (1-\Theta)\{\delta T\}^t) \\ &+ [H_c](\Theta\{\delta q_c\}^{t+\Delta t} + (1-\Theta)\{\delta q_c\}^t) \\ &+ [H_{pert}](\Theta\{\delta q_{pert}\}^{t+\Delta t} + (1-\Theta)\{\delta q_{pert}\}^t).\end{aligned} \tag{A.31}$$

The range of values for the approximation parameter Θ is defined by $0 \leq \Theta \leq 1$. $\Theta = 0$ results in an explicit scheme. If Θ moves in the range of $0 < \Theta < 1$ the scheme is semi-implicit. For the design of the filter-controller system in this work, an implicit formulation of the scheme with $\Theta = 1$ is chosen in contrast to the semi-implicit approach used in [6]. The Θ method is necessarily stable for values between $0.5 \leq \Theta \leq 1$ [83] and has smaller displacements for higher values of Θ. The experimental setup used in this work to validate the approach has been simulated with both, implicit and semi-implicit, formulations of the differential equations. The important part in those simulations is the integration of the limitations due to the technical capabilities of the experimental setup, such as the maximum in applicable control heating power. While the required control heating power was similar in both cases, the displacement for the respective DOF is better controlled for the implicit formulation.

Substituting $\Theta = 1$ for the implicit Euler method [83] into equation A.31 and rearranging for $\{\delta T\}^{t+\Delta t}$ leads to

$$\begin{aligned}\{\delta T\}^{t+\Delta t} = &+ ([I] + \Delta t[H_T])^{-1}\{\delta T\}^t \\ &+ ([I] + \Delta t[H_T])^{-1}\Delta t[H_c]\{\delta q_c\}^{t+\Delta t} \\ &+ ([I] + \Delta t[H_T])^{-1}\Delta t[H_{pert}]\{\delta q_{pert}\}^{t+\Delta t}.\end{aligned} \tag{A.32}$$

With the substitutions

$$[\mathcal{H}_T] = ([I] + \Delta t[H_T])^{-1}, \tag{A.33}$$

$$[\mathcal{H}_c] = ([I] + \Delta t[H_T])^{-1}\Delta t[H_c], \tag{A.34}$$

$$[\mathcal{H}_{pert}] = [I] + \Delta t[H_T])^{-1}\Delta t[H_{pert}] \tag{A.35}$$

Equation A.32 can be compactly expressed as

$$\{\delta T\}^{t+\Delta t} = [\mathcal{H}_T]\{\delta T\}^t + [\mathcal{H}_c]\{\delta q_c\}^{t+\Delta t} + [\mathcal{H}_{pert}]\{\delta q_{pert}\}^{t+\Delta t}. \tag{A.36}$$

This equation can be used as a basis for developing a discrete-time control loop. A LQR is a common approach to control linear, discrete-time systems in space technology [56] and has been implemented by [6]. Figure A.1 illustrates the principle of operation of the LQR as a block diagram.

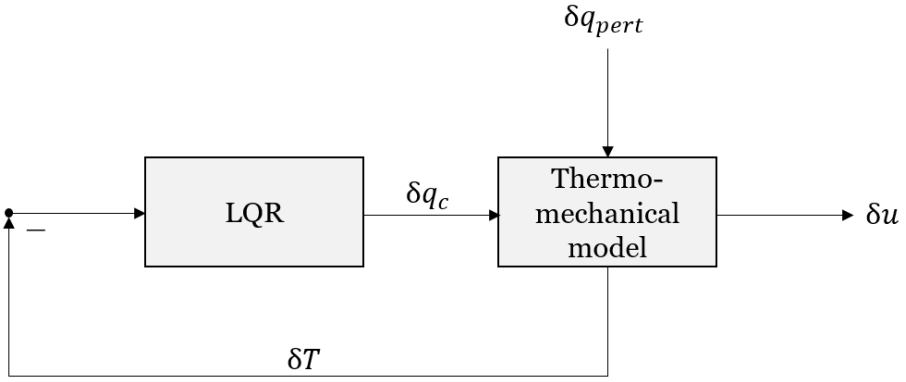

Figure A.1 Block diagram LQR

The LQR is described by a linear controlled system defined by the state space and the quadratic cost function

$$J = \int_0^\infty \left(\{Y\}^2 + \rho_W\{U\}^2\right) dt, \tag{A.37}$$

with Y being the output, U the control input and ρ_W a relative weight factor between input and output. According to equation A.37 there has to be a certain control input, so that the integrand converges to zero and the integral becomes finite.

The control input is given by the heat vector $\{\delta q_c\}$, so that

$$\rho_W \{U\}^2 = \{\delta q_c\}^T [R] \{\delta q_c\} \tag{A.38}$$

with $[R]$ being a weight matrix between each control input with respect to the output. In this work, each control HE has the same weight. Hence, $[R]$ becomes a multiple of the identity matrix. The multiplication factor must be determined by simulations and experimentally.

A special feature of the presented approach is not to cancel certain thermal modes and thus minimize the effect of thermal fluctuations on the displacement field, but to directly control the displacement at certain positions. As shown in Section A.2 the displacements of the nodes within the FEM model depend on the temperature changes. If Equation A.20 is reduced by the contributions of interia and damping, since perturbations of thermal origin can be regarded as quasi-static, the following is obtained by rearrangement

$$\{\delta u^r\} = [K_u^r]^{-1} [F_T^r] \{\delta T\} = [\mathcal{F}_T] \{\delta T\}. \tag{A.39}$$

Since only a few DOF are controlled the outputs are reduced to the associated cells of the $\{\delta u^r\}$ vector. These reduced outputs $\{\delta u^r\}_{out}$ are then also reflected in the corresponding rows of $[\mathcal{F}_T]$ according to

$$\{\delta u^r\}_{out} = [\mathcal{F}_T]_{out} \{\delta T\}. \tag{A.40}$$

Based on Equation A.40 the output Y of the cost function in Equation A.37 can be calculated as

$$\{Y\}^2 = \{\delta u\}_{out}^T \{\delta u\}_{out} = \{\delta T\}^T [\mathcal{F}_T]_{out}^T [\mathcal{F}_T]_{out} \{\delta T\} = \{\delta T\}^T [Q] \{\delta T\}, \tag{A.41}$$

where $[Q]$ is the weight matrix assigning different weights to the cells of the $\{\delta T\}$. This matrix can be scaled to the desired ratio to the weighting matrix $[R]$ of the control input. Substituting Equations A.38 and A.41 into the cost function A.37 yields to

$$J = \int_0^\infty \left(\{\delta T\}^T [Q] \{\delta T\} + \{\delta q_c\}^T [R] \{\delta q_c\} \right) dt. \tag{A.42}$$

As shown in the block diagram in Figure A.1 the LQR feedback loop applies a proportional gain to the output, so that the control input $\{\delta q_c\}$ minimizes J. Using this gain matrix the control input can be calculated as

$$\{\delta q_c\}^t = -[K_{LQR}] \{\delta T\}^t. \tag{A.43}$$

$[K_{LQR}]$ is calculated [57] in the discrete-time case according to

$$[K_{LQR}] = ([R] + [\mathcal{H}_c]^T[P][\mathcal{H}_c])^{-1}[\mathcal{H}_c]^T[P][\mathcal{H}_T]. \tag{A.44}$$

$[P]$ is the solution of the discrete-time algebraic Riccati equation

$$\begin{aligned}[P] =&[\mathcal{H}_T]^T[P][\mathcal{H}_T] + [Q] \\ &- ([\mathcal{H}_T]^T[P][\mathcal{H}_c])([R] + [\mathcal{H}_c]^T[P][\mathcal{H}_c])^{-1}([\mathcal{H}_c]^T[P][\mathcal{H}_T]),\end{aligned} \tag{A.45}$$

which can be solved iteratively or by using i.e. *MATLAB*'s own function *idare*. Substituting Equation A.43 in Equation A.36 the closed loop system of equations of the state space results in

$$\begin{aligned}([I] + [\mathcal{H}_c][K_{LQR}])\{\delta T\}^{t+\Delta t} = [\mathcal{H}_T]\{\delta T\}^t + [\mathcal{H}_{pert}]\{\delta q_{pert}\}^{t+\Delta t} \\ \{\delta u\}^{t+\Delta t} = [H]\{\delta T\}^{t+\Delta t}.\end{aligned} \tag{A.46}$$

Matrix $[H]$ describes the relation between the temperature changes and the displacement changes based on the transfer function of the mechanical model derived in equation A.24. The control loop requires complete knowledge of all nodal temperatures, which is technically impractical for an experimental implementation because not every node in the FEM model can be equipped with a temperature sensor. Hence, a sensor strategy has been developed in [6] to mathematically reconstruct the thermal field of the structure based on temperature measurements at a few specific nodes in the FEM model through sensors. Which sensors were used, how and why, is explained in Appendix B.2.

The initial equation for the thermal modal expansion is Equation A.15 from Section A.1, which defines the temperature field by

$$\{\delta T\} = [\phi]\{\tau\}. \tag{A.47}$$

Since the total temperature field $\{\delta T\}_n$ can be reconstructed for all nodes n with a sufficiently high accuracy from a reduced number of m modes with the highest weighting factors τ , only the corresponding rows and columns of the eigenvector matrix $[\phi]$ need to be evaluated. Thus, Equation A.47 can be rewritten to

$$\{\delta T\}_n = [\phi]_{n\times m}\{\tau\}_m. \tag{A.48}$$

If the temperature is measured only at the s nodes where a temperature sensor is mounted, Equation A.48 can be expressed as

$$\{\delta T_{sensors}\}_s = [\phi]_{s\times m}\{\tau\}_m. \tag{A.49}$$

The number of sensors is usually not equal to the number of modes, which makes the

matrix $[\phi]$ non-square and therefore not invertible. However, if the condition $s > m$ is valid, the pseudoinverse $[\phi]^{+}_{m\times s}$ can be formed from the reduced matrix $[\phi]_{s\times m}$. Using this pseudoinverse, the least squares solution of the modal coordinate vector can be calculated as

$$\{\bar{\tau}\}_m = [\phi]^{+}_{m\times s}\{\delta T_{sensors}\}_s. \tag{A.50}$$

Substituting Equation A.50 into A.48, an estimation of the temperature field can be obtained as

$$\{\delta\bar{T}\}_n = [\Psi]\{\delta T_{sensors}\}_s \tag{A.51}$$

using the abbreviation

$$[\Psi] = [\phi]_{n\times m}[\phi]^{+}_{m\times s}. \tag{A.52}$$

It must also be taken into account that the temperature field, which deviates from the steady state, is not only determined by the perturbation HEs, but also depends on the influence of the control HEs. Thus, the response of the system is composed of

$$\{\delta T\} = \{\delta T_{pert}\} + \{\delta T_c\}, \tag{A.53}$$

where $\{\delta T_{pert}\}$ represents the temperature changes due to the perturbation HEs and $\{\delta T_c\}$ represents the temperature changes due to the control HEs. The contribution of the perturbation is unknown and needs to be estimated, whereas the contribution of the control can be modeled by adapting Equation A.53 to

$$\{\delta\dot{T}_c\} + [H_T]\{\delta T_c\} = [H_c]\{\delta q_c\}, \tag{A.54}$$

because the control heating power $\{\delta q_c\}$ is known. As the temperature sensors measure the entire response of the system, the contribution of the control needs to be substracted before applying the thermal modal expansion and added afterwards. This results in

$$\{\delta\bar{T}\}_n = [\Psi](\{\delta T_{sensors}\}_s - \{\delta T_c\}_s) + \{\delta T_c\}. \tag{A.55}$$

The reduced vector $\{\delta T_c\}_s$ can be calculated from vector $\{\delta T_c\}$ using a mapping matrix of dimensions $s \times n$ according to

$$\{\delta T_c\}_s = [\Pi]\{\delta T_c\}. \tag{A.56}$$

Equation A.55 simplifies to

$$\{\delta\bar{T}\}_n = [\Psi]\left(\{\delta T_{sensors}\}_s - [\Pi]\{\delta T_c\}\right) + \{\delta T_c\}. \tag{A.57}$$

For modeling the system based on an actual temperature vector $\{\delta T\}$, the next step is to take into account the inaccuracies of the sensors in the form of noise, thus artificially degrading the vector, which has been done in [6]. Each sensor measurement represents a subset of the actual temperature vector with an added bias and noise. Thus, the sensor measurement can be modeled for the simulation as

$$\{\delta T_{sensors}\} = [\Pi]\left(\{\delta T\} + \{\epsilon_T\} + \{\epsilon_{\Delta T}\}\right). \tag{A.58}$$

Substituting Equation A.58 into Equation A.57 and rearranging leads to

$$\{\delta \bar{T}\}_{n_{sim}} = \Big[[I] - [\Psi][\Pi] \quad [\Psi][\Pi]\Big] \begin{Bmatrix} \{\delta T_c\} \\ \{\delta T\} + \{\epsilon_T\} + \{\epsilon_{\Delta T}\} \end{Bmatrix}. \tag{A.59}$$

For the application of the model in the real case, this step is not necessary, because the sensor measurements are inherently noisy. The challenge here is to make the sensor measurements as accurate and reproducible as possible. The steps carried out for this are described in Section B.2. The same applies to the control of the actuators. The commanded control heating powers cannot correspond exactly to the actual powers and must therefore also be adapted for adequate modeling. This step is also not necessary for the real application, since the HEs have inherent inaccuracies. For the simulation of the model, these uncertenties can be expressed as

$$\{\delta q_{applied}\} = ([I] + [\Gamma])\{\delta q_{commanded}\} + \{\delta q_{offset}\} \tag{A.60}$$

where $[\Gamma]$ is a diagonal matrix with multiplicative factors representing the standard deviation of the heater following a Gaussian distribution and $\{\delta q_{offset}\}$ is a vector with additive factors, which are negligible for electric heaters. In order to take these inaccuracies into account and compensate for them as best as possible, a Kalman filter is integrated in the next step. Characterizing the sources of error is thus necessary for the filter to work adequately in the subsequent real application.

A.4.3 Kalman Filter

The Kalman filter represents a possibility to estimate the system state in real time based on noisy measurements. Not only the variances of the observation noise, but also those of the process noise are taken into account and are weighted in the estimation. The process noise describes the inaccuracies that occur in the modeling of the system [84]. Using a Kalman filter is a two-step process: First, the system states are predicted by a model of the system dynamics. Second, the prediction is corrected using a measurement of the system states. The correction is performed by weighting the measured and modeled variables. A Kalman gain is calculated which assigns a greater weight to either the modeled or measured values. The corrected optimal estimate of the system states can then be calculated from the weighted average of these parameters [85]. A

conventional Kalman filter uses an initial estimate of the covariance matrix of noise in the prediction step, and also an adjustment of the Kalman gain and a correction of the covariance matrix of noise in the second step. However, in this work, a stationary Kalman filter will be used, which eliminates the correction of the Kalman gain as well as the prediction and the correction of the covariance matrix of the noise. Using a stationary Kalman filter is possible at this point because the state space is described by a linear and time invariant system [85].

The Kalman filter is the link in the state feedback between the thermomechanical model and the LQR. Figure A.2 shows the position of the Kalman filter in the block diagram.

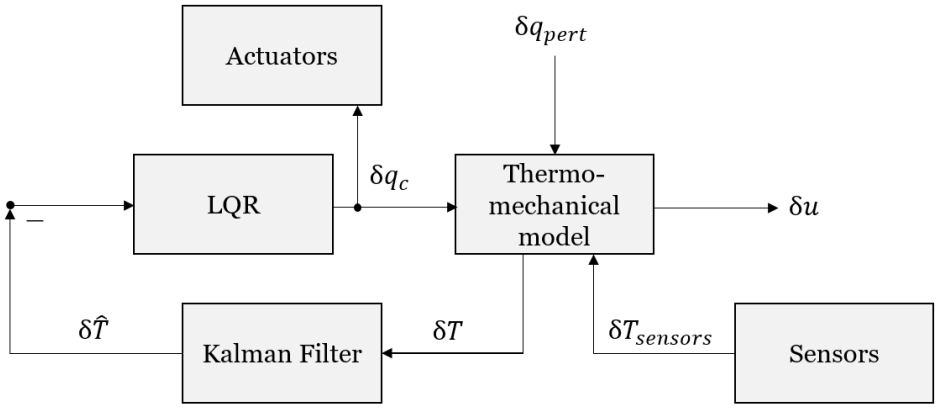

Figure A.2 Block diagram state feedback with Kalman filter

In order to implement the Kalman filter between the LQR and the thermomechanical model, sensors are required to provide measured values for the Kalman filter correction step.

Based on Equation A.32, which is restated here for clarity,

$$\begin{aligned}\{\delta T\}^{t+\Delta t} = &+ ([I] + \Delta t[H_T])^{-1}\{\delta T\}^t \\ &+ ([I] + \Delta t[H_T])^{-1}\Delta t[H_c]\{\delta q_c\}^{t+\Delta t} \\ &+ ([I] + \Delta t[H_T])^{-1}\Delta t[H_{pert}]\{\delta q_{pert}\}^{t+\Delta t},\end{aligned} \tag{A.61}$$

the prediction step as the first step in implementing a Kalman filter can be derived using the known system variables. Substituting Equation A.43 with replacing the temperature vector for the estimated temperature vector $\{\delta\hat{T}\}$ as well as the model of the uncertanties according to Equation A.60 into Equation A.61 lead after rearranging to

$$\begin{aligned}\{\delta\hat{T}\}^{t+\Delta t} = &+ ([I] + \Delta t[H_T] + \Delta t[H_c][K_{LQR}])^{-1}\{\delta\hat{T}\}^t \\ &- ([I] + \Delta t[H_T] + \Delta t[H_c][K_{LQR}])^{-1}\Delta t[H_c][\Gamma][K_{LQR}]\{\delta\hat{T}\}^{t+\Delta t} \\ &+ ([I] + \Delta t[H_T] + \Delta t[H_c][K_{LQR}])^{-1}\Delta t[H_{pert}]\{\delta q_{pert}\}^{t+\Delta t}.\end{aligned} \tag{A.62}$$

By introducing the abbreviations

$$[A^*] = ([I] + \Delta t[H_T] + \Delta t[H_c][K_{LQR}]), \tag{A.63}$$

$$[B_1^*] = -([I] + \Delta t[H_T] + \Delta t[H_c][K_{LQR}])^{-1}\Delta t[H_c], \tag{A.64}$$

$$[B_2^*] = ([I] + \Delta t[H_T] + \Delta t[H_c][K_{LQR}])^{-1}\Delta t[H_{pert}] \tag{A.65}$$

Equation A.62 can be simplified to

$$\{\delta\hat{T}\}^{t+\Delta t} = [A^*]\{\delta\hat{T}\}^t + [B_1^* \quad B_2^*]\begin{Bmatrix}[\Gamma][K_{LQR}]\{\delta\hat{T}\}^{t+\Delta t} \\ \{\delta q_{pert}\}^{t+\Delta t}\end{Bmatrix}. \tag{A.66}$$

In Equation A.66, only the left-hand summand contains known terms and is therefore suitable for an initial estimation of the vector $\{\delta\hat{T}\}^{t+\Delta t}$, so that this estimation can be calculated as

$$\{\delta\hat{T}\}_*^{t+\Delta t} = [A^*]\{\delta\hat{T}\}^t. \tag{A.67}$$

In a Kalman filter the prediction is followed by the correction with the incoming measured values, which is called innovation. This is described by

$$\{\delta\hat{T}\}^{t+\Delta t} = \{\delta\hat{T}\}_*^{t+\Delta t} + [K_K]\left(\{\delta\bar{T}\}_n^{t+\Delta t} - \{\delta\hat{T}\}_*^{t+\Delta t}\right). \tag{A.68}$$

$[K_K]$ represents the Kalman innovation gain described at the beginning of this Section, which weights the difference between estimation and measurement. Substituting Equation A.57 for the application of the model for the real case into Equation A.68 leads to

$$\begin{aligned}\{\delta\hat{T}\}^{t+\Delta t} = \{\delta\hat{T}\}_*^{t+\Delta t} + \\ [K_K]\left([\Psi](\{\delta T_{sensor}\}_s - \{\delta T_c\}_s) + \{\delta T_c\} - \{\delta\hat{T}\}_*^{t+\Delta t}\right).\end{aligned} \tag{A.69}$$

For the simulation of the model, by analogy, Equation A.59 can also be substituted into Equation A.68, so that

$$\begin{aligned}\{\delta\hat{T}\}_{sim}^{t+\Delta t} = [K_K]\left(\left[[I] - [\Psi][\Pi] \quad [\Psi][\Pi]\right]\begin{Bmatrix}\{\delta T_c\}_{sim}^{t+\Delta t} \\ \{\delta T\}_{sim} + \{\epsilon_T\} + \{\epsilon_{\Delta T}\}^{t+\Delta t}\end{Bmatrix}\right) \\ + ([A^*] - [K_K][A^*])\{\delta\hat{T}\}^t.\end{aligned} \tag{A.70}$$

The Kalman innovation gain matrix $[K_K]$ is a function of the expected noise from the actuators and sensors. The noise is in turn represented by the covariance matrices $[Q_K]$ and $[R_K]$, respectively. As the model includes control inputs, the process noise variance $[Q_K]$ is represented by the second term in the right-hand side of Equation A.66, which is known as the input transition matrix, and can be calculated as

$$[Q_K] = [B_1^* \quad B_2^*] \begin{bmatrix} \sigma_1^2 & & & & & & \\ & \ddots & & & & & \\ & & \sigma_i^2 & & & & \\ & & & \sigma_a^2 & & & \\ & & & & \ddots & & \\ & & & & & \sigma_j^2 \end{bmatrix} [B_1^* \quad B_2^*]^T, \tag{A.71}$$

where σ_1^2 to σ_i^2 represent the variances of the respective control HEs and σ_a^2 to σ_j^2 represent the variances of the respective perturbation HEs. $[Q_K]$ remains constant over time.

The measurement noise of the temperature sensor measurements, which is defined by the variance σ_S^2, determines the size of the covariance matrix $[R_K]$ according to

$$[R_K] = \sigma_S^2[I], \tag{A.72}$$

via a multiplication with the identity matrix $[I]$, whose dimension corresponds to the number of nodes $n \times n$, as long as all sensors have the same level of noise. This assumption is valid in the demonstrated case because all temperature sensors are of the same design. The more accurately the variances of Equations A.71 and A.72 can be determined, the better are the improved estimates of the Kalman filter.

The Kalman innovation gain $[K_K]$ can be calculated from those variances as

$$[K_K] = [P_K][C_K]^T([R_K] + [C_K][P_K][C_K]^T)^{-1} \tag{A.73}$$

and remains constant over time in this control loop because a stationary Kalman filter is used due to the linearity and time invariance of the system [85]. In the above equation, $[C_K]$ corresponds to the observation model which maps the actual state space to the observed space. As the measured temperatures are expanded through the thermal modal they match the state space. Hence, $[C_K]$ becomes the identity matrix. $[P_K]$ is the covariance matrix of the errors and can be calculated as

$$[P_K] = [A^*][P_K][A^*]^T + [Q_K] - [A^*][P_K]([R_K] + [P_K])^{-1}[P_K][A^*]^T. \tag{A.74}$$

This dicrete-time algebraic Riccati equation [85, 86] can be solved numerically using *MATLAB*'s *idare* function.

A.4.4 Closed-Loop Filter and Controller System

In Section A.4.2, a system was derived that uses an LQR to calculate the control heating power required to minimize displacements due to changes in thermal conditions at specific points in a structure. This system was extended to include a sensor and actuator model so that instead of measuring the temperature of all nodes in the FEM model, only a fraction is measured and modal expansion is used to extrapolate the temperature field of the entire structure. The measurements are enhanced by a Kalman filter. The calculations required for all these steps must now be performed simultaneously and coupled. For this purpose, a distinction between the simulation of the model, i.e. the simulation of sensor measurements as well as perturbations of the thermal boundary conditions, analogous to [6], and the application of the model for the real experiment is necessary, since in both cases different system equations have to be combined.

A.4.4.1 Simulation of the Model

For the simulation of the model, three different temperatures were used in the previous sections: The actual temperatures $\{\delta T\}$, the estimated temperatures $\{\delta\hat{T}\}$, and the temperatures $\{\delta T_c\}$ resulting from the thermal modal expansion due to the control elements. Those three vectors are coupled and have to be solved simultaneoulsy to simulate the time evolution of the system. In order to distinguish them from the application of the model, all temperature vectors are expressed with a subscript "sim".

$\{\delta T_c\}_{sim}$ can be calculated using Equation A.54 in implicit dicrete-time form in combination with Equation A.60 and is expressed as

$$([I] + \Delta t[H_T])\{\delta T_c\}_{sim}^{t+\Delta t} = \{\delta T_c\}_{sim}^{t} - \Delta t[H_c]([I] + [\Gamma])[K_{LQR}]\{\delta\hat{T}\}_{sim}^{t+\Delta t}. \quad \text{(A.75)}$$

The evolution of the actual temperatures $\{\delta T\}_{sim}$ can be calculated according to Equation A.32 in combination with Equation A.60 as

$$\begin{aligned}([I] + \Delta t[H_T])\{\delta T\}_{sim}^{t+\Delta t} = \{\delta T\}_{sim}^{t} &- \Delta t[H_c]([I] + [\Gamma])[K_{LQR}]\{\delta\hat{T}\}_{sim}^{t+\Delta t} \\ &+ \Delta t[H_{pert}]\{\delta q_{pert}\}^{t+\Delta t}.\end{aligned} \quad \text{(A.76)}$$

Finally, the estimated temperature vector $\{\delta\hat{T}\}_{sim}$ is calculated according to the Kalman filter approach described in Section A.4.3 expressed through Equation A.70 as

$$\begin{aligned}\{\delta\hat{T}\}_{sim}^{t+\Delta t} = [K_K]\left(\begin{bmatrix}[I]-[\Psi][\Pi] & [\Psi][\Pi]\end{bmatrix}\begin{Bmatrix}\{\delta T_c\}_{sim}^{t+\Delta t}\\ \{\delta T\}_{sim}+\{\epsilon_T\}+\{\epsilon_{\Delta T}\}^{t+\Delta t}\end{Bmatrix}\right)\\ +([A^*]-[K_K][A^*])\{\delta\hat{T}\}^t.\end{aligned} \tag{A.77}$$

When combining the Systems of Equations A.75, A.76 and A.77 the closed-loop simulation of the model can be expressed in matrix-vector notation as

$$\begin{aligned}&\begin{bmatrix}[I]+\Delta t[H_T] & 0 & \Delta t[H_c]([I]+[\Gamma])[K_{LQR}]\\ 0 & [I]+\Delta t[H_T] & \Delta t[H_c]([I]+[\Gamma])[K_{LQR}]\\ [K_K]([\Psi][\Pi]-[I]) & -[K_K][\Psi][\Pi] & [I]\end{bmatrix}\begin{Bmatrix}\delta T_c\\ \delta T\\ \delta\hat{T}\end{Bmatrix}_{sim}^{t+\Delta t} =\\ &\begin{bmatrix}[I] & 0 & 0\\ 0 & [I] & 0\\ 0 & 0 & [A^*]-[K_K][A^*]\end{bmatrix}\begin{Bmatrix}\delta T_c\\ \delta T\\ \delta\hat{T}\end{Bmatrix}_{sim}^{t} +\\ &\begin{bmatrix}0\\ \Delta t[H_{pert}]\\ 0\end{bmatrix}\{\delta q_{pert}\}^{t+\Delta t}+\begin{bmatrix}0\\ 0\\ [K_K][\Psi][\Pi]\end{bmatrix}(\{\epsilon_T\}+\{\epsilon_{\Delta T}\}^{t+\Delta t}).\end{aligned} \tag{A.78}$$

A.4.4.2 Application of the Model

For the application of the presented approach in the real experiment only 2 instead of 3 coupled equations are necessary. The control heating power is calculated via the estimated temperature vector of the Kalman filter $\{\delta\hat{T}\}$, which in turn only requires the vector $\{\delta T_c\}$. The actual temperature vector $\{\delta T\}$ can be omitted here, since it is not necessary for the thermal modal expansion according to Equation A.69. Furthermore, the approach is simplified since the measurement uncertainties $\{\epsilon_T\}$ and $\{\epsilon_{\Delta T}\}$ of the temperature sensors do not need to be simulated, nor does the perturbation heat flux $\{\delta q_{pert}\}$.

$\{\delta T_c\}$ can be calculated using Equation A.54 in implicit dicrete-time form in combination with Equation A.60 as well and is expressed as

$$([I]+\Delta t[H_T])\{\delta T_c\}^{t+\Delta t} = \{\delta T_c\}^t - \Delta t[H_c]([I]+[\Gamma])[K_{LQR}]\{\delta\hat{T}\}^{t+\Delta t}. \tag{A.79}$$

Substituting Equation A.67 into Equation A.69 allows the calculation of the estimated temperature vector $\{\delta\hat{T}\}$ as

$$\begin{aligned}\{\delta\hat{T}\}^{t+\Delta t} = [K_K]\left([\Psi](\{\delta T_{sensor}\}_s-\{\delta T_c\}_s)+\{\delta T_c\}\right)\\ +([A^*]-[K_K][A^*])\{\delta\hat{T}\}_*^{t+\Delta t}.\end{aligned} \tag{A.80}$$

Finally, the complete System of Equations which simultaneously solves the coupled Equations A.78 and A.79 can be expressed as

$$\begin{bmatrix} [I] + \Delta t[H_T] & \Delta t[H_c]([I] + [\Gamma])[K_{LQR}] \\ [K_K][\Psi][\Pi] - [K_K] & [I] \end{bmatrix} \begin{Bmatrix} \delta T_c \\ \delta \hat{T} \end{Bmatrix}^{t+\Delta t} = \begin{bmatrix} [I] & 0 \\ 0 & [A^*] - [K_K][A^*] \end{bmatrix} \begin{Bmatrix} \delta T_c \\ \delta \hat{T} \end{Bmatrix}^{t} + \begin{bmatrix} 0 \\ [K_K][\Psi] \end{bmatrix} \{\delta T_{sensor}\}_s^{t+\Delta t}. \tag{A.81}$$

The equations in this system are time invariant. With the abbreviations

$$[A_{kal}] = \begin{bmatrix} [I] + \Delta t[H_T] & \Delta t[H_c]([I] + [\Gamma])[K_{LQR}] \\ [K_K][\Psi][\Pi] - [K_K] & [I] \end{bmatrix}, \tag{A.82}$$

$$[B_{kal}] = \begin{bmatrix} [I] & 0 \\ 0 & [A^*] - [K_K][A^*] \end{bmatrix}, \tag{A.83}$$

$$[C_{kal}] = \begin{bmatrix} 0 \\ [K_K][\Psi] \end{bmatrix} \tag{A.84}$$

the system can be simplified and rearranged to

$$\begin{Bmatrix} \delta T_c \\ \delta \hat{T} \end{Bmatrix}^{t+\Delta t} = [A_{kal}]^{-1}[B_{kal}] \begin{Bmatrix} \delta T_c \\ \delta \hat{T} \end{Bmatrix}^{t} + [A_{kal}]^{-1}[C_{kal}]\{\delta T_{sensor}\}_s^{t+\Delta t}. \tag{A.85}$$

The matrices $[A_{kal}]$, $[B_{kal}]$ and $[C_{kal}]$ can be preprocessed for a specific test setup with specific system parameters. For each new measurement, Equation A.85 can be solved to determine a new temperature vector. Equation A.43 can then be used to directly determine the necessary control heating power $\{\delta q_c\}$ for this new time step.

Appendix B

Experimental Setup

The experimental setup has been presented in Section 3.1. This chapter aims to describe the laboratory setup required around the experimental test setup, as well as going into more detail about the sensors and actuators used, their data acquisition, control and calibration.

B.1 TVC and PCU

First, this section describes the relevant key points of vacuum technology and the resulting setup of the institute's TVC [87]. A TVC is individually constructed depending on the field of application and the resulting requirements for the pressure range to be achieved. The following Table B.1 designates the categories of different vacuums according to prevailing pressure. The TVC used for the experiments reaches the upper limit of the high vacuum with a pressure of 10^{-7} mbar.

Table B.1 Categories of different vacuums

Categorie	**Pressure range**
low (rough) vacuum	10^{3} mbar - 1 mbar
medium (fine) vacuum	1 mbar - 10^{-3} mbar
high vacuum	10^{-3} mbar - 10^{-7} mbar
ultra-high vacuum	below 10^{-7} mbar

The pumping system consists of various booster and main pumps, each operating in different pressure ranges, which are matched to each other and connected in series. For this purpose, the maximum achievable vacuum of the respective pump must be at least one order of magnitude greater than the required vacuum so that unavoidable microleaks as well as surface-related desorption and outgassing can be compensated.

In vacuum technology, the leakage rate is an important parameter and is described by the following equation:

$$q_{leak} = V \cdot \frac{\Delta p}{\Delta t} \tag{B.1}$$

The leakage rate q_{leak} is a measure of the leaktightness and degree of contamination of a TVC. The following example serves for an intuitive understanding of the leakage rate: An evacuated chamber with a volume V of $1\,\mathrm{m}^3$ has a leakage rate q_{leak} of $1\,\mathrm{m}^3\,\mathrm{mbar}\,\mathrm{s}^{-1}$. Thus, within a time interval Δt of 1 s the pressure Δp inside the evacuated chamber increases by 1 mbar. Since the pressure p in an evacuated chamber increases steadily, each system is characterized by a leakage rate. Therefore, the pumps must be operated continuously for constant evacuation of the TVC.

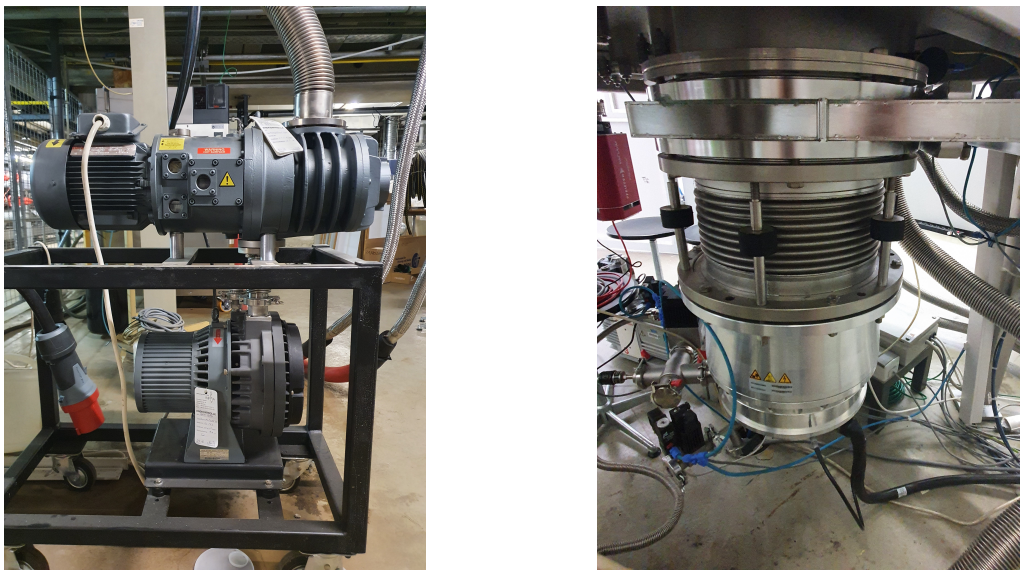

(a) Backing pumps **(b)** Main pump

Figure B.1 Pump system of laboratory setup

The pump system of the institute's own TVC consists of two backing pumps, a scroll pump, a roots pump, and a turbopump as the main pump, shown in Figure B.1. Inside the scroll pump (bottom pump in Figure B.1a), two counter-rotating spirals compress the gas volume to be pumped out and blow it out through an outlet. The scroll pump operates with low vibration and ensures an oil-free pumping chamber. By incorporating this backing pump, the start-up procedure of the downstream roots pump is improved. This roots pump (top pump in Figure B.1a) also operates according to the compression principle. Two counter-rotating pistons rotate contactlessly in a pump housing, realizing a high speed and enabling an oil-free housing. The contactless rotation causes a gap between the rotating pistons and the housing wall, through which gas backflow occurs at high pressure differentials. The core of the pump system is the turbomolecular pump (refer to Figure B.1b), whose motor operates in a fine vacuum. For this reason, the backing pumps are required, which reach this pressure level and

establish the starting condition of the main pump. The motor drives a rotor with several disks, whereby speeds of up to 75000 rpm are achieved depending on the size. Stator disks are located between the rotor disks. Slots milled at opposite angles are located in both disks, resulting in a vane effect. The suction effect of the turbomolecular pump is ensured by precisely these opposite angles of attack of the disks, since the probability of molecular movement is greater in the direction of delivery, i.e. from high vacuum to fine vacuum, than in the opposite direction due to momentum conservation.

Figure B.2 TVC with bell opened (left) and closed (right)

Figure B.2 shows the TVC with the bell opened and closed. In the open state, the black table can be seen, on which the mounting system including the test object is set up. The opening and closing of the TVC is done with the help of a crane. On the inner wall of the bell, which is also black, as well as on the underside of the table, thermofluid pipes made of copper are welded, through which the temperature control fluid flows. Figure B.3 shows a part of the copper pipes. The black coating applied to the stainless steel surfaces of the TVC provides a uniform radiation background.

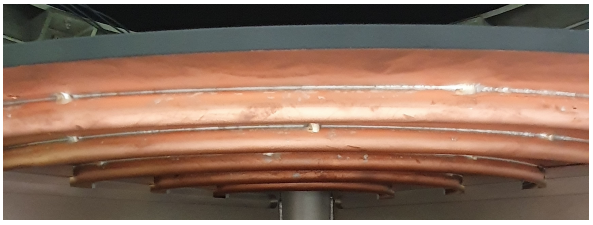

Figure B.3 Copper thermofluid pipes

The thermofluid pipes of the TVC are connected to a process cooling unit, which enables temperature control, and form a closed circuit. The unit, shown in Figure B.4, has an operating range of $-90\,°C$ to $200\,°C$. Depending on the specified temperature,

thermal energy is either extracted from or supplied to the thermal fluid via a heat exchanger [16], so that cooling or heating of the medium is achieved. A feed pump is used to pump the temperature-controlled fluid through the TVC within the closed circuit. Due to their excellent thermal conductivity, the copper pipes enable optimal heat exchange [88]. Although, according to the manufacturer, the PCU exhibits a temperature constancy of $0.05\,\mathrm{K\,min^{-1}}$ [40], temperature stability has proven to be problematic as described in Sections 3.1 and 4.3.1.

Figure B.4 Process Cooling Unit

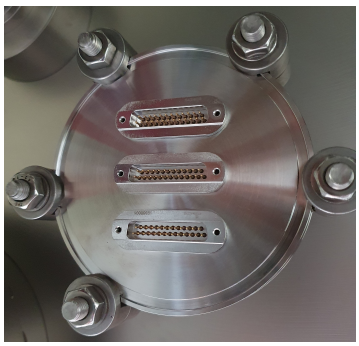

Figure B.5 Flange connection with three D-sub connectors

Sensors and actuators are attached to the aluminum plate for carrying out the experiment. The connection between the inside of the chamber and the environment is ensured by flange connections. For electrical connections, a total of five 25-pin D-sub

connectors are available on two flange connections, as shown in Figure B.5. The male connector is located outside the chamber, the female connector inside in the bottom of the vacuum chamber. In addition, flange connections with viewports of various designs are installed in the bell of the vacuum chamber.

B.2 Sensor and Actuator Technology

This section focuses on sensors and data processing as well as actuators and controls and the necessary further components of the experimental setup.

B.2.1 Sensor Technology and Data Acquisition System

For the experimental setup used in this work, infrared sensors in the form of thermal imaging cameras, for example, are not suitable because they do not achieve the required accuracy of 0.1 K and resolution. In addition, the experimental setup already requires one side of the plate to be positioned in front of a viewport for imaging with the validation system, so simultaneous filming with an IR camera is not technically feasible. Although TC are most commonly used in satellite construction, the choice for the experimental setup was RTD in the form of Pt-100 elements. This had several reasons:

1. Pt-100 sensors have a very high accuracy and can be used stably over a sufficiently wide temperature range. Although the response time of Pt-100 sensors is longer than that of TC, this plays only a minor role because the temperature changes are slow and the sensor measurements for the control loop need to be available only at discrete time steps.
2. Pt-100 sensors are inexpensive, easy and quick to obtain in large quantities. They are small and well suited for spot application to the surface of the structure to measure a nodal temperature.
3. They can be used flexibly and can be wired individually so that different connection types can be tested. Connection to a DAS is made easy by the stranded wires via a standardized screw terminal system.

Figure B.6 shows a schematic representation of the control and measurement loop connected to computer 1.

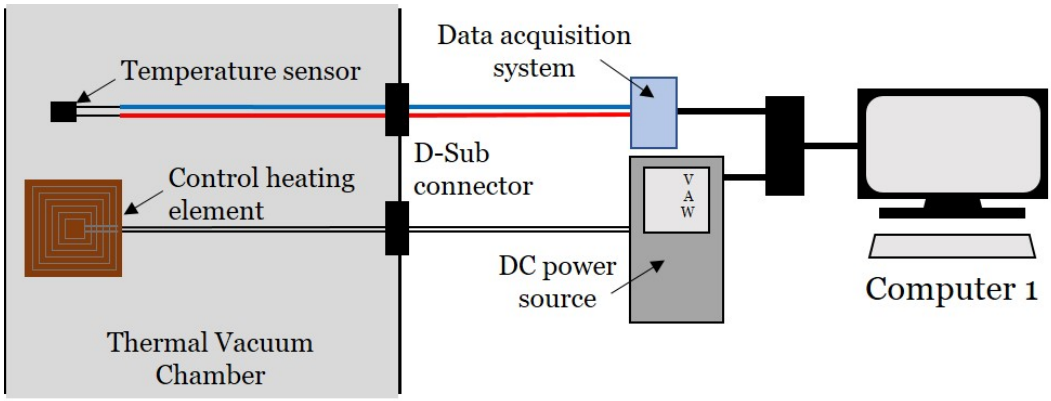

Figure B.6 schematic representation of the control and measurement loop

M422A Pt-100 temperature sensors in thin film technology are used for temperature measurement, attached to the aluminum plate and connected to a DAS for evaluation. Vacuum-compatible stranded wires are soldered to each sensor, which end at a D-sub connector plugged into the corresponding flange on the inside of the TVC. On the outside of the TVC, the stranded wires are again fed through a D-sub connection to the DAS. This in turn is connected to Computer 1 via a USB connection.

Figure B.7a shows one of the Pt-100 sensors including a size comparison. They are made from a high purity ceramic substrate, a platinum layer created by evaporation or vacuum sputtering, and a final glass layer [27]. M422 is the manufacturer's series designation. The sensors are characterized by long-term stability and high accuracy over a wide temperature range. The letter A stands for an accuracy of 0.1 K to 0.2 K in the temperature range from −50 °C to 300 °C [60].

In principle, the Pt-100 sensors determine their own temperature, which is why optimum heat transfer between the sensors and the plate is necessary. When mounting them, it is important to ensure that the contacts between the plate and the sensors are sufficiently large and aligned flat to each other. A silver-based thermal adhesive is used to mount the Pt-100 temperature sensors in shallow holes or directly on the surface of the plate, which can be seen in Figure B.7b. This is based on a two-component system and is an epoxy adhesive. As a result of the high thermal conductivity of $7.5\,\mathrm{W\,m^{-1}\,K^{-1}}$ [89], very good heat transfer is ensured between the structure and the sensor [90]. Stick-on TC for space applications are mounted as a stacked assembly using high vacuum adhesive tape and adhesive transfer tape in order to assure high thermal conductive coupling [26]. The covering tape should have the same thermo-optical properties as the objets surface the sensors are attached to in order to prevent heat sinks. If the conductive coupling due to a bad attachement is weaker than the radiative link to the surrounding environment, sensors detect colder or warmer temperatures depend-

ing on which direction the temperature gradient is pointing. This is especially relevant for solar panels or radiators where large temperature gradients are measured on both sides, although due to the mostly thin wall thickness heat conduction is the dominant effect and thus the surface temperatures should be very similar. Therefore, sensors are usually fixed on both sides and their measurements are averaged [91]. This is not possible in this experimental setup, but also not necessary. Therefore, the thermal conductive adhesive was selected, which already has the same thermo-optical properties as aluminum due to its silver content and therefore makes an additional covering of the sensor unnecessary.

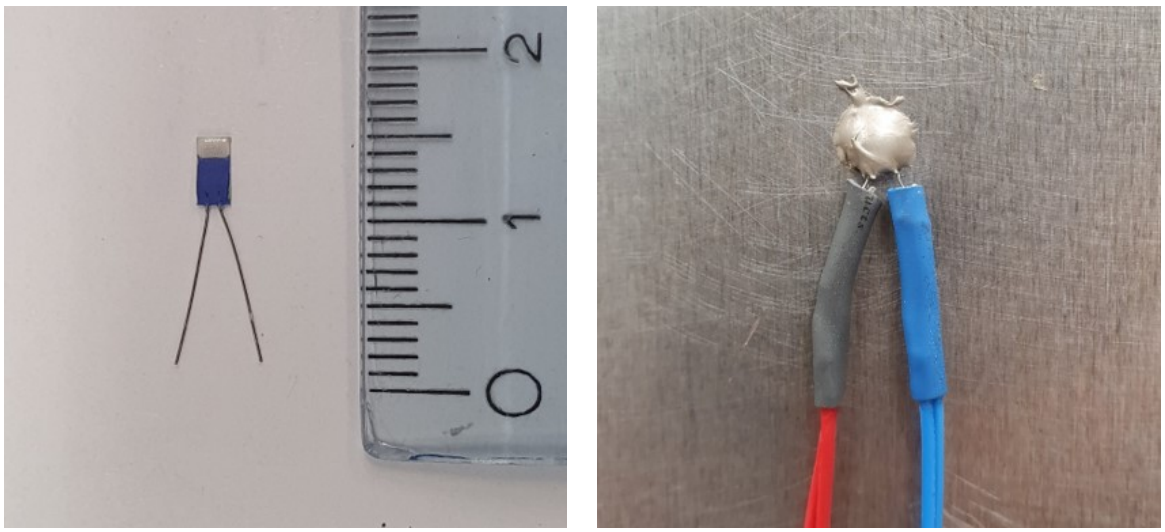

(a) Basic configuration **(b)** Attached to test object

Figure B.7 Pt-100 temperature sensor

In order to be able to determine the temperature-dependent resistance of the Pt-100 sensors, they must be connected to a measuring device. In the experimental setup, several iNet-512 [92] wiring boxes are used. They are in turn each connected to Computer 1 via the USB DAS iNet-600 [92], an analog-to-digital converter with 16 channels. The combination of those two components is shown in Figure B.8. The sensors are connected to the DAS using the 4-wire cable differential wiring. Due to the length of the vacuum suitable wires and the D-Sub connections the additional lead and connection resistance can falsify correct temperature measurements. The 4-wire measurement eliminates errors from voltage drops on current carrying wires through two measuring circuits. Within the first a known electrical current flows, which is independent of the lead and connection resistances. The voltage drop takes place at the resistor of the Pt-100 sensor itself. This drop is measured across the second measuring circuit, through which approximately no current flows due to a high-impedance shunt resistor. Ohm's law is used to calculate the electrical resistance of the sensor and the resulting temperature is derived via characteristic curves [93].

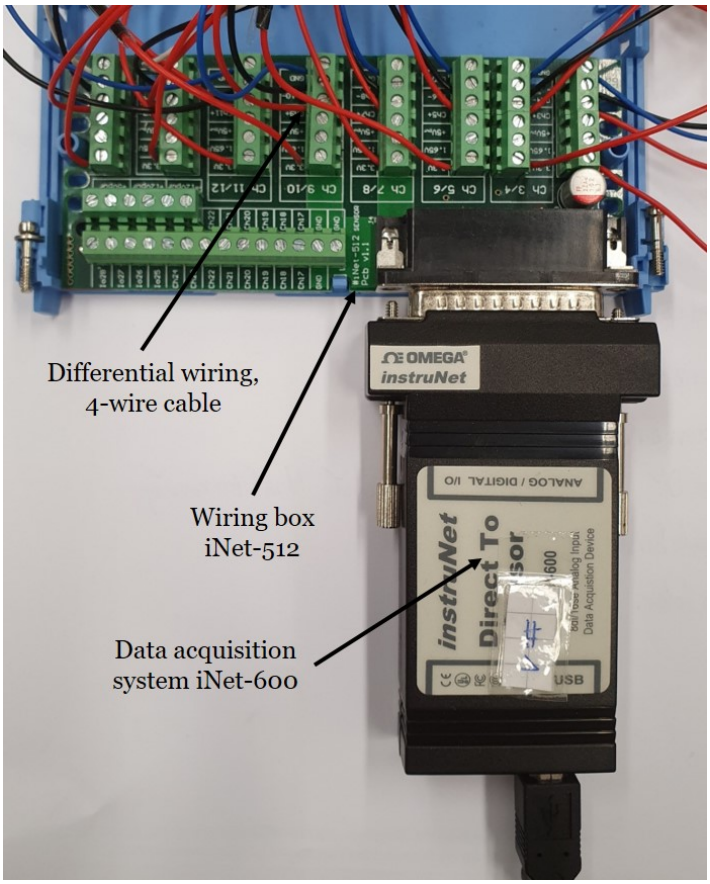

Figure B.8 Wiring box and DAS

The measured values digitized by the DAS are visualized and processed using the LabView based Data Acquisition System Laboratory (DASYLab) program [94]. The user interface of this software, shown in Figure B.9, is intuitively structured in the form of block diagrams. Each sensor is individually represented by one channel and can be calibrated, named and edited seperately. At a sampling rate of approximately 120 Hz the measured voltage signals are translated into temperature values. The measurements are merged at another block module, that digitize the values for a real-time display and form the arithmetic mean of the high-frequency sampled measurement values in order to reduce the measurement noise. One discrete value is thus generated every 1.69 s. Finally, DASYLab saves the temperature measurement values in text documents.

The number of temperature sensors is limited in the current configuration of the TVC by the available D-Sub connections. Due to the 4-wire measurement, only six sensors each and thus a total of 24 sensors can be connected to the D-sub connectors, as one connector is required for the power supply of the HEs and the lighting for the validation system. Since a large number of different error sources can influence the measurements, the Kalman filter is required.

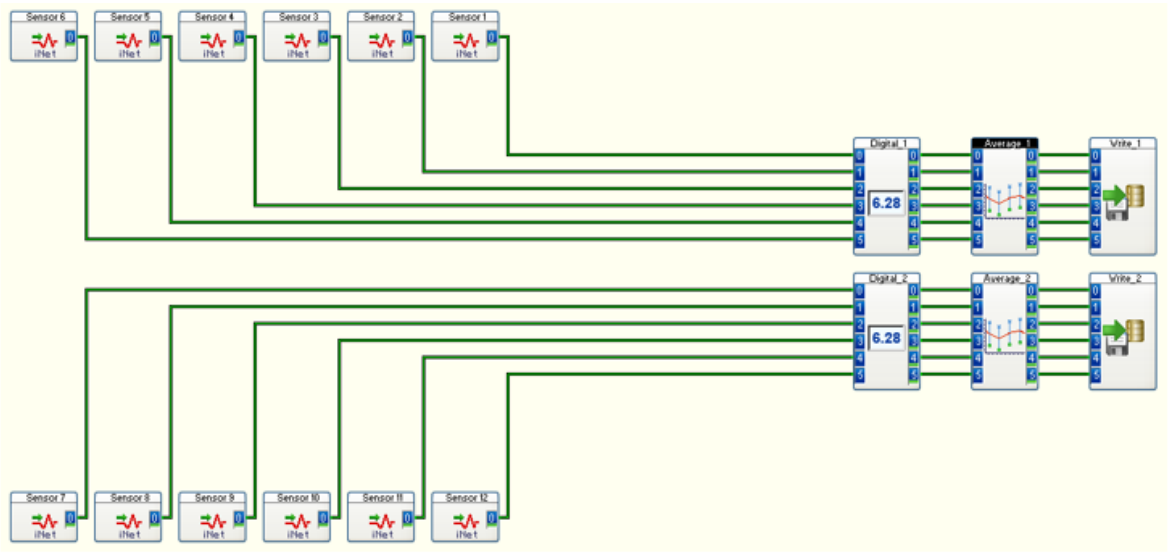

Figure B.9 User interface of the DASYLab software

B.2.2 Actuator Technology and Control

As already shown in Figure B.6, the control and measurement loop also includes an actuator component. For the approach described in this work, actuators are to be used to specifically introduce a heat change into the structure. Surface bondable HEs were selected as actuators for validating the approach. Since they must be suitable for vacuum, many commercially available HEs are not applicable, so that custom-made products must be used. The HEs selected for this experiment are heating foils made of Kapton with a special adhesive suitable for vacuum with high crosslinking capability and very good heat transfer. The heating foils are characterized by high heating power in a small area and a very uniform distribution of heat energy over the entire surface. They are available in various sizes and configurations [33]. Since the FEM model consists of regular hexahedra, heating foils with square areas that exactly match the size of a surface element are particularly well suited. Figure B.10 shows a HE of size 30 mm × 30 mm sticked onto the aluminum plate.

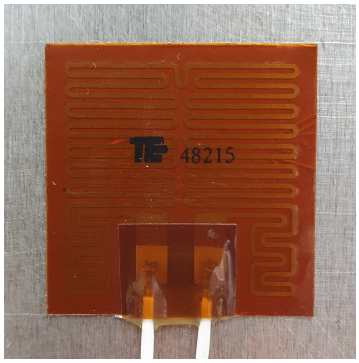

Figure B.10 Stick-on HE

Figure B.11 shows the schematic representation of the control of the perturbation elements, which is basically analogous to the command of the control elements shown in Figure B.6. The desired current or voltage values are calculated within the model on a computer and transferred to a DC voltage source via a serial interface. Those values set then generate power via Ohm's law due to the known resistance of 14 Ω of the HEs, which is converted into thermal energy at the HE. Because of the wiring from the DC voltage source through the D-Sub connector to the HE, the total resistance of the circuit increases. The resistance of the HE can be considered to be in series with the loss resistances through the wiring and connector. Since the current through each resistor in a series circuit is constant, it is possible to calculate the voltage required to be set at the DC voltage source to drop the desired power at the HE. Since each HE must be able to provide an individual heat output, each perturbation and control element is connected to an individual DC voltage source. Control via the serial interfaces is made user-friendly by the *MATLAB Instrument Toolbox*. Since measurement and control should be independent of the perturbation, the measurement and control circuit was physically separated from the perturbation so that it is connected here to a dedicated computer for just generating the random perturbations.

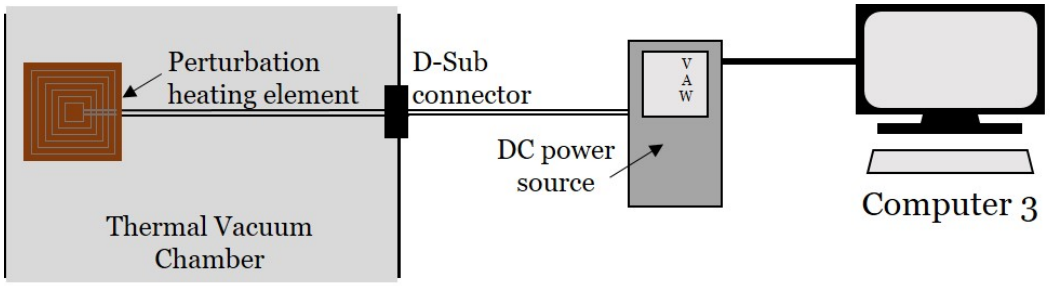

Figure B.11 schematic representation of the perturbation element

Through a large number of reference measurements, it could be shown that the HEs have an efficiency of approximately 100 % through the presented control. For this purpose, the Kapton surfaces of the HEs are modeled with the emissivity of 0.95, which is a common value in the literature [95, 96].

B.2.3 Errors of the Measuring Equipment

First and foremost, temperature measurement through the Pt-100 sensor itself is distorted and noisy. These sensors have a manufacturer-specified accuracy, in this case ranging from 0.1 K to 0.2 K. A DAS records the voltage difference between the two ends of the Pt-100 sensor and converts it into temperatures using calibrated characteristic curves. This data acquisition with the iNet-600 is as error-prone as the conversion process. To convert the voltage signal, resistance is required. This resistance increases with the long cables and additional connectors on the TVC but can be circumvented by the previously described 4-wire circuit, making the lead resistance negligible compared

to the 10 kΩ shunt resistance. However, the 10 kΩ shunt resistors themselves only have an accuracy of ± 1 %, which, in turn, affects the conversion of the voltage signals.

Since the temperature sensors measure only their own temperature, the greatest uncertainty arises from the attachment of the sensors to the plate and the associated heat coupling between the sensor and the test object. As described in detail in Section B.2.1, a silver-based thermal paste with very high thermal conductivity was used to ensure that no temperature gradient occurs between the sensor and the plate. However, depending on the quality of the attachment, deviations can still occur, which can be estimated at approximately 2 % to 3 % on average through tests before and after attachment to the plate.

Therefore, the error in temperature measurement accumulates to approximately 5 %. In addition to absolute and relative errors caused by the setup and attachment of the sensors, sensor measurements in the DAS exhibit noise with a bandwidth of about 0.3 K. Since a deviation of 5 % and significant noise that affects the use of discrete individual measurements have a substantial impact on temperature field reconstruction, suitable measures must limit these errors. A large portion of these error sources can be compensated for through averaging, filtering, and calibration. The corresponding methods are described in Section B.2.4.

For the model, an isotropic heat source of size 30 mm × 30 mm is assumed. Although the HEs have this size, the heating coils are technically confined to a smaller area. Due to the current flow through a conductor, the heating does not occur entirely uniformly. If a power of 1 W is applied to the heating element, this 1 W is converted into heat energy across the entire resistance. In addition to the manufacturer-specified resistance of 14 Ω for the heating element itself, a significantly greater total resistance is generated through the cabling and connectors to the TVC. Therefore, not all the power is dissipated at the heating element itself, necessitating a higher electrical power to generate 1 W of heat energy. Calibration is required for this, which is described in Section B.2.4.1. This calibration can only reduce the error, not fully compensate for it.

The HE has an efficiency of nearly 100 % since the electrical power is almost entirely converted into heating power. This results in heating of the HE, which, in turn, transfers its heat to the plate on one side and radiates it into the environment on the other side. The radiation from the Kapton surface is modeled with an emissivity of 0.95 and has been confirmed through measurements. Heat conduction occurs through a special vacuum-compatible adhesive film and an additional layer of aluminum, which further increases heat conduction. Nevertheless, heat transfer is not ideally uniform, so there may be minor losses, but these can be compensated by initially slightly higher electrical power. Furthermore, the resistance of the HEs is temperature-dependent, so a temperature to power characteristic must be created through calibration, which is also described in Section B.2.4.1.

Finally, the control of the HEs using the DC voltage sources is a source of error. Through the Matlab interface, only the values for current and voltage can be commanded, so the resulting electrical power is calculated according to Ohm's law. The devices can only resolve up to two decimal places accurately, resulting in an additional error of up to 1 %. Taken together, considering all these sources of error, the adjustment of the commanded power is only provided with an uncertainty of approximately 10 % when the occurring losses are taken into account. As this is also outside the required accuracy, calibration of the devices is necessary (see Section B.2.4.1). In addition, the uncertainty in actuator control is addressed through the use of the Kalman filter.

B.2.4 Calibration

The successful calibration of the sensors and actuators forms the basis for validating the model. This Section addresses the calibration of the HEs and temperature sensors, outlining the calibration procedures and presenting the resulting outcomes.

A perfect representation of the reality is not possible on both sides, the FEM model, as well as the experimental setup. The combination of model and experimental setup causes errors, especially in the interfaces with sensors and actuators.

From the thermomechanical model, simplifications are made in favor of the performance. These include the neglect of the mechanical short-term dynamics and the influences of the weight force on the plate. In addition, the plate is modelled to be in free space. Thus, thermal influences of the isostatic support and the experimental setup are negligible small. The accuracy of the FEM model is further limited by the size of the HEs as actuators, since the minimum size of a surface element in the FEM model must be equal to the size of a HE. Thus, the description of the system remains coarse, but still valid and performant.

On the side of the experimental setup, an optimal placement of the HEs and temperature sensors cannot be guaranteed. Losses occur due to bonding, cabling and radiation as well as inhomogeneous heat input due to the nature of the HEs.

The objective is to optimize the control of the HEs and improve temperature measurements to ensure consistency, repeatability, and alignment with the model. Since the calibration process differs for each configuration of the experimental setup, these steps need to be repeated for each setup. As a result, MATLAB functions are developed to read the performed temperature measurements, apply a temperature-dependent correction to the measured temperature vector, pass it to the filter and controller system, and perform a temperature-dependent resistance adjustment of the HEs based on the corrected temperature measurement.

B.2.4.1 Calibration of the Actuators

The calibration of the HEs is performed using two different methods: Since the resistance of the HEs is specified by the manufacturer with 14 Ω [33], the resistance of the wiring and feed-through can be regarded as connected in series, taking into account Ohm's law, and thus the necessary current for a desired heating power can be calculated directly. Therefore, in the first step, the specified resistance value needs to be verified, and in the second step, the additional resistance introduced by the wiring needs to be determined. This allows for the determination of the temperature dependency of the resistance, which enables the derivation of a characteristic curve.

The specific resistance ρ_R at temperature T is material-dependent and can be calculated according to Equation B.2 [97]

$$\rho_R = \rho_Z \cdot [1 + \alpha_Z (T - T_Z)] \,. \tag{B.2}$$

Here, T_Z represents the reference temperature at which the resistance is ρ_Z, and α_Z represents the temperature coefficient, which is generally referenced to 20 °C. In the temperature range from 0 °C to 200 °C, the change in specific resistance is linear with respect to temperature variation [97]. For the conducted experiments, assuming a linear relationship between temperature change and resistance change is sufficient. In addition to the inaccuracies in the HEs and the unknown total resistance caused by the circuitry, the DC power supply itself can introduce errors. Since each HE is powered by its own power supply, each HE should be operated with its corresponding power supply used in the experiment. Therefore, the two different setups for calibrating the HEs are as shown in Figure B.12.

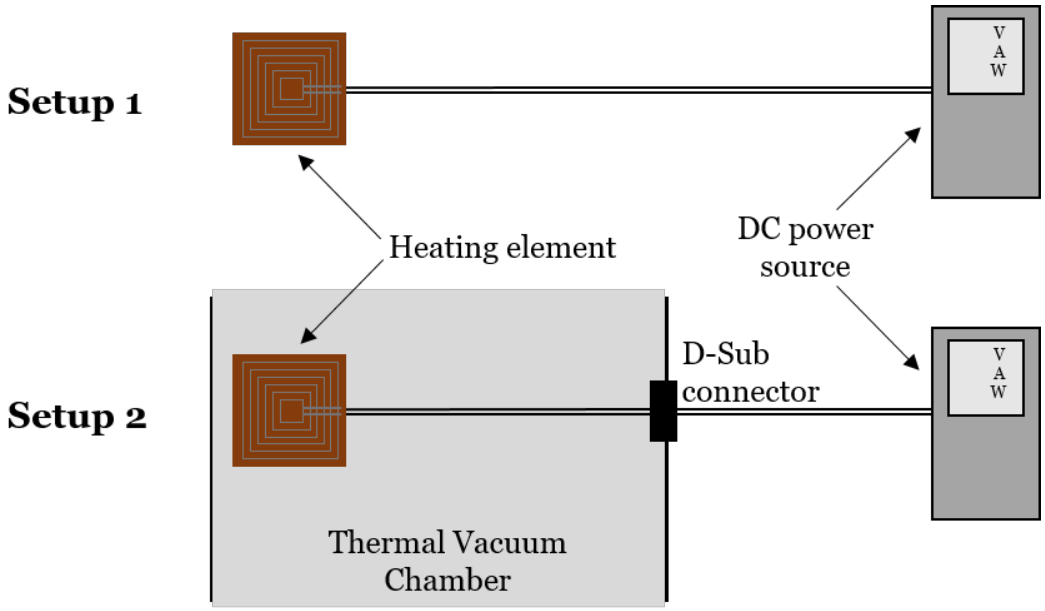

Figure B.12 Calibration setups for HEs

In the first setup, the HEs are directly connected to the power supplies without any additional wiring. In the second setup, the HEs are controlled through the D-SUB connections and additional wiring into the vacuum chamber. Additionally, the temperatures in close proximity to the HEs are measured to determine the temperature-dependent resistance characteristics. In the second setup, the vacuum chamber is evacuated and different ambient temperatures are set by the PCU, so that after a certain time in a steady state, the plate on which the HEs are mounted reaches the set ambient temperature. At each DC power supply, an output power of 1 W and 2 W is set for each setup and each temperature. For each HE, the voltage and current at the power supply are read, and the resistance is calculated from these values. The experiments are repeated multiple times and averaged. The following tables provide examples of such calibrations. Table B.2 includes the results of the calibration in setup 1 at room temperature in the laboratory. Tables B.3 and B.4 list the values of the calibration in setup 2 in a vacuum at 25 °C and 5 °C, respectively.

Table B.2 Calibration of the HEs, setup 1

Calibration of the HEs, setup 1					
HE	**Voltage** [V]	**Current** [A]	**Resistance** [Ω]	**Power** [W]	**Temperature** [°C]
1	3.76	0.26	14.46	0.99	24.0
	5.32	0.38	14.00	2.00	24.0
2	3.69	0.26	14.19	0.96	24.3
	5.26	0.37	14.22	1.96	24.3
3	3.72	0.26	14.31	0.97	24.3
	5.30	0.37	14.32	1.97	24.3
4	3.75	0.26	14.42	0.97	24.4
	5.34	0.37	14.43	1.98	24.4
5	3.77	0.27	13.96	1.01	24.4
	5.32	0.38	14.00	2.02	24.4

Table B.3 Calibration of the HEs, setup 2 at 25 °C

Calibration of the HEs, setup 2					
HE	**Voltage [V]**	**Current [A]**	**Resistance [Ω]**	**Power [W]**	**Temperature [°C]**
1	3.97	0.25	15.88	1.00	25.0
	5.60	0.36	15.56	2.00	25.0
2	3.90	0.25	15.60	0.98	25.0
	5.63	0.36	15.64	2.04	25.0
3	3.92	0.25	15.68	0.98	25.0
	5.51	0.35	15.74	1.94	25.1
4	3.94	0.25	15.76	0.99	25.1
	5.55	0.35	15.86	1.95	25.1
5	3.99	0.26	15.35	1.03	25.0
	5.56	0.36	15.44	2.01	25.0

Table B.4 Calibration of the HEs, setup 2 at 5 °C

Calibration of the HEs, setup 1					
HE	**Voltage [V]**	**Current [A]**	**Resistance [Ω]**	**Power [W]**	**Temperature [°C]**
1	3.91	0.26	15.04	1.00	5.6
	5.52	0.36	15.33	2.00	5.8
2	3.82	0.25	15.28	0.96	5.7
	5.52	0.36	15.33	2.00	5.8
3	3.84	0.25	15.36	0.97	5.5
	5.55	0.36	15.42	2.01	5.6
4	3.86	0.25	15.44	0.97	5.6
	5.58	0.36	15.50	2.02	5.8
5	3.89	0.26	14.96	1.01	5.7
	5.42	0.36	15.06	1.96	5.9

From Table B.2, it can be seen that the resistance specified by the manufacturer of 14 Ω is achieved with an accuracy of approximately 3 % through this circuit. However, since the display resolution of the power supply is only at 2 decimal places, this accuracy also corresponds to the accuracy of the power supply itself. Table B.3 clearly shows that the additional resistance introduced by the connectors and wiring is approximately 1.5 Ω.

The experiment also confirms the application of Ohm's law, as it can be observed that the same current as in the first setup is required to achieve a power of 1 W or 2 W across each HE. Table B.4 provides clear evidence supporting the hypothesis regarding the temperature dependence of the total resistance, as the resistance is, on average, approximately 0.35 Ω lower due to the 20 K lower temperature. However, the additional heat loss resulting from the additional circuit resistance is minimal and is compensated for by the temperature control of the PCU.

B.2.4.2 Calibration of the Sensors

Due to various potential measurement errors caused by the experimental setup, the accuracy of temperature sensors can deviate significantly from the manufacturer's specifications of 0.1 °C. These include device errors within the measurement instrumentation, resistance noise of resistors, self-heating of sensors due to current flow, temperature gradients in the measurement environment, resistance of the wiring, and thermoelectric voltages arising from contact points between different materials within the measurement circuit [90]. The combination of these potential errors results in a decrease in the individual accuracy of the sensors after installation and electrical connection to the data acquisition system. Hence, there is an offset, the sum of systematic and random errors, between the true and measured temperature. Some of these error sources can be corrected through sensor calibration specific to the experimental setup. Therefore, temperature sensor calibration needs to be conducted through different approaches to compensate for various types of errors.

The filter and controller system calculates the control heat fluxes based on temperature deviations from a previously achieved and system-known steady state. The goal of the first part of sensor calibration is, therefore, a uniform adjustment of temperature values based on previous steady states, ensuring reproducible and highly precise measurements. The placement and wiring of the sensors within the experimental setup were chosen to mitigate potential errors before the measurement. The four-wire measurement is used to compensate for line resistances. The measurement noise, caused in part by sensor resistance noise, is reduced through high-frequency averaging using DASYLab. The use of thermal adhesive to glue the sensors within the structure circumvents the issue of fluctuating ambient temperatures. Additionally, the self-heating effect is dampened by the adhesive, as heat is transferred to the surrounding structure.

For the first part of the calibration, the test object is positioned in the TVC, before the heaters, which exhibit different radiations due to their emissivity differing from that of the aluminum plate, are placed on it, acting as heat sinks. Various ambient temperatures are set using the PCU and kept constant for at least 24 h. This allows sufficient time for the interior of the TVC and the experimental setup to reach the ambient temperature through radiation exchange, establishing a steady-state. Thus, all sensors should show the same temperature, the steady-state temperature. Figure B.13 shows an example of such a calibration test run. It depicts the average temperature of

all sensors on the test object as well as the average temperature of the PCU. Ambient temperatures of 5 °C, 10 °C, 15 °C, 30 °C, and 35 °C were set.

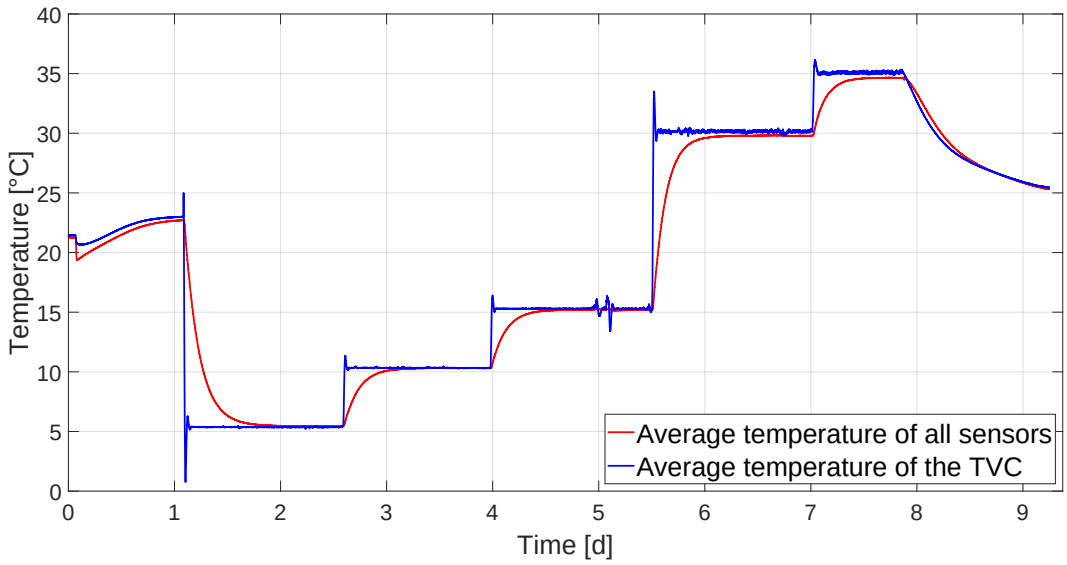

Figure B.13 Sensor calibration test run, average values

It can be observed that the PCU is unable to maintain a constant temperature consistently across all temperature ranges. This is a problem that is reflected in many test runs in the evaluation and affects some of the experimental results. As mentioned in Section B.1, the proper functioning of the PCU posed a significant problem for a long time. Although the PCU should have a temperature stability of less than 0.05 K min^{-1} [40], it is already evident here that the system was not capable of achieving that level of stability. Both software and hardware issues with the internal temperature control system arose, which could only be gradually resolved over time. The correct adjustment of the PCU by the manufacturer took almost 3 years and numerous repair works to accomplish. The calibration process shown here, spanning approximately 9 days, was taken from the first series of experiments with the first setup. Due to time and resource constraints, not all experiments were repeated with all setups after the PCU's final adjustment.

Assuming an ideal experimental setup with perfectly calibrated sensors, all temperature sensors should measure the same temperature in their respective steady-states. Figure B.14 shows the profiles of each individual sensor for this calibration test. Just by looking at the thickness of the graph, it is evident that not all sensors measure the same temperature.

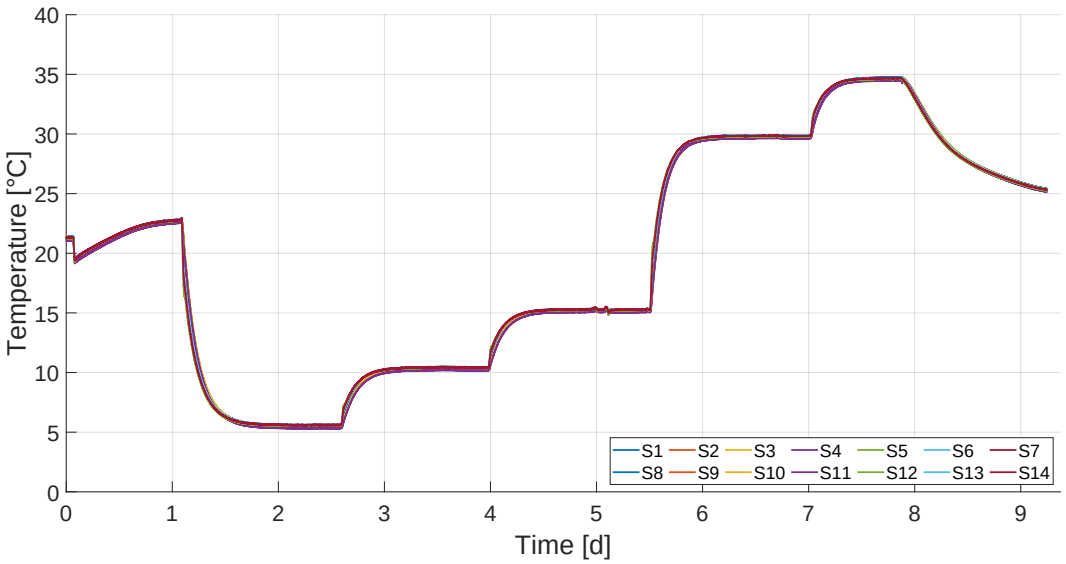

Figure B.14 Sensor calibration test run, all sensors

This becomes even more apparent when examining the detailed plot of the first steady state at approximately 5 °C, around 48 h after the start of the test, as shown in Figure B.15.

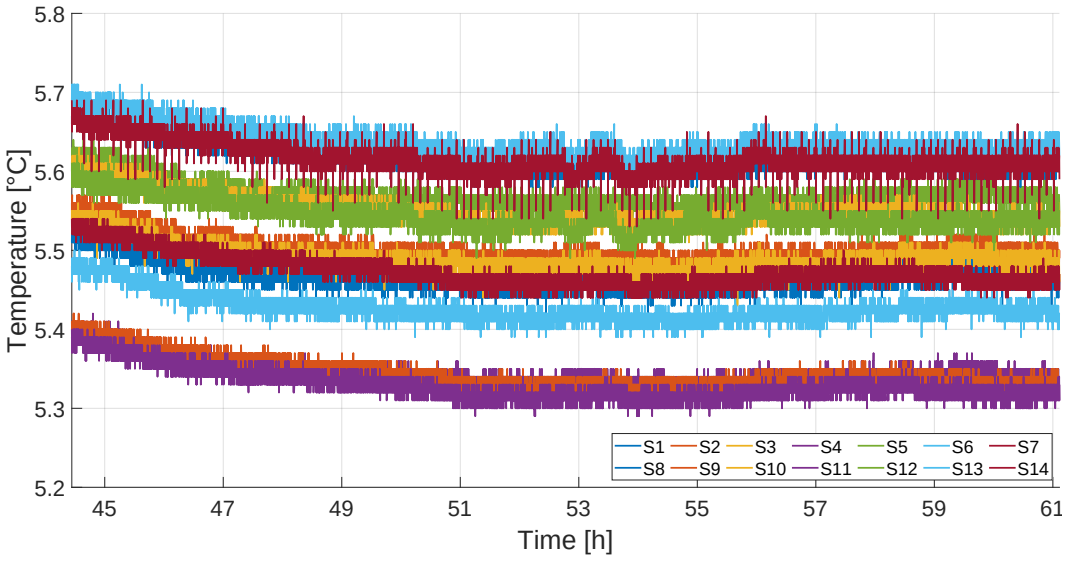

Figure B.15 Sensor calibration test run, all sensors at 5 °C

This plot illustrates several aspects:

1. The sensor measurements are highly noisy but fluctuate evenly around a mean value. Using discrete individual measurements in the filter and controller approach is therefore not recommended. Instead, smoothing can be achieved by averaging the measurements. Since only low-frequency temperature changes occur, and a control command to the HEs every 30 s is sufficient, averaging the temperature measurements over 15 s can be performed.

2. In the range of 53 h to 61 h, the individual temperature measurements of the sensors fluctuate by significantly less than 0.05 degrees. Therefore, a steady-state condition can be assumed in this range.

3. The commanded temperature value of 5 °C by the PCU is not achieved inside the TVC. This can be attributed to heat losses in the tempering medium pipes and the non-ideal insulation between the temperature-controlled inner wall of the TVC and the outer shell of the bell. Therefore, an offset between the programmed and actual ambient temperature needs to be considered in the model.

4. The deviations between the smallest and largest measurements are approximately 0.4 K with no discernible systematic pattern indicating that sensors at certain positions on the experimental setup measure higher or lower temperatures. To achieve the goal of a uniform temperature field on the aluminum alloy plate, all sensors could be offset by a certain amount so that they measure the same temperature. The average of all sensor measurements at the respective steady state would thus serve as a calibration point.

As described earlier, the sources of errors can be of various nature and can have different effects at different temperatures. Some errors may cause a constant offset in a positive or negative direction, while others may result in a linear offset. There could also be non-linear deviations that are challenging to model. Only by examining multiple steady states a correlation can be established between the deviations of individual sensor measurements and the respective mean value of all sensor measurements at the steady state. Several test runs were conducted with different steady states, as listed in Table B.5. Exemplary deviations of temperature measurements for sensors 1 and 12 from their respective mean values at each steady state are also provided in the table. It is noticeable that steady temperatures of 5 °C and 10 °C were frequently used for calibration, as they represent the temperature range in which the filter and controller approach will be validated in subsequent tests. The calibration utilizes the measured reference temperature inside the TVC instead of the commanded ambient temperature of the PCU. Consequently, it becomes evident that the measured reference temperature is higher than the commanded temperature of 5 °C due to losses through the pipes at temperatures below room temperature in the laboratory. Similarly, at higher temperatures, such as 40 °C, the measured reference temperature is lower.

Table B.5 Steady state conditions and temperature deviations

Steady state conditions and temperature deviations			
Test	**Ambient temperature [°C]**	**Deviation sensor 1 [K]**	**Deviation sensor 12 [K]**
1	5.43	0.01	-0.16
2	5.44	0.01	-0.09
3	5.46	0	-0.14
4	5.46	0.02	-0.1
5	5.46	0.01	-0.08
6	10.31	0	-0.09
7	10.33	0.03	-0.13
8	10.68	-0.01	-0.15
9	20.01	-0.01	-0.08
10	20.08	-0.02	-0.04
11	34.67	-0.1	0.01
12	39.51	-0.11	0.04

If the deviations from the respective mean values are plotted against the steady states, it is possible to form a best-fit regression line using the method of least squares [98]. These best-fit regression lines are shown for the exemplary selected sensors 1 and 12 in Figures B.16a and B.16b.

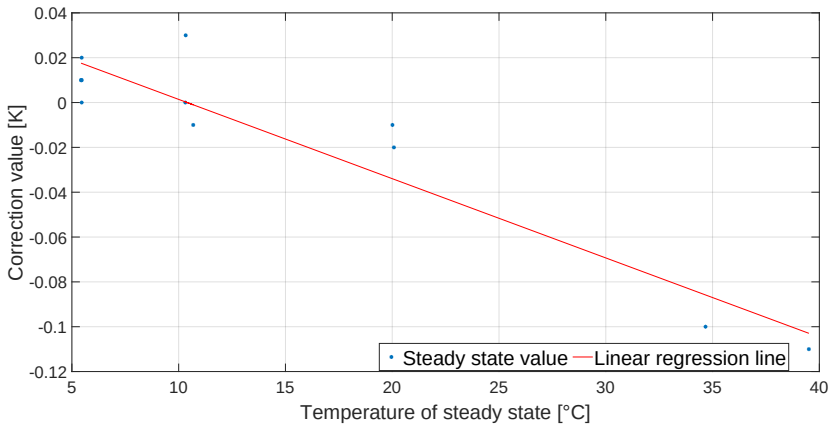

(a) Sensor 1

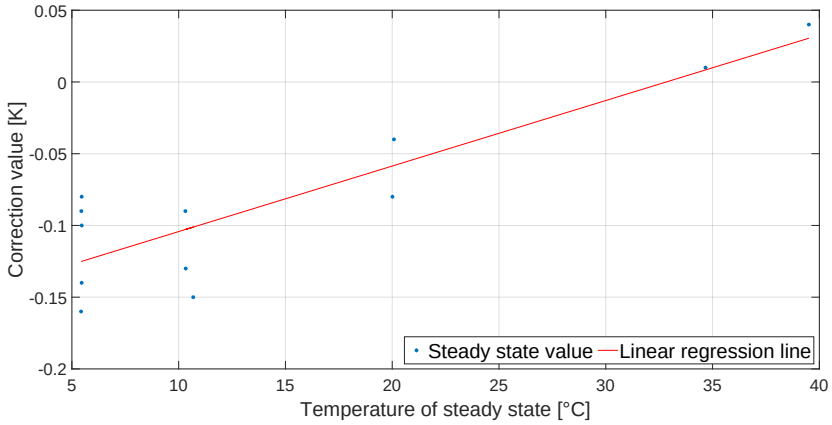

(b) Sensor 12

Figure B.16 Linear regression for the temperature-dependent sensor correction, homogeneous temperature

For each sensor, such a best-fit line is formed for each steady-state condition. Based on the mean value of all sensor measurements, a correction is then applied to each sensor measurement using the parameters of the corresponding best-fit line.

In a second calibration step, the HEs were applied to their corresponding positions for each setup, and the calibrations were repeated for different steady-state conditions. Due to the significantly higher emissivity of 0.95 for the HEs made of Kapton foil, the temperature field changes slightly in the presence of inhomogeneous states, as the radiative cooling effect is more pronounced. However, as the experiments have shown, this effect does not occur in homogeneous steady states, as all surfaces inside the TVC reach the same temperature after a sufficient amount of time.

In an extension of the calibration of the sensors for steady state, homogeneous temperature fields, the differences between the model side and the experimental side for steady state, inhomogeneous temperature fields are considered in the third part of the calibration. Inhomogeneous steady-state temperature fields are referred to as those temperature distributions that are established after at least 12 h of heating the HEs with constant power. Table B.6 lists the five tested cases, which differ in the total

power P_{tot} and control of individual HEs. The temperature field case 5 serves as the initial steady-state for most of the experimental validations for the second test setup.

Table B.6 Parameters of inhomogeneous steady state conditions

Case	HE 1	HE 2	HE 3	HE 4	HE 5	P_{tot}
1	0.5 W	0 W	0 W	0 W	0 W	0.5 W
2	1 W	0 W	0 W	0 W	0 W	1 W
3	0 W	0 W	0 W	0 W	1 W	1 W
4	0 W	1 W	1 W	0 W	0 W	2 W
5	1 W	0.5 W	0.5 W	0.5 W	0.5 W	3 W

Figure B.17a shows for different steady-state, inhomogeneous conditions, which differ mainly by the applied heating power, a linear dependence between applied total heating power P_{tot} and the average measured temperature. Figure B.17b shows the temperature deviations ΔT between simulation and measurement of one individual sensor i (here Sensor 8, exemplary) for those different steady-state conditions. The deviations are in a range of $\pm$ 0.4 K and are thus larger than the standard deviation of the sensors, which is why they must be compensated. This systematic deviation can be attributed to errors of the model as well as those of the experimental setup, as described before. The power dependence of the resistance of the cabling seems plausible due to the observed linearity. Additionally, temperature-dependent heat sinks may occur at the bonding of the temperature sensors, which can influence the measurement behavior. Although thermal decoupling through the PTFE isostatic mounting is assumed to be perfect, heat transfer can still occur with increasing power and, consequently, temperature. Furthermore, the mounting system consisting of the aluminum extruded profiles are neglected in the simulation, so the experimental setup is modelled to be only in radiation exchange with the inner walls of the TVC bell and table. This simplification has proven to be valid as a first approximation and does not introduce significant errors. However, with increasing temperature gradient between the setup and its surroundings, the effects become measurable, but they could not be isolated seperately from other error sources and, hence, confirmed experimentally. It seems plausible that the effects are individually negligible but appear as a cumulative error, leading to the deviations shown in Figure B.17b.

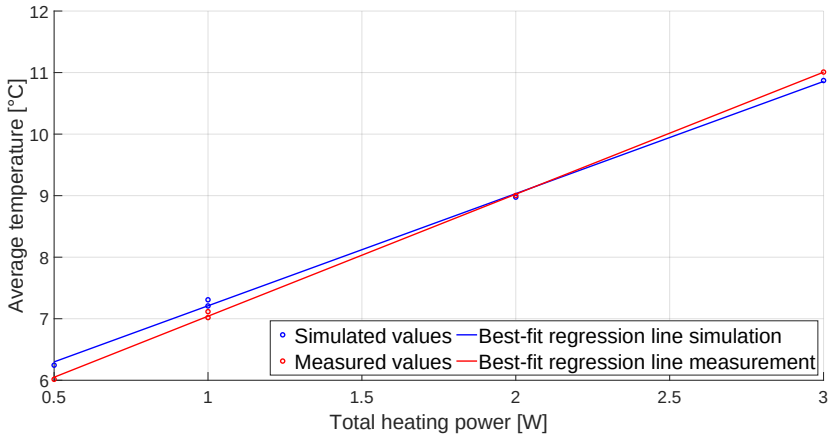

(a) $\bar{T}$ to P_{tot}

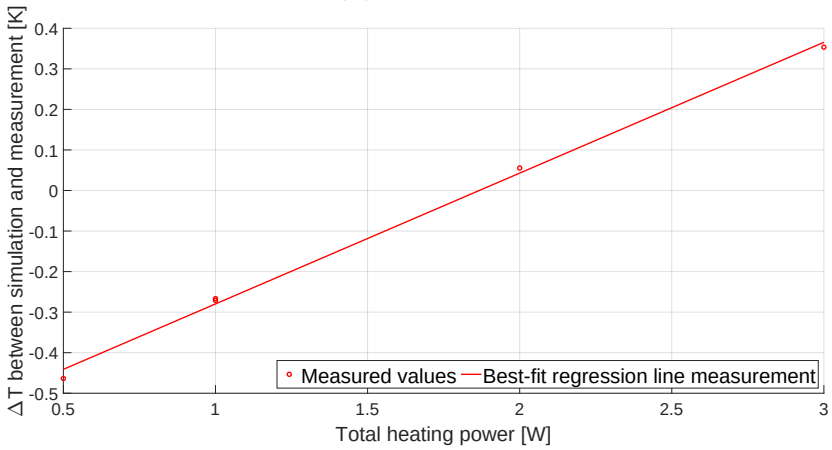

(b) ΔT to P_{tot} sensor 8

Figure B.17 Linear regression for the temperature-dependent sensor correction, inhomogeneous temperature

The model-based correction of the experimental setup would not only change transfer functions but also negatively affect the performance of the filter and controller system due to increased computational complexity. Considering the higher potential for errors in the temperature measurements, a correction of the sensor data was pursued.

This correction indirectly offers additional advantages resulting from a closer examination of the Kalman filter described in Section A.4.3. The Kalman filter calculates an optimized estimate from the weighted average of measured and modelled temperature values. The weighting of the measurement and model values is determined by the Kalman gain, which is calculated based on the variances [84]. Accordingly, the system noise and measurement noise are represented within the filter and controller system. The inaccuracies of the modeling are represented by the system noise [85], and inaccuracies of the measurements are represented by the measurement noise [84]. Adjusting the measured values based on the model values, i.e., calibrating the measurements to the simulation, reduces the difference between measured and model values. As a result, the weighting between measured and model temperature shifts towards

the model without changing the Kalman gain. Starting from the initial assumption that there is a higher potential for errors in the measurements, the measured values are corrected. By correcting those measured values, they can be weighted more heavily, which is achieved by adjusting the Kalman gain factor. This balance of relations can be achieved by reducing the standard deviation of the temperature sensors σ_S implemented in the Kalman filter. Hence, in Section 3.5, in cases 5 and 9, $\sigma_S = 0.075\,\mathrm{K}$ was chosen to investigate its effects on control quality and system dynamics, and to draw conclusions about the validity of the initial assumptions. To maintain the objectivity of the measurements, it is essential to ensure that only the measured values passed to the filter and controller system are corrected. This prevents potential interactions between validation and control.

In order to derive a dynamic correction function for the temperature measurements, the linear relationships were used, which can be expressed by Equations B.3 and B.4

$$P_{tot} = a \cdot \bar{T} + b, \tag{B.3}$$

$$\delta T_i = c_i \cdot P_{tot} + d_i. \tag{B.4}$$

Here a and b stand for the linear factors of the best-fit regression line from Figure B.17a and c_i and d_i for the linear factors of the best-fit regression line for each sensor i, shown exemplary for sensor 8 in Figure B.17b. The linear factors are determined from the measured values using the least squares method [98]. Combining both correlations, the measured average temperature of the plate $\bar{T}$ can be used to approximate the total applied heating power P_{tot}. By substituting this total heating power P_{tot} into Equation B.4 a temperature correction value δT_i for each sensor i can be calculated.

For each experimental setup and sensor configuration, these calibration steps need to be repeated. This places high demands on the preparation. However, once the calibration is completed, the correction values derived from Equations B.3 and B.4 can be stored and easily loaded for each validation experiment. This allows for a streamlined and efficient process during subsequent validation tests.

The calibration between simulation and experimental setup for the temperature measurements allows for the correction of errors that arise from simplifications in the FEM model and the technical implementation of the experiment in a real setup. The correction is performed efficiently without the need for complex modeling processes, by examining the sum of errors in the calibration test rather than considering individual errors in isolation.

Appendix C

Results of Further Test Cases

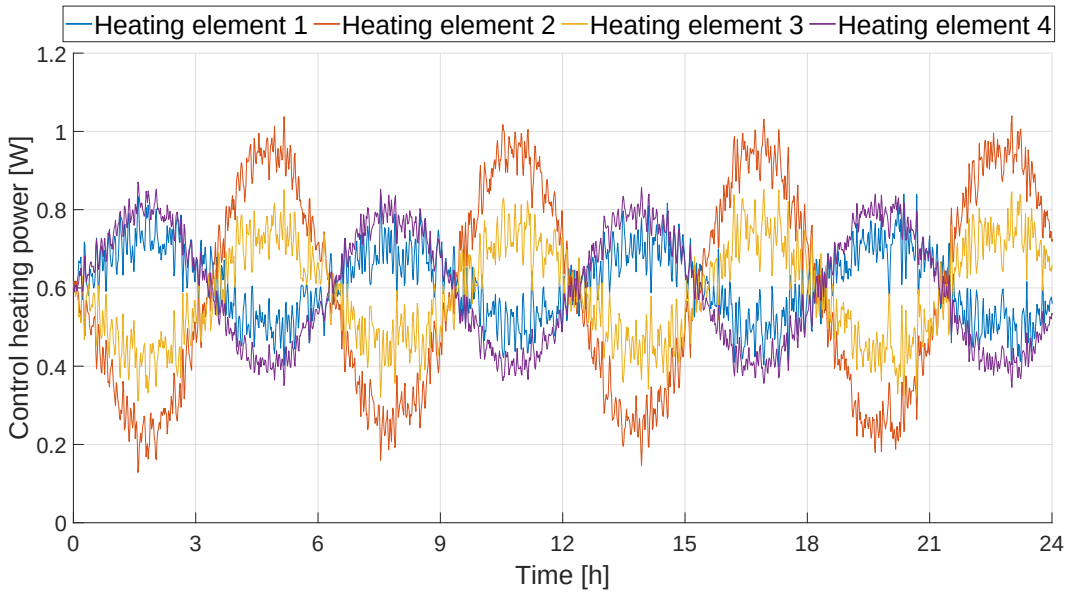

(a) Simulation

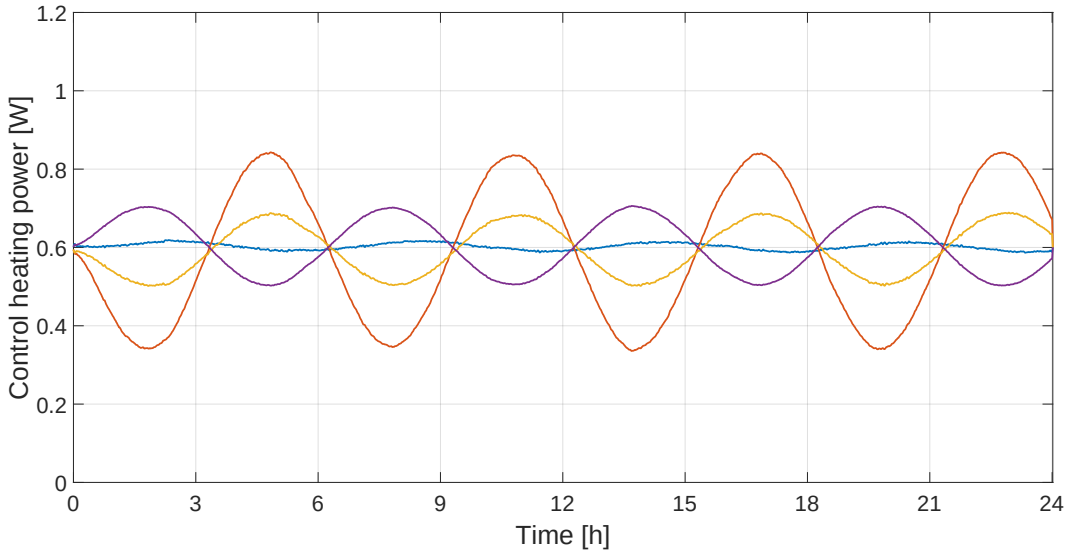

(b) Experiment

Figure C.1 Controlled case 3 with $\sigma_S = 0.18\,\mathrm{K}$ and $\sigma_H = 0.02\,\mathrm{W}$: Control heating power, configuration 1

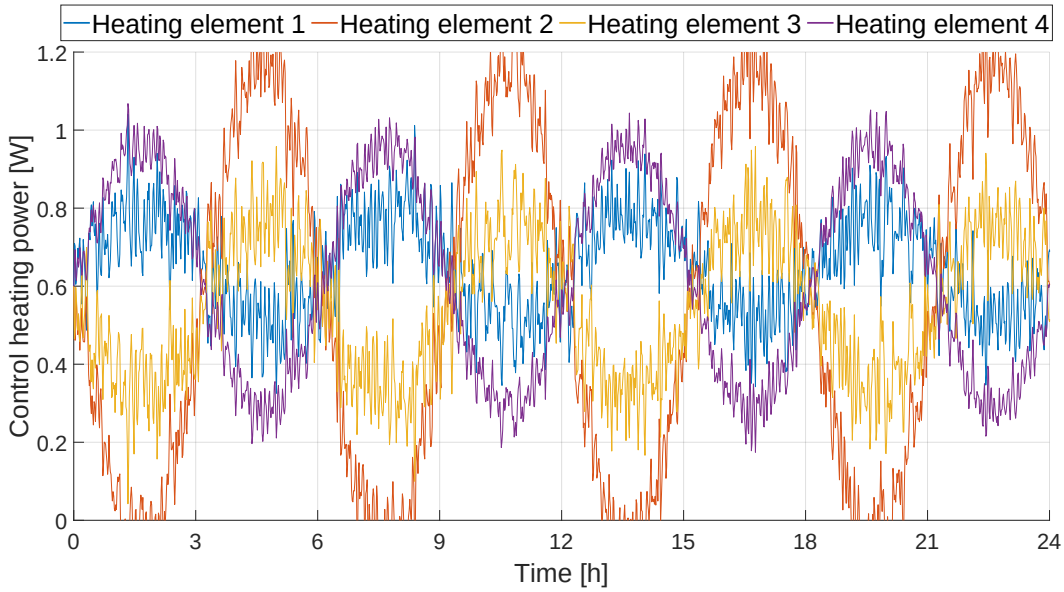

(a) Simulation

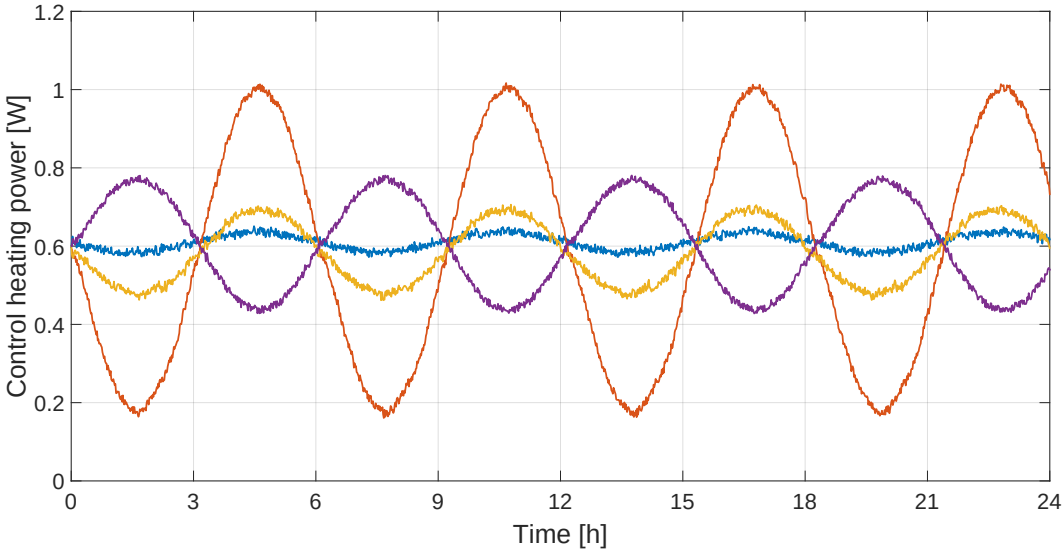

(b) Experiment

Figure C.2 Controlled case 5: $\sigma_S = 0.10\,\mathrm{K}$ and $\sigma_H = 0.02\,\mathrm{W}$: Control heating power, configuration 1

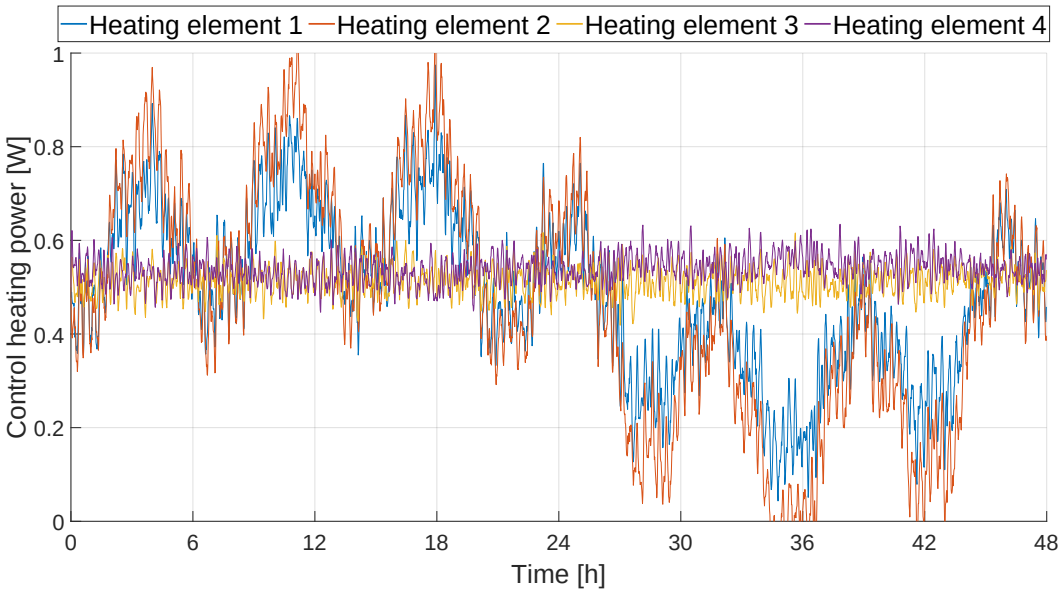

(a) Simulation

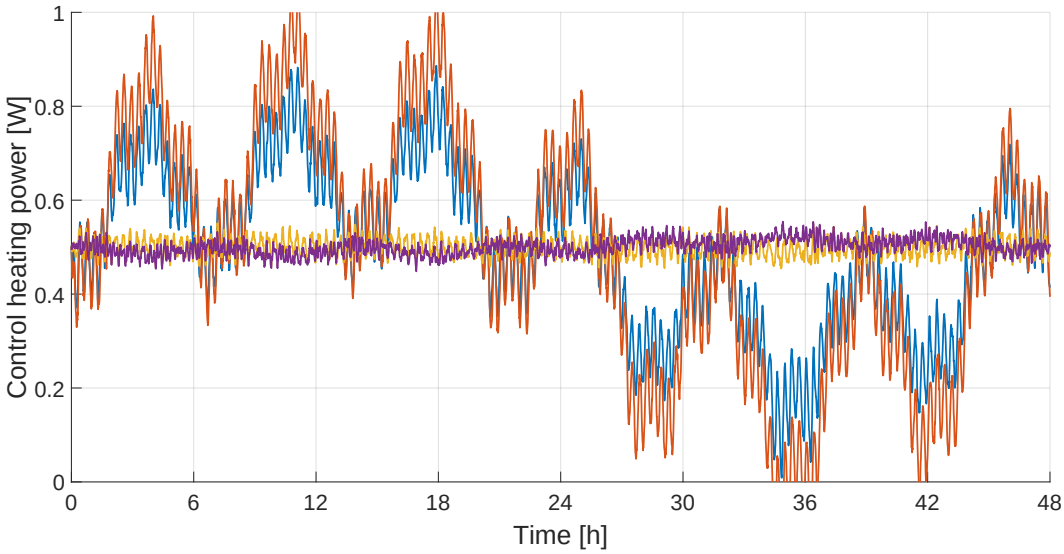

(b) Experiment

Figure C.3 Controlled case 3 with $\sigma_S = 0.10\,\mathrm{K}$ and $\sigma_H = 0.02\,\mathrm{W}$: Control heating power, random perturbation, configuration 2

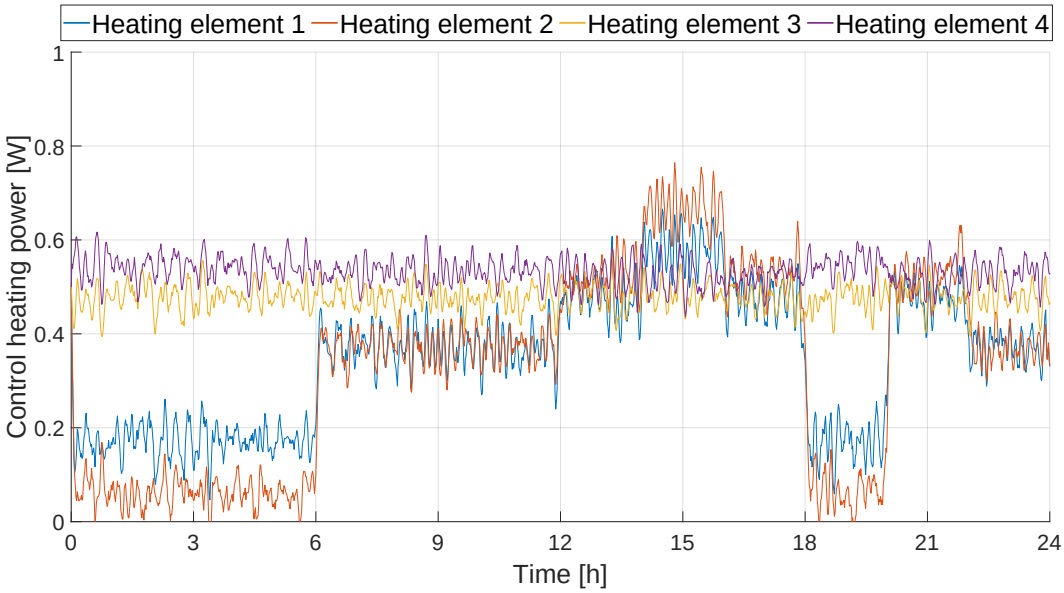

(a) Simulation

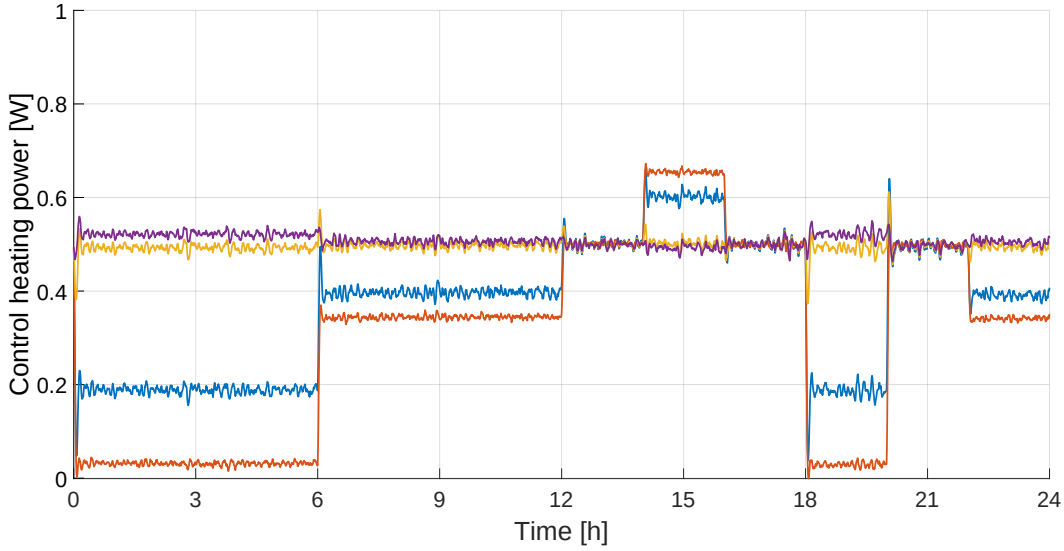

(b) Experiment

Figure C.4 Controlled case 3 with $\sigma_S = 0.10\,\mathrm{K}$ and $\sigma_H = 0.02\,\mathrm{W}$: Control heating power, stepped perturbation, configuration 2